Time varying Interaction of Europa's Atmosphere-Ionosphere and its Conducting Ocean with the Jovian Magnetosphere

Inaugural–Dissertation

zur

Erlangung des Doktorgrades

der Mathematisch–Naturwissenschaftlichen Fakultät

der Universität zu Köln

vorgelegt von

Nico Schilling

aus Chemnitz

Köln 2006

All these worlds are yours, except Europa. Attempt no landings there.

Arthur C. Clarke

Abstract

A time-dependent 3D magnetohydrodynamic (MHD) model has been developed to investigate the temporal periodic interaction between Europa and the Jovian magnetosphere. The temporal variations are caused by the periodic variations of the magnetospheric plasma at Europa. As a new feature compared to existing stationary models, periodic induced magnetic fields, caused by electromagnetic induction in a potential subsurface ocean, are included. The MHD-flow problem and the internal induction problem are solved simultaneously by making use of the periodicity and the quasi-stationarity of the problem. The ideal MHD equations have been extended in order to account for the effects of Europa's neutral atmosphere and the internal periodic induced magnetic fields on the plasma interaction.

At the beginning of this work, Galileo magnetometer data acquired on four passes by Europa were used to investigate whether a fixed permanent dipole moment is present in the interior of the moon in addition to the induced dipole moment previously identified. We thereby confirm the presence of an inductive response and find that the dipole coefficients of the constant intrinsic field contribute at best in a very minor way to the magnetic field.

The induced magnetic fields caused by the time variable plasma interaction are calculated in an interactive process. It is shown that the influence of these secondary induced magnetic fields is small compared to the induction caused by the time-varying background field. In addition, the influence of the induction on the plasma interaction is being studied. It is shown that the Alfvén current system is deformed and displaced due to the induced magnetic fields. Furthermore, the plasma wake of Europa is deformed due to the induction. The resulting structure of Europa's plasma wake could explain why Galileo measurements did not detect high plasma densities along the E4 trajectory.

By comparing the simulation results to the Galileo spacecraft measurements of three passes by Europa, we place the so far strongest constraints on the conductivity and the thickness of Europa's subsurface ocean. We find for the conductivity of Europa's ocean values of 500 mS/m or larger to be most suitable to explain the magnetic flyby data. If the ocean conductivity is less than 1 S/m, we suggest that the internal ocean has to be thicker than 25 km.

The magnetic field and the plasma density measured during the Galileo E4 flyby are reproduced fairly well in the simulation. For the agreement between the data and our model, we see no need for a deviation of the upstreaming plasma flow from the nominal corotation direction.

Zusammenfassung

Die vorliegende Dissertation beschäftigt sich mit der zeitabhängigen Plasmawechselwirkung zwischen dem Jupitermond Europa und der Jupitermagnetosphäre unter Berücksichtigung der elektromagnetischen Induktion im Satelliteninneren. Europa, der kleinste der vier Galileischen Monde, gehört besonders aufgrund der Hinweise auf die Existenz eines flüssigen Ozeans unter der Eiskruste und den damit verbundenen Spekulationen über mögliches Leben auf Europa zu den interessantesten Körpern in unserem Sonnensystem. Diese Arbeit liefert die bisher präzisesten Abschätzungen für Dicke und Leitfähigkeit eines solchen Ozeans.

Erste Anzeichen für die Existenz eines Ozeans unter der Eiskruste ergaben bereits die Beobachtungen des Voyager-Imagingexperiments [*Squyres et al.*, 1983] und später Oberflächenbeobachtungen durch das Galileo Imagingexperiment [*Carr et al.*, 1998; *Pappalardo et al.*, 1998]. Von Galileo durchgeführte Schweremessungen [*Anderson et al.*, 1998] bei Europa sind zudem mit einer äußeren Schicht Europas aus Wassereis (flüssig oder gefroren) konsistent. Eine mögliche Wärmequelle, die das Wasser unter der Oberfläche teilweise flüssig hält, wird in Gezeitenreibung gesehen [*Cassen et al.*, 1979]. Die bisher stärksten Indizien für die Existenz eines flüssigen Ozeans basieren auf den Magnetfeldmessungen der Raumsonde Galileo [*Kivelson et al.*, 2000]. In den Magnetfelddaten sind neben den Störungen durch die Plasmawechselwirkung Europas mit der Jupitermagnetosphäre Hinweise auf elektromagnetische Induktionseffekte aufgrund des zeitlich variablen Hintergrundfeldes zu erkennen. Diese Induktionseffekte könnten von einem salzhaltigen Ozean unter der dicken Eiskruste des Satelliten stammen.

In dieser Arbeit wird zum ersten Mal ein dreidimensionales zeitlich variierendes Modell zur Beschreibung der periodischen zeitlichen Variationen der Wechselwirkung zwischen dem Satelliten Europa und der Jupitermagnetosphäre entwickelt. Die zeitliche Abhängigkeit der Plasmawechselwirkung von Europa entsteht dabei durch die Rotation Jupiters, wobei die Bahnperiode von Europa, kombiniert mit der Rotationsperiode von Jupiter, eine synodische Rotationsdauer von 11.1 Stunden ergibt. Betrachtet man die innere Magnetosphäre Jupiters bis über die Europabahn bei $9.4\,R_J$ hinaus als starr mit dem Planeten verbunden, so variieren die Plasmaparameter sowie das Magnetfeld, dem Europa ausgesetzt ist, periodisch, allerdings nicht harmonisch. Das zeitlich variable Magnetfeld induziert elektrische Ströme im Ozean, die ihrerseits ein Magnetfeld aus dem Satelliteninneren hervorbringen, das die Plasmawechselwirkung stark beeinflusst.

Ein Teil des anströmenden Plasmas trifft auf die Oberfläche von Europa und wird dort absorbiert. Dies ist verbunden mit Sputtering von Sauerstoffmolekülen aus der Eisoberfläche als Quelle für die Atmosphäre. In dieser entsteht hauptsächlich durch Stoßionisation energiereicher Elektronen eine dichte, elektrisch leitfähige Ionosphäre. Aufgrund der Relativbewegung zwischen dem anströmenden Plasma und der Atmosphäre entsteht ein elektrisches Feld, welches Ströme durch die leitfähige Ionosphäre treibt, die sich in den Alfvénflügeln von Eu-

ropa fortsetzen. Das magnetosphärische elektrische Feld wird dabei teilweise kurzgeschlossen. Das Magnetosphärenplasma und –magnetfeld wechselwirken somit mit der dünnen Atmosphäre und Ionosphäre von Europa und mit dem zeitlich variablen Magnetfeld aus dem Satelliteninneren, welches hauptsächlich durch elektromagnetische Induktion entsteht. Die zeitlich variablen Plasmaeigenschaften am Ort Europas führen dazu, dass die Ströme in der Atmosphäre und im weiteren Außenraum ihrerseits induzierte elektrische Ströme und Felder im Inneren Europas erzeugen.

Als neuer Effekt gegenüber den bisherigen stationären Modellen treten in unserem zeitabhängigen magnetohydrodynamisches (MHD) Modell periodische Magnetfelder aus dem Europainneren auf, welche durch elektromagnetische Induktion in einem elektrisch leitenden Ozean unter der Eiskruste von Europa hervorgerufen werden. Mit Hilfe unseres Modells beschreiben wir die Dichte, die Geschwindigkeit, das Magnetfeld und die innere Energie des Plasmas selbstkonsistent, während wir für die Temperatur der magnetosphärischen Elektronen eine ortsabhängige Parametrisierung einführen. Der zugehörige Kalibrierungsfaktor wird durch den Vergleich der Modellergebnisse mit Vorbeiflugsdaten von Galileo zu Zeiten bestimmt, zu denen sich Europa in der Mitte der Plasmaschicht befindet, d.h. der Induktionseffekt am geringsten ist. Außerdem benutzen wir eine stark vereinfachte Energiegleichung. Der wesentliche Vorteil unseres Modells gegenüber allen früheren Arbeiten liegt in der zeitabhängigen Behandlung des Problems. Durch den Vergleich unserer Modelldaten mit den Galileodaten können bestimmte Aspekte der Wechselwirkung des Satelliten mit der Jupitermagnetosphäre besser verstanden werden als dies mit bisherigen stationären Modellen möglich war. Wir sind dadurch in der Lage einerseits der Frage nachzugehen, inwieweit das induzierte Magnetfeld die Plasmawechselwirkung beeinflusst und andererseits zu untersuchen, wie groß der Anteil der zeitlich variablen Plasmaströme am induzierenden Magnetfeld ist, d.h. inwieweit die zeitlich variable Plasmawechselwirkung die Induktion beeinflusst.

Ein kleinerer permanenter Magnetfeldanteil aus dem Inneren Europas, etwa durch Dynamowirkung, konnte bisher nicht ausgeschlossen werden. Deshalb beginnen wir unsere Arbeit mit der Frage, ob zusätzlich zu dem induzierten Anteil des inneren Magnetfeldes noch ein permanenter innerer Anteil existiert. Um diese Frage zu beantworten, passen wir Magnetfelddaten von verschiedenen Galileo Vorbeiflügen mit Hilfe einfacher Modelle an. Durch das Einbeziehen der Induktion in die Modelle wird eine wesentliche Verbesserung der Anpassung erreicht. Wir können eine obere Grenze für das innere Feld angeben, die bei ~ 25 nT liegt. Damit können wir zeigen, dass der Anteil des inneren Feldes am Gesamtmagnetfeld sehr gering ist.

Bevor wir unser komplexes Modell anwenden, untersuchen wir die Induktion in einer radialsymmetrischen Leitfähigkeitsverteilung zunächst analytisch. Wir können dadurch zeigen, inwieweit eine Bestimmung der Ozeanunterkante aus den gegebenen Daten möglich ist, und dass man bei höheren Ozeanleitfähigkeiten den Einfluss der Induktion im Mantel bzw. im Kern vernachlässigen kann.

In unserem kompletten Modell werden das MHD-Strömungsproblem im Außenraum und das Induktionsproblem im Innenraum simultan gelöst. Da dies im Direktverfahren numerisch sehr schwierig ist, benutzen wir hierfür ein iteratives Verfahren. Zu Beginn einer synodischen Rotation Jupiters geben wir als Anfangsbedingung zunächst ein zeitlich variierendes Magnet-

feld aus dem Inneren Europas fest vor. Im ersten Iterationsschritt wird dafür die analytische Lösung der Induktion durch das als homogen angenommene magnetosphärische Magnetfeld benutzt. Die Leitfähigkeitsverteilung (Ozean) im Inneren Europas wird dabei als radialsymmetrisch angenommen. Wir lösen dann für verschiedene Zeitpunkte, die gleichverteilt sind über eine synodische Rotationsperiode Jupiters, das stationäre Strömungsproblem. Mit den Ergebnissen bestimmen wir anschließend das durch die zeitlich variablen Plasmaströme induzierte Magnetfeld. Der zeitlich variierende Anteil der Kombination aus magnetosphärischem Magnetfeld und dem Magnetfeld der Plasmaströme bestimmt dann das neue induzierende Magnetfeld extern zur Ozeanoberfläche in der als nicht leitend angenommenen Eiskruste von Europa. Wir wiederholen in einem weiteren Iterationsschritt das ganze Verfahren bis der Unterschied der internen Felder aufeinander folgender Iterationsschritte klein ist.

Der magnetosphärische Anteil des induzierenden Magnetfeldes ist in sehr guter Näherung homogen in Europanähe, so dass das dadurch induzierte Feld durch ein Dipolfeld beschrieben werden kann, dessen Dipolmoment in der Äquatorebene von Europa rotiert. Das mit Hilfe unseres Modells bestimmte induzierte Magnetfeld der Plasmaströme ist komplizierter und enthält auch höhere Multipole. Die dominierenden Terme sind dabei die Quadrupolterme. Die plasmainduzierten Magnetfelder sind am stärksten, wenn Europa im Zentrum der Plasmaschicht ist und am schwächsten wenn Europa sich zwischen den zwei Extrembedingungen (Zentrum/außerhalb) befindet. Die harmonischen Koeffizienten des durch die zeitlich variablen Ströme induzierten Magnetfeldes sind deutlich kleiner als die Koeffizienten des durch das homogene Hintergrundfeld induzierten Feldes. Sie liegen damit im gleichen Bereich wie die von uns bestimmten Koeffizienten für das permanente innere Magnetfeld. Wir schließen daraus, dass der Einfluss der Plasmawechselwirkung auf die Induktion gering ist. Nahe der Oberfläche können die plasmainduzierten Magnetfelder allerdings auch Teile der unteren Ionosphäre beeinflussen. Stärkere zeitlich variable Ströme, wie sie eventuell bei Kallisto vorkommen, könnten einen wesentlich größeren Einfluss auf die Induktion ausüben.

Mit Hilfe unseres Modells können wir den Einfluss der Induktion auf die Plasmawechselwirkung untersuchen. Wir finden, dass die Berücksichtigung der Induktion zu einer Verformung und Verschiebung des Alfvènstromsystems führt, ein Effekt, der auch schon theoretisch vorhergesagt wurde [*Neubauer*, 1999]. Wenn sich beispielsweise Europa in der nördlichen Magnetfeldhemisphäre Jupiters befindet, so ist der nördliche Alfvènflügel in Richtung Jupiter versetzt, während der südliche Alfvènflügel in die entgegengesetzte Richtung verschoben wird. Infolge der Induktion kommt es auch zu Asymmetrien im Stromsystem und zu einer Verringerung des Röhrenquerschnitts.

Durch Anpassung unserer Magnetfelddaten an die vom Galileoraumfahrzeug gemessenen Daten wird eine bessere Bestimmung der Leitfähigkeit und der Dicke des Ozeans unter der Eiskruste Europas erreicht als in früheren Arbeiten. Wir benutzen dazu Daten der Vorbeiflüge E4, E14 und E26. Während dieser Vorbeiflüge befand sich Europa außerhalb der Plasmaschicht, und der Induktionseffekt war somit am stärksten. Wir finden, dass Ozeanleitfähigkeiten von mindesten 500 mS/m benötigt werden, um die Magnetfelddaten zu erklären. In diesen Leitfähigkeitsbereichen ist die Induktion für Ozeandicken größer als 100 km gesättigt, so dass eine Bestimmung der Unterkante des Ozeans leider nicht möglich ist. Die Sättigung hat auch zur Folge, dass wir keine Aussagen über eine obere Grenze der Ozeanleitfähigkeit

treffen können. Benutzen wir als Ozeandicke 25 km oder weniger, was den Extremfall einer dünnen leitfähigen Schicht repräsentiert, so werden Ozeanleitfähigkeiten von wenigstens 1 S/m benötigt. Zum Vergleich: die Leitfähigkeit von Meerwasser auf der Erde beträgt ca. 5 S/m.

In unseren Simulationen erhalten wir eine Ionosphäre, deren Dichte mit den Radio-Okkultationsergebnissen von Galileo [*Kliore et al.*, 1997] übereinstimmt. Gleichzeitig können wir auch der Fragestellung nachgehen, was mit dem ionosphärischen Plasma passiert, wenn es stromabwärts transportiert wird, und warum es nicht von Galileomessungen detektiert wurde. Auch hier spielt die Induktion eine wesentliche Rolle. Wir können zeigen, dass zum einen das Plasma in Europas Schweif in der xz-Ebene verteilt wird und zum anderen die Induktion Asymmetrien im Schweif hervorruft. Aufgrund dieser Asymmetrien sind die höchsten Plasmadichten nicht mehr im Äquatorbereich zu erwarten. In unserer Simulation erhalten wir dann Plasmadichten, wie sie auch vom Plasmaexperiment auf Galileo [*Paterson et al.*, 1999] gemessen wurden. Eine Rotation des anströmenden Plasmas, wie sie z.B. von *Kabin et al.* [1999] benötigt wurde, erachten wir nicht für notwendig.

Mit unserem Modell können wir zum ersten mal die zeitabhängige Plasmawechselwirkung Europas unter Berücksichtigung eines leitfähigen inneren Ozeans behandeln und eine Reihe interessanter Fragestellungen untersuchen. Durch die bessere Abschätzung der Ozeanparameter dürfte auch eine verbesserte Bestimmung der chemischen Zusammensetzung des Ozeans möglich sein. Im Hinblick auf die noch ungeklärten Fragestellungen, wie zum Beispiel eine genauere Bestimmung von Ozeandicke und Tiefe, wäre eine Orbitermission zu Europa wünschenswert. Die immer stichhaltiger werdenden Indizien für die Existenz eines Ozeans unter der eisigen Oberfläche von Europa, dessen Wassermassen größer sein könnten als alle Ozeane auf der Erde zusammengenommen, dürften auch zu weiteren Spekulationen über Leben im Sonnensystem außerhalb der Erde Anlass geben.

Contents

INTRODUCTION

The findings of the Galileo spacecraft supported the evidence that a large ocean of liquid water lies below the ice-encrusted surface of Europa. Since any life in the universe will probably require liquid water, the likely presence of an ocean makes Europa a prime candidate as a habitat for extraterrestrial life.

Europa is named after a Phoenician princess who, according to Greek mythology, was abducted by Zeus, who transformed himself into a white bull and carried Europa away to the island of Crete. The Jovian satellite Europa was discovered in 1610 by Galileo Galilei and is the smallest of the four Galilean moons named in his honor. Europa is very unique; it is one of the smoothest and brightest objects in the solar system.

The space exploration of Jupiter's satellite system began with the Pioneer and Voyager flyby missions which verified earth based astronomical observations of Europa and discovered new characteristics. In 1995, the Galileo spacecraft began gathering significant new discoveries about the properties of Europa's interior, surface, and atmosphere. Data from various instruments on the Galileo spacecraft indicate that an Europan ocean might exist.

In this dissertation, we study the time-dependent interaction of Europa with the Jovian magnetosphere. This includes the local plasma interaction of Europa's atmosphere and ionosphere as well as the interaction of a potential internal ocean with the magnetosphere of Jupiter. Due to Jupiter's rotation with respect to Europa and the inclination of Jupiter's magnetic dipole moment, the magnetospheric plasma density and the background magnetic field vary at the position of Europa. The time varying magnetic fields induce currents in an electrically conducting ocean below the Europan ice crust. These currents generate a time varying induced magnetic field which influences the plasma interaction. In addition, the periodic variations of the magnetospheric plasma lead to a second order induction effect. To study this time-dependent interaction, we develop, for the first time, a three dimensional single-fluid

MHD-model which includes periodic magnetic fields from the interior of the moon.

The kernel of our model is the Zeus 3D code [*Stone and Norman*, 1992*a*], an ideal time-dependent single-fluid MHD code. To account for the influence of the internal magnetic field and the neutral atmosphere, we have extended the MHD equations. With our model we describe self-consistently the density, the velocity, and the internal energy of the fluid, and the magnetic field. However, we choose a simplified equation for the internal energy, and do not calculate the temperature of the magnetospheric electrons self-consistently. In order to compensate the overestimation of the electron impact production rate, we solve a separate continuity equation for the magnetospheric electrons and implement a spatial dependent calibration factor for the temperature of the magnetospheric electrons. The main inputs of our model are the time-varying magnetospheric conditions, the neutral atmosphere, and the properties of Europa's internal ocean, which is assumed to be global.

The coupling of the internal induced magnetic fields and the external plasma interaction requires a simultaneous solution of the MHD-flow problem and the internal induction problem. This is done in our model by making use of the periodicity and the quasi-stationarity of the problem. In order to describe the diffusion of the magnetic field into the moon properly, we model the interior of Europa as a plasma with special characteristics. The calculation of the plasma induced magnetic fields is done in an iterative process.

Before we apply our complex model to Europa, we address the question whether a fixed permanent dipole is present in the interior of Europa in addition to the induced dipole moment. Therefore, data from several low altitude passes have been fitted to models of increasing complexity. Furthermore we study the induction process analytically.

One of our model's main advantages when compared to other models is our consideration of the time varying induction effects. This enables us to draw conclusions about the relative importance of the plasma induced magnetic fields, i.e., the influence of the plasma interaction on the induction process. In addition, we are also able to study the influence of the induction on the plasma interaction. We show that the internal induced magnetic field changes not only the local current system at Europa, but also affects the structure of Europa's plasma wake. The time-dependency of these effects can be observed.

One objective of our work is to compare our results with the Galileo spacecraft measurements. The simultaneous solution of the MHD-flow problem and the internal induction problem enables us to get some closer constraints on the conductivity and the thickness of Europa's subsurface ocean than earlier works.

This dissertation starts with a description of the observations which are relevant for the internal structure of Europa as well as for the local plasma interaction at the moon. We also give an overview of previous models of Europa's plasma interaction with the Jovian magnetosphere. In the third chapter we investigate whether a fixed permanent dipole moment is present in the interior of Europa. We use this as a preparatory study for our complex model described later. The classical induction problem applied to Europa is examined in chapter 4. There, we neglect the magnetospheric plasma and the atmosphere of the moon. This enables us to investigate the influence of a conducting core and a conducting mantle on the induction signature outside the moon. In addition, we get an idea as to what extent the thickness and the

conductivity of Europa's ocean can be determined. In chapter 5 we introduce our model of the plasma interaction and describe how the induction is implemented into our model. There we also describe the procedure used to determine the plasma induced magnetic fields. In chapter 6 we then present the results of our full numerical model. These results will be compared with the Galileo spacecraft in situ measurements. In chapter 7 the main contributions and conclusions of this thesis are summarized.

OBSERVATIONS AND PREVIOUS MODELS

The Galilean satellites, Io, Europa, Ganymede, and Callisto, were discovered by Galileo Galilei in 1610. Europa, the smallest of the Galilean moons, is about 90 % of the size of Earth's Moon. It is located deep within the Jovian magnetosphere. Due to an orbital resonance between Io, Europa, and Ganymede, Europa experiences tidal forces. At Io, where these tidal forces are strongest, they drive strong volcanic activity. At Europa this tidal flexing is thought to provide sufficient energy to liquefy some portion of Europa's icy crust. The presence of liquid water as well as evidence for relatively recent geologic activity are suggested by Voyager and particularly by Galileo measurements.

The magnetospheric plasma couples basically to the rotation period of Jupiter, which is smaller than the orbital period of Europa (see table 2.1). Therefore, the plasma flows past Europa, and the tenuous atmosphere of Europa interacts with the Jovian magnetospheric environment. This interaction is less intense compared to Io, but is influenced by magnetic induction effects taking place in a possible subsurface ocean.

Significant new discoveries about Europa, and the other Galilean moons were made by the Galileo spacecraft during its prime and extended missions between 1995 and 2003. In the following we give an overview of observations made in the past and relevant for our interaction model described in chapter 5. Subsequently, we discuss previous models developed for Europa's interaction with the Jovian magnetosphere.

Jupiter

Equatorial radius R_J	71492 km
Rotation period	9h 55min
Dipole field at equator	430000 nT
Dipole inclination	9.4°

Europa

Radius	1561 km
Orbital distance to Jupiter	9.38 R_J
Rotation period	3.551 days
Mean density	3014 kg/m^3

Table 2.1:   *General properties of Jupiter and Europa. After Weiss [2004].*

2.1   Properties of Europa

2.1.1   Structure and composition of the surface and the deep interior

Early Earth-based telescopic observations indicate that Europa's surface is predominantly water ice [*Kuiper*, 1957; *Moroz*, 1966]. The first close-up view of Europa was provided by the twin Voyager spacecraft in 1979. Voyager pictures show long cracks run for thousands of kilometers over a smooth, bright surface [*Smith et al.*, 1979b;a]. None of these features are higher than a few kilometers. The relative lack of impact craters led to the idea that Europa's surface may be remarkably young.

A number of new insights about Europa were produced by the Galileo spacecraft which was orbiting Jupiter between 1995 and 2003. High resolution data obtained with the Solid State Imaging (SSI) system show evidence of a young and thin, cracked and ruptured ice shell (e.g., *Belton et al.* [1996], *Carr et al.* [1998]). The geological observations imply that warm, convecting material lay at shallow depths within the subsurface at the time of its recent geological deformation. Global-scale tectonic patterns can be explained by nonsynchronous rotation and tidal flexing of a thin ice shell above a liquid water ocean [*Geissler et al.*, 1998; *Greenberg et al.*, 2000]. However, while the evidence for liquid water in the past is favorable, there is no unambiguous indication from spacecraft imaging that such conditions exist today [*Pappalardo et al.*, 1999].

Thermal models indicate that a significant portion of the outer ice shell could be liquid today (e.g., *Squyres et al.* [1983], *Schubert et al.* [1986], *Spohn and Schubert* [2003]). One energy source for maintaining a liquid water ocean is tidal heating caused by the three-body Laplace resonance with Io and Ganymede. This process could offset the freezing of the water ocean by subsolidus ice convection (e.g., *Cassen et al.* [1979]). The major uncertainty in modeling is the rheology of ice [*Durham and Stern*, 2001]. Also, the rate of freezing of the internal
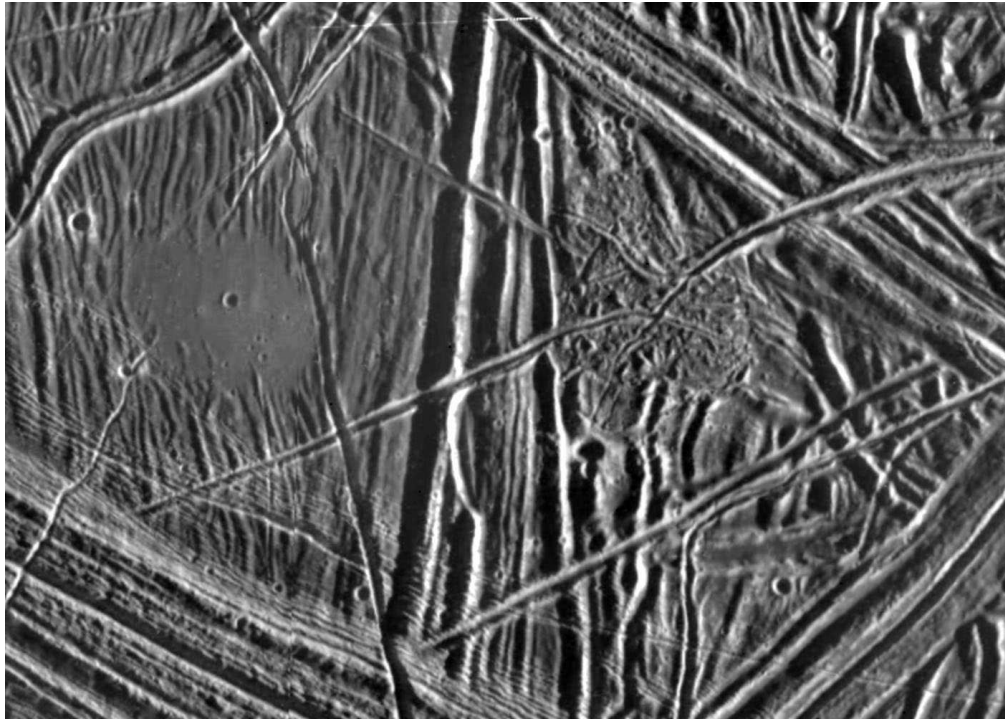
Figure 2.1:   *Close-up view of the icy surface of Europa. The view is about 11 kilometers by 16 kilometers and has a resolution of 26 meters. The Sun illuminates the scene from the east (right). (Courtesy of NASA/JPL-Caltech.)*

ocean depends on its composition, since the occurrence of minor constituents in the ice and ocean such as salts [*McCord et al.*, 1998] and ammonia [*Kargel et al.*, 1991; *Deschamps and Sotin*, 2001] effect the rheology of the ice and the freezing temperature of the ocean.

Minor species detected in the surface of Europa are H_2O_2 [*Carlson et al.*, 1999], SO_2 [*Lane et al.*, 1981] and CO_2 [*Carlson et al.*, 1996]. In addition, data from Galileo's Near-Infrared Mapping Spectrometer (NIMS) indicate the presence of hydrated salt minerals and sulfates [*McCord et al.*, 1998; 1999]. Magnesium sulfate is expected in large quantities [*Kargel et al.*, 1991; 2000] but not yet identified unambiguously [*McCord et al.*, 2001].

Analyses of the radio Doppler data indicate that Europa is a differentiated body, consisting of a metallic core, a silicate mantle and a water-liquid outer shell [*Anderson et al.*, 1997a; 1998]. The radius of Europa's metallic core is uncertain in part because of its unknown composition. It could be as large as 45% of Europa's radius if the composition is Fe-FeS, or only as large as about 13% of Europa's radius if the composition is mainly Fe [*Sohl et al.*, 2002]. The thickness of the outer H_2O layer must lie in a range between 80 to 170 km, with smaller layers corresponding to larger metallic cores and smaller mantle densities [*Anderson et al.*, 1998]. Since the densities of solid ice and liquid water are very close to each other, gravity models cannot distinguish between the two.

The H_2O layer is likely composed of three sub-layers: an outer elastic ice layer, an underlying ductile layer of potentially convecting ice, and a lower layer of liquid. Estimates of the thickness of the outer ice layer range from smaller than 1 km (e.g., *Billings and Kattenhorn* [2005], *Carr et al.* [1998]) to 20 km [*Schenk*, 2002]. Thermodynamic analyses suggest that

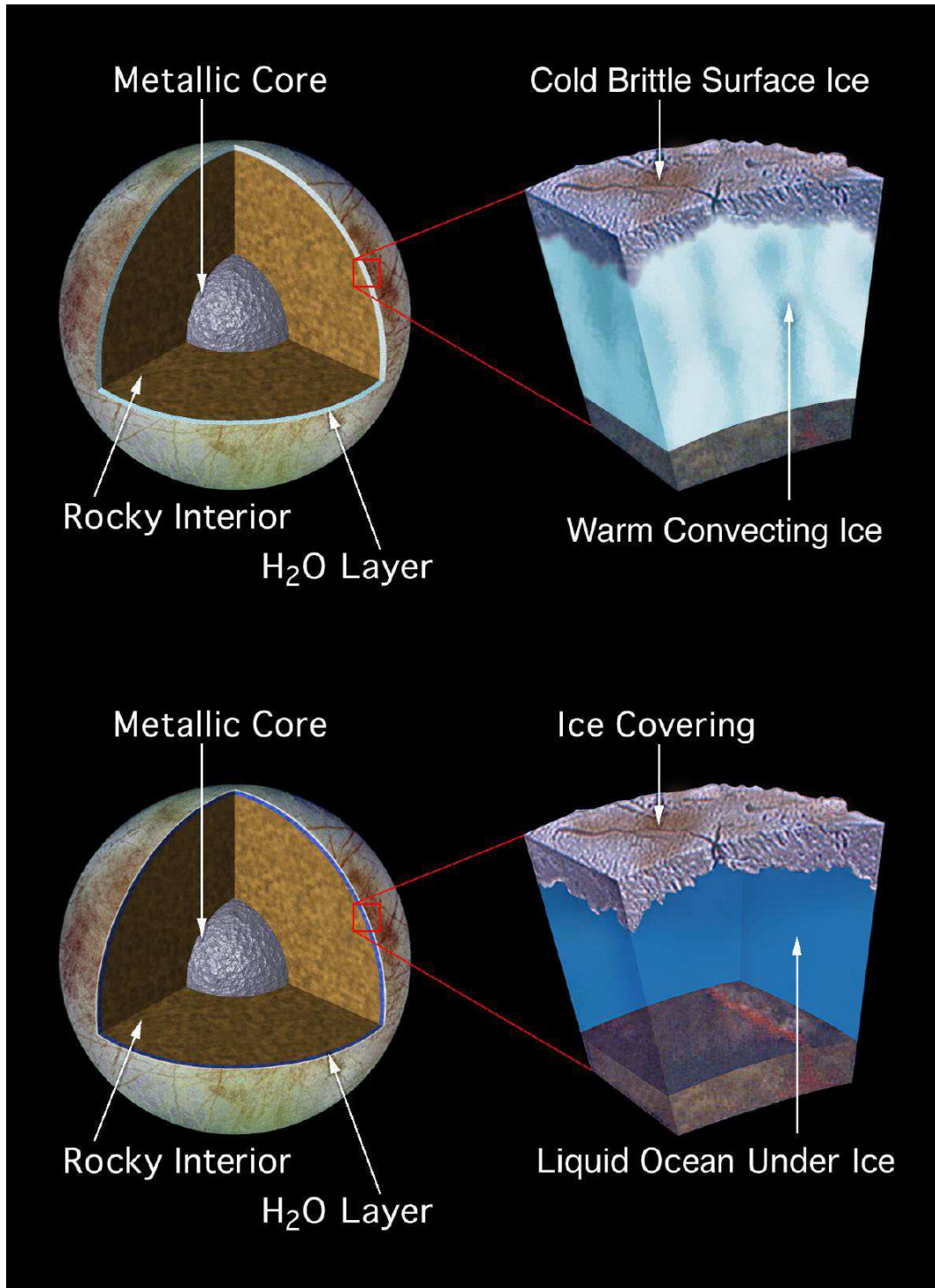***Figure 2.2:*** *Artist's drawings of two proposed models of the subsurface structure of Europa. The geologic features on the surface might be explained either by the existence of a warm, convecting ice layer, located several kilometers below a cold, brittle surface ice crust (top model), or by a layer of liquid water with a possible depth of more than 100 kilometers (bottom model). (Courtesy of NASA/JPL-Caltech.)*

the ocean should be located at a depth of 30 to 60 km [*Hussmann et al.*, 2002; *Spohn and Schubert*, 2003].

2.1.2 Neutral atmosphere and ionosphere

Europa's atmosphere was first detected by *Hall et al.* [1995] using the Hubble Space Telescope Goddard High–Resolution Spectrograph (GHRS). They observed atomic oxygen emission at 135.6 and 130.4 nm and interpreted the observed intensity ratio as evidence for electron impact dissociative excitation of O_2. The absolute intensities imply a molecular oxygen atmosphere with column density of $(1.5 \pm 0.5) \times 10^{19}$ m^{-2} on Europa. The oxygen atmosphere has been confirmed by *Hall et al.* [1998] inferring molecular oxygen column densities in the range of $\sim(2 - 14) \times 10^{18}$ m^{-2} on Europa.

The atmosphere of Europa is produced by the interaction of energetic charged particles with Europa's surface in which processes that give rise to chemical changes occur (radiolysis). Besides the ejection of surface material by energetic charged particles (sputtering), radiolysis, and radiation damage also contribute to Europa's atmosphere [*Johnson et al.*, 2004; *Paranicas et al.*, 2001; 2002]. Several numerical models to study various aspects of Europa's atmosphere have been developed. *Pospieszalska and Johnson* [1989] studied the spatial distribution of the impacting torus ions depending on their velocity distributions. *Saur et al.* [1998] find, by using a 3D plasma interaction model, that suprathermal torus ions with a contribution of thermal ions sputter O_2 from the surface water ice and that the primary loss is due to atmospheric sputtering by thermal torus ions. They also show that the re-sputtering mechanism proposed by *Ip* [1996] contributes only in a very minor way to the total sputtering rate. *Shematovich and Johnson* [2001] developed a collisional 1-D Monte Carlo model of Europa's atmosphere which was then extended by *Shematovich et al.* [2005]. They calculate atmospheric density, temperature and escape flux as a function of the surface source rate. In their model the primary atmospheric loss mechanism is electron-impact ionization and pick-up.

Recent images of Europa's atmosphere obtained with the HST Space Telescope Imaging Spectrograph (STIS) show a surprisingly inhomogeneous OI 135.6 nm emission pattern [*McGrath et al.*, 2004]. They show a maximum emission on the anti-Jovian hemisphere within the disk of Europa. This feature is not yet understood and might indicate an inhomogeneous or even dynamic atmosphere at Europa.

Atomic Na and K are observed in the extended atmosphere [*Brownlee et al.*, 1996; *Brown*, 2001]. They occur in a ratio different from that at Io, and from meteoritic or solar abundance ratios [*Brown*, 2001; *Johnson et al.*, 2002]. Therefore a subsurface source of alkalis is suggested [*Johnson et al.*, 2002; *Leblanc et al.*, 2002].

Recently, a large neutral cloud, with the most likely constituents being hydrogen and oxygen species, was detected near Europa's orbit based on Cassini's energetic neutral atom (ENA) image of the Jupiter system acquired with the Cassini Magnetospheric Imaging Instrument (MIMI) [*Mauk et al.*, 2003]. They found that this neutral cloud is comparable in its amount of material to Io's neutral cloud, which suggests that Europa's atmosphere has a substantial es-

caping flux of neutrals. The smaller oxygen component was directly observed by the Cassini UltraViolet Imaging Spectrograph (UVIS) [*Hansen et al.*, 2005].

Kliore et al. [1997] detected an ionosphere on Europa by using Galileo radio occultation measurements. They derived a maximum electron density of about 10,000 cm^{-3} with a scale height of 240 km. By assuming a radial symmetric ionosphere, *Kliore et al.* [1997] found a strong asymmetric ionosphere with maximum densities on the flanks and minimum densities downstream.

Plasma observations by *Paterson et al.* [1999] and *Gurnett et al.* [1998] have not detected a strong ionospheric signature for Europa's wake region during the E4 flyby.

2.1.3   Plasma parameters

Based on Voyager I plasma conditions at Io, *Bagenal* [1994] predicts thermal plasma densities at Europa's orbit of 35–40 cm^{-3} off the equator and values of 80–110 cm^{-3} near the equator. The analysis of the Voyager I plasma science (PLS) measurements shows that plasma electrons at Europa's orbital distance are composed of a cold component with density $n_e = 38$ cm^{-3} and temperature $T_e = 20$ eV, and a hot component with density $n_e = 2$ cm^{-3} and temperature $T_e = 250$ eV [*Sittler and Strobel*, 1987; *Bagenal*, 1994].

Ion density, bulk velocity and ion temperature were obtained during the Galileo E4 and E6 flybys by PLS plasma measurements [*Paterson et al.*, 1999]. Upstream values found for the ion number densities are ~24 cm^{-3} and ~12 cm^{-3} respectively. The observations show evidence for pickup ions in the downstream region. Also, an increase in ion densities by factors less than 3 at altitudes of 600–700 km as well as deflection of the plasma flow is observed. In addition, evidence of boundaries in the near wake that indicate a structured wake are found. Flow speeds in the upstream region are consistent within 20% of the speed of rigid corotation. Major constituents found are O^+, O^{2+} and S^{2+}.

Plasma wave observations were obtained with the PWS experiment on Galileo during various Europa flybys [*Gurnett et al.*, 1998; *Kurth et al.*, 2001]. By using the upper hybrid resonance band they determined the electron density profiles during each of the Europa flybys. The background densities vary between 18 and 250 cm^{-3} depending on Europa's position in the plasma sheet. *Kurth et al.* [2001] report that electron cyclotron emissions are often seen upstream of Europa at distances of 2–3 R$_E$, while a band of whistler mode emissions with a bandwidth of ~2 kHz centered near 3 kHz is often seen within an R$_E$ of the surface, except in the downstream region. They also observe electrostatic solitary structures in the wake of Europa.

Data from the Energetic Particle Detector (EPD) show significant count rate decreases when Galileo is in Europa's wake [*Paranicas et al.*, 2000]. For the E4 flyby they find that the energetic particle wake is shifted toward Jupiter. *Paranicas et al.* [2000] find that the radial extent of the wake is comparable to the satellite dimensions. By analyzing pitch angle distributions of energetic ions they suggest flow speeds upstream of Europa of 65–70 km/s. However, ultraviolet emissions from the footprints of Io, Ganymede and Europa studied with the HST STIS by *Clarke et al.* [2002] suggest that the plasma at Europa's position nearly corotates.

Jovian magnetic field	420 nT
Electron number density	18-250 cm^{-3}
Corotation plasma flow speed	104 km/s
Ion mass	18.5 amu
Ion temperature	100 eV
Electron temperature	100 eV
Alfvén Mach number	0.47
Sonic Mach number	0.9
Fast Mach number	0.42
Plasma beta	0.32

Table 2.2:   *Averaged plasma and field parameters of the ambient magnetospheric plasma at Europa. After Kivelson et al. [2004]*

.

Typical parameters of the ambient magnetospheric plasma at Europa are shown in Table 2.2.

2.1.4 Magnetic field

From magnetometer data acquired during the primary phase of the Galileo mission and the subsequent Galileo Europa Mission an interesting picture of the magnetic environment at Europa emerged [*Kivelson et al.*, 2000; 1999; *Khurana et al.*, 1998]. Besides magnetic field perturbations owing to the interaction of Europa's atmosphere with the Jovian magnetospheric plasma, there is evidence for electromagnetic induction taking place in the interior of Europa due to the time varying external magnetic field [*Neubauer*, 1998*b*;*a*]. Therefore, the observations support the idea, that a global subsurface conducting layer may be present. While induction signatures are clearly visible in the data when Europa is well outside Jupiter's current sheet, the strong plasma interaction dominates and hides the induction effect when Europa is close to the center of the current sheet [*Kivelson et al.*, 1999].

First bounds on the characteristics of the current carrying layer were set by *Zimmer et al.* [2000] (see section 2.2). *Neubauer* [1999] investigated the influence of the induction effects on the Alfvén wing. He showed that as a consequence of the induction effects the Alfvén wing is modified, e.g, for a small Alfvén Mach number, the maximum Alfvén wing current is reduced.

2.2   Models of Europa's magnetospheric interaction

Theoretical models of the electrodynamic interaction of a satellite with the Jovian magneto-sphere were initially developed for Io. The first model which describes the electrodynamic interaction between Io and Jupiter was the unipolar inductor model by *Piddington and Drake* [1968], which was then improved by *Goldreich and Lynden-Bell* [1969]. They proposed that Io is coupled to Jupiter's ionosphere via field-aligned currents through the magnetospheric plasma which is moving relatively to Io. Thereby they suppose the Jovian field to be frozen into Io. After the discovery of the Io plasma torus by Voyager I, the way of electrodynamic interaction had to be reconsidered and a full MHD description was necessary. *Drell et al.* [1965] developed a linear Alfvén wave model, which was extended to the nonlinear interaction case by *Neubauer* [1980]. Further aspects of the Alfvénic interaction were addressed by *Goertz* [1980] and *Southwood et al.* [1980]. *Neubauer* [1998b] developed a general Alfvén wing model which includes the unipolar inductor model [*Piddington and Drake*, 1968; *Goldreich and Lynden-Bell*, 1969] and the Alfvén wing model [*Drell et al.*, 1965; *Neubauer*, 1980; *Goertz*, 1980] as two extreme cases depending on the travel time of an Alfvén wave propagating from Io to Jupiter. A more detailed review of the theoretical concepts of the interaction can be found, e.g., in *Saur et al.* [2004].

Saur et al. [1998] developed a stationary 3D, two fluid model to describe the local plasma interaction of Europa with the Jovian magnetosphere as well as the sources and sinks of Europa's atmosphere. In their model they calculate self-consistently plasma density, velocity, and temperature for the electrons and one ion species, and the electric current and electric field, but do not self-consistently calculate the magnetic field. Besides their results on Europa's atmosphere (see section 2.1.2) they find that electron impact ionization can generate Europa's ionosphere at the electron densities measured by *Kliore et al.* [1997]. In their calculation the electron impact ionization rate is 1.9×10^{-6} s^{-1}, which is more than one order of magnitude larger than the photoionization rate.

Kabin et al. [1999] developed a 3D single fluid model which solves the ideal MHD equations. They thereby neglect recombination and have no resistivity included in the code. *Kabin et al.* [1999] calculate plasma density, velocity, pressure, and magnetic field in the vicinity of Europa and compare their results with the Galileo E4 flyby data. Their results suggest that during the Galileo E4 flyby, the plasma flow may have been deviated from the nominal corotation direction by about 20°, which was also indicated by the PLS measurements [*Paterson et al.*, 1999]. For the internal magnetic field they use a fixed permanent dipole with orientation close to that of an induced dipole.

Liu et al. [2000] studied Europa's interaction with Jupiter's magnetosphere by using a two species ideal MHD model. Two species means, in their case, they solve two continuity equations, one for the upstream magnetospheric plasma and one for the ionospheric species. According to this definition our model (described in chapter 5) can also be considered as a two species model. Although they include ion-neutral collisions in the momentum equation, they therein neglect mass loading as well as resistivity in the induction equation. They also use a fixed permanent magnetic dipole as an internal field of Europa and a rotated plasma flow upstream of Europa. *Liu et al.* [2000] compare their results with the Galileo E4 flyby data.

Zimmer et al. [2000] investigated the implications of the observed induced magnetic fields for the electrical structure of Europa's interior. By using a simple shell model they are able to sets bounds on the characteristics of the current carrying layer. They find that the magnetic signature at Europa is consistent with more than 70% of the induced dipole moment expected for a perfectly conducting sphere. Therefore, currents are required which flow in a shell with conductivity of at least 60 mS/m and close to the surface (within a 200–300 km depth). They argue that solid ice, an ionosphere or a conducting core cannot reproduce the amplitude of the observed magnetic perturbation. In addition, *Zimmer et al.* [2000] argue that it seems to be very unlikely that the magnetic signature can be explained by induction taking place in a conducting mantle only. They therefore support the idea of a subsurface ocean. However, they do not use a numerical model in order to take the plasma interaction of Europa with the Jovian magnetosphere into account. Instead they treat magnetic perturbations due to local plasma currents as noise. Therefore, a detailed numerical modeling can help to narrow the estimation of the induced fields and can thus further constrain the conductivity distribution (see also discussion in *Zimmer et al.* [2000]).

None of the numerical models so far have included periodic time varying magnetic fields, i.e., induced magnetic fields, from the interior of Europa. Therefore, we develop a model to study the time dependent plasma interaction between Europa and the time varying Jovian magnetospheric plasma. We thereby have a different approach than, e.g., *Saur et al.* [1998] who studied in detail the sources and sinks of Europa's neutral atmosphere.

LIMITS ON AN INTRINSIC DIPOLE MOMENT IN EUROPA

In this chapter we investigate whether a fixed permanent dipole moment is present in the interior of Europa in addition to the induced dipole moment previously identified. Therefore, we fit Galileo magnetometer data acquired on several low altitude passes to models of increasing complexity. This procedure is used as a preparatory study for our interaction model which is subject to later sections. We do not use our time-dependent MHD-model (described in chapter 5) for the following analysis.

3.1 Posing the problem

The magnetic field at Europa arises from a number of different sources. First, there is the time-varying background field of Jupiter that varies periodically at the moon's synodic period owing to the tilt of Jupiter's dipole moment. In addition, external magnetohydrodynamic (MHD) interaction currents (Alfvén wing currents) flow within the plasma of Jupiter's magnetosphere and close through Europa's surroundings as pickup currents and ionospheric Pedersen currents [*Neubauer*, 1998*b*]. The closure currents increase the field magnitude upstream of Europa and decrease it downstream and can therefore mimic internal moments in a limited data set. Those currents generate local magnetic perturbations near Europa. Besides these signatures, evidence for electromagnetic induction, theoretically discussed by *Neubauer* [1998*b*], was found in the data [*Khurana et al.*, 1998; *Kivelson et al.*, 1999; 2000]. The electromagnetic induction requires a global scale conducting shell close to the surface of the moon [*Zimmer et al.*, 2000]. As a consequence of the induction effects the Alfvén wing is modified *Neubauer* [1999]. In addition, it is possible that there is also a permanent internal

Flyby	System III 1965.0			Europa planetographic			Magnetospheric	
	R	Lat	W Lon	Alt (km)	Lat	E Lon	Mag Lat	Data?
E4	9.43	-0.21	156.8	695.1	-1.65	322.4	6.54	Yes
E6	9.43	-0.49	341.7	589.3	-17.02	34.7	-7.80	No MAG
E11	9.35	-0.30	222.7	2046.3	25.73	218.7	8.67	Yes
E12	9.46	-0.13	117.7	204.0	-8.66	134.3	0.91	Yes
E14	9.49	0.01	184.3	1647.1	12.20	131.2	9.15	Yes
E15	9.51	-0.32	292.8	2517.5	15.00	225.4	-0.46	Yes
E16	9.38	-0.13	123.5	1837.2	-25.65	133.6	1.78	No Data
E17	9.39	-0.65	139.9	3585.4	-42.43	220.2	3.83	Yes
E18	9.34	0.25	308.9	2273.8	41.34	139.8	-2.53	No Data
E19	9.29	-0.14	260.7	1442.4	30.52	28.1	4.83	Yes
E26	9.46	-0.58	2.3	346.4	-47.09	83.4	-9.51	Yes

Table 3.1:   *Characteristics of the Europa encounters*

magnetic moment hidden in the signatures of the above contributions to the magnetic field.

Here we look for evidence of a permanent magnetic dipole. The problem thereby is different from that addressed by *Kivelson et al.* [2002] for Ganymede where the induction effect is small compared to the permanent internal dipole moment. On Europa, there is a strong signature of an induced magnetic field, which *Zimmer et al.* [2000] have shown to be nearly in phase with the inducing background field (see their Figures 6a and b, which show that a phase delay of zero degrees gives the best fit to the B_y perturbations and that the B_x perturbations are too strongly affected by the Alfvénic bends of the field to provide a consistent estimate of the phase delay). The maximum of the inductive field appears to be significantly stronger than the permanent internal dipole field that we seek to quantify here. This fact makes it complicated to establish the properties of the internal multipoles of Europa and to separate them from the inductive response. In addition, strong perturbations are imposed by the external currents mentioned above when Europa is located near the center of the plasma sheet.

We approach the problem by fitting the data from all Europa passes at altitudes < 1800 km to increasingly complex models. The cutoff altitude is based on the following argument. For passes well off the equator, field fluctuations from local plasma currents of order 20 nT are very common. The amplitude of an inductive response to the 200 nT amplitude time varying field near Europa is less than 200 nT $\left(\frac{R_E}{r}\right)^3$. Here R_E is the radius of Europa = 1562 km and r is the distance from the center of Europa. At 1800 km altitude, this field equals 20 nT. Information on Europa encounters is shown in Table 3.1. Initially we represent Europa's internal sources as a dipole moment fixed for all flybys and seek the best fit to the data, representing the external perturbations by a uniform field that varies from pass to pass. We next allow also for an inductive response and improve the fits by determining a single additional parameter, the efficiency with which this response is generated. Next, we assume that the fixed internal permanent sources include quadrupole as well as dipole moments. Subsequently we approximate the dominant perturbations from the magnetohydrodynamic interaction with the flowing plasma of Jupiter's magnetosphere using a simplified model of

the Alfvén wing current system and solving for the field with the Biot-Savart equation.

Before proceeding with a discussion of the analysis, we need to comment on the coordinate systems used. The magnetic field of Jupiter's magnetosphere is conveniently analyzed in the EphiO coordinate system centered at Europa with its z-axis along Jupiter's spin axis ($\Omega \rightarrow$ "O" represents the Jovian spin axis direction), the y-axis along the radius vector towards Jupiter (positive inward) and the x-axis azimuthal ("phi" represents the azimuthal direction) with respect to Jupiter. The internal moments are calculated in a Europa-centered spherical coordinate system with colatitude measured from Europa's spin axis and longitude measured from the nominal Jupiter-facing meridian. The actual Jupiter-facing longitude can be as much as 2.2° off of the reference direction because of the finite eccentricity of the orbit and slight inaccuracies in the definition of the planetary longitude. These small angular inaccuracies are within the errors of fit from other sources and are therefore not considered. The 0.5° inclination of Europa's spin axis relative to the spin axis of Jupiter is also ignored. The rotation period and the sidereal period are identical to 7 significant places (IAU-2000), so it is not necessary to correct for non-synchronous rotation [*Geissler et al.*, 1998] during the Galileo mission.

3.2   Fitting Europa's Internal Sources

3.2.1   Method

3.2.1.1   Selection of Data

Coefficients for best-fit dipole models (for two of the early Galileo passes) can be found in *Kivelson et al.* [2000]. These dipole moments are inconsistent from one pass to another. Therefore, as a first step, we attempt to fit the data from all relevant passes to a single best-fit dipole moment. As discussed above, we focus only on passes that came within 1800 km of the surface so that signatures of internal sources can be clearly detected. Following the convention of labeling passes by a letter indicating the particular moon (E for Europa) and the number of the Galileo orbit on which it was encountered, we identify passes E4, E14, E19 and E26 as satisfying the altitude criterion. In order to characterize a possible permanent dipole, passes on Europa at different longitudes must be included (see Table 3.1). Figure 3.1 shows that collectively, the four passes are well separated in Europa longitude.

Pass E12 was a low altitude pass, but it occurred when Europa was located close to the center of the magnetospheric current sheet, where exceptionally large perturbations due to strong pickup are found [*Kivelson et al.*, 2000]. Because of these perturbations, it is very hard to identify contributions to the magnetic field of internal origin. Therefore, this flyby was not optimal for analysis of internal sources and was not used for our fit. However, E14 was nearly at the same Europan longitude, so elimination of E12 does not affect coverage of Europan longitudes.

Below we will show that a fixed internal dipole moment does not provide a good fit to the full data set. Improvements are significant when the effect of induction is included in the
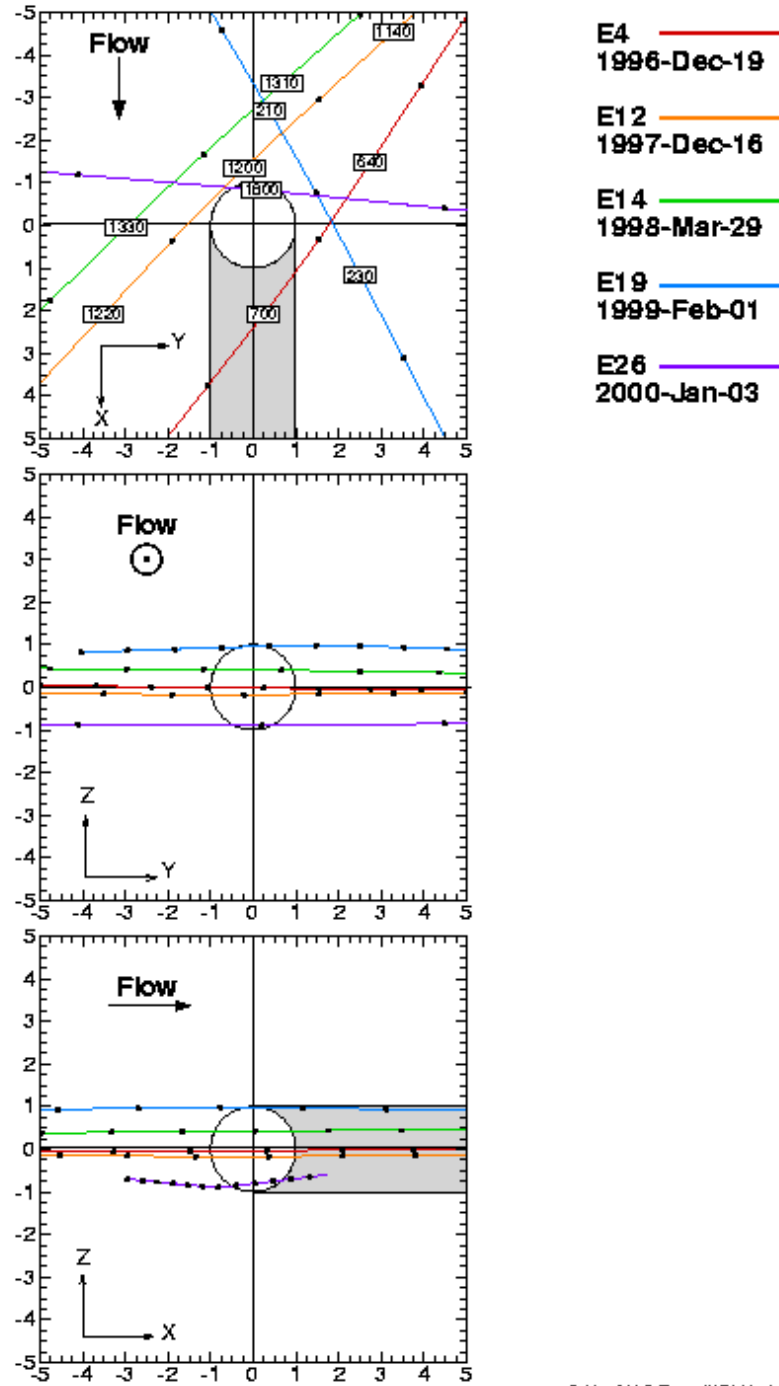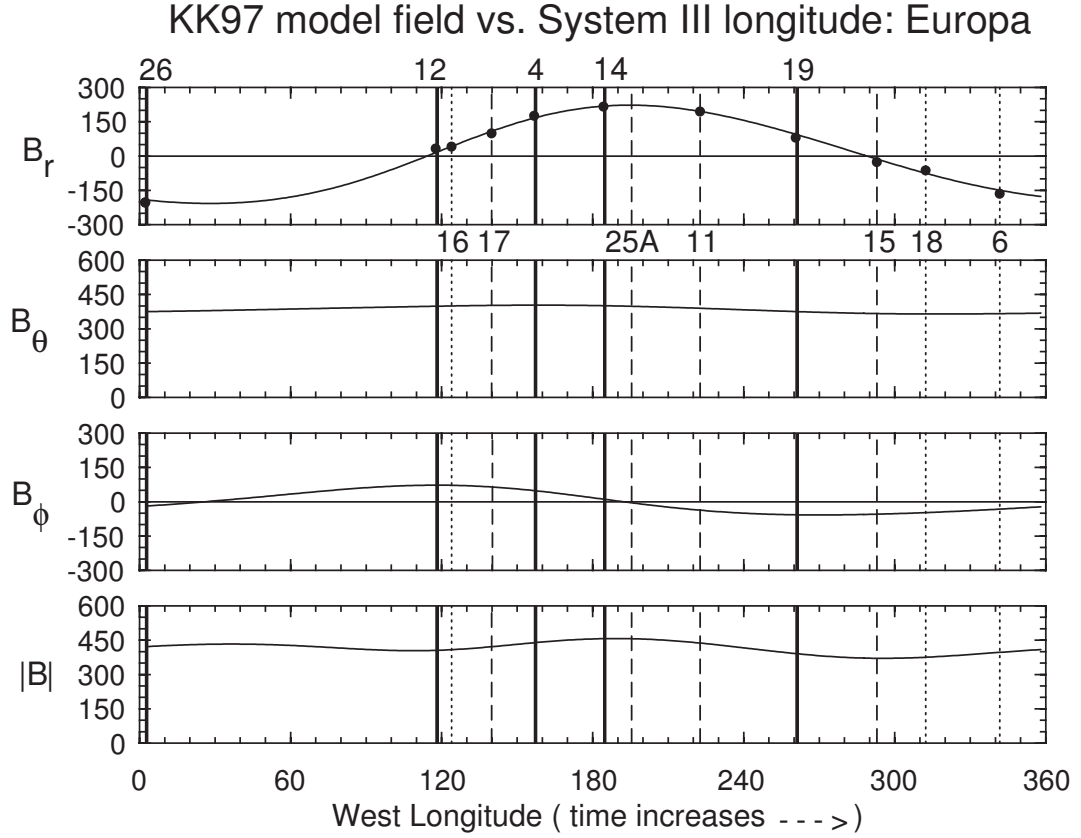
Figure 3.1: *Plots of Galileo's passes by Europa. In the Cartesian Coordinate System (EPhiO), X is along flow direction, Y is along the Europa-Jupiter vector and Z is along the spin axis.*

KK97 model field vs. System III longitude: Europa

UCLA MAG: July 10, 2001 (solid = data available, CA < 1800km
dashed = data available, CA > 1800km
dotted = no data available)

Figure 3.2: *KK97 field model [Khurana, 1997], representing the radial, polar and azimuthal components of the magnetic field at the position of Europa as a function of its west longitude relative to the origin of System III. Labels are given on top for passes below 1800 km with data and are placed above the 2nd row for passes that had no magnetometer data (dotted) or had data but were above 1800 km (dashed). Vertical markers showing where the passes occur relative to west longitude. The dots on B_r represent the value inferred from the data taken near CA on the relevant passes.*

calculations. An induced response depends on the amplitude and orientation of the external inducing field, the time varying part of Jupiter's magnetic field at Europa's location. The dominant variation is in the radial component which is outward above the magnetospheric current sheet and inward below. In order to determine whether an inductive response is present, it is critical to include data from passes at different positions relative to the current sheet. The E4 and E14 flybys occurred when Europa was well above the current sheet, while the E26 flyby occurred when Europa was located well below the current sheet as can be seen from Figure 3.2 after *Khurana* [1997]. The E19 flyby occurred when Europa was slightly above the current sheet. Because this set of passes provides measurements over the full range of orientations of the inducing field, it is well suited to determining if an induced magnetic field is present.

3.2.1.2   Mathematical Method

In order to determine the internal moments we use a least squares fitting technique described in *Kivelson et al.* [2002]. For each pass, the background field of Jupiter's magnetosphere ($\mathbf{B_{bg}}$) is obtained from a polynomial fit to the field data measured before and after the interval in the vicinity of Europa and this background field is subtracted from the data. The extrapolated background field is plotted as a black curve in Figures 3.3 - 3.6. For each of the passes (i = 1 - 4), we calculated $\delta\mathbf{B^i} = \mathbf{B^i} - \mathbf{B_{bg}^i}$ for each data point in pass i. Next the data from all four flybys were combined to form a single data set. Only those portions of the flyby data that yield information useful for characterizing internal field sources were retained. The intervals selected are tabulated in Table 3.2. In order to determine both fixed and varying internal moments, global coverage that balances the contributions from different planetary longitudes and latitudes is desired. By weighting the passes with a factor that depends inversely on the maximum perturbation encountered on the pass, we improve the sensitivity of our model to measurements taken at varying locations and at varying phases of the driving field. We avoid a disproportionate focus on modeling accurately the data from a single pass and erroneously interpreting its instantaneous inductive field as a permanent field. Without weighting, passes with clear but relatively small perturbations, whose phases and amplitudes provide valuable information, contribute virtually nothing to the model, as discussed in *Kivelson et al.* [2002]. Following *Kivelson et al.* [2002], we define the weighting factor for pass i as $w_i = \frac{|\delta B_{max}^i|}{\sqrt{\frac{1}{4}\Sigma_i(\delta B_{max}^i)^2}}$ where $\delta B^i = \sqrt{(\delta B_x^i)^2 + (\delta B_y^i)^2 + (\delta B_z^i)^2}$. Here δB_{max}^i is the maximum perturbation field strength in the *i*th pass. The measured perturbation data are related to the matrix of the model field coefficients $\mathbf{x}$ by a Matrix $\mathbf{A}$ that represents the spatial dependence of the measured data. The model parameters are determined from

$$\mathbf{x} = (\mathbf{WA^TWA})^{-1}\mathbf{WA^TW}\delta\mathbf{B} \tag{3.1}$$

where $\mathbf{W}$ is a diagonal weighting matrix composed of w_i^{-1}. In order to confirm if the model provides a good representation of the data we calculate the root mean square deviation from the data (rms). To balance contributions from passes at different altitude we calculate also the weighted rms deviation (rmsw) defined by

$$rmsw = \sqrt{\sum_{i,n}\left(\frac{\left(\delta B_{data}^{in} - \delta B_{model}^{in}\right)^2}{w_i^2}\right)\frac{1}{4N}} \tag{3.2}$$

where N is the total number of data points over all passes and $(\delta B_{data}^{in} - \delta B_{model}^{in})$ is the difference between the measured and the modeled data point n in the *i*th pass.

To validate the least square analysis and to estimate the validity of the fits we use a generalized inverse technique, referred to as Singular Value Decomposition (SVD) [*Lanczos*, 1961]. This technique is commonly used and has proved to be very useful for inversion problems in the field of applied geophysics [e.g., *Jackson* [1972]; *Pedersen* [1975]. *Connerney et al.* [1981] applied the technique to the analysis of planetary magnetic fields and *Kivelson et al.* [2002] applied the technique to infer an inductive response from Ganymede. This work relies heavily

pass	Start	Finish
E04	06:42:58	07:00:58
E14	13:10:16	13:32:16
E19	02:04:50	02:30:50
E26	17:53:02	18:07:02

Table 3.2:   *Time intervals used for calculations*

on the methodology developed in the latter paper. SVD decomposes the Matrix **A** in order to get the Least Square Inverse **H** by introducing additional matrices as follows:

$$\mathbf{A} = \mathbf{U\Lambda V^T} \;\; \Rightarrow \;\; \mathbf{H} = \mathbf{V\Lambda U^T} \tag{3.3}$$

U, Λ and **V** satisfy the following eigenvalue problems:

$$\mathbf{AA^T U} = \mathbf{U\Lambda}^2 \tag{3.4}$$

$$\mathbf{A^T AV} = \mathbf{V\Lambda}^2 \tag{3.5}$$

The properties of **U**, $\mathbf{\Lambda}$ and **V** give insights into the inversion process, and were used in the analysis described below. It is important to point out that $\mathbf{\Lambda}$ is a diagonal matrix whose elements (ordered from largest to smallest) are referred to in the geophysical literature as eigenvalues [*Jackson*, 1972; *Wiggins*, 1972; *Pedersen*, 1975]. There is ground for confusion in the nomenclature. In commonly used software like Matlab, Mathematica, and IMSL, the square root of the eigenvalues of $A^T A$ (see equations 3.4 and 3.5) are referred to as singular values yet they are identical with the eigenvalues of the geophysical literature whose conventions we follow here.

3.2.2   Europa's Internal Sources Fitted With a fixed Dipole Moment

At first data were fitted with a single centered internal dipole moment, which was not allowed to vary, and a uniform magnetic field that was allowed to vary from pass to pass. These uniform fields provide a first order approximation to the contributions arising from local plasma currents. In section 3.2.4 we model the external field more realistically. The uniform field that we begin with appears in the multipole fit as the first order external coefficients. The model requires 15 parameters: 4 different sets of 3 parameters that represent the uniform fields of the different flybys and 3 additional parameters to characterize the fixed internal dipole moment. The results are shown in Table 3.3. The calculated parameters are consistent with an internal dipole characterized by an equatorial surface field magnitude M = 79 nT tilted by 61° from the spin axis and rotated by 12° from the Jupiter-facing meridian toward the leading hemisphere. The rms-error of 32 nT is large for the entire data set and the rms of 69 nT for E26 is especially large. The same is true for the weighted rms-error (see Table 3.11).

pass	g_1^0	g_1^1	h_1^1	G_1^0	G_1^1	H_1^1	rms
	38 ± 5	68 ± 3	-14 ± 3				
E04				-17 ± 2	-7 ± 1	8 ± 1	21
E14				10 ± 1	2 ± 1	2 ± 1	8
E19				15 ± 1	-3 ± 1	-6 ± 1	10
E26				8 ± 3	-14 ± 3	10 ± 3	69
							32

Table 3.3: *Fit to a fixed dipole moment with external UMF varying from pass to pass. Units are nT for all entries.* $g_1^0 = M_z$, $g_1^1 = M_y$, $h_1^1 = -M_x$ *are the internal moment coefficients. The external coefficients of the fit relate to the uniform magnetic field components in EPhiO by* $G_1^0 = -UFZ$, $G_1^1 = -UFY$, $H_1^1 = UFX$.

There is strong evidence for an induced magnetic field on Europa [*Kivelson et al.*, 2000]. Therefore, in the second fit, we introduce an additional parameter to account for the effect of induction. The dominant variability of the background field is in the direction radial from Jupiter (Y-direction in EphiO) and to a lesser extent in the direction of corotation with regard to Jupiter (X-direction in EphiO). We assume therefore that the z-component of the induced dipole moment vanishes for all passes and that $M_x(t)$ and $M_y(t)$ respond to the time varying driving field $B_{bgx}(t)$ and $B_{bgy}(t)$ as $M_x(t) = M_{x0} - \alpha B_{bgx}(t)$ and $M_y(t) = M_{y0} - \alpha B_{bgy}(t)$. M_{x0} and M_{y0} are the X- and Y-components of the constant dipole moment, and the inductive contribution is opposite to the driving field. The factor α describes the efficiency of response to the driving field. For a perfectly conducting Europa the response factor α would be equal to 1. Values of $\alpha < 1$ arise because of finite electrical conductivity and the limited spatial dimension of the conducting layer.

Using the same fitting technique as above, we get the results shown in Table 3.4. The dipole coefficients change when induction is included. The g_1^0-term is slightly enhanced, while the g_1^1-term is strongly reduced, leading to a dipole moment with surface field magnitude M = 55 nT tilted by 16° from the spin axis and rotated by 4° from the leading hemisphere toward the anti-Jupiter-facing meridian. The reduction of the rms-error to 17 nT over the full data set and of the weighted rms-error (see Table 3.11) is considerable and this reduction provides strong support for the actual presence of induction effects on Europa. However, the response factor

pass	g_1^0	g_1^1	h_1^1	α	G_1^0	G_1^1	H_1^1	rms
	53 ± 3	-1 ± 2	-15 ± 2	1.10 ± 0.02				
E04					-20 ± 1	-8 ± 1	5 ± 1	22
E14					8 ± 1	3 ± 1	0 ± 1	6
E19					11 ± 1	-4 ± 1	-6 ± 1	8
E26					16 ± 2	-10 ± 2	6 ± 2	29
								17

Table 3.4: *Fit to a fixed dipole moment including induction with external UMF varying from pass to pass. Units of the multipole coefficients and the rms are in nT*

g_1^0	g_1^1	h_1^1	g_2^0	g_2^1	g_2^2	h_2^1	h_2^2
-17 ± 6	80 ± 3	1 ± 3	94 ± 8	80 ± 5	-10 ± 3	83 ± 5	-62 ± 4

pass	G_1^0	G_1^1	H_1^1	rms
E04	-8 ± 2	-13 ± 1	12 ± 1	17
E14	12 ± 1	4 ± 1	0 ± 1	6
E19	12 ± 1	0 ± 1	-4 ± 1	9
E26	28 ± 2	-12 ± 1	24 ± 2	56
				26

Table 3.5:   *Fit to fixed dipole and quadrupole moments with external UMF varying from pass to pass*

is somewhat over 100 %, which is unphysically high unless the currents flow in an extended ionosphere. *Zimmer et al.* [2000] showed that an ionosphere or a cloud of pickup ions is too resistive to produce the observed induction response. Nevertheless currents flowing through the ionosphere or along the Alfvén wing can produce signatures of dipole and higher order moments which are not included by using a uniform magnetic field (UMF) for the external field. Before we try to take this effect into account, we investigate if the discrepancy above can be reduced by adding higher order internal moments.

3.2.3   Europa's Internal Sources Fitted With Fixed Dipole and Quadrupole Moments

In this section we consider whether contributions of internal higher multipole moments are important. We do the calculations both including and excluding the induction effects and once again we use different uniform fields for each pass to characterize the effect of plasma currents as a first order approximation. With 5 additional parameters needed to represent the quadrupole coefficients, we now fit 21 (20 without induction) parameters. By using the same fitting techniques as above, we get the results shown in Tables 3.5 and 3.6. Again we can see that the fits are considerably improved (smaller rms-errors) when we include the induction effect.

Very apparent is the change of the dipole coefficients especially for the g_1^0-term. By comparing the coefficients in Table 3.4 and Table 3.6, one can see that the strength of the dipole coefficients drops when the perturbations are represented in terms of quadrupole coefficients. The introduction of induction changes the permanent internal dipole, which is found to have a surface field magnitude M = 39 nT, tilted by 22° from the spin axis and rotated by 18° from the Jupiter-facing meridian toward the leading hemisphere. The induction response factor is slightly reduced by the addition of quadrupole terms. However, comparing the results in Tables 3.4 and 3.6 (both including induction) one sees that the addition of internal quadrupole moments produces only a small reduction of the weighted rms-error (see Table 3.11). The improvement is not as large as would be anticipated in a model with 5 additional parameters. Also the resulting quadrupole coefficients are large compared to the dipole coefficients which

g_1^0	g_1^1	h_1^1	α	g_2^0	g_2^1	g_2^2	h_2^1	h_2^2
31 ± 5	22 ± 3	-7 ± 2	1.00 ± 0.03	68 ± 6	13 ± 4	-24 ± 2	63 ± 4	-38 ± 3

pass	G_1^0	G_1^1	H_1^1	rms
E04	-10 ± 1	-11 ± 1	8 ± 1	15
E14	7 ± 1	3 ± 1	-1 ± 1	4
E19	9 ± 1	-2 ± 1	-5 ± 1	7
E26	30 ± 2	-10 ± 2	11 ± 2	41
				19

Table 3.6: *Fit to fixed dipole and quadrupole moments including induction with external UMF varying from pass to pass*

is not realistic if the quadrupole moments have an internal origin in view of the maximum size of the core available for dynamo action. These results suggest that the external field may be poorly represented by our modeled uniform field and that plasma currents should be taken into account.

3.2.4   Model Including an Alfvén Wing Current System

In the vicinity of Europa the interaction between the ionosphere and the magnetospheric plasma plays an important role. Plasma approximately corotating with Jupiter interacts with Europa and both the field and the flow are affected. In particular, an Alfvén wing current system develops [*Neubauer*, 1980]. The interaction causes the field to drape over Europa, pulled downstream by the flow. At the same time, the closure currents enhance the field magnitude upstream of Europa and decrease it on the downstream side. As a first order approximation we can model the most important aspects of this interaction with a 'wire frame model' used for Io by *Khurana et al.* [1997] and described below. Although the interaction currents are distributed in space and the wires are not, the dominant field perturbations are represented quite well away from the local regions in which the wires are present.

3.2.4.1   Description of the Wire Current Model

In the model of *Khurana et al.* [1997], the Alfvén wing currents are modeled by current-carrying sets of wires distributed on two cylindrical surfaces that intersect the ionosphere ($R = 1.08R_E$ with the radius of Europa (R_E) equal to 1562 km) of Europa at $\pm 20°$ latitude. The wires align with the Alfvén characteristics

$$\mathbf{v_A^{\pm}} = \mathbf{v_0} \pm \frac{\mathbf{B_0}}{\sqrt{\mu_0 \rho}} \tag{3.6}$$

The current is distributed over the cylinder by a $\sin\phi$-law, where ϕ is the azimuthal angle measured from the positive x-axis and the wires are separated by $\Delta\phi = 4°$. The wires have

Pass	Ion Number Density	Total Current $\left[\frac{I}{I_{max}}\right]$		
	[cm^{-3}]	Dip+Ind	Ind	Dip+Quad+Ind
E04	75	0.14 ± 0.01	0.10 ± 0.01	0.27 ± 0.01
E14	60	0.29 ± 0.01	0.31 ± 0.01	0.25 ± 0.01
E19	150	0.22 ± 0.01	0.23 ± 0.01	0.22 ± 0.01
E26	30	0.27 ± 0.02	0.33 ± 0.02	0.31 ± 0.02

Table 3.7: *Ion number densities used and total current obtained for the different flybys in the Alfvén wing model*

a finite thickness of 0.02 R_E in order to avoid infinities. At the position of the spacecraft we calculate the magnetic field due to the Alfvén wing currents by solving the Biot-Savart equation for each wire current. The Alfvén wing current rotates the background magnetic field but should not change its magnitude, B_m. In order to impose this condition, we transform the field calculated from currents flowing in one wing into the Alfvén wing coordinate system, whose z-axis corresponds to the axis of the Alfvén wing cylinder [*Neubauer*, 1999]. We then set

$$B'_z = -\sqrt{B_m{}^2 - B'^2_x - B'^2_y} \qquad (3.7)$$

The primed quantities are in the Alfvén wing system. Thereafter we transform back to our original coordinate system. The currents are closed near the moon by three ring currents at $-20°$, $0°$ and $20°$ latitudes with a *cos*ϕ distribution around the moon. These closure currents enhance the field upstream and reduce it downstream. The currents are equally distributed among the ring currents, so that 1/3 of the total Alfvén wing current flows in each ring.

3.2.4.2 Input and Results

For each flyby we determine the current strength needed to model the data. The theoretical maximum current in one Alfvén wing is given by *Neubauer* [1980]

$$I_{max} = 4E_0 R_W \Sigma_A \qquad (3.8)$$

where E_0 is the electrical field across the moon, R_W is the radius of the Alfvén wing and Σ_A is the Alfvén conductance given by

$$\Sigma_A = \frac{1}{\mu_0 v_A \sqrt{1 + M_A^2 + 2M_A sin\theta}}. \qquad (3.9)$$

However, if the Alfvén conductivity is not negligible compared to the ionospheric Pedersen conductivity of Europa, the total current I flowing in one Alfvén wing will be less than I_{max} [*Neubauer*, 1998*b*], 1998]. Therefore we include an additional parameter $\frac{I}{I_{max}}$ which is allowed to vary from pass to pass. In this case the external parameters are $\frac{I}{I_{max}}$ for each pass, so

pass	g_1^0	g_1^1	h_1^1	α	rms
	12 ± 3	20 ± 1	0 ± 2	0.96 ± 0.03	
E04					19
E14					7
E19					9
E26					29
					16

Table 3.8:   *Fit to a fixed dipole moment including induction with Alfvén wing model*

the number of external parameters drops to 4. The ion number density, required to calculate the Alfvén velocity v_A, is estimated from PWS data measured by *Kurth et al.* [2001]. In Table 3.7 we list the ion number densities that we used and the calculated total current strengths for the different flybys. Again the background field of Jupiter was subtracted, and the fitting techniques described previously were used to infer the internal moments. The number of internal parameters to be determined drops to four: three parameters for the fixed internal dipole moment, one parameter to characterize the effect of induction.

In our model we did not take into account the effects of induction on the geometry of the Alfvén wing [*Neubauer*, 1999]. Also our Alfvén wing model (AWM) has a circular cross section; we did not allow for a distortion of the Alfvén wing. This simplification may result in a phase shift in some components of the model compared to the measured magnetic field. However, the Alfvén wing model describes the local plasma currents more realistically than the uniform magnetic field.

Results of the calculations are shown in Table 3.8. The calculated dipole coefficients differ from those found when we represented effects of external currents by using a uniform field. The resulting permanent internal dipole has a surface field magnitude M = 23 nT, is tilted by 59° from the spin axis and directed toward the Jupiter-facing meridian. The calculated response factor for the induced field is 96 %. Although the number of internal parameters is reduced to four, the rms-error (and the weighted rms-error) is comparable to those of the other models. Also we show in the discussion that using the wire current model improves the fits to some field components measured on the different flybys.

Because the dipole coefficients resulting from the calculations above are quite small, we

pass	α	rms
	0.98 ± 0.01	
E04		22
E14		6
E19		10
E26		26
		17

Table 3.9:   *Fit to induction response with Alfvén wing model*

g_1^0	g_1^1	h_1^1	α	g_2^0	g_2^1	g_2^2	h_2^1	h_2^2
42 ± 3	7 ± 1	14 ± 3	1.00 ± 0.03	9 ± 4	30 ± 3	18 ± 2	-33 ± 3	54 ± 2

pass	rms
E04	14
E14	4
E19	7
E26	30
	15

Table 3.10:   *Fit to fixed dipole and quadrupole moments including induction with Alfvén wing model*

now investigate whether any permanent internal dipole moment is required by including only induction effects. Again we subtracted the background field and the contributions from the Alfvén wing currents and used the same fitting technique as above. Results in Table 3.9 show, that the induction response is identical within the error bounds whether or not we fit permanent dipole moments. The weighted rms-error and the rms-error are comparable, with 3 fewer parameters.

To complete our investigations and as we show in the discussion to reduce the remaining discrepancy between the modeled magnetic field and the magnetic field data, we finally allow for permanent internal dipole plus quadrupole moments and induction effects, using the Alfvén wing model to describe the external local currents. Comparing the results in Table 3.10 with Table 3.8, we find an enhanced permanent dipole moment and enhanced induction response factor. The weighted rms-error decreases, but again the magnitude of the quadrupole moment of the internal field is greater than the magnitude of the dipole moment, suggesting that the additional parameters are predominantly representing external perturbations. We will discuss this later.

3.3   Discussion

We start by examining the SVD matrices to add insight into the inversion process. The ratio of the largest to the smallest eigenvalue (or, in common software packages, the ratio of the largest to the smallest singular values) gives the condition number of the matrix **A**. Although the condition number includes no information about individual parameter errors or correlations among the model parameters, it is relevant to the invertibility of matrix **A** and the accuracy of the solution. If the condition number is close to one, the matrix is well conditioned which means its inverse can be computed with good accuracy whereas large condition numbers imply inaccurate inverse matrices. Typically in applications to internal fields of planets one desires condition numbers ≤ 60 (see, for example, *Connerney et al.* [1981]). The condition numbers for the different models used are displayed in Table 3.11. One can see that the condition numbers are relatively small for all of the fits.

From the matrix **V**, estimates of the errors of the fit parameters can be obtained. The standard
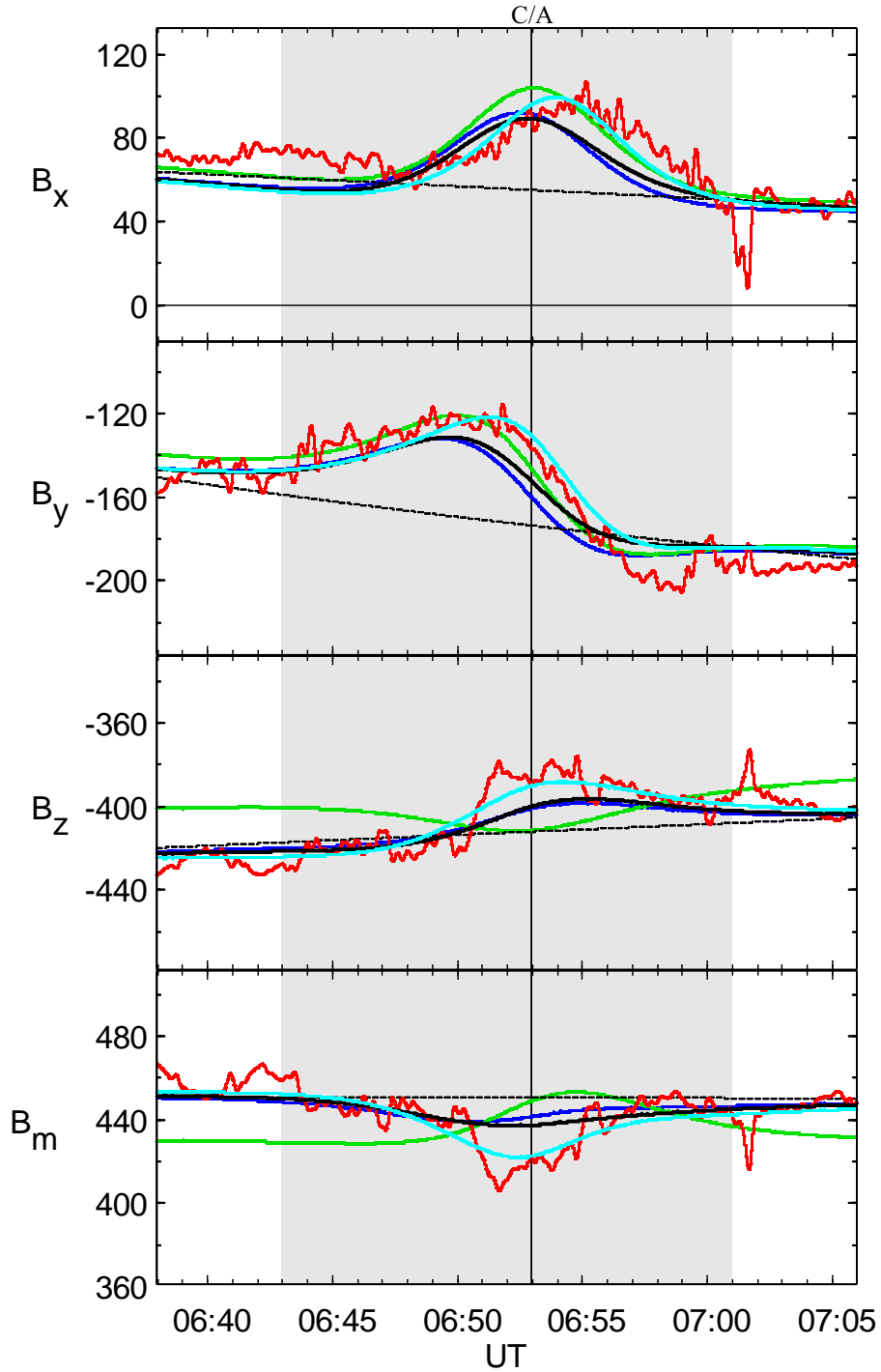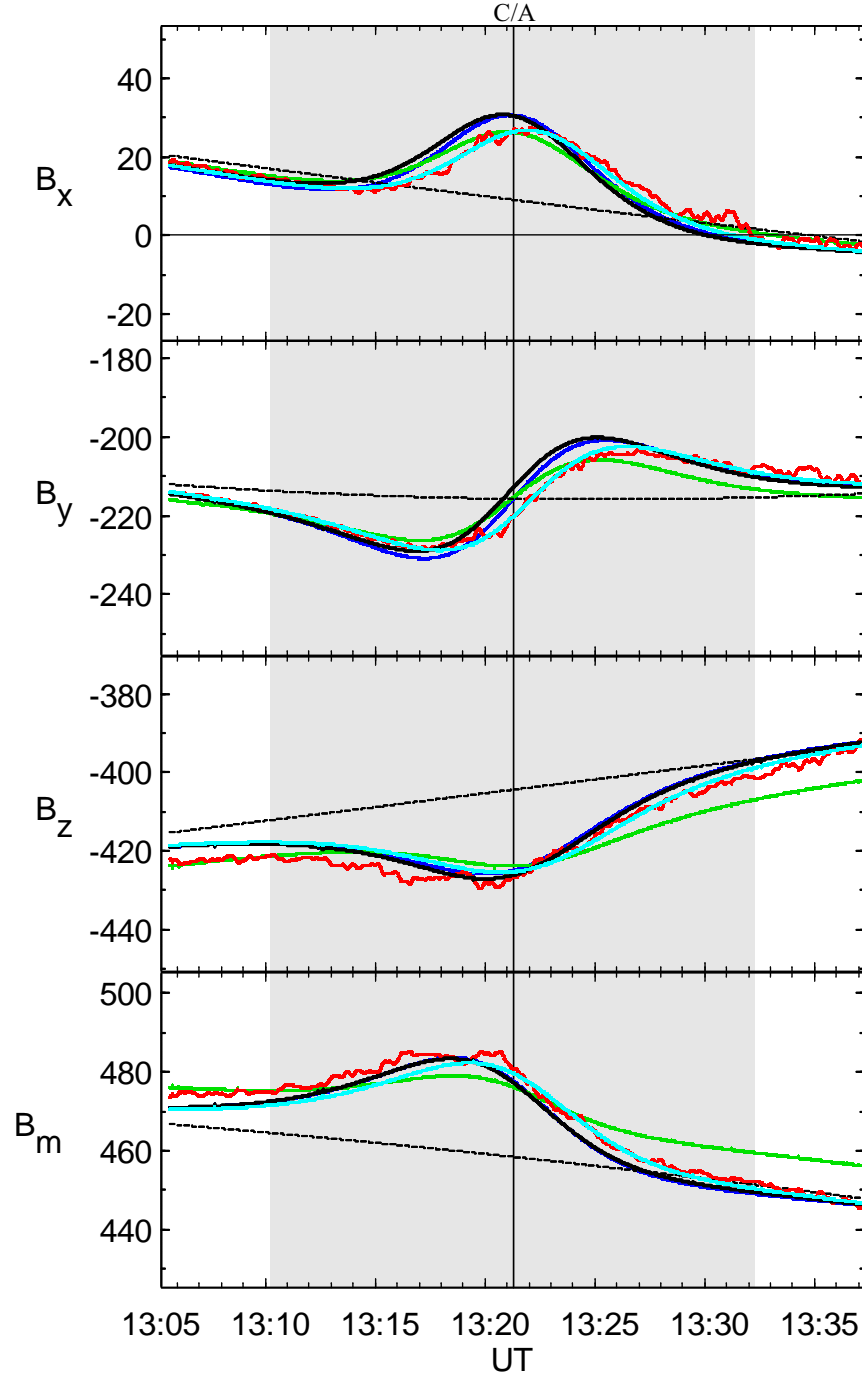
Figure 3.3: *Observed and modeled field for the Europa flyby E4 in the EPhiO coordinate system. The red curve shows the filtered measured field. The thin black curve shows the background field. The solid green curve shows the predicted field for the internal permanent dipole plus induction by using the UMF for the external field (see Table 3.3). The predicted field by using the Alfvén wing model to describe the external local currents is shown for the internal sources: induction only (solid blue) (see Table 3.9), induction plus dipole (solid black) (see Table 3.8) and induction plus dipole plus quadrupole (cyan curve) (see Table 3.10)*
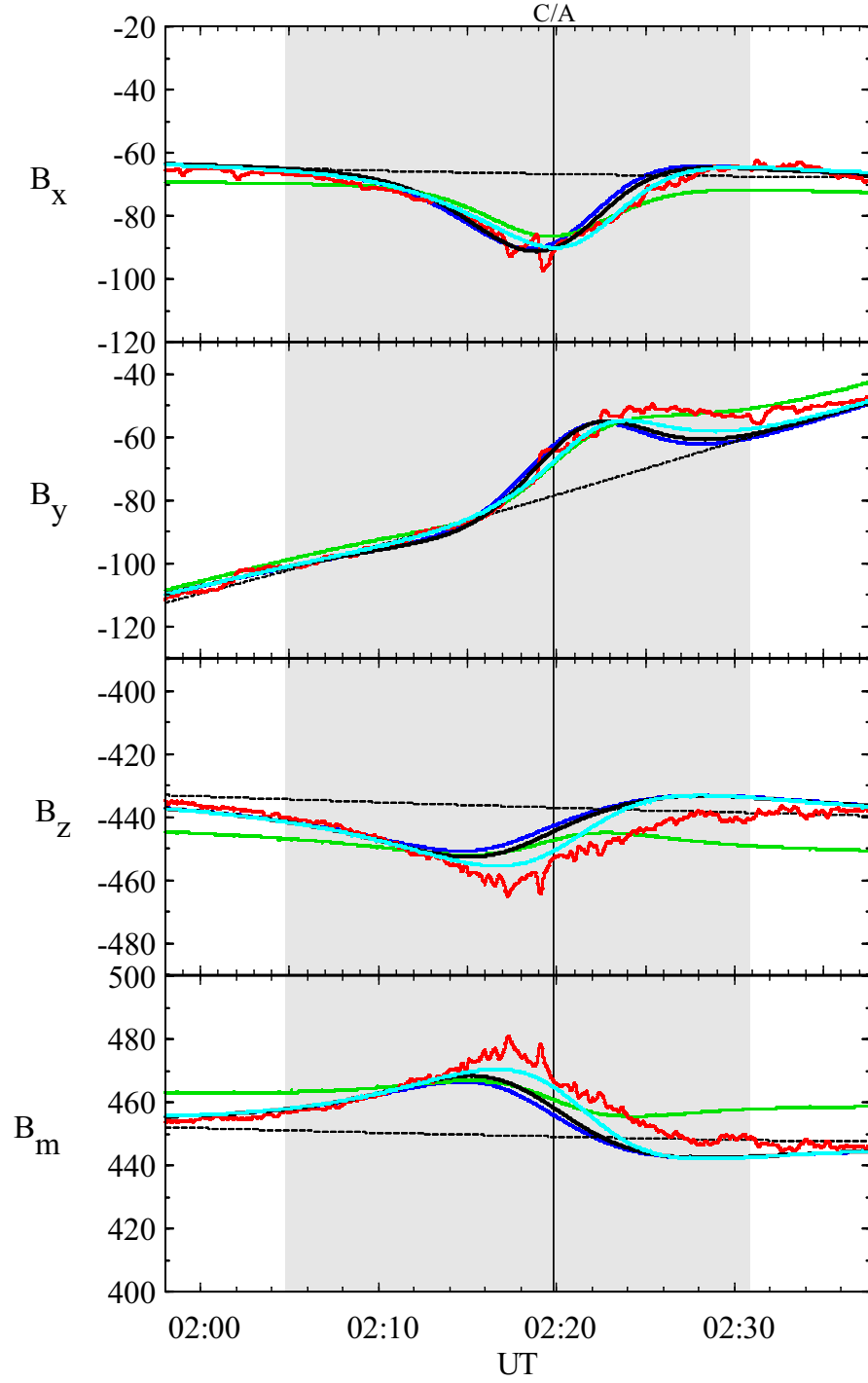
Figure 3.4: *Observed and modeled field for the Europa flyby E14 in the EPhiO coordinate system. The red curve shows the filtered measured field. The thin black curve shows the background field. The solid green curve shows the predicted field for the internal permanent dipole plus induction by using the UMF for the external field (see Table 3.3). The predicted field by using the Alfvén wing model to describe the external local currents is shown for the internal sources: induction only (solid blue) (see Table 3.9), induction plus dipole (solid black) (see Table 3.8) and induction plus dipole plus quadrupole (cyan curve) (see Table 3.10)*

Model	summed rms	summed rmsw	Cond. number	# fitted parameters
Dip + UMF	32	27	10.9	15
Dip + Ind + UMF	17	20	16.9	16
Dip + Quad + UMF	26	21	20.2	20
Dip + Quad + Ind + UMF	19	17	24.5	21
Dip + AWM + Ind	16	20	6.9	4 + 4
Dip + Quad + Ind + AWM	15	16	10.2	9 + 4
Ind + AWM	17	21	3.5	1 + 4

Table 3.11:   *RMS errors and condition numbers*

error of the jth parameter is given by

$$S_j = \sigma_B \sqrt{\sum_{i=1}^{M} \frac{V_{ij}^2}{\lambda_i^2}} \qquad (3.10)$$

where M is the number of model parameters and σ_B is the standard uncertainty associated with the measurements. In this work we use $\sigma_B = rms$ which overestimates the error of measurement. Equation 3.10 gives the error of the fit parameter under the assumption that the chosen model is the correct one. Its magnitude can be attributed principally to the high frequency fluctuations in the magnetic field. However, more pertinent to selecting a probable model for the internal magnetic field of Europa is the rms or rmsw. Ab initio one cannot assert that any specific model represents the actual properties of the system. However, if several reasonable models lead to very similar rms error of fit but yield significantly different values of the model parameters, one must conclude that the data are inadequate for robust determination of those parameters. On the other hand, if the inclusion or exclusion of some element of the model correlates strongly with changes of the rms error of fit, one may safely conclude that that element is essential. In further narrowing the acceptable models, we shall invoke Occam's razor to favor the model with the fewest parameters.

If we compare the different models we have used to describe the internal and external components of the magnetic field on Europa, we find that the rms-error diminishes if induction is included. Adding 5 quadrupole parameters to the internal field model improves the fit very little. All of the models yield rather small dipole coefficients. The model that we find most acceptable includes a simple Alfvén wing model and induction effects, although results obtained by including an additional permanent dipole moment are comparable. The model then implies that the permanent dipole moment probably is zero but is surely smaller than 25 nT. Compared with the magnitude of the induced field, which can be of order 100 nT or more, a fixed internal dipole moment contributes at most in a minor way to the magnetic field. In both of these models, the rms-error is comparable with those of the other models but the fit requires fewer free parameters.

In Figures 3.3 - 3.6 we show fits for different models on different flybys. The dipole plus induction model, supplemented with a uniform external magnetic field (see Table 3.4), is able

Figure 3.5: *Observed and modeled field for the Europa flyby E19 in the EPhiO coordinate system. The red curve shows the filtered measured field. The thin black curve shows the background field. The solid green curve shows the predicted field for the internal permanent dipole plus induction by using the UMF for the external field (see Table 3.3). The predicted field by using the Alfvén wing model to describe the external local currents is shown for the internal sources: induction only (solid blue) (see Table 3.9), induction plus dipole (solid black) (see Table 3.8) and induction plus dipole plus quadrupole (cyan curve) (see Table 3.10)*
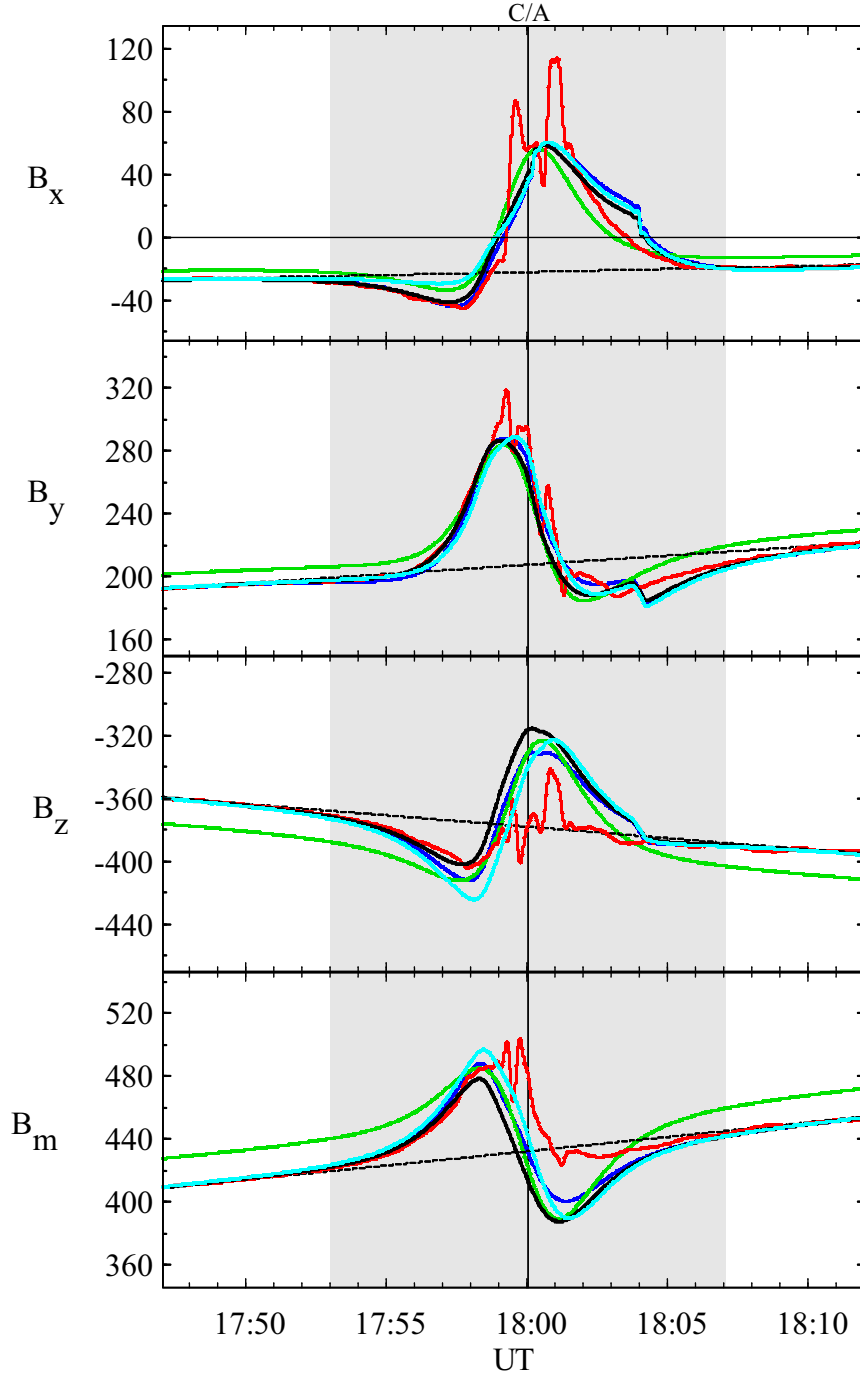
Figure 3.6:   *Observed and modeled field for the Europa flyby E26 in the EPhiO coordinate system. The red curve shows the filtered measured field. The thin black curve shows the background field. The solid green curve shows the predicted field for the internal permanent dipole plus induction by using the UMF for the external field (see Table 3.3). The predicted field by using the Alfvén wing model to describe the external local currents is shown for the internal sources: induction only (solid blue) (see Table 3.9), induction plus dipole (solid black) (see Table 3.8) and induction plus dipole plus quadrupole (cyan curve) (see Table 3.10)*

to fit the B_x and B_y components for the different flybys, but it fails to provide a good fit to the B_z component, particularly for the flybys E4 and E19. By using the physically motivated wire current model to describe the external fields, the fits for dipole plus induction (see Table 3.8) and induction only (see Table 3.9) are quite similar. The fits to the B_z components improve, even for the E4 and E14 flybys. For the E14 flyby we are able to fit the B_z component very well. B_x and B_y are slightly overestimated, but still fit the data well. For E19 the wire current model improves the fit for B_x while not eliminating a phase shift in B_y and B_z. For the E26 flyby we are able to fit the components in general, but are not able to fit the peak structure in detail. However, E26 was at very low altitude so that the data are strongly affected by the distribution of the ionospheric currents which have been very crudely represented in our Alfvén wing model. Therefore artifacts of the wire distribution can be found in the fits, e.g., in the B_x component. For the E4 flyby we also get good fits for all components (particularly B_z), but a phase shift remains in the B_x component. Fitting additional internal quadrupole moments (see Table 3.10) reduces this phase shift, even for the E4 flyby. We are then able to fit E4 and E14 very well and we get good fits for E19 and E26.

By fitting additional internal quadrupole moments (see Table 3.10) we improve our results. The weighted rms-error drops and the phase shift in some components improves. However, to the extent that the moments in Table 3.10 are meaningful, the fact that the quadrupole moments are larger than the dipole moments suggests that the permanent field is not dynamo driven. The fact that both the fixed dipole and quadrupole moments change markedly depending on the external field model used (compare Tables 3.6 and 3.10) suggests that these internal moments are compensating for inadequacies of the external field model. Because of that, we speculate that the true dipole and quadrupole moments are extremely small. We believe that an improved model for the plasma currents would greatly reduce the deviation from the data. Probably a distortion of the Alfvén wing and asymmetries related to the effect of internal multipoles [*Neubauer*, 1999] should be taken into account to reduce the phase shifts seen in some components.

Using our most ambitious model (see Table 3.10) we get a small permanent internal dipole. However, we get nearly as good results by using only induction effects (see Table 3.9) or by including a fixed dipole moment plus induction (see Table 3.8). The inductive response in both of the latter models is $\sim 97\%$. Therefore, we argue there is no need for an internal permanent dipole moment in Europa, although we cannot rule out a small contribution. In addition, although we have good coverage over Europa longitude, a more extensive spatial coverage of the magnetic field would allow for a more exact investigation of the internal sources. These, together with an improved external field model, would provide a more stringent upper limit to a permanent dipole moment.

3.4 Conclusions

We conclude that there is no need for a permanent internal dipole moment in Europa. However, we cannot rule out a small contribution of a permanent dipole moment with an upper limit of 25 nT, which is small compared to the magnitude of the induced magnetic field.

Therefore, we do not account for a permanent internal dipole when investigating the time-dependent interaction of Europa with the Jovian magnetospheric plasma.

The results derived in this chapter strongly confirm an induction response at a level of $\sim$ 97% of the theoretical maximum for a highly conducting sphere. If we assume conductivity comparable to or higher than terrestrial sea water our calculations would be consistent with burial of the conducting layer at a depth of ~ 20 km below the surface.

A more exact modeling of the plasma interaction of Europa could better constrain the estimate of the internal sources of Europa. We address this task in the following by using a three-dimensional interaction model described in chapter 5.

Ultimately, future spacecraft missions will improve the spatial coverage and eliminate much of the remaining uncertainty.

THE INDUCTION EFFECT

Before we start to address the complex problem of the interaction of Europa with the Jovian magnetosphere, we want to examine the classical induction problem applied to Europa by neglecting the magnetospheric plasma and the atmosphere of the moon. This enables us to investigate the influence of a conducting core and a conducting mantle on the induction signature outside the moon. In addition, we can analyze to what extent the determination of the conductivity and the thickness of the ocean is possible.

We start this chapter by giving a basic overview of the properties of the electrical conductivity in natural materials. Thereafter we examine the problem of electromagnetic induction taking place in a homogenous sphere, which is a well understood problem in earth physics and a good initial point for more complex problems. After deriving the solution of the Laplace equation for this problem we turn to the more realistic case of induction taking place in a body consisting of different conductible shells, e.g., core, mantle, ocean. Finally, we address the problem with respect to Europa and investigate the influence of the inner structures regarding their thickness and conductivity.

Gravity data obtained by the Galileo spacecraft suggest that Europa owns a silicate mantle below its outer water ice-liquid shell and has an internal metallic core [*Anderson et al.*, 1997*b*; 1998]. In addition, Galileo measurements of the magnetic field at Europa indicate the existence of electromagnetic induction taking place in the interior of the moon [e.g. *Kivelson et al.* [2000]]. Earlier works have shown that the main induction signal could not be produced by a conducting core or mantle only [*Kuramoto et al.* [1998], *Zimmer et al.* [2000]]. In fact they indicate the existence of a conducting subsurface layer, which is very likely to be a substantial ocean.

In natural materials the electrical conductivity σ varies by about 25 orders of magnitude. A few examples are shown in table 4.1. In addition, for comparison, values of the electrical

	conductivity [S m^{-1}]
Quartz	$10^{-11} - 10^{-14}$
Glacier ice (temperate)	$10^{-7} - 10^{-8}$
Glacier ice (polar)	$10^{-5} - 10^{-6}$
Silicates	$10^{-6} - 10^{-3}$
Sand and gravel	$10^{-3} - 10^{-2}$
Clays	$10^{-2} - 1$
Sea water	5
Saline waters (20%)	20
Iron	10^7
Copper	10^8
Earth mantle (upper)	10^{-2}
Earth mantle (lower)	$1 - 10$
Earth outer core	3×10^5

Table 4.1: *Conductivities of geological materials and inside the Earth. The values are mean values [Telford et al. [1990], Reynolds [1997], Stacey [1992]].*

conductivity inside the earth are given in table 4.1. Metals are highly conductive but rarely found in geologically large continuous masses except in planetary interiors. The conductivity of rocks is strongly influenced by the presence of groundwater, which acts as an electrolyte. Generally most rocks are poor conductors at low temperatures, but in porous rocks the conductivity varies with the volume and arrangement of the pores and even more with the conductivity and amount of contained water. These observations are summarized in an empirical formula, called Archies Law (e.g., [*Lowrie*, 1997]).

$$\sigma = \frac{\Phi^m}{a} \sigma_w S^n \tag{4.1}$$

where σ_w is the conductivity of the pore water, Φ is the porosity, S is the volume fraction of pores with water and a, m, n are constants with $0.5 \leq a \leq 2.5$, $1.3 \leq m \leq 2.5$, $n \sim 2$. In addition, the conductivity of particular rock types vary with age, temperature and pressure.
Water conductivity varies considerably depending on the amount and conductivity of dissolved minerals. Some groundwater and glacial meltwater on earth can have conductivities as low as 10^{-3} S/m while saline groundwater can have a conductivity of 20 S/m.

The depth of penetration of a time-varying magnetic field of frequency ω in a conductor of electrical conductivity σ is

$$\delta = \sqrt{\frac{2}{\sigma \mu_0 \omega}} \tag{4.2}$$

The quantity δ is called skin depth. While the skin depths for inducing fields with Jupiter's rotational period in a core similar to the earth core would be only $\sim$180 m, it would be $\sim$1000

km in the earth lithosphere. In Sea water the skin depths would be $\sim$45 km. This means that a conducting layer with a thickness larger than the skin depth in this layer can effectively shield an underlying layer even if this one has a large conductivity. For instance a conducting subsurface layer at Europa which is thick enough can effectively shield a conducting mantle or core from induction effects.

4.1   Induction in a homogeneous sphere

We start our investigation with the simple case of a homogenous sphere with finite conductivity. The problem of electromagnetic induction in uniform spherical conductors has been treated, e.g., by *Wait* [1951], *Ward and Hohmann* [1987] or *Kaufman and Eaton* [2001]. Therefore the derivations will not be given in great detail here.

The fundamental equation of electromagnetic induction in stationary conductors is the diffusion equation

$$\frac{\partial \mathbf{B}}{\partial t} = \frac{1}{\sigma \mu} \nabla^2 \mathbf{B} \tag{4.3}$$

which can be obtained from Maxwell's equations.

Here we have ignored the displacement currents which for our applications are much smaller than the conduction currents [*Nabighian*, 1988]. For the sake of simplicity the permeability μ will be taken everywhere equal to the vacuum permeability μ_0.

Each component of $\mathbf{B}(t)$ can be expressed by a series of superimposed sine waves of various frequencies. Because equation 4.3 is linear in $\mathbf{B}$ we can examine one sine wave of a single frequency. The total field can then be determined by superimposition. Generally, the potential of the external inducing field can be expanded in spherical harmonics. For a radial symmetric conductivity distribution each surface spherical harmonic S_n^m of the inducing field gives rise to only the same S_n^m of the induced field [*Parkinson*, 1983]. Therefore we can deal with each harmonic separately and superimpose the solutions.
Without loss of generality we can assume an inducing magnetic field with a potential:

$$U_e = a B_e \left(\frac{r}{a}\right)^n S_n^m(\theta, \phi) e^{-i\omega t} \tag{4.4}$$

where a is the radius of the sphere, n and m are degree and order of the inducing field.

Generally a divergenceless field can be partitioned into a toroidal and a poloidal part. In our case, by using spherical polar coordinates, this means we can divide the vector potential into parts parallel to and perpendicular to $\mathbf{r}$ by writing

$$\mathbf{A} = T\mathbf{r} + \nabla S \times \mathbf{r} \tag{4.5}$$

so that the magnetic field becomes

$$\mathbf{B} = \nabla \times T\mathbf{r} + \nabla \times \nabla \times S\mathbf{r} = \mathbf{T} + \mathbf{S} \tag{4.6}$$

where T and S are scalar functions and $\mathbf{T}$ and $\mathbf{S}$ are called toroidal field and poloidal field. It can be seen that the toroidal field has no radial component and thus cannot be detected outside the sphere nor can it be induced by external fields. We therefore will not further consider this component. The poloidal field within the conductor can be expressed as [*Parkinson*, 1983]

$$B_r = C\frac{F(r)}{r}n(n+1)S_n^m e^{-i\omega t} \tag{4.7}$$

$$B_\theta = \frac{C}{r}\frac{\mathrm{d}rF(r)}{\mathrm{d}r}\frac{\partial S_n^m}{\partial \theta}e^{-i\omega t} \tag{4.8}$$

$$B_\phi = \frac{C}{r\sin\theta}\frac{\mathrm{d}rF(r)}{\mathrm{d}r}\frac{\partial S_n^m}{\partial \phi}e^{-i\omega t} \tag{4.9}$$

where C is a constant and $F(r)$ is a function which has to be determined. By defining

$$k^2 = -i\omega\mu\sigma \tag{4.10}$$

and using equations 4.3 and 4.4, one can show that $F(r)$ has to satisfy the equation [*Lahiri and Price*, 1939]

$$\frac{\mathrm{d}^2F}{\mathrm{d}r^2} + \frac{2}{r}\frac{\mathrm{d}F}{\mathrm{d}r} - \left[k^2 + \frac{n(n+1)}{r^2}\right]F = 0 \tag{4.11}$$

This is Bessel's equation for which the solutions can be written as

$$F_1(r) = \sqrt{\frac{\pi}{2}}(rk)^{-\frac{1}{2}}I_{n+\frac{1}{2}} \tag{4.12}$$

$$F_2(r) = \sqrt{\frac{\pi}{2}}(rk)^{-\frac{1}{2}}K_{n+\frac{1}{2}} \tag{4.13}$$

where $I_{n+\frac{1}{2}}$ and $K_{n+\frac{1}{2}}$ are the modified spherical Bessel functions of first and third order. As $F_2(r)$ in equation 4.13 approaches infinity as r approaches zero, this solution is omitted for a homogeneous sphere. In the insulating regions, outside the sphere, the field satisfies

$$\nabla^2\mathbf{B} = 0 \tag{4.14}$$

Therefore, outside the sphere the field can be expressed by a scalar potential of the induced and the inducing fields [*Ward and Hohmann*, 1987]

$$U = U_e + U_i = a\left[B_e\left(\frac{r}{a}\right)^n + B_i\left(\frac{a}{r}\right)^{n+1}\right]S_n^m(\theta,\phi)e^{-i\omega t} \tag{4.15}$$

Applying the usual boundary conditions at $r = a$, we then get for the induced field outside the sphere:

$$B_r^{ind} = (n+1) \left(\frac{a}{r}\right)^{n+2} B_i S_n^m e^{-i\omega t} \tag{4.16}$$

$$B_\theta^{ind} = -\left(\frac{a}{r}\right)^{n+2} B_i \frac{\partial S_n^m}{\partial \theta} e^{-i\omega t} \tag{4.17}$$

inside the sphere:

$$B_r^{ind} = \frac{a}{r} \frac{F(rk)}{F(ak)} (n+1) B_i S_n^m e^{-i\omega t} \tag{4.18}$$

$$B_\theta^{ind} = -\frac{a}{r} \frac{F'(rk)}{F'(ak)} B_i \frac{\partial S_n^m}{\partial \theta} e^{-i\omega t} \tag{4.19}$$

It is:

$$\frac{B_i}{B_e} = \frac{n}{n+1} \frac{\frac{F'(ak)}{F(ak)} - (n+1)}{\frac{F'(ak)}{F(ak)} + n} = \frac{n}{n+1} A e^{i\Phi} \tag{4.20}$$

with reflection factor (or amplitude) $A \leq 1$ and phase lag $\Phi \leq 90°$. For a homogenous inducing field ($n = 1$), the induced field is a dipole field.

For a perfect conducting sphere ($\sigma \to \infty$) it is:

$$\lim_{\sigma \to \infty} \frac{B_i}{B_e} = \frac{n}{n+1} \tag{4.21}$$

Therefore, for a conducting sphere with arbitrary conductivity, the induced field can be related to the field of a perfect conducting sphere $\mathbf{B}_{ind}^\infty$ through:

$$\mathbf{B}_{ind}(t) = A \mathbf{B}_{ind}^\infty \left(t - \frac{\Phi}{\omega}\right) \tag{4.22}$$

This means, that the induced field of a sphere with finite conductivity is identical to the field of a perfect conducting sphere with reduced amplitude and delayed phase.

4.2 Induction in a sphere with variable conductivity

A more realistic problem with regard to Europa is a sphere with three different conducting layers (Figure 4.1) which are radial symmetric. Similar problems were solved by *Lahiri and Price* [1939] for an increase of conductivity with depth and by *Srivastava* [1966] for a sphere made up of concentric shells, each with uniform conductivity. Here we assume a conductible core, a mantle and an outer shell. The crust is assumed to be not conductible. Again we assume the inducing magnetic field from equation 4.4. The induction equation (equation 4.3) then must be solved within each shell and in the central region. This time equation 4.13 is also a valid solution of equation 4.11 in the outer two layers. The problem is then solved
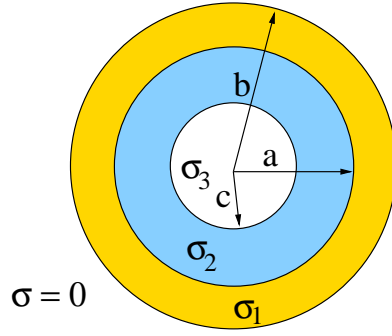
Figure 4.1: *Sphere with three conducting layers*

analogue to those in section 4.1, but the boundary conditions at each shell has to be taken into account.

Outside the sphere we then get

$$B_r^{ind} = (n+1) \left(\frac{b}{r}\right)^{n+2} B_i S_n^m e^{-i\omega t} \tag{4.23}$$

$$B_\theta^{ind} = -\left(\frac{b}{r}\right)^{n+2} B_i \frac{\partial S_n^m}{\partial \theta} e^{-i\omega t} \tag{4.24}$$

From the boundary conditions at each shell we get

$$\frac{B_i}{B_e} = \frac{n}{n+1} \frac{\left[\frac{F_1'(bk_1)}{F_1(bk_1)} - (n+1)\right] + \frac{F_2(bk_1)}{F_1(bk_1)} \frac{D}{C} \left[\frac{F_2'(bk_1)}{F_2(bk_1)} - (n+1)\right]}{\left[\frac{F_1'(bk_1)}{F_1(bk_1)} + n\right] + \frac{F_2(bk_1)}{F_1(bk_1)} \frac{D}{C} \left[\frac{F_2'(bk_1)}{F_2(bk_1)} + n\right]} \tag{4.25}$$

with

$$\frac{D}{C} = \frac{F_1(ak_1)}{F_2(ak_1)} \frac{\frac{F_1'(ak_2)}{F_1(ak_2)} - \frac{F_1'(ak_1)}{F_1(ak_1)} + \frac{F_2(ak_2)}{F_1(ak_2)} \frac{G}{E} \left[\frac{F_2'(ak_2)}{F_2(ak_2)} - \frac{F_1'(ak_1)}{F_1(ak_1)}\right]}{\frac{F_2'(ak_1)}{F_2(ak_1)} - \frac{F_1'(ak_2)}{F_1(ak_2)} + \frac{F_2(ak_2)}{F_1(ak_2)} \frac{G}{E} \left[\frac{F_2'(ak_1)}{F_2(ak_1)} - \frac{F_2'(ak_2)}{F_2(ak_2)}\right]} \tag{4.26}$$

and

$$\frac{G}{E} = \frac{F_1(ck_2)}{F_2(ck_2)} \frac{\frac{F_1'(ck_2)}{F_1(ck_2)} - \frac{F_1'(ck_3)}{F_1(ck_3)}}{\frac{F_1'(ck_3)}{F_1(ck_3)} - \frac{F_2'(ck_2)}{F_2(ck_2)}} \tag{4.27}$$

Here k_1, k_2 and k_3 are the wave numbers in the ocean, mantle and core respectively. Equation 4.25 is similar to equation 4.20. Hence, we can relate the induced magnetic field in a sphere with multiple conducting shells to that of a perfect conducting sphere by defining an amplitude and a phase lag (see previous section). Therefore, equation 4.22 is also valid in this case.

4.3   Influence of the inner structure of Europa

Galileo measurements of Europa's gravitational field show Europa to be a differentiated satellite consisting of a metallic core, a silicate mantle and a water ice-liquid outer shell. The minimum water ice-liquid outer shell thickness is about 80 km for plausible mantle densities [*Anderson et al.*, 1998]. The H_2O layer is likely comprised of three sub-layers: an outer, brittle/elastic ice layer, an underlying ductile layer of potentially convecting ice, and a lower layer of liquid. Estimates of the thickness of the ice layer (including the lower ductile layer) range from a few km to 60 km [e.g. *Greenberg et al.* [2000], *Pappalardo et al.* [1998], *Schenk* [2002], *Hussmann et al.* [2002]].

Although the liquid water shell is thought to be the main source for the induction process its still possible that the induction signature is influenced by the underlaying structures for lower conductivities of the ocean. Therefore, in the following we like to investigate the influence of the core size, the mantle conductivity and the thickness of a conducting outer layer in connection to the conductivity of such a layer on the induction signature outside the moon. Here, the inducing time-varying magnetic field experienced by Europa is a uniform alternating field ($n = 1$) due to the synodical period of Jupiter, which is 11h 14min. We calculate the induced magnetic field by using the equations derived above.

4.3.1   Influence of a conducting core

We start with a model consisting of an outer water ice shell of d_{ice} = 50 km thickness, representing the upper two sub-layers of Europa's water shell. This shell is, because of the low values in table 4.1, assumed to be not conductive. Beneath this outer shell, we have a conducting layer with variable conductivity, which represents the lower part of Europa's water shell. The thickness of this layer is at first assumed to be d_{oc} = 100 km. The radius of Europa's core is uncertain because of its unknown composition and because of the thickness of the water ice-liquid shell. In the following we deal with a metallic core with $\sigma_c = 5 * 10^5$ S/m which is nearly the conductivity of the Earth core. Please note that a mainly Fe core would have a larger conductivity. However, models show that such a core would also have a smaller radius [*Anderson et al.*, 1998] and therefore, because of its r^{-3} dependence, the induced magnetic field would be weaker outside the moon.

Figure 4.2 illustrates the influence of the core size on the induction signature. Plotted are the normalized amplitude, obtained from equations 4.22 and 4.25, and the phase lag of the induced response. For the silicate mantle we start with a conductivity of $\sigma_m = 1$ mS/m, which is smaller then the conductivity found in the upper mantle region of the earth (see table 4.1). By using this small value for the mantle conductivity we probably overestimate the influence of Europa's core. A higher value leads to a smaller skin depths of the inducing signal and therefore to a shielding of the core.

A perfect conductor will have an amplitude of 1 and a zero phase lag. For a non perfect conducting body the amplitude of the induced field is always smaller than 1 and the phase lags behind the inducing field up to 90°. Please note that because of the fixed outer ice shell thick-
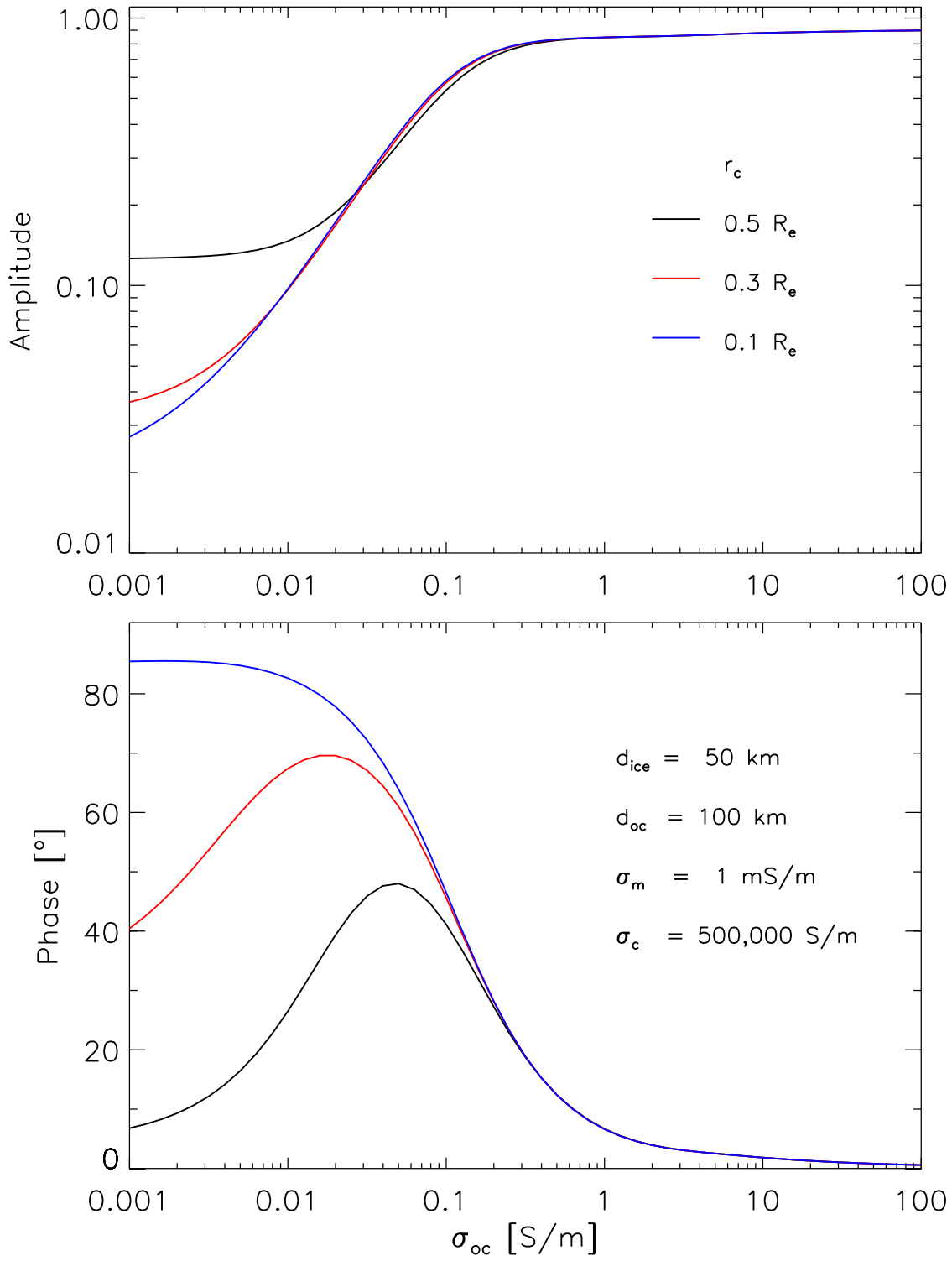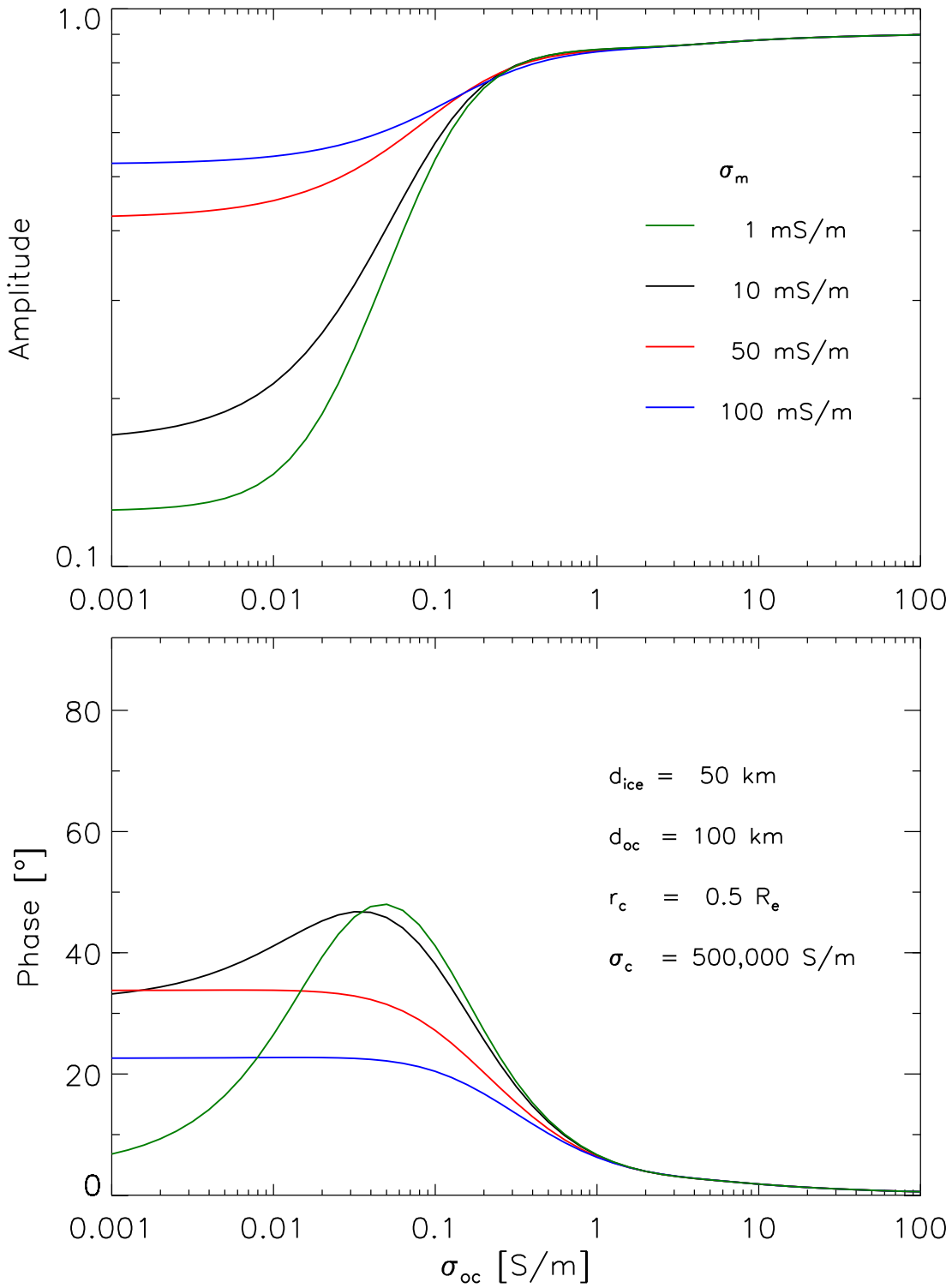
Figure 4.2:   *Influence of core size on the induction signature when using Jupiter's synodical period as excitation period for the inducing field.*

ness, in our case the limit for the Amplitude is 0.9 instead of 1. Results from Figure 4.2 show that by using Jupiter's synodical period as excitation period for the induction, a conducting core independent of its size is almost not detectable outside Europa for conductivities of the subsurface layer larger than 60 mS/m as they are suggested by *Zimmer et al.* [2000].

4.3.2   Influence of a conducting mantle

The influence of the mantle conductivity on the induced magnetic field outside Europa is illustrated in Figure 4.3. Here we use a fixed core size of $r_c = 0.5\,\mathrm{R}_E$ and vary the conductivity of the silicate mantle from 1 mS/m to 100 mS/m. Higher values of the mantle conductivity are found in the lower earth mantle, but seem pretty unrealistic in Europa's mantle because they would either require higher pressure than the pressure expected in Europa's mantle [*Greeley et al.*, 2004] or high temperatures, which would probably lead to a melting of the upper ice layer as it was also suggested by *Zimmer et al.* [2000].

Unlike the core, an influence of the mantle on the amplitude of the induced magnetic field is visible for conductivities of the subsurface water shell in the range of the lower limit given by *Zimmer et al.* [2000]. Of course the influence is getting stronger with smaller values of σ_{oc}. However, for σ_{oc} larger than 100 mS/m, no influence on the induction signal is visible. The mantle than is effectively shielded by the upper conducting layer. A similar picture appears from the phase lag (lower panel).

The lower limit for the amplitude of the induced field given by *Zimmer et al.* [2000] is $A = 0.7$. If there would be a conducting mantle only, the maximum response by using $\sigma_m = 100$ mS/m is slightly smaller than 0.7. However, as mentioned above, mantle conductivities in this range are difficult to justify without a melting of the upper ice layer. Therefore, we support the statement of *Zimmer et al.* [2000], that a conducting mantle alone cannot explain the induction signature found in the Galileo magnetic field data. In addition, an influence on the induction signature, when using Jupiter's synodical period as the excitation period for the induction, is only expected for $\sigma_{oc} \leq 100$ mS/m. Our results derived in chapter 3 suggest that by considering the influence of the plasma interaction on the magnetic field signature measured by Galileo, a higher induction response than A = 0.7 is required. Hence, the influence of the mantle on the induction signature would be very small.

A different picture would arise if one would use the orbital period of Europa (3.5 day's) for the excitation of the induction. This period is not available from the Galileo data. However, a Europa orbiting spacecraft could provide the data needed. By using Europa's orbital period the field can penetrate deeper into the moon and would therefore allow for a stronger influence of the mantle (and also the core) on the induction signal. The influence of the mantle conductivity on the amplitude and the phase lag of the induced magnetic field is shown in Figure 4.4 when using Europa's orbital period as excitation period for the inducing field. Figure 4.4 indicates that in this case the influence of the mantle conductivity is visible up to values of σ_{oc} of a few 100 mS/m.
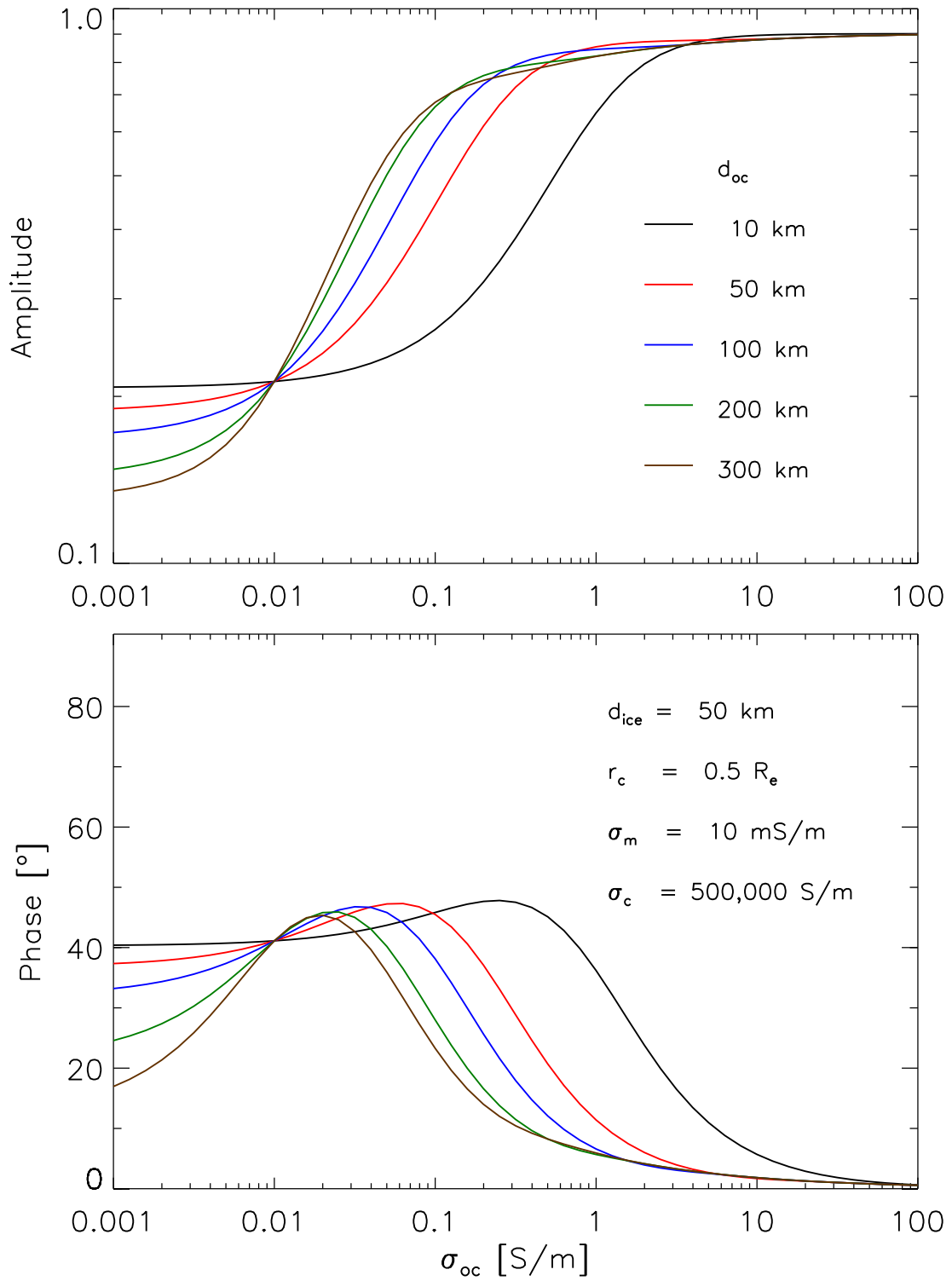
Figure 4.3: *Influence of mantle conductivity on the induction signature when using Jupiter's synodical period as excitation period for the inducing field.*
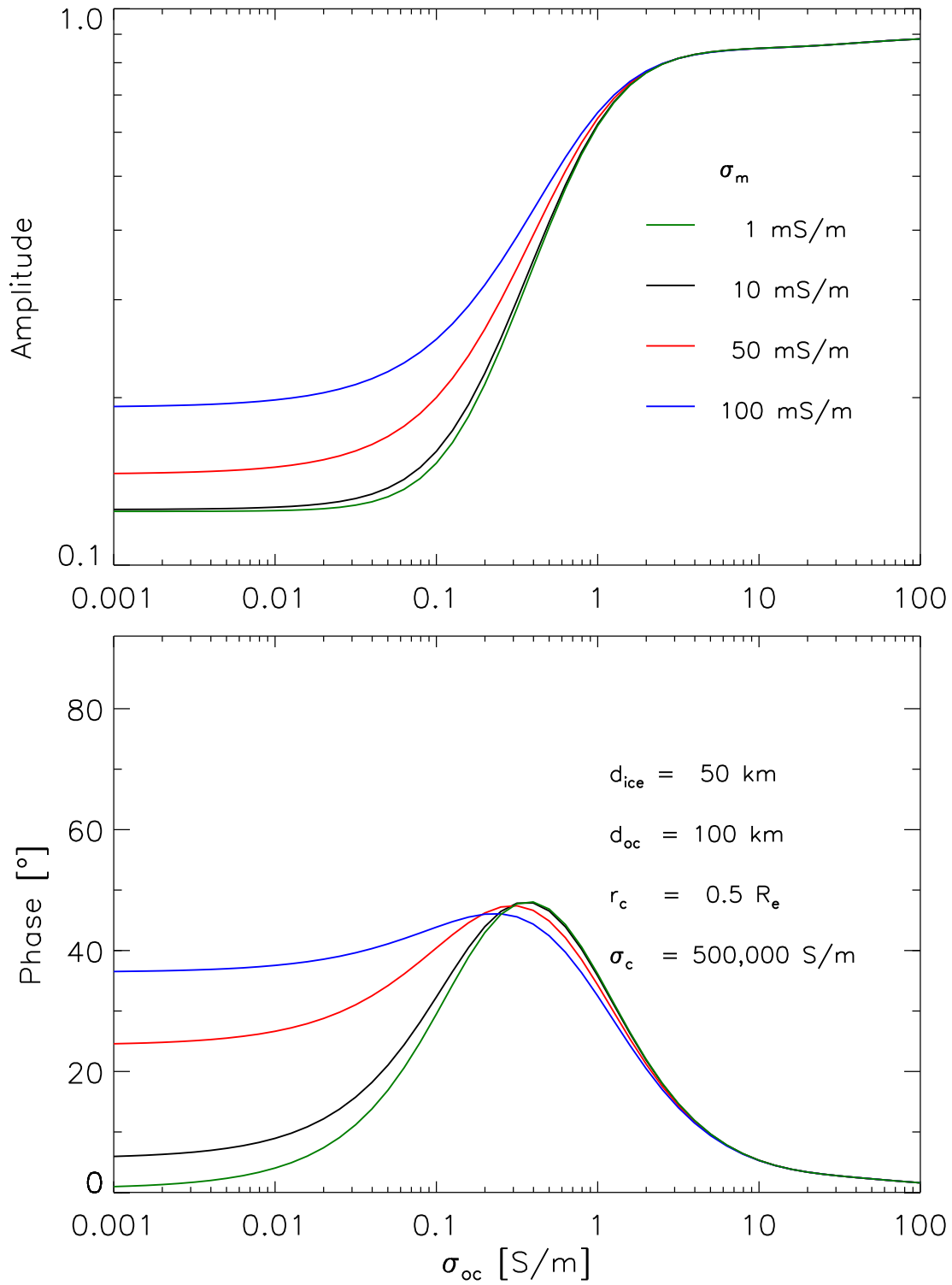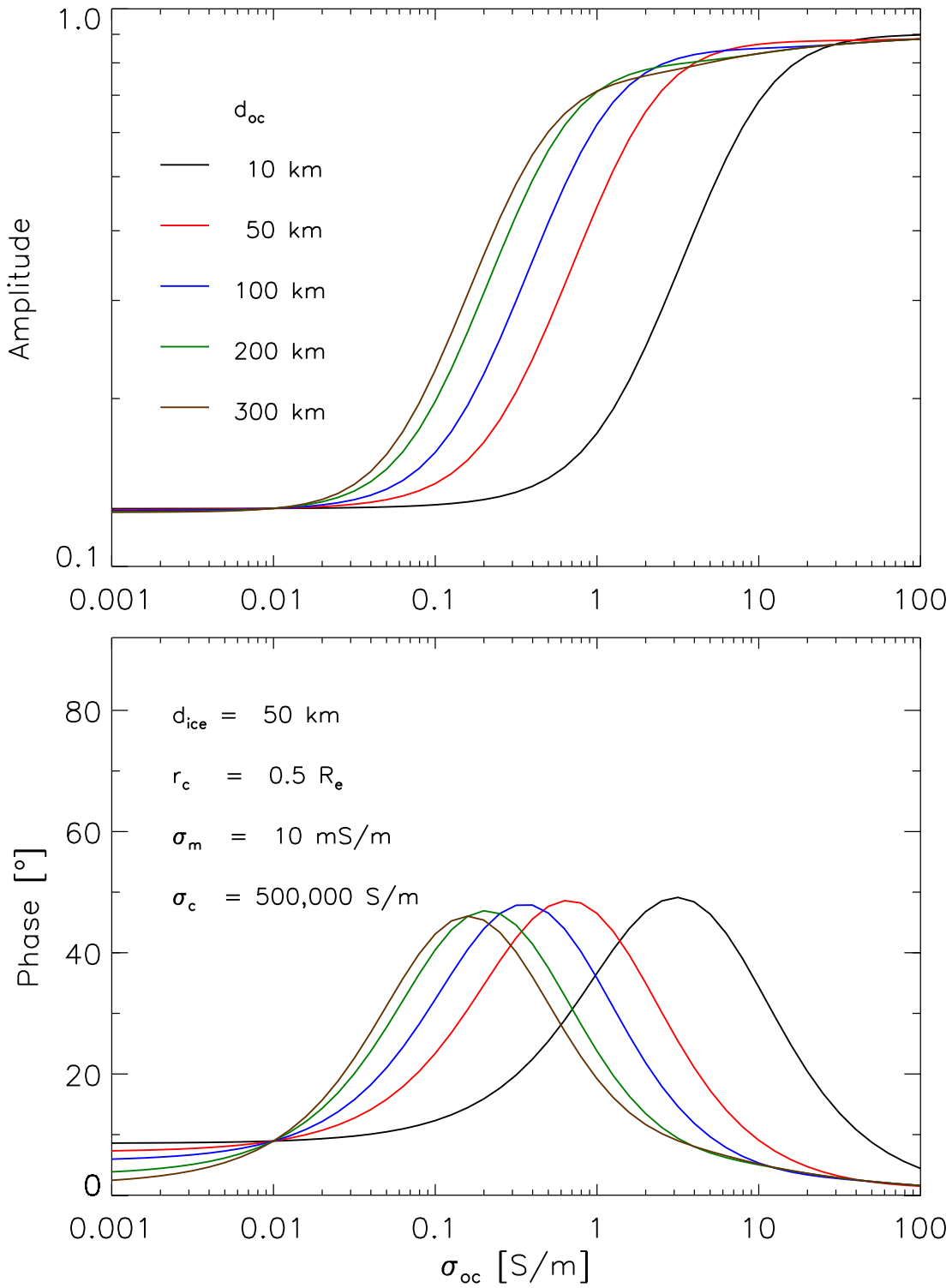
Figure 4.4:   *Influence of mantle conductivity on the induction signature when using Europa's orbital period as excitation period for the inducing field.*

4.3.3   Influence of the thickness of the ocean

In order to investigate the influence of the thickness of the conducting subsurface layer on the induction signal, we use a model with a conducting core with $\sigma_c = 5 * 10^5$ S/m and $r_c = 0.5$ R_E, a conducting mantle with $\sigma_m = 10$ mS/m and an outer water ice shell with $d_{ice} = 50$ km. Figure 4.5 displays the amplitude and the phase lag of the induced magnetic field for different assumed ocean thicknesses when using Jupiter's synodical period as excitation period for the induction.

Please note, that the amplitude and the phase lag of the induced field in Figure 4.5 depend on the conductivity and the thickness of the conducting ocean. Therefore, the same amplitude or phase lag can be achieved by using a thin conductible ocean as well as by using a thicker but less conducting ocean layer.

Figure 4.5 indicates that for ocean conductivities larger than 100 mS/m a resolution of the oceans lower boundary is almost not possible if the ocean thickness is larger than 100 km. In addition, the lower boundary of the ocean can not be resolved if the ocean is thicker than 10 km and the ocean conductivity is larger than 1 S/m. As mentioned above, Europa's minimum water ice-liquid outer shell is about 80 to 170 km thick. Therefore, we are probably not able to resolve the lower boundary of a possible ocean from the Galileo data for a thick conducting subsurface layer. Note that the point of intersection of the graphs at $\sigma_{oc} = 10$ mS/m is a result of the mantle conductivity of $\sigma_m = 10$ mS/m. Hence, it corresponds to the case of a two shell model. For smaller values of σ_{oc} the underlaying mantle has a higher conductivity than the subsurface ocean.

As in the previous section, the use of Europa's orbital period as excitation period for the inducing field would yield a different result (see Figure 4.6). In this case a resolution of the lower boundary of the water shell is still almost not possible for large ocean conductivities σ_{oc} if the ocean is larger than 50 km. However, one could identify the lower boundary if the ocean conductivity is in the range of a few 100 mS/m.

Figure 4.5: *Influence of the oceans thickness on the induction signature when using Jupiter's synodical period as excitation period for the inducing field.*

Figure 4.6: *Influence of the oceans thickness on the induction signature when using Europa's orbital period as excitation period for the inducing field.*

INTERACTION MODEL

In this chapter our model that describes the time-dependent interaction of Europa with the Jovian magnetosphere is presented. We start with a general introduction in which we briefly give an overall picture of the interaction and introduce our idea of the simulation concept. Subsequently we describe the model we use for the plasma interaction. Then we explain our model of the neutral atmosphere. Afterwards we describe how we implemented the induction process into our model and how we account for the time-dependence of Europa's interaction with the Jovian magnetosphere. In this context we also present the modified MHD-equations we solve with our model. Finally, we give an overview of the initial conditions we use.

5.1 Statement of the problem

The basic idea of this dissertation is the study of the time dependent plasma interaction of Europa's atmosphere and its proposed internal ocean with the Jovian magnetosphere. To accomplish this task we use a three-dimensional MHD model and solve the MHD flow problem and the internal induction problem simultaneously. Our main motivation is to compare the simulation results with the Galileo magnetic field measurements in order to get stronger constraints on the conductivity and the depth of Europa's internal ocean compared to earlier attempts.

Figure 5.1 illustrates the idea of the primary induction process. The starting point is the tilted dipole moment of Jupiter which has an inclination of $9.6°$ against the rotation axis of Jupiter. One can split up the dipole moment in one part which is aligned with the rotation axis and constant in time and one part which is rotating in the equatorial plane. As the rotation period of Jupiter is about 9h 55min while the orbit period of Europa is about 3.55 days, this leads to a time varying inducing field at the location of Europa with a synodical period of
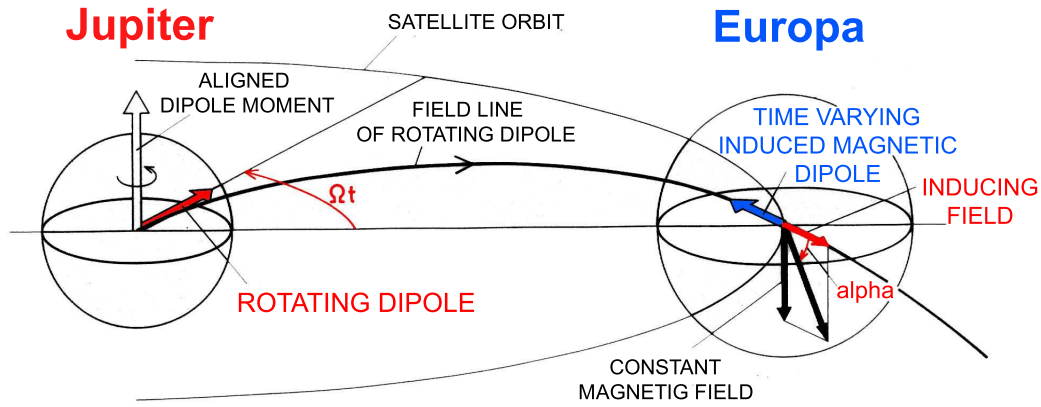
Figure 5.1: *Illustration of the magnetic field at a satellite due to the rotating tilted Jovian dipole moment (after Neubauer [1999]).*

11.1h. If one assumes a conducting subsurface layer at Europa, the time varying inducing field drives currents in the conducting layer which generate a time varying induced magnetic dipole field. The strength of the induced dipole moment depends on the inclination angle alpha and therefore on the orientation of the rotating dipole moment which is determined by the angle Ωt. The angles $\Omega t = 0°$ and $\Omega t = 180°$ are associated with a minimum inclination angle and a maximum induction effect.

The orbit of Europa is located at the outer edge of the Io plasma torus close to the transition to the middle magnetosphere of Jupiter where the plasma corotation with Jupiter's magnetosphere gradually breaks down [*Khurana et al.*, 2004]. A thin current sheet exists at the position of Europa. Azimuthal currents are large in this current sheet and create magnetic field perturbations. Thus, the background magnetic field at Europa consists not only of the internal originated field of Jupiter as we will see in section 5.6.

Simultaneously, magnetospheric plasma and magnetic fields interact with Europa's tenuous atmosphere and ionosphere and also with the time varying magnetic field from the interior of the moon. The induced magnetic fields therefore influence the plasma interaction as it is discussed in *Neubauer* [1999].

The plasma interaction generates currents, e.g., Alfvénic and ionospheric currents, in the vicinity of Europa. In section 5.6 we demonstrate that the magnetospheric plasma at the location of Europa is also varying in time. Therefore, Europa experiences different magnetospheric conditions during one synodical rotation and the currents generated by the plasma interaction in the vicinity of Europa are also time dependent. This leads to a secondary induction effect, where the magnetic fields induced by the plasma currents contain also higher order moments [*Neubauer*, 1999]. One objective of this work is to determine the strength of those secondary induced magnetic fields.

One crucial point is that Europa's atmosphere and ionosphere cannot shield the plasma entirely from the surface. Therefore, parts of the streaming plasma hit the surface and will be

absorbed. This is linked to the sputtering of molecules on the surface as source for the neutral atmosphere (see, e.g., *Saur et al.* [1998]). Additionally, magnetic field lines can penetrate the interior of Europa. A proper description of the interior is therefore needed, to describe the external plasma interaction accurate.

5.2   MHD model

In this section we focus on the interaction of Europa's atmosphere with the ambient magnetospheric plasma. The internal induction problem will be subject to later sections.
We are mainly concerned about the bulk properties of the plasma rather than on single particle motion. Therefore, we choose a fluid approach to model the plasma interaction. We start with a brief overview of the derivation of the fluid equations and a discussion of the applicability of a fluid approach to the case of Europa.

A precise description of a plasma is given by particle distribution functions in phase space. This leads to a kinetic equation which describes the evolution of the coarse-grained phase space density in time and space. One way to simplify the kinetic equation is to account only for correlations between particles themselves via collisions, which leads to the Boltzmann equation (see, e.g., *Baumjohann and Treumann* [1996])

$$\frac{\partial f_s}{\partial t} + \mathbf{v}_s \cdot \nabla_x f_s + \mathbf{a}_s \cdot \nabla_v f_s = \frac{\delta f_s}{\delta t} \tag{5.1}$$

where f_s is the distribution function of the particles, $\mathbf{v}_s$ the velocity and $\mathbf{a}_s$ the acceleration of the particles. The term on the right-hand side is the time rate of change of f_s due to all kinds of collisions. The Boltzmann equation has an infinite number of solutions. When collisions dominate, the species distribution function is driven toward a drifting Maxwellian [*Schunk and Nagy*, 2000].

Macroscopic physical parameters, like density or temperature, do not depend on velocities of single particles, but only on space and time. Thus, they are obtained by integrating over the entire velocity space and they are called moments where the i-th moment is given by

$$M_i(\mathbf{x}, t) = \int f(\mathbf{v}, \mathbf{x}, t) \mathbf{v}^i d^3 v \tag{5.2}$$

where $\mathbf{v}^i$ denotes an i-fold dyadic product.

The fluid equations are derived by finding the evolution equations for the basic macroscopic moments (see, e.g., *Cravens et al.* [1997]). The obtained set of equations is not closed, because at any order a new moment of next higher order appears. A truncation of the equation hierarchy can be achieved, e.g., by assuming an equation of state, depending on the form of the pressure tensor, e.g., by assuming adiabatic conditions.

One important prerequisite forming a fluid description for the plasma rather than particle distribution functions is quasi-neutrality. This is justified when the length scale is much larger

than the Debye length. Furthermore, for the validity of the fluid approach it is required that variations occur on length scales L larger than the gyro radius r_g ($L \gg r_g$) and on time scales τ larger than the gyro period $1/\omega_g$ ($\tau \gg 1/\omega_g$), which means fluid scales must be much larger than gyrokinetic scales. At Europa the gyro radii of thermal and pickup ions are around 20 km or less [*Kivelson et al.*, 2004], which is small compared to the satellite radius. Using the cyclotron frequencies given by *Kivelson et al.* [2004] one gets time scales on the order of $1/\omega_g \lesssim 0.5$ s. This time scale has to be compared with the time it takes for the plasma to propagate a typical length scale. With a background velocity of 104 km/s one gets a time of $\tau \sim 15$ s, which is larger than the gyrokinetic scale. Thus, the fluid approach to Europa's interaction is justified. In that case the ideal MHD equations (see, e.g., *Cravens et al.* [1997]) can be derived from the multi-fluid equations. The kernel of our model (the Zeus 3D code [*Stone and Norman*, 1992a;b]) solves the ideal MHD equations:

Continuity equation:

$$\frac{\partial \rho}{\partial t} + \nabla \cdot \rho \mathbf{u} = 0 \tag{5.3}$$

Momentum equation:

$$\rho \left(\frac{\partial \mathbf{u}}{\partial t} + \mathbf{u} \cdot \nabla \mathbf{u} \right) = -\nabla p + \frac{1}{\mu_0} (\nabla \times \mathbf{B}) \times \mathbf{B} \tag{5.4}$$

Induction equation:

$$\frac{\partial \mathbf{B}}{\partial t} = \nabla \times (\mathbf{u} \times \mathbf{B}) \tag{5.5}$$

Energy equation:

$$\frac{\partial e}{\partial t} + \nabla \cdot e \mathbf{u} = -p \nabla \cdot \mathbf{u} \tag{5.6}$$

where $\mathbf{B}$ is the magnetic field and p is the thermal pressure. Thereby for a plasma consisting of one ion species (subscript i) and one electron species (subscript e) the bulk variables for mass density ρ, velocity $\mathbf{u}$ and internal energy e are given by

$$\rho = \rho_i + \rho_e \tag{5.7}$$

$$\mathbf{u} = \frac{\rho_i \mathbf{u}_i + \rho_e \mathbf{u}_e}{\rho_i + \rho_e} \tag{5.8}$$

$$e = \frac{3}{2} p = \frac{3}{2} (p_i + p_e) \tag{5.9}$$

Europa has a thin neutral gas atmosphere, which interacts with the streaming plasma. This interaction introduces additional terms to the ideal MHD equations, e.g., production and loss rates, momentum and energy transfer as well as the diffusion of the magnetic field. A detailed derivation of the single fluid equations can be found elsewhere [*Schunk and Nagy*, 2000;

Cravens et al., 1997]. In the following we give a detailed overview of the physical processes implemented in our model and the assumptions we make. In a first step, we concentrate on the plasma-atmosphere interaction and skip the interaction with the solid body.

5.2.1   Continuity equation

In our model the plasma consists of one ion and one electron species. Magnetospheric plasma is convected into the atmosphere of Europa where the density is modified by ionization and recombination processes. Thus, equation 5.3 has to be extended by loss and production processes. As described in section 6.36, magnetospheric electrons at the location of Europa are divided basically in two populations, a thermal Maxwellian and a suprathermal non-Maxwellian population. For the suprathermal population we use a density of $n_{sth} = 2$ cm^{-3} at $T_{e,sth} = 250$ eV [*Sittler and Strobel*, 1987]. For the thermal population we use $T_{e,th} = 20$ eV [*Sittler and Strobel*, 1987], while their density varies with the position of Europa in the plasma sheet (see section 5.6). For the upstream magnetospheric plasma we use an ion mass $m_i = 18.5$ amu [*Kivelson et al.*, 2004]. Furthermore, quasi-neutrality is assumed and as mentioned above the velocity of the neutral gas is neglected.

Multiple charged ions were observed at the orbit of Europa [*Crary et al.*, 1998; *Paterson et al.*, 1999]. In our model an ionospheric single charged ion population with $m_{O_2} = 32$ amu is produced and the correct mass density is then added to the plasma. Some processes, e.g., recombination, require explicitly the mass of the ions. Those processes affect mainly regions where the ionospheric plasma dominates. Therefore, we set throughout the model $m_i = 32$ amu. Furthermore, as the multiple charged ions dominate the density only in the regions where the terms containing the number density n are negligible, we use $z = 1$ throughout the model. For the calculation of the production rate, the magnetospheric electron number density is required. Following *Kivelson et al.* [2004], we use for the determination of the magnetospheric electron density an ion charge of the upstreaming plasma of $z = 1.5$.

The evolution of the bulk density is then given by

$$\frac{\partial \rho}{\partial t} + \nabla \cdot \rho \mathbf{u} = (P - L) m_i \tag{5.10}$$

where P is the production rate and L is the loss rate. *Saur et al.* [1998] find that electron impact ionization is the dominant process to generate Europa's ionosphere. They calculate an electron impact ionization rate of 1.9×10^{-6} s^{-1}. Photoionization is over an order of magnitude smaller with a diurnally averaged value of $3 \times 10^{-8} s^{-1}$ at solar maximum [*McGrath et al.*, 2004]. Therefore, we only include electron impact ionization as a source process of the production of ionospheric plasma.

The production rate is then given by

$$P = \sum_{j=th,sth} f_{e,j}(T_{e,j}) n_{e,j} n_n \tag{5.11}$$
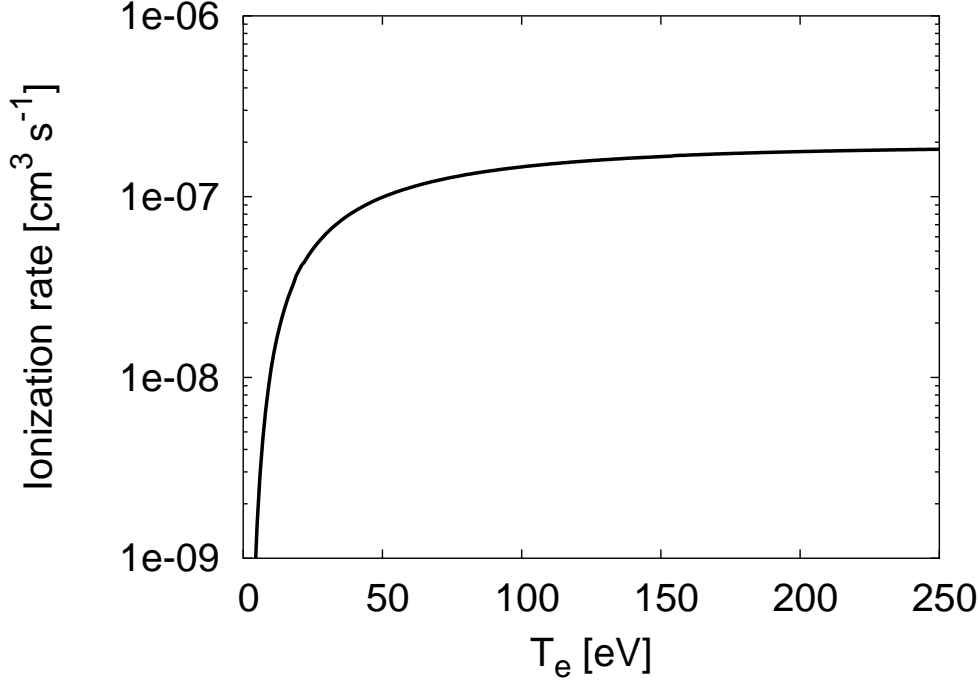
Figure 5.2:   *Electron impact ionization rates of O_2 as a function of electron temperature.*

where n_n is the neutral gas density. The ionization rate is given by

$$f_{e,j}(T_{e,j}) = \int_{E_{ion}}^{\infty} dE\, f_E(E)\, \sigma_j(E)\, v_e(E) \tag{5.12}$$

with a velocity at a given energy of $v(E) = \sqrt{2E/m_e}$, f_E denotes the normalized distribution function in energy space

$$f_E(E) = \frac{2\sqrt{E}}{\pi} (kT_e)^{-\frac{3}{2}} e^{-\frac{E}{kT_e}} \tag{5.13}$$

The ionization cross sections σ_j are taken from the NIST database [*Kim et al.*, 1997]. From 5.12 we calculate the ionization rates of O_2 as a function of electron temperature shown in Figure 5.2.

Ionospheric electrons which are produced by electron impact are much cooler than the magnetospheric electrons and therefore are not involved into the ionization process. While the number of the ionospheric electrons is determined by equation 5.10, we need a separate continuity equation for the magnetospheric electrons. Electron impact ionization does not change the number of the magnetospheric electrons and the loss of those electrons is negligible due to their low density and high temperature. We assume the magnetospheric electrons to move with the bulk velocity (see section 5.2.4). Thus, we solve the following continuity equation for the magnetospheric electrons

$$\frac{\partial n_{e,ms}}{\partial t} + \nabla \cdot n_{e,ms} \mathbf{u} = 0 \tag{5.14}$$

For the loss process in equation 5.10 we include dissociative recombination with a recombination rate [*Torr*, 1985]

$$\alpha_D = 2 \times 10^{-13} \left(\frac{300}{T_e} \right)^{0.7} m^3/s \tag{5.15}$$

The loss rate is then given by (see, e.g., [*Schunk and Nagy*, 2000])

$$L = \alpha_D n_e^2 \tag{5.16}$$

5.2.2 Momentum equation

For the derivation of the plasma momentum equation we apply the following assumptions. First, we assume quasi-neutrality since the spatial scales we are interested in are larger than the Debye lengths, and a negligible neutral gas velocity. Second we neglect gravity. Third we neglect displacement currents since the magnetosonic velocity is much lower than the speed of light. In addition, we assume the pressure to be isotropic.

These assumptions yield the following total plasma momentum equation:

$$\rho \left[\frac{\partial \mathbf{u}}{\partial t} + \mathbf{u} \cdot \nabla \mathbf{u} \right] = \mathbf{j} \times \mathbf{B} - \nabla p - P m_i \mathbf{u} - \left(\frac{m_e}{m_i} \nu_{en} + \nu_{in} \right) \rho \, \mathbf{u} \tag{5.17}$$

which is an extension of equation 5.4. Here ν_{en} is the electron-neutral collision frequency and ν_{in} is the ion-neutral collision frequency.

If one derives the single-fluid equations from the multi-fluid equations, a second frictional term appears which is proportional to the current density $\mathbf{j}$. This term usually becomes important in regions where the bulk velocity is very small compared to the relative velocity of ions and electrons, i.e., where the current is large. This term can be shown to be negligible at Europa for our purposes.

The collision frequency of the ions with the neutrals is independent of temperature [*Banks and Kockarts*, 1973]

$$\nu_{in} = 2.6 \times 10^{-9} n_n \sqrt{\frac{\alpha_0}{\mu_a}} \; s^{-1} \tag{5.18}$$

where α_0 is the polarizability of the neutral gas in units of 10^{-24} cm^{-3}, and μ_a is the reduced mass in amu. We use $\alpha_0 = 1.59$, the value for O_2 given by *Banks and Kockarts* [1973].

The collision frequencies of the electrons depend on the electron temperature. In our model we assume the mean temperature of ions and electrons to be equal. Furthermore, we choose a constant electron temperature in the electron neutral collision frequency. Hence, the electron collision frequency depends only on the neutral gas density (in cm^{-3}) through $\nu_{en} = 10^{-9} n_n$ s^{-1}, which we calculated by using the momentum-transfer cross sections given by *Itikawa*

et al. [1989]. In section 5.2.4 we show, that we choose a calibration factor for the magneto-spheric electron temperature in order to compensate the overestimation in the production rate. However, the electron collision frequency depends not as strong on the electron temperature as the electron impact ionization rate. For instance, in the temperature range between 10eV and 100eV the ionization rate varies, over two orders of magnitude (see Figure 5.2), while the variation of the electron collision frequency is less than a factor of two in the same range [*Itikawa et al.*, 1989]. Therefore, we do not use a calibration factor in the electron collision frequency.

5.2.3 Induction equation

Inclusion of the collision terms and the production and loss processes modifies the ideal MHD induction equation 5.5 as follows:

$$\frac{\partial \mathbf{B}}{\partial t} = \nabla \times \left((\mathbf{u} \times \mathbf{B}) - \frac{m_e}{n\,e^2} \left(\nu_{en} + \frac{m_e}{m_i} \nu_{in} \right) \mathbf{j} - \frac{m_e}{n^2\,e^2} L \mathbf{j} \right) \tag{5.19}$$

Note that we neglect the influence of the Hall term, which would introduce new wave modes into the system, e.g., whistler waves and Hall drift waves. The time scale of such waves is some orders of magnitude lower than the time scale of sonic and Alfvénic waves in our case [*Huba*, 2003] and therefore would lead to a massive increase of simulation time. In regions where the diffusion term is negligible, the Hall term causes the magnetic field to be no longer frozen into the bulk plasma but, into the electron fluid. By neglecting the Hall term one assumes that the magnetospheric electrons as well as the ionospheric electrons move with the bulk velocity. *Saur et al.* [1998] have shown that, contrary to Io, the Hall effect at Europa gives only a small contribution.

If one derives the induction equation from the momentum equations of electrons and ions, an additional frictional term ($\sim \nu_{in}\,\mathbf{u}$) appears besides the diffusion term. This term can be of the same order of magnitude as the diffusion term at Europa. However, the dominant term in our model is the advection term, whereas the frictional term is negligible, as one can easily estimate. Since the diffusion term is the important term for our description of the interior of Europa (see section 5.4), we use this term to get a consistent description of the interior and the exterior of the moon.

5.2.4 Energy equation

The interaction of the plasma with the neutral gas (inelastic as well as elastic processes) changes the internal energy of the plasma. Therefore, the electron temperature, which we assume to be equal to the ion temperature, is reduced. At the same time the plasma torus around Europa exhibits a very extensive energy reservoir, which can provide energy via electron heat conduction along the magnetic field lines. This process is extremely effective at Europa [*Saur et al.*, 1998]. Although this energy reservoir is strictly speaking limited, it is legitimated to assume an unlimited energy reservoir for our purposes. Moreover, we assume infinite heat

conductivity along the field lines. The result is that if a part of a flux tube is cooled down due to its interaction with the neutral gas, energy from the warmer torus is transfered instantaneously via heat conduction to the cold part of the flux tube. We therefore use the following approach for the internal energy:

$$\frac{\partial e}{\partial t} + \nabla \cdot e\,\mathbf{u} = 0 \tag{5.20}$$

For the magnetospheric electrons this represents an isothermal approach. This is not the case when mass loading occurs. In an isothermal plasma, the thermal pressure is proportional to the plasma density. Changes in plasma density, due to mass loading, are reflected only secondary in equation 5.20. However, the influence of the internal energy on the other MHD-equations is given only by the gradient of the thermal pressure in equation 5.17. Consequences of neglecting the direct contribution of mass loading in equation 5.20 will be discussed in chapter 6.

Saur et al. [1998] show that the electron temperature is reduced strongest close to the surface and on the flanks where the electron density reaches its maximum, because of the longer transport time for a plasma fluid element through the dense part of the atmosphere. By maintaining a constant temperature for the magnetospheric electrons one overestimates the production rate in these regions. Hence, the plasma density is overestimated. In order to compensate this deficiency, we implement a calibration factor for the temperature of the magnetospheric electrons. This factor has the following spatial dependence:

$$T_e = T_e^{ms}\left(1 - \left(1 - t_0\cos\frac{\phi}{2}\right)e^{-\frac{h}{H}}\right) \tag{5.21}$$

where h is the height, and the angle ϕ varies in the xy-plane from $0°$ (upstream) to $180°$ (downstream). The factor t_0 and the scale height H are the calibration parameters to be determined. We determine these parameters by comparing our model with measurements of flybys during which Europa was located in the middle of the current sheet (e.g., E12), i.e., where induction effects are negligible.

5.3 Neutral atmosphere

The dominant molecular species in Europa's atmosphere is oxygen. In addition there are a few other constituents like water molecules and trace elements such as sodium and potassium (see section 2.1.2). In this work we regard molecular oxygen as the only neutral species and we neglect the dynamics of the neutral gas, i.e., $u_n \ll u$.

We use a hydrostatic atmosphere with a scale height of 145 km and a surface density $n_{0,0} = 1.7 \times 10^7$ cm^{-3}. This is consistent with an O_2 column density of $N_{col} = 5 \times 10^{18}$ m^{-2} estimated in *Saur et al.* [1998]. Thereby we neglect the density enhancement in the near surface region ($h \leq 100$ km) presented in *Shematovich et al.* [2005]. This is reasonable, because we do not attempt to study Europa's atmosphere in detail. Hence, processes which act on scales

less then 100 km are in the order of the grid size of our code and therefore not well resolvable. *Pospieszalska and Johnson* [1989] demonstrate that sputtering is not uniform over the surface of Europa, but is decreasing from the trailing to the leading hemisphere. We follow *Saur et al.* [1998] in assuming that the surface density $n_0(\theta)$ varies in direct proportion to the normalized flux variation calculated by *Pospieszalska and Johnson* [1989]. The surface density then has the following spatial dependence:

$$n_0(\theta) = n_{0,0}\left[1.08\,H(\frac{\pi}{2} - \theta)\cos\theta + 0.885(\cos\frac{\theta}{2} + 1.675)\right] \qquad (5.22)$$

where $H(\frac{\pi}{2} - \theta)$ is the Heaviside step function and the angle θ varies from $0°$ (pole of trailing hemisphere) to $180°$ (pole of leading hemisphere).

5.4 Implementation of Induction

In the previous section we derived the single-fluid equations we use for our simulation. In order to account for possible induction in the interior of the moon, we expand our equations.

In this section we show the implementation of induction into the equations as well as the treatment of Europa's solid body.

The magnetic field at Europa consists of different components. First, the time varying background magnetic field of Jupiter and the magnetospheric current sheet $\mathbf{B}_0$. Second, the magnetic field caused by the interaction of the magnetospheric plasma with Europa's atmosphere

$$\mathbf{B}_P = \mathbf{B}_{P,i} + \mathbf{B}_{P,e} \qquad (5.23)$$

where $\mathbf{B}_{P,e}$ is the magnetic field of all currents flowing in the exterior of Europa, and $\mathbf{B}_{P,i}$ is the the magnetic field of all currents flowing in the interior of the moon, except for the induced currents due to $\mathbf{B}_0$ and $\mathbf{B}_{P,e}$. Finally, we have the induced magnetic field due to the time varying background field and the plasma currents.

$$\mathbf{B}^{ind} = \mathbf{B}^{ind}(\mathbf{B}_0) + \mathbf{B}^{ind}(\mathbf{j}_P) \qquad (5.24)$$

We assume the background magnetic field $\mathbf{B}_0$ to be a time varying homogeneous magnetic field at Europa. The periodicity of the background field is given by the synodic rotational period of Jupiter. Doing so, we do not account for other excitation periods, e.g., Europa's orbital period or asymmetries of Jupiter's magnetospheric field.

The total magnetic field $\mathbf{B}_{tot}$ at Europa is then given by

$$\mathbf{B}_{tot} = \mathbf{B}_0 + \mathbf{B}_P + \mathbf{B}^{ind}(\mathbf{B}_0) + \mathbf{B}^{ind}(\mathbf{j}_P) \qquad (5.25)$$

In contrast to other bodies, e.g., Titan, the thin atmosphere of Europa cannot shield completely the surface of Europa from the streaming plasma flow. Plasma which hits the surface

of Europa will be lost, while the magnetic field can diffuse into the moon. This problem can be solved in two ways: First, inner boundary conditions could be set at the surface. This solution is impractical, because it would request a correct description of the diffusion into the moon at the boundaries. As the description of a solid body is not included in the single-fluid equations a priori, it is easier to describe the interior of Europa as a "exotic" plasma to approach the real situation. Thereby, the total magnetic field has to fulfill the induction equation in the interior as well as in the exterior of the moon. Generally, this equation can be written as (see equation 5.19)

$$\frac{\partial \mathbf{B}_{tot}}{\partial t} = \nabla \times (\mathbf{u} \times \mathbf{B}_{tot}) - \nabla \times (\eta \nabla \times \mathbf{B}_{tot}) \tag{5.26}$$

where $\mathbf{u}$ is the bulk velocity in the respective medium and η is the magnetic diffusivity. As mentioned above we neglect displacement currents.

In principle, the problem could be solved by solving the single-fluid equations in the exterior and the diffusion equation in the interior of the moon. However, because of the Courant-Friedrich-Lewy (CFL) criteria, which states that information should not propagate more than one grid box in one timestep, the time steps needed for the description of the plasma interaction are very small compared to the time scale on which the induction process takes place. Thus, the simulation time needed for a stable periodic solution would be unrealistic long.
In order to reduce simulation time, we have to make use of the periodicity and the quasi-stationarity of the problem. Quasi-stationarity means that the plasma flow at a special time depends only on the background conditions and the phase lagged induced magnetic field at this special time. This approximation is fulfilled if the time T_c, which the flow needs to respond to a new constant background condition and a new constant internal field, is small compared to Jupiter's synodic period. The time T_c can be approximated by the time a plasma parcel needs to cross Europa's interaction region, which is usually given by $T_c = \int_s \frac{ds}{v(s)}$. Using $3R_E$ as the radius of interaction, a background velocity $v_0 = 104$ km/s and a velocity dropping to $1/5v_0$ we assess:

$$T_c = \frac{2R_E}{0.5\,v_0} + \frac{2R_E}{0.2\,v_0} + \frac{2R_E}{0.5\,v_0} \approx 270\,s \tag{5.27}$$

This time is small compared to the synodic period of Jupiter $T_{syn} \approx 11$ h. Thus, the problem can be considered as quasi-stationary.

In the following we deal with the interior and the exterior of Europa separately. This can be done, because we assume Europa's icy crust to be electrically non-conducting.

5.4.1   Description of the exterior

As mentioned in chapter 4 we assume the outer ice crust of Europa to be electrically non-conducting, which causes the current systems outside and inside Europa to be isolated against each other. Thus, $\mathbf{B}_0$ and $\mathbf{B}^{ind}(\mathbf{B}_0)$ are potential fields outside the moon. Equation 5.26 can then be written

$$\frac{\partial(\mathbf{B}_P + \mathbf{B}^{ind}(\mathbf{j}_P))}{\partial t} = \nabla \times (\mathbf{u} \times \mathbf{B}_{tot}) - \nabla \times (\eta \nabla \times (\mathbf{B}_P + \mathbf{B}^{ind}(\mathbf{j}_P)))$$
$$- \frac{\partial(\mathbf{B}_0 + \mathbf{B}^{ind}(\mathbf{B}_0))}{\partial t} \tag{5.28}$$

where $\mathbf{B_0}(t)$ and $\mathbf{B}^{ind}(\mathbf{B}_0)$ are known analytically (see section 5.6). The time varying background magnetic field and the thereby induced magnetic field are determined by:

$$\mathbf{B}_0 = -84\, nT\, \sin(\Omega t)\hat{\mathbf{x}} - 210\, nT\, \cos(\Omega t)\hat{\mathbf{y}} \tag{5.29}$$

$$\mathbf{B}^{ind}(\mathbf{B}_0) = A\, f_1(\mathbf{x})\, 84\, \text{nT}\, \sin(\Omega t - \phi)\hat{\mathbf{x}} - A\, f_2(\mathbf{x})\, 200\, \text{nT}\, \cos(\Omega t - \phi)\hat{\mathbf{y}} \tag{5.30}$$

where A is the reduction factor and ϕ the phase lag defined in section 4.1. From that $\frac{\partial \mathbf{B}_0}{\partial t}$ and $\frac{\partial \mathbf{B}^{ind}(\mathbf{B}_0)}{\partial t}$ can be computed. Both expressions are assumed to be constant during one simulation run.

Note that we solve the induction equation for the plasma magnetic field and the thereby induced magnetic field. In order to highlight various contributions, we present a more comprehensive form of induction equation 5.28 for the exterior:

$$\frac{\partial(\mathbf{B}_P + \mathbf{B}^{ind}(\mathbf{j}_P))}{\partial t} = \nabla \times \left[\mathbf{u} \times (\mathbf{B}_P + \mathbf{B}^{ind}(\mathbf{j}_P)) \right]$$
$$- \nabla \times \left[\frac{m_e}{n e^2} \left(\nu_{en} + \frac{m_e}{m_i} \nu_{in} + \frac{L}{n} \right) \nabla \times (\mathbf{B}_P + \mathbf{B}^{ind}(\mathbf{j}_P)) \right]$$
$$+ \nabla \times \left[\mathbf{u} \times (\mathbf{B}_0 + \mathbf{B}^{ind}(\mathbf{B}_0)) \right] - \frac{\partial(\mathbf{B}_0 + \mathbf{B}^{ind}(\mathbf{B}_0))}{\partial t} \tag{5.31}$$

The term on the left hand side and the first term on the right hand side are those which are originally implemented in the Zeus3D-Code. The second term on the right hand side represents the interaction with the neutral atmosphere due to collisions and loss processes. The last two terms on the right hand side contain the coupling with the internal induction process as well as the slow change of the background field and the induced magnetic field.

Induction effects also have to be accounted for in the momentum equation (equation 5.17). In the extended representation this equation then reads:

$$\rho \left(\frac{\partial \mathbf{u}}{\partial t} + \mathbf{u} \cdot \nabla \mathbf{u} \right) = \left(\nabla \times (\mathbf{B}_P + \mathbf{B}^{ind}(\mathbf{j}_P)) \right) \times (\mathbf{B}_P + \mathbf{B}^{ind}(\mathbf{j}_P)) - \nabla p$$
$$- \left(\frac{m_e}{m_i} \nu_{en} + \nu_{in} + \frac{P}{n} \right) \rho \mathbf{u} + \left[\nabla \times (\mathbf{B}_P + \mathbf{B}^{ind}(\mathbf{j}_P)) \right] \times (\mathbf{B}_0 + \mathbf{B}^{ind}(\mathbf{B}_0))$$
$$+ \left[\nabla \times (\mathbf{B}_0 + \mathbf{B}^{ind}(\mathbf{B}_0)) \right] \times (\mathbf{B}_0 + \mathbf{B}_P + \mathbf{B}^{ind}(\mathbf{B}_0) + \mathbf{B}^{ind}(\mathbf{j}_P)) \tag{5.32}$$

Again, the terms in the first line are those originally solved by Zeus3D-Code when using equation 5.31 as induction equation. The last two terms include the coupling with the internal induction process.

5.4.2   Description of the interior

In our plasma interaction model, we assume Europa to be a homogeneous conducting sphere ($\eta_i = const.$). The magnetic field inside Europa has to satisfy equation 5.26. As we will see in section 5.5, we use an iterative process to calculate the plasma induced magnetic fields. In the first iteration we consider induction by the homogeneous background magnetic field only. For the induced magnetic field inside Europa, we use as a starting point

$$\frac{\partial(\mathbf{B}_0 + \mathbf{B}^{ind}(\mathbf{B}_0))}{\partial t} = -\nabla \times (\eta_i \nabla \times (\mathbf{B}_0 + \mathbf{B}^{ind}(\mathbf{B}_0))) \tag{5.33}$$

In that case equation 5.26 simplifies to

$$\frac{\partial(\mathbf{B}_P + \mathbf{B}^{ind}(\mathbf{j}_P))}{\partial t} = \nabla \times (\mathbf{u} \times \mathbf{B}_{tot}) - \nabla \times (\eta_i \nabla \times (\mathbf{B}_P + \mathbf{B}^{ind}(\mathbf{j}_P))) \tag{5.34}$$

As noted earlier, plasma cannot penetrate into the solid body, but is absorbed by the surface and interacts with it respectively. Thus, the interior of Europa is free of plasma. Since we use single fluid equations to model the plasma interaction, the description of a solid body is not included automatically. For numerical reasons the area of the solid body cannot be free of plasma. In order to account for the diffusion of the magnetic field into the moon properly (by fulfilling equation 5.33) we modify the characteristics of the plasma such that, the magnetic Reynold number is small, i.e., we manually decrease the plasma velocity. Simultaneously, loss processes are implemented in order to reduce the plasma density in the interior of the moon. If the plasma density drops below a minimum value, a production rate is turned on. Thus, the plasma density inside Europa is at a minimum value. Additionally, the magnetic diffusivity has to be adjusted to the desired value to be consistent with the analytical solution for the induction. Equation 5.19 illustrates that the magnetic diffusivity in the interior η_i is proportional to n_n/ρ. Hence, we control η_i by adjusting the neutral gas density in every time step at every grid point in the interior depending on the local plasma density.

For the plasma momentum equation, equation 5.32 is also valid in the interior. In addition with the statements above we solve equation 5.10 and equation 5.20 inside Europa.

5.5   Procedure and model summary

We use an iterative process to calculate the plasma induced magnetic fields. As a starting point we include the induction by a homogeneous background field only. Thereby we use the time varying components of the background magnetic field shown in Figure 5.4. Details are given in the next section. We then have the analytical solution of equation 4.3, derived in chapter 4.2, as an initial condition for the internal magnetic field.

Then we solve a stationary problem for 8 different times t_i which are equally distributed over the synodic period of Jupiter ($\Omega t = 0°, 45°, 90°, ...$). This is done by solving the continuity equation (equation 5.10), the momentum equation (equation 5.32), the induction equation

(equation 5.31 and equation 5.34) and the equation for the internal energy (equation 5.20) with our code. Note that the background plasma conditions vary considerably at the different times t_i as shown in Figure 5.5.

The kernel of our model consists of Zeus3D [*Stone and Norman*, 1992*a*;*b*], a three-dimensional time dependent code which solves the ideal MHD equations. The extra terms added to the equations 5.3 – 5.6 account for the effects of the neutral atmosphere and the coupling with the periodically induced magnetic fields from the interior. They are included as source terms for the MHD-equations. For the treatment of the diffusion term in the induction equation we include the semi-implicit Crank-Nicholson scheme [*Press et al.*, 1986]. In order to account for the electron impact ionization we solve a separate continuity equation for the magnetospheric electrons. The solid body of Europa is treated as a plasma with properties described above.

In the second step the induced magnetic field $\mathbf{B}^{ind}(\mathbf{j}_P)$ due to the time varying currents in the exterior is determined. Therefore, we first acquire the time variable part of the external plasma magnetic field $\mathbf{B}'_p$ on the surface of the conducting sphere at a given time:

$$\mathbf{B}'_p \; = \; (\mathbf{B}_p + \mathbf{B}^{ind}(\mathbf{j}_P)) \; - \; < \mathbf{B}_p + \mathbf{B}^{ind}(\mathbf{j}_P) > \tag{5.35}$$

where the over one synodic period averaged constant part is calculated by

$$< \mathbf{B}_p + \mathbf{B}^{ind}(\mathbf{j}_P) > \; = \; \frac{1}{2\pi} \int_0^{2\pi} \mathbf{B}_p(t) + \mathbf{B}^{ind}(\mathbf{j}_P)\, dt \tag{5.36}$$

Subsequently, we determine the harmonic coefficients of the induced magnetic fields for each time t_i. A Fourier expansion of these harmonic coefficients determines the plasma induced magnetic fields $\mathbf{B}^{ind}_p(\mathbf{j}_P)$ for any time t. The analytical description of the plasma induced fields together with the induced field $\mathbf{B}^{ind}(\mathbf{B}_0)$ from the first iteration yields the new initial internal magnetic field. We then repeat the above procedure until we reach convergence for the determined harmonic coefficients.

5.6   Initial conditions

The background magnetic field varies mainly in the B_y- and to a minor degree in the B_x-component at the position of Europa. It contains contributions both from the internal magnetic field of Jupiter and the magnetic field due to the magnetospheric current sheet.

Figure 5.3 shows the variation of the B_x- and B_y-components of Jupiter's magnetospheric field at Europa's location. The dotted ellipse shows an ideal Jovian dipole field with an inclination of $9.6°$ unaffected by the plasma sheet, the solid ellipse is a fit to the data points using equation 5.29 and the shaded model of *Kivelson et al.* [2000]. The shaded model shows a slight asymmetric behavior which would probably lead to higher harmonics of the inducing background field. However, as there are too few data points we do not consider the asymmetries in this work.
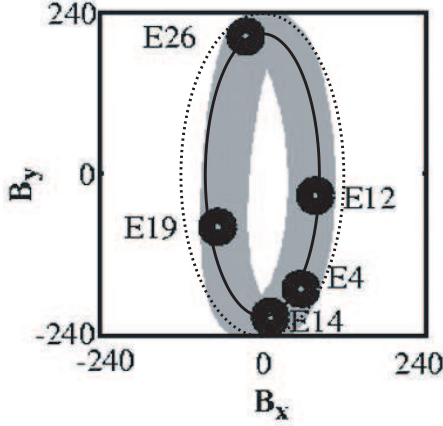
Figure 5.3:   *Variation of the B_x- and B_y-components of Jupiter's magnetospheric field at Europa over one synodic period [Kivelson et al., 2000].*

We use a constant $B_z = -410 nT$ for the iteration process in our model. Figure 5.4 shows the used values of B_x and B_y, with Ωt the angle between the rotating dipole moment of Jupiter and the line of sight Jupiter-Europa [*Neubauer*, 1999]. Apparently, the inducing field is strongest when the rotating dipole moment of Jupiter points towards ($\Omega t = 0°$) or away from Europa ($\Omega t = 180°$). Figure 5.5 shows that Europa is outside the plasma sheet at this times. Contrarily the weakest induction effects are expected when Europa is in the center of the plasma sheet (for $\Omega t = 90°$ and $\Omega t = 270°$). During one synodical rotation the magnetic background field changes its orientation at the location of Europa by roughly $20°$.

The variation of the background plasma density (in Figure 5.5) stems from the tilt of the plasmasheet against Europa's orbital plane by about $7°$ [*Dessler*, 1983]. In addition, the rotational velocity of the plasma is larger than the orbit velocity of Europa. Thus, Europa passes through different plasma regimes during one synodic rotation of Jupiter. The electron number density in the vicinity of Europa is derived from the Galileo PWS data for different flybys [*Kurth et al.*, 2001] while Galileo PLS data from the first two Europa flybys give an idea of the plasma density at Europa [*Paterson et al.*, 1999]. By assuming the plasma to be symmetric around the centrifugal equator and to vary periodically we derive a simple model for the electron number density shown in Figure 5.5. Thereby we use a minimum electron number density of $n_e = 18$ cm^{-3} when Europa is outside the plasma sheet and a maximum value of $n_e = 250$ cm^{-3} when Europa is in the center of the plasma sheet. In between we assume the density to fall of with $exp - (z/H)^2$, where H is the scale height of the plasma and z is the distance of Europa from the center of the plasma sheet [*Thomas et al.*, 2004]. We then calculate the plasma mass density by using an ion charge of 1.5.

Due to the time varying magnetospheric conditions at Europa, the plasma beta and the Alfvén Mach number are changing. However, we always deal with a sub-Alfvénic plasma with a mean value for the Alfvén Mach number of $M_A = 0.5$. Therefore, no fast bow-shock forms. The strong magnetic field of Jupiter dominates the plasma interaction at Europa. This is expressed by the undisturbed plasma beta, i.e., the ratio of the total plasma pressure to the magnetic pressure, which varies in our model from 0.01 to 0.2.

If not indicated otherwise we use the EPhiO coordinate system, defined in chapter 3. The center of Europa is in the origin of the coordinate system and the plasma streams along the x-axis.

At $t = 0$ the plasma velocity is constant (104 km/s) everywhere except for a sphere around Europa with a radius of 5 R_E. In the shell from 5 R_E to 3 R_E the velocity decreases linearly to zero, the value inside the sphere with radius 3 R_E. Magnetic field, thermal pressure and plasma mass density are constant everywhere at the beginning with the respective values.
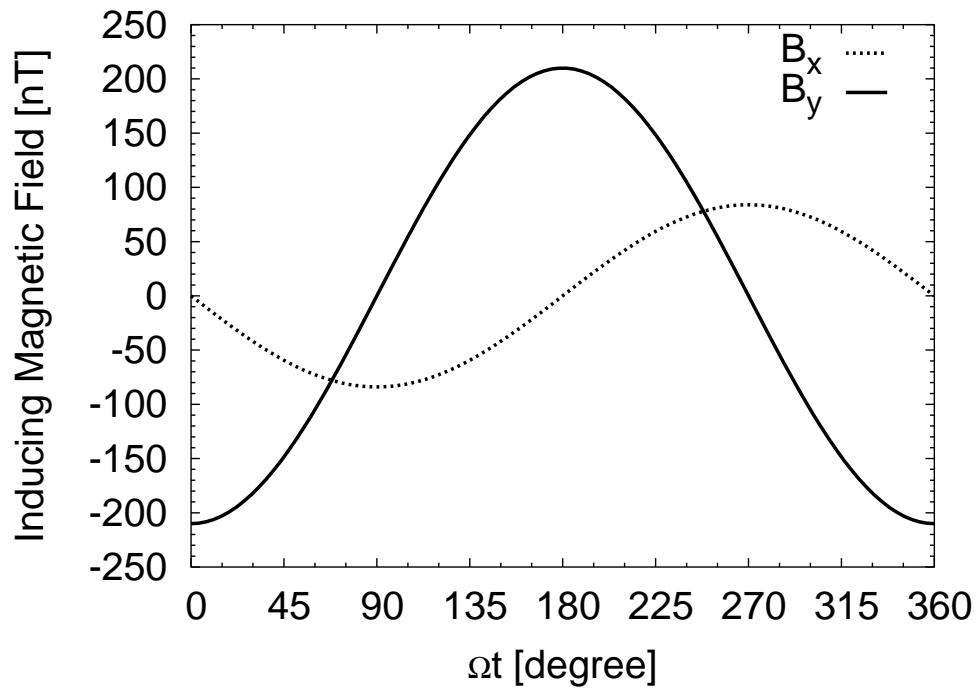
Figure 5.4:   *Background magnetic field. Values are obtained by fitting an ellipse to the magnetic field data given by Kivelson et al. [2000].*
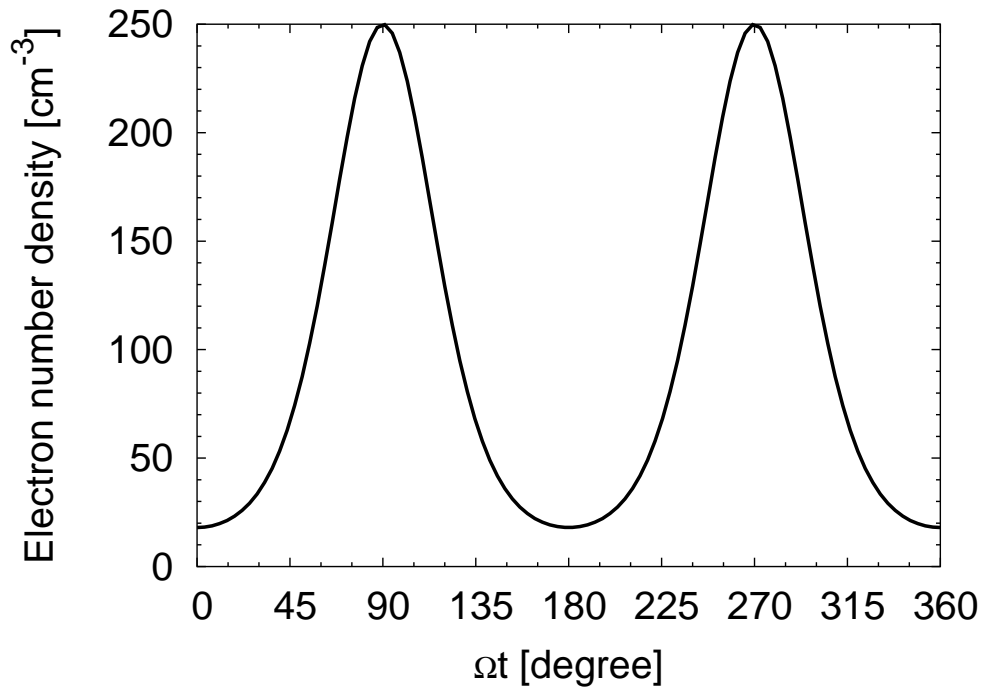
Figure 5.5:   *Background electron number density. Values are estimated from PWS [Kurth et al., 2001] and PLS data [Paterson et al., 1999].*

We use a Cartesian grid divided into four regions with different spatial resolution: a very high resolution region from -1.5 R_E to 1.5 R_E in all three directions in space with a grid size of 80 km, a high resolution region up to a distance of 3 R_E in all three directions in space with a grid size of 157 km, followed by a medium resolution region with a grid size of 795 km and finally a low resolution region with a grid size of 1569 km. The total grid volume is [[-10,10],[-10,10],[-60,60]] R_E.

RESULTS

This chapter presents the results of our numerical model, which is described in the previous chapter. The primary goal is to find closer constraints on the conductivity and the thickness of the internal ocean than earlier studies. We accomplish this aim by comparing the results from our advanced model to the magnetic field data. To simplify matters, we use in this chapter the term "ocean" instead of conducting subsurface layer, although its not clear yet whether a substantial ocean exists below the icy surface of Europa.

We start with the results of the global plasma interaction of Europa with the Jovian magnetosphere (section 6.1). The focus here is on the E4 model conditions, i.e., when Europa is located outside the plasma sheet, and we neglect the induction effect, which influence is discussed later. Subsequently, we investigate the influence of the plasma interaction on the induction process (section 6.2). For this second order induction effect, caused by periodic variations of the magnetospheric plasma, we derive the harmonic coefficients of the induced magnetic fields. Then we discuss the influence of the induction on the plasma interaction (section 6.3). Subsequently, we verify our model description of Europa's interior (section 6.4). Afterwards, we compare our model results with the Galileo flyby data and determine the so far strongest constraints on the conductivity of Europa's ocean (section 6.5). In addition, we can explain the lack of higher ionospheric density signatures in the wake during the E4 flyby. Finally, we discuss our results (section 6.6).

Estimates of the thickness of the solid ice crust (elastic + ductile) vary from a few km to 60 km (see section 4.3), a range which we can not resolve with our model. In addition, the limited data set does not allow us to resolve ice crust thicknesses in this range. Therefore, we choose a thickness of the solid ice crust of 50 km when calculating the internal induced magnetic fields analytically.

The coordinate system we use is determined as follows: The -z-axis is along the background

magnetic field. The x-axis is perpendicular to the background magnetic field, and such that the incident plasma velocity vector of the bulk plasma is contained in the xz-plane. The y-axis completes the triad ($\hat{\mathbf{y}} = \hat{\mathbf{z}} \times \hat{\mathbf{x}}$). Note that for the cases $\Omega t = 0°$ and $\Omega t = 180°$ the x-axis is along the corotational flow direction. In these cases our coordinate system is equivalent to the EPhiB coordinate system. This coordinate system is most suitable to show the symmetries related to the magnetic field, e.g., the Alfvén wing system. For the comparison with the Galileo flyby data we use the EPhiO coordinate system.

6.1 Global plasma interaction

This chapter presents the global plasma interaction of Europa with the Jovian magnetosphere, at times when Europa is located outside the plasma sheet. Here we neglect the induction effects. We start with the results for the global plasma flow and the magnetic field geometry. Subsequently, we show the results for the plasma density and discuss the structure of Europa's plasma wake. Afterwards, we show the electric current system at Europa.

6.1.1 Global plasma flow and magnetic field geometry

The magnetic field of Jupiter exceeds the field arising from the external currents at the orbit of Europa [*Kivelson et al.*, 1999]. In addition, the plasma beta in the undisturbed region is smaller than 1. As mentioned above the strong influence of the magnetic field is also reflected in the small Alfvénic Mach number which is the ratio of the bulk flow velocity to the Alfvén velocity. This subalfvénic interaction is well known for Io's interaction with the plasma torus [*Saur et al.*, 2004]. The interaction problem at Europa can be considered as a scaled-down version of the interaction problem at Io when the induction is neglected.

The interaction of Europa with the Jovian magnetospheric plasma is affected by properties of the three independent MHD wave modes that propagate in different directions and at different speeds. These modes are the slow, the intermediate, and the fast MHD mode. In the linear case, the intermediate mode, also referred to as the Alfvén mode, carries currents along the magnetic field. Alfvén waves in general transport energy and momentum along the magnetic field, but not across the magnetic field.

The Alfvén waves travel along the magnetic field with the Alfvén velocity. The group velocity is exactly parallel to the magnetic field. Taking into account the bulk velocity of the plasma flow $\mathbf{u}_0$, these waves propagate along the Alfvén characteristics $\mathbf{v}_a^{\pm} = \mathbf{u}_0 \pm \frac{\mathbf{B_0}}{\sqrt{\mu_0 \rho}}$. This is also true for the non-linear case [*Neubauer*, 1980].

The slow mode also propagates along the magnetic field, but with a velocity close to the sound speed (in the far field of Europa). The group velocity of the fast mode is largest perpendicular to the magnetic field. The fast mode can carry energy in all directions.

Figure 6.1 shows the bulk velocity of the plasma flow in the xz-plane, and Figure 6.2 shows the projection onto the xy-plane for E4 flyby conditions. The Alfvén characteristics are plotted for comparison. The model results clearly identify the Alfvén wings as regions with very

↑ 100 km/s
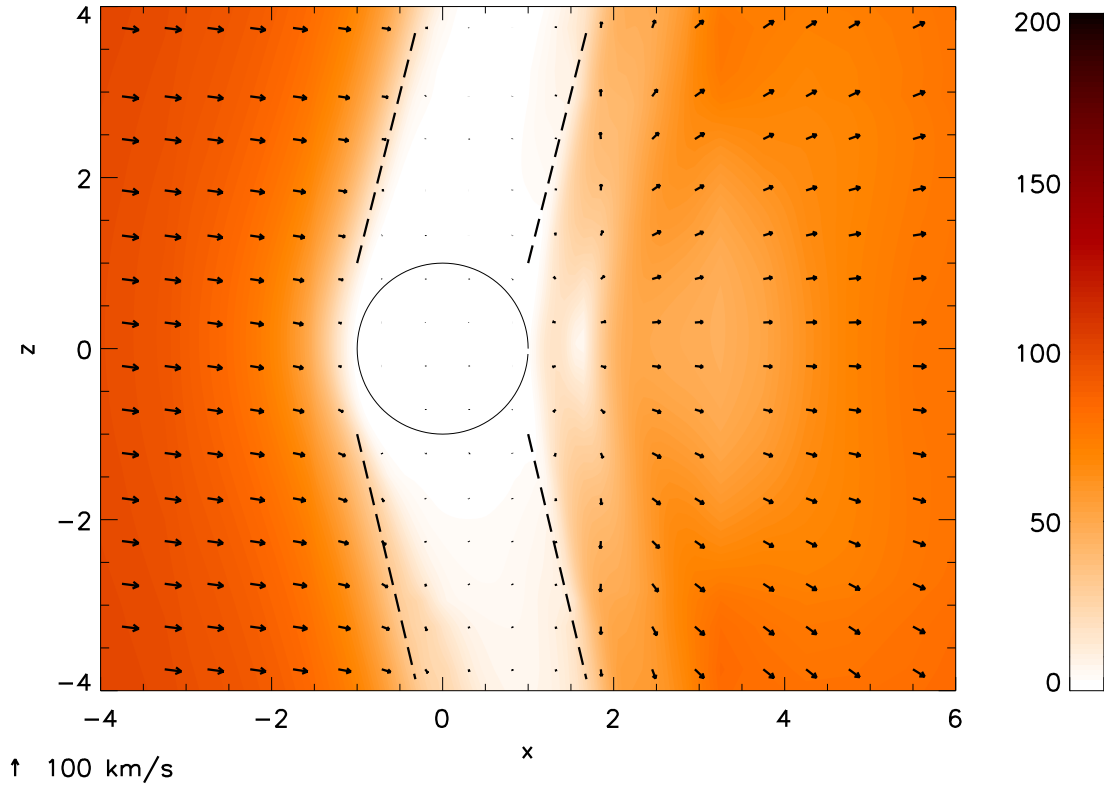
Figure 6.1:   *Plasma bulk velocity in km/s in the xz-plane. The Alfvén characteristics are shown as black dashed lines. The color scale determines the velocity magnitude.*

↑ 100 km/s
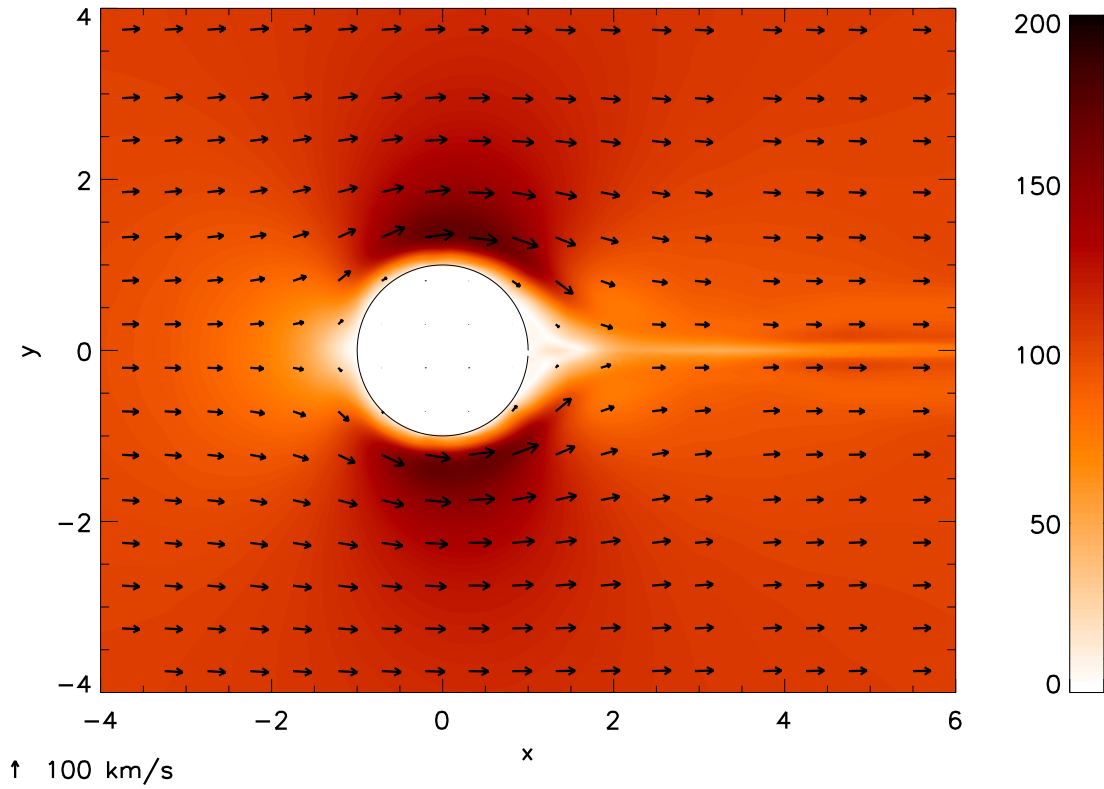
Figure 6.2:   *Plasma bulk velocity in km/s in the equatorial plane. The color scale determines the velocity magnitude.*
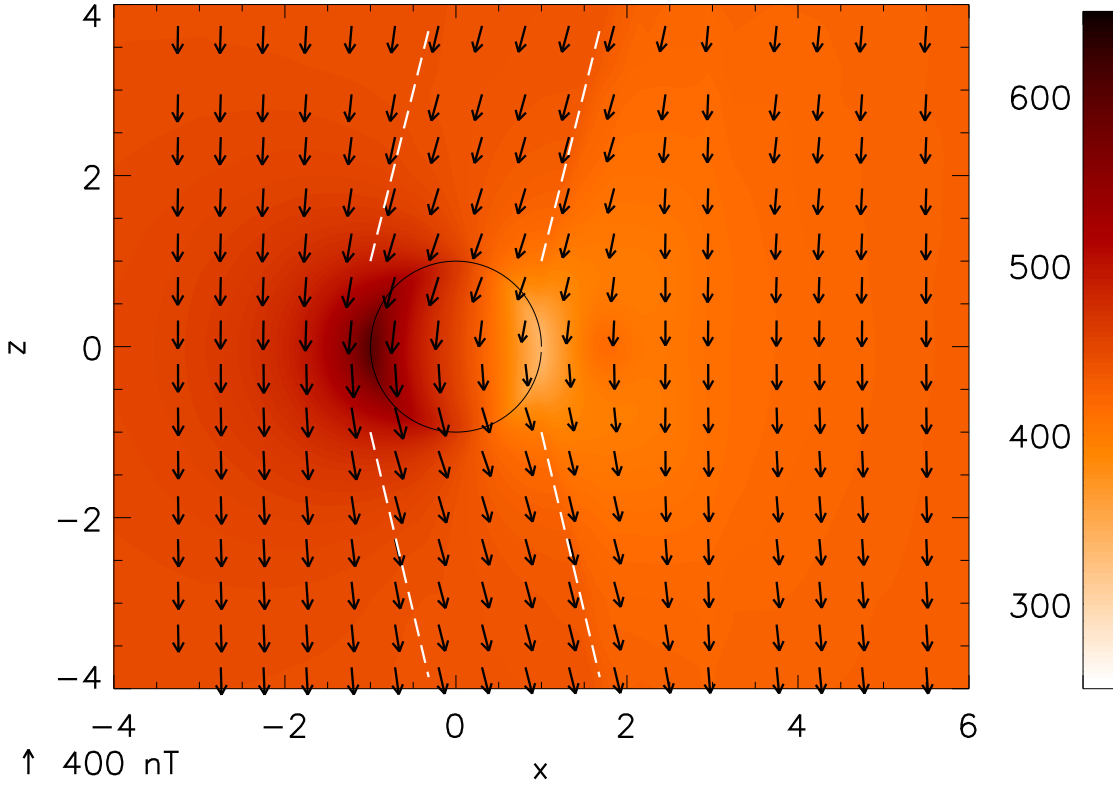
Figure 6.3: *Magnetic field vectors and magnitude in nT in the xz-plane. The Alfvén characteristics are shown as white dashed lines. The color scale determines the magnetic field magnitude.*

small velocities compared to the incident flow velocity. Note that for E4 flyby conditions the magnetic field and the direction of the plasma flow are not perpendicular. Therefore, a small negative z-component of the bulk velocity remains. Due to this small component the symmetry in Figure 6.1 is broken.

Figure 6.3 shows that the magnetic field inside the Alfvén wings is nearly parallel to the Alfvén characteristics. The magnetic field magnitude is almost constant inside the wings. While Alfvén waves cannot change the magnetic field magnitude in the linear case, this is possible in the non-linear case.

Upstream of Europa the plasma is slowed down (see Figure 6.2) by compressional perturbations propagating with the fast mode. This wave mode is generated by the collision of the plasma with the neutrals, and by the pickup processes. Associated with the slow down of the plasma is a compression and a bending of the magnetic field (see Figure 6.3). Downstream of Europa the plasma flow from the two flanks is combined and is reaccelerated. The magnetic field strength decreases because of the slow diffusion of the magnetic field through Europa. Figure 6.2 suggests that the radial extent of Europa's wake in the equatorial plane is smaller than the moons diameter. This is in agreement with the result of *Saur et al.* [1998] but in contrast to the analysis of *Paranicas et al.* [2000].

The flow is diverted around the moon. However, parts of the flow reach the satellite surface and are absorbed. Figure 6.4 shows that the divergence of the flow also occurs around the

↑ 100 km/s
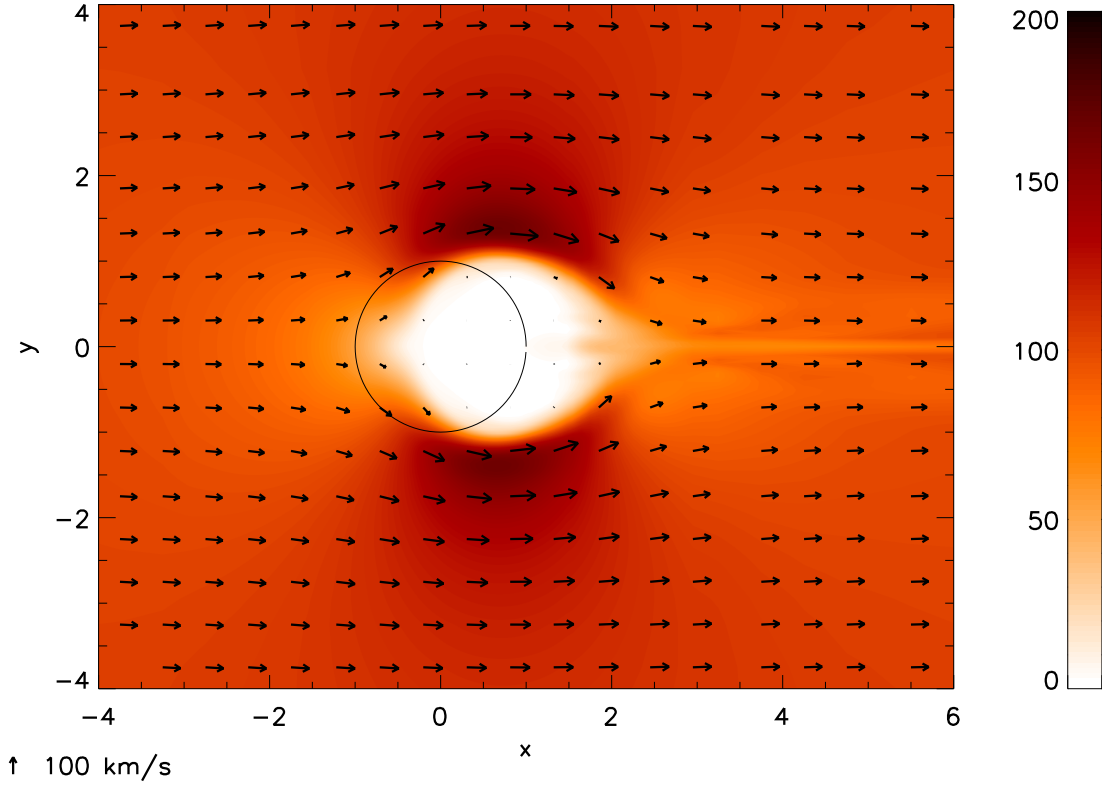
Figure 6.4:   *Plasma bulk velocity in km/s in the xy-plane at z = 2.75 R_E. The thin black circle illustrates the radius and position of Europa.*

Alfvén wings and that the flow speed is most reduced inside this region. On the flanks of Europa (and also of the Alfvén wing) there are regions of increased velocity with flow speeds up to 150 km/s.

6.1.2   Plasma density

When magnetospheric plasma is convected into Europa's atmosphere, magnetospheric electrons ionize atmospheric O_2-molecules by impact and create electrons and ions. Hence, the plasma density is increased (see equation 5.10) while the plasma bulk velocity is reduced (see equation 5.17), i.e., the plasma is decelerated, conserving momentum.

Figure 6.5 shows the ion number density in the equatorial plane for the E4 flyby conditions. The maximum of the density is found on the flanks and upstream of Europa close to the surface with values of several thousand cm^{-3}. Further downstream the plasma density decreases and the ionosphere becomes detached from the surface. The ionospheric plasma is swept into the wake region. Here the mass-loaded flux tubes that pass Europa converge and the pick-up plasma is concentrated along the x-axis.

We solve a separate continuity equation (see equation 5.14) for the magnetospheric electrons. Figure 6.6 shows the electron number density of the magnetospheric electrons. Electrons which reach Europa's surface will be lost. Most of the population is swept around Europa
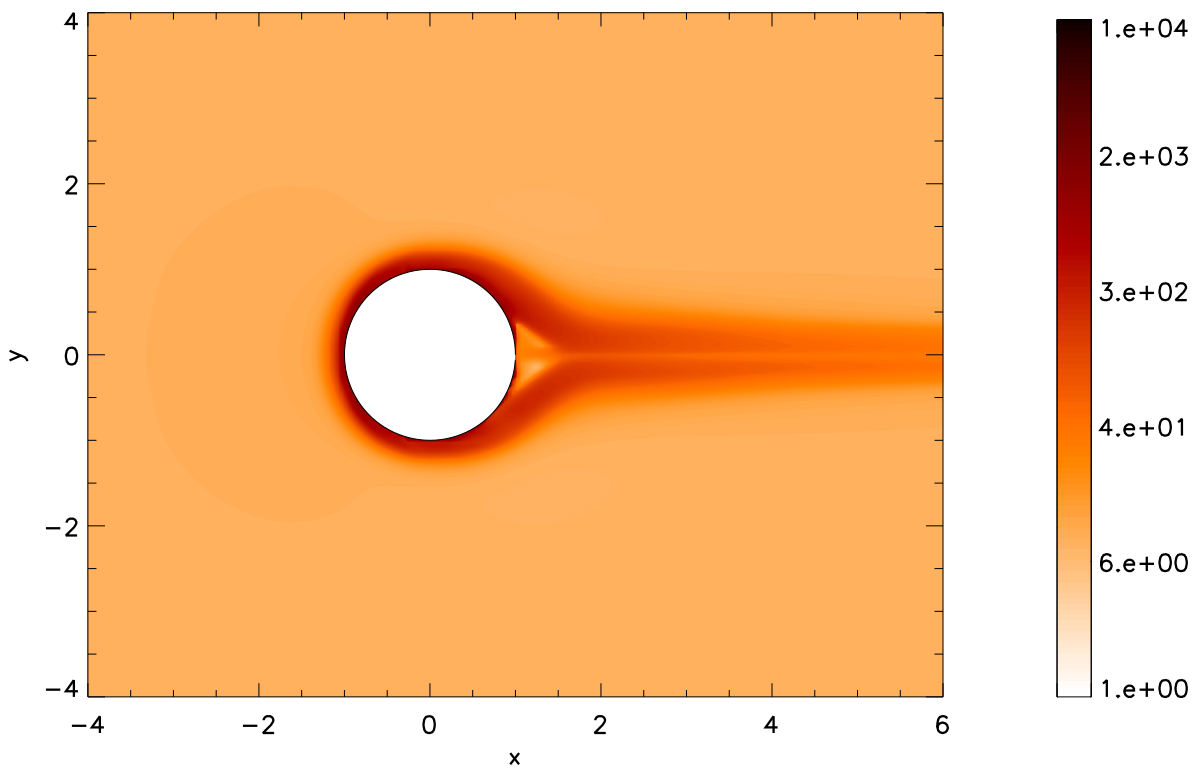
Figure 6.5:   *Ion number density in cm^{-3} in the xy-plane.*
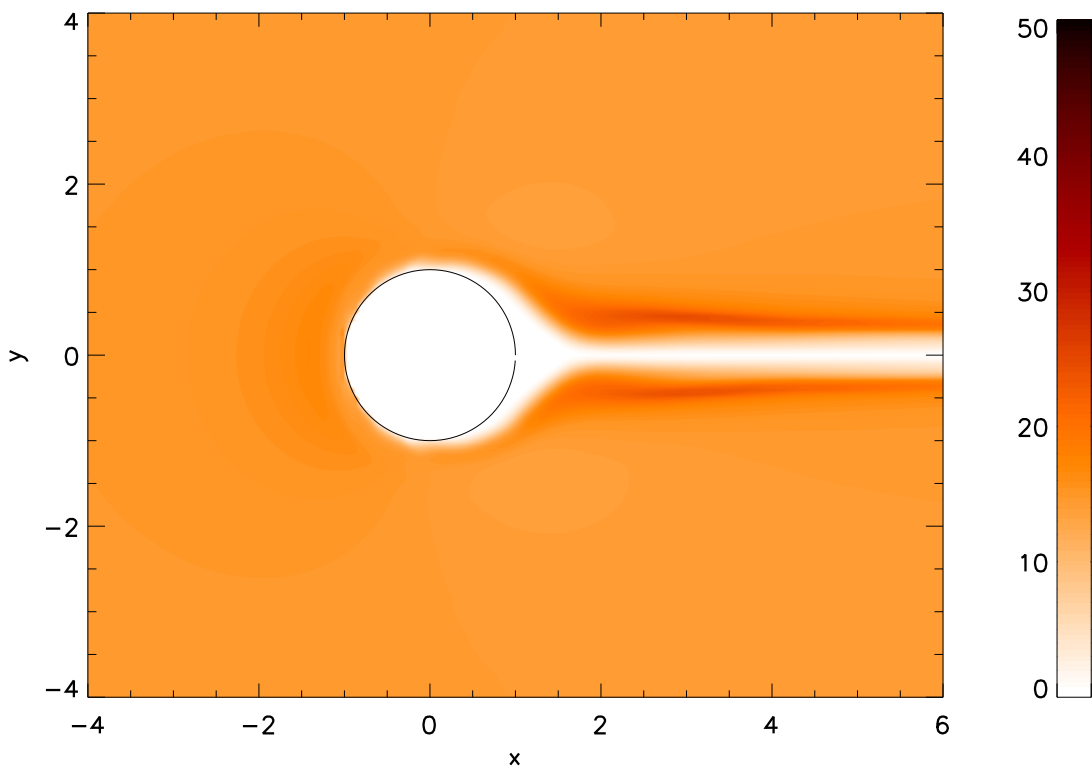
Figure 6.6:   *Magnetospheric electron number density in cm^{-3} in the xy-plane.*

and forms a wake along the x-axis. The downstream region and the inner wake region are free of magnetospheric electrons. Figure 6.6 shows a density enhancement on the flanks of the wake. This is a result of the flow divergence. Figures 6.6 and 6.5 again suggest that the diameter of Europa's wake is smaller than the diameter of Europa.

Figure 6.7 shows that the enhanced plasma density in the wake expands along the z-axis. At x = 2.75 R_E most of the plasma is concentrated around the equatorial plane. This is a consequence of the plasma flow and the pick-up process. While most of the plasma is picked up at the flanks (see Figure 6.8), the plasma pickup north and south of Europa is very small because of the very low plasma flow over the poles. At x = 5.5 R_E the density in the tail is decreased. Numerical results by *Backes* [2004] show a similar wake structure for Titan, although the fine structure is different there because of different magnetospheric conditions.

The convergence of the flow and the increased density in the tail is associated with an enhancement of the thermal pressure. The expansion of the density enhancement along the magnetic field lines is then achieved by slow mode waves, which tend to reduce the plasma pressure.

Figure 6.9 shows the plasma flux density in the wake at x = 2.75 R_E and x = 5.5 R_E. The regions with very low plasma flux are associated with the signatures of the Alfvén wing. At x = 2.75 R_E the increased plasma flux extends to around 5 R_E, the beginning of the Alfvén wing signature. This suggests a transport of these perturbations with (or close to) the Alfvén velocity up to this distance. This is a consequence of the fact, that up to this distance, the sonic Mach number is in the order of (or even smaller than) the Alfvénic Mach number and the slow mode propagates with a velocity close to the Alfvén velocity.

At x = 5.5 R_E the enhanced plasma flux has traveled only a small distance further along the z-axis. The signature of increased plasma flux can not follow the Alfvén wing signature. At x = 5.5 R_E the Alfvénic Mach number is ~ 0.4 and therefore much smaller than the sonic Mach number (~ 1.8) at this distance. Hence, slow mode waves travel with the sound velocity.

The convergence of the flow on the downstream side leads to an enhancement of the total plasma pressure. Figure 6.10 shows thermal, dynamic, magnetic, and the pressure due to the magnetic stress (or tension) along the y- and the z-axis at x = 1.5 R_E. We use the following expressions to calculate the pressures shown in Figure 6.10:

Thermal pressure

$$p_{th} = \frac{2}{3} e \tag{6.1}$$

Magnetic pressure

$$p_{mag} = \frac{B^2}{2\mu_0} \tag{6.2}$$

Magnetic tension

$$p_{tension} = \frac{1}{\mu_0} \int_{x_i} dx_i (\mathbf{B} \cdot \nabla) B_i \tag{6.3}$$

Dynamic pressure

$$p_{dyn} = \rho \, u_i^2 \tag{6.4}$$

The index *i* indicates the y- and z-component respectively.
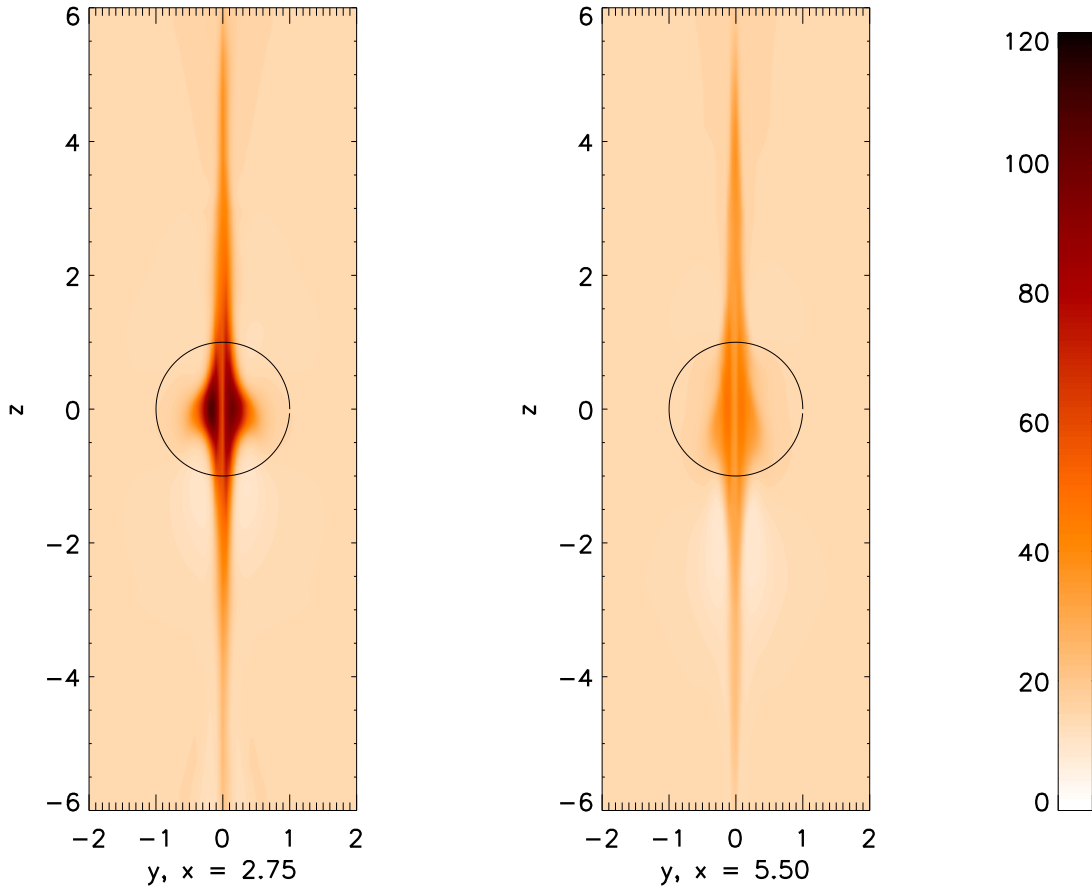
Figure 6.7:   *Electron number density in cm^{-3} in the tail. Shown is the yz-plane at x = 2.75 R$_E$ and x = 5.5 R$_E$.*
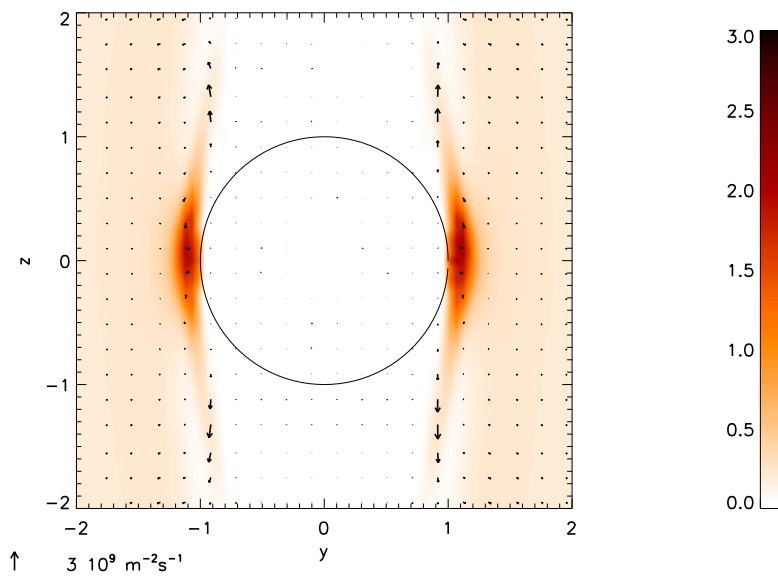
Figure 6.8:   *Plasma flux density n**u** in 10^{10} m^{-2}s^{-1} in the yz-plane.*
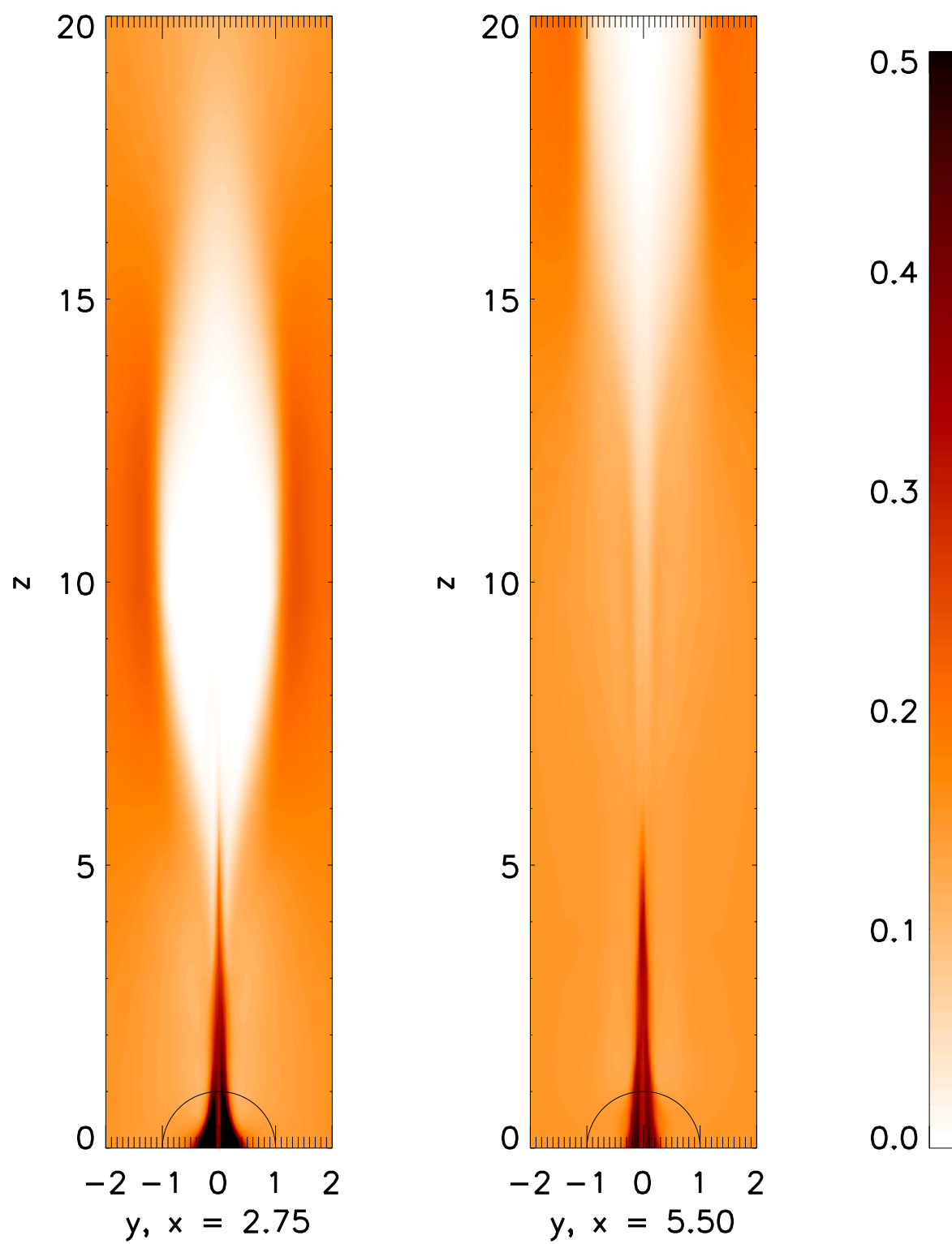
Figure 6.9:   *Plasma flux density n**u** in 10^{10} $m^{-2}s^{-1}$ in the tail in the yz-plane at x = 2.75 R_E and x = 5.5 R_E.*
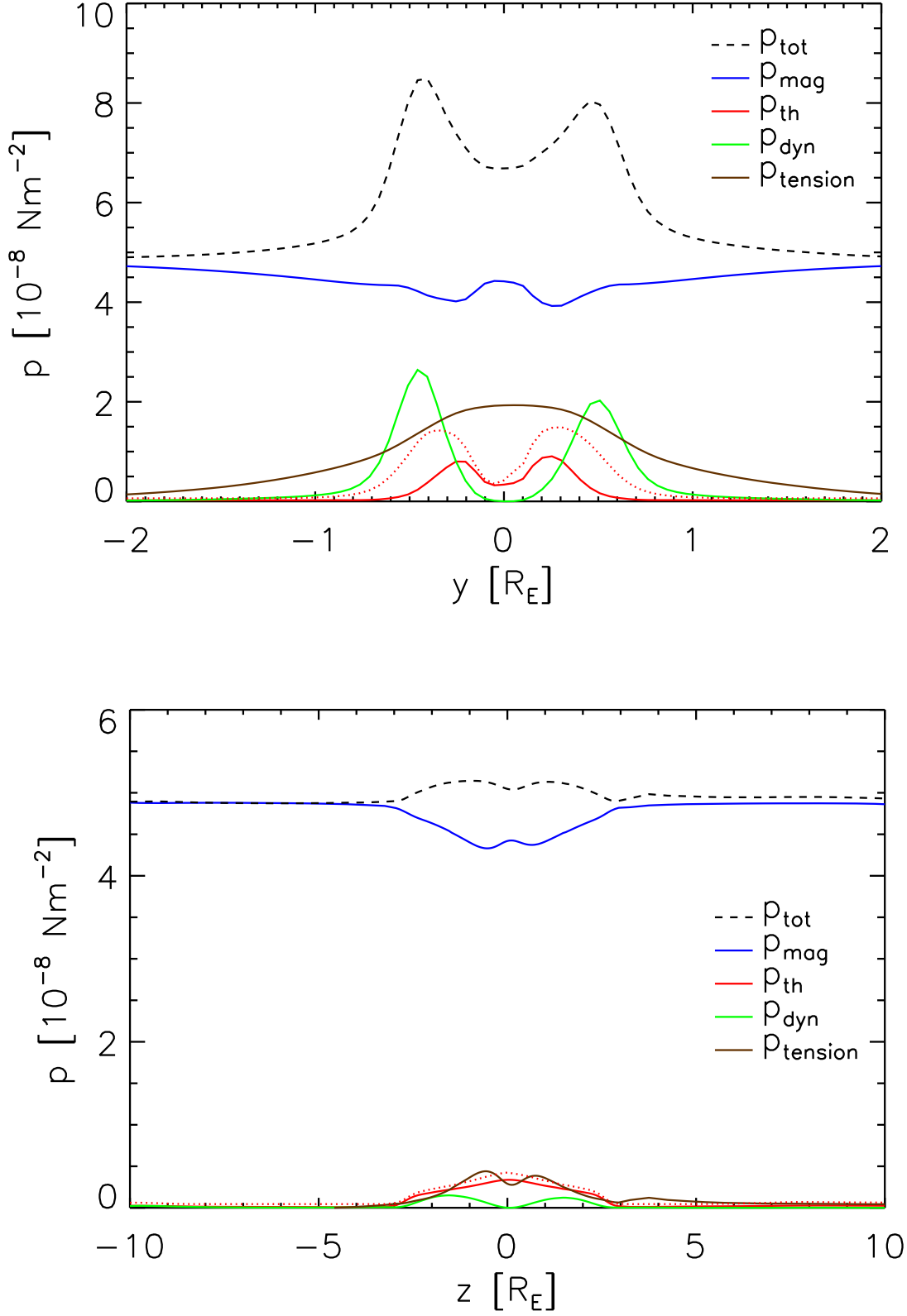
Figure 6.10:   *Magnetic (blue), thermal (red), dynamic (green), magnetic tension (brown), and total (dotted) pressure along the y-axis (top) and the z-axis (bottom) in the wake at x = 1.5 R_E. The dotted red line represents the thermal pressure p'_{th} calculated by assuming an isothermal plasma (see text for details).*
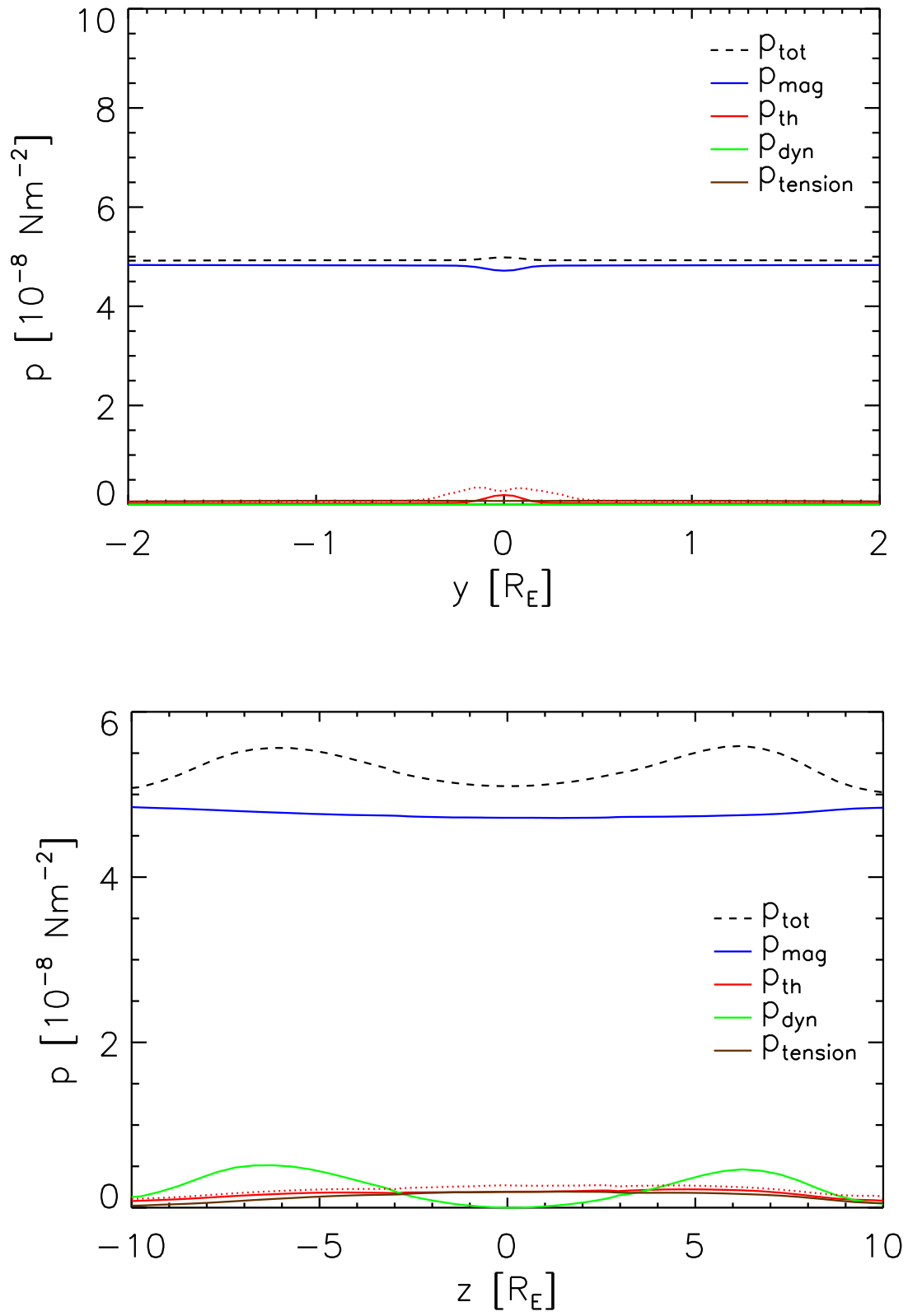
Figure 6.11:   *Same as Figure 6.10 at x = 5.5 R_E.*

The enhanced sum of magnetic tension, thermal and magnetic pressure is overcompensated by the dynamic pressure, resulting in a net acceleration of the plasma towards $y = 0$ along the y-axis. Along the z-axis the plasma is accelerated away from $z = 0$ (see also Figure 6.1) due to the enhanced thermal pressure and the magnetic tension which acts to reduce the curvature of the magnetic field. Hence, the plasma is redistributed along the xz-plane.

Figure 6.11 shows the pressure components at x = 5.5 R_E. The pressure enhancement along the y-axis has decayed. Along the z-axis the enhanced pressure, due to the dynamic pressure, is only visible at larger distances.

In our model, we use a simplified energy equation (see equation 5.20) where we neglect the direct contribution of mass loading (see chapter 5.2.4). The dotted red line in Figures 6.10 and 6.11 represents the thermal pressure p'_{th} calculated by assuming an isothermal plasma, i.e., $p'_{th} \sim \rho$. We calculate this by using $p'_{th} = nkT$, with $T = T_0 = 100$ eV. Figures 6.10 and 6.11 (lower panels) show that along the z-axis, the difference between p'_{th} and p_{th} is marginal. Along the y-axis at $x = 1.5$ (see upper panel in Figure 6.10), p'_{th} is larger than p_{th}. However, the overall structure of the thermal pressure remains the same and p'_{th} is still smaller than $p_{tension}$. Therefore, the statements we make above are still valid. If we would use a pure isothermal energy equation, the slightly larger thermal pressure would probably increase the expansion of plasma along the z-axis. However, the wake structure would be the same as that shown above.

6.1.3   Electric current system

When neglecting displacement currents, changes of the magnetic field curvature are connected to electric currents via Ampere's law ($\mathbf{j} = \frac{1}{\mu_0} \nabla \times \mathbf{B}$). Therefore, they have to be divergence-free. In Figure 6.12 we display the projection of the electric current density in the yz-plane, while Figure 6.13 shows the electric currents in the equatorial plane. This yields a good picture of the current system at Europa.

The current flows down in the northern Alfvén wing and up in the southern on the Jupiter facing side ($y > 0$) . The current then enters Europa's ionosphere where it continues mainly in the direction away from Jupiter. The current escapes from Europa's ionosphere on the anti-Jupiter side into the Alfvén wings where it flows away from Europa. The current system is closed in Jupiter's ionosphere.

In Europa's ionosphere currents flow from the Jupiter facing side to the opposite side on the upstream and the downstream sides of Europa. Besides the ohmic current, diamagnetic and inertial currents are visible in Figure 6.13. These currents are calculated by:

$$\mathbf{j}_{dia} = \frac{\mathbf{B} \times \nabla p}{\mathbf{B}^2} \tag{6.5}$$

$$\mathbf{j}_{inert} = \frac{\mathbf{B} \times \rho \mathbf{u} \nabla \mathbf{u}}{\mathbf{B}^2} \tag{6.6}$$

For a better view, diamagnetic and inertial currents are displayed separately in Figure 6.14.
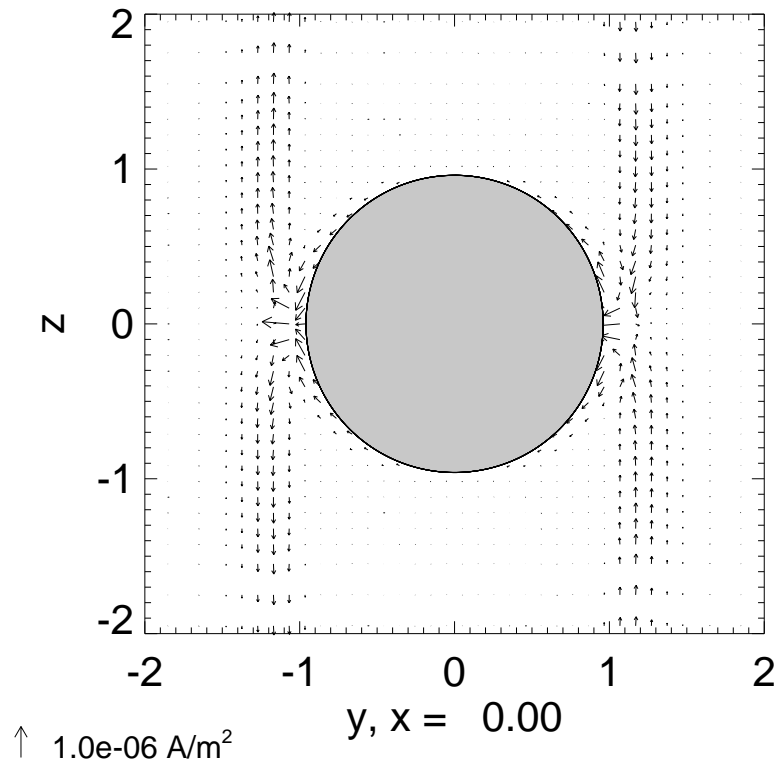
Figure 6.12:   *Electric current in the yz-plane at x = 0 for E4 flyby conditions without induction.*
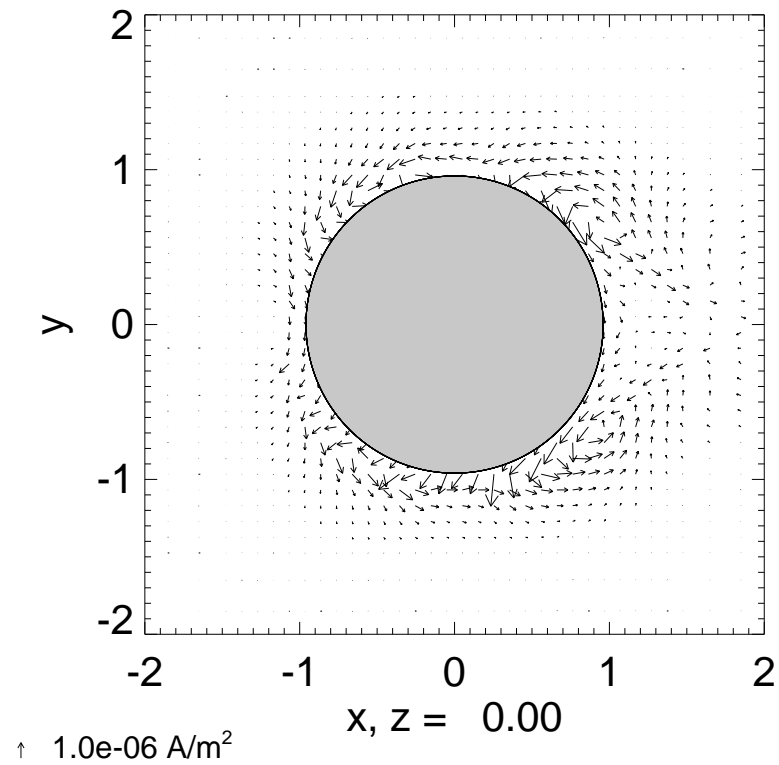
Figure 6.13:   *Electric current in the equatorial plane for E4 flyby conditions without induction. The length of the arrows is scaled in a logarithmical way.*
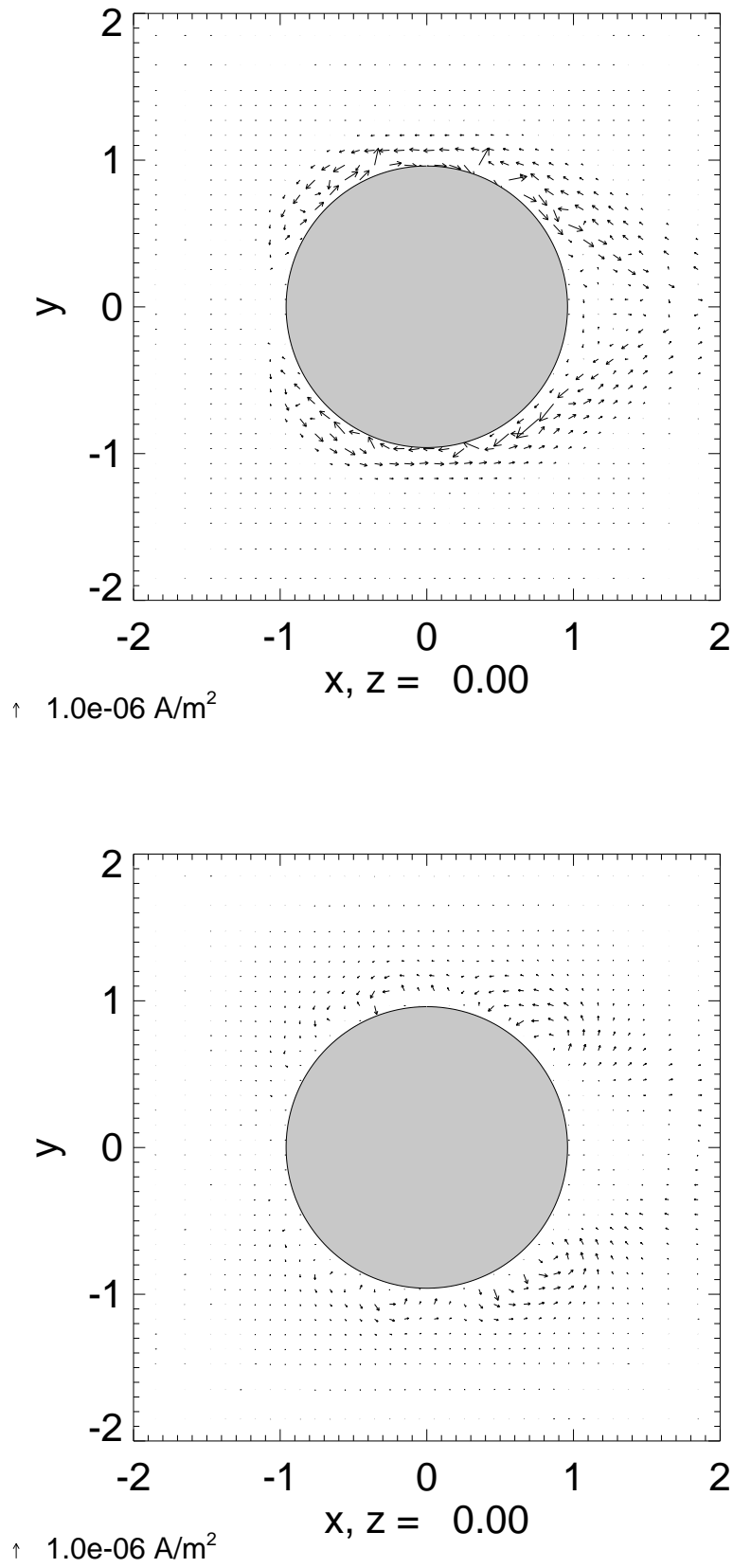
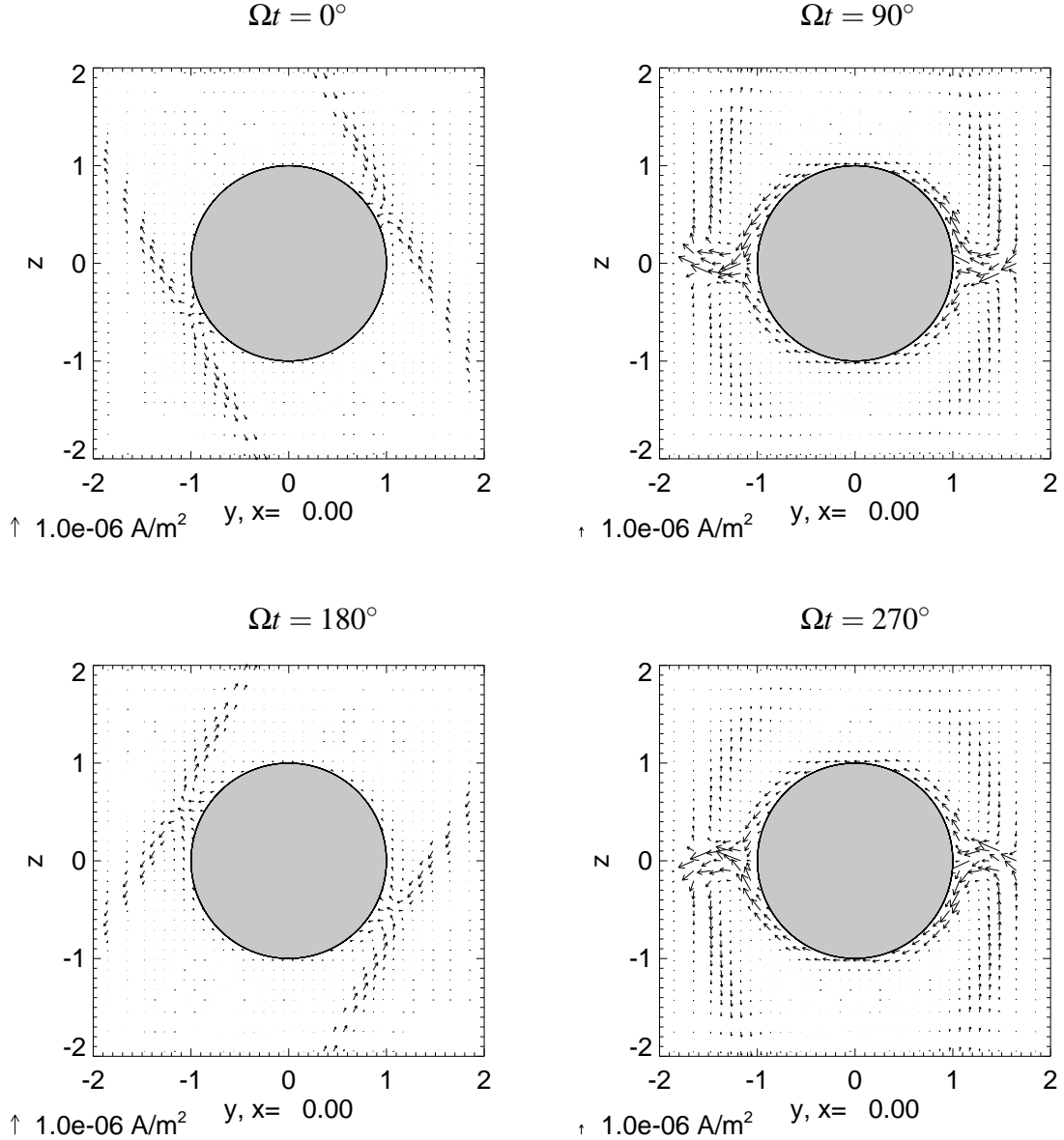***Figure 6.14:*** *Diamagnetic (upper panel) and inertial (lower panel) currents in the equatorial plane for the E4 flyby conditions without induction. The length of the arrows is scaled in a logarithmical way.*

Figure 6.15: *Electric current in the yz-plane at x = 0 for $\Omega t = 0°$ (upper left), 90° (upper right), 180° (lower left), and 270° (lower right). The EPhiO coordinate system is used in these plots.*

The diamagnetic current is due to plasma pressure gradients. On the Jupiter-facing side, this current is mainly in the downstream direction while on the other side of the wake it flows mainly in the upstream direction. Inertial currents are visible on the flanks of Europa. They correspond to regions with main particle flux.

Away from Europa currents flow along the Alfvén characteristics. In addition, perpendicular currents encircle the Alfvén wing and deflect the plasma flow around the wings. We will discuss the structure of the Alfvén wing current system in more detail in section 6.3.2.

The magnetospheric conditions at Europa are changing during a synodical period of Jupiter (see Figure 5.4 and 5.5). Therefore, the electric current system at Europa also varies. Figure

6.15 shows the current system in the yz-plane at Europa in the EPhiO coordinate system during Jupiter's synodical period. A variation in orientation and strength is clearly visible. Due to the opposit magnetospheric conditions, the cases $\Omega t = 0°$ and $\Omega t = 180°$ are perfect symmetric (see section 5.6). That applies also to the cases $\Omega t = 90°$ and $\Omega t = 270°$. The currents are strongest when Europa is located in the current sheet ($\Omega t = 90°$ and $270°$). A time varying current system leads to time varying magnetic fields, which drive currents in the conducting interior of Europa. We will investigate this secondary induction effect in the following section.

6.2 Harmonic coefficients of the plasma induced magnetic fields

In this chapter we calculate the induced magnetic field due to the periodic variations of the magnetospheric plasma. We find that the influence of the plasma interaction on the induction process is weak compared to the induction by the background magnetic field for the assumed atmospheric and magnetospheric conditions at Europa.

We calculate the plasma induced magnetic field in an iterative process as described in section 5.5. As a starting point we include the induction by the homogeneous Jovian background field only. For this purpose, we calculate the initial internal magnetic fields analytically (see section 4.2). Next, we model the interaction of Europa with the Jovian magnetospheric plasma for different times t_i, i.e., for different magnetospheric conditions. Therefore, we are able to determine the induced magnetic field due to the time variable plasma currents on the surface of Europa's internal ocean for each time t_i. Hence, we can determine the harmonic coefficients of the induced magnetic fields for each time t_i. This is done by expanding the inducing magnetic field by spherical harmonics. The accuracy of reproducing the inducing field in terms of a spherical harmonic expansion depends on the number of grid points on the surface of Europa's ocean. Studies on the numerical accuracy are carried out in *Schilling* [2000]. Following these results, we consider coefficients up to degree and order 35 for the spherical harmonic expansion.

After deriving the harmonic coefficients (also called Gauss coefficients) for each time t_i, we do a Fourier expansion of these coefficients. This enables us to calculate the harmonic coefficients at any time t. Hence, we are able to calculate the plasma induced magnetic field at any point and at any time t. Figure 6.16 shows the harmonic dipole and quadrupole coefficients of the plasma induced magnetic fields during Jupiter's synodical period for an assumed ocean thickness of 100 km, an ocean conductivity of 5 S/m and a thickness of the ice crust of 50 km. We choose this set of parameters in order to get the maximum induction effect (see section 4.3.3).

The Gauss coefficients for a given expansion can be grouped under three headings; zonal, sectoral, and tesseral harmonics. In the EPhiO coordinate system, zonal harmonics are those of order zero. Note that none of the h coefficients can be of order zero. The zonal harmonics represent fields whose moments are aligned with the z-axis. Therefore, the g_1^0 term describes
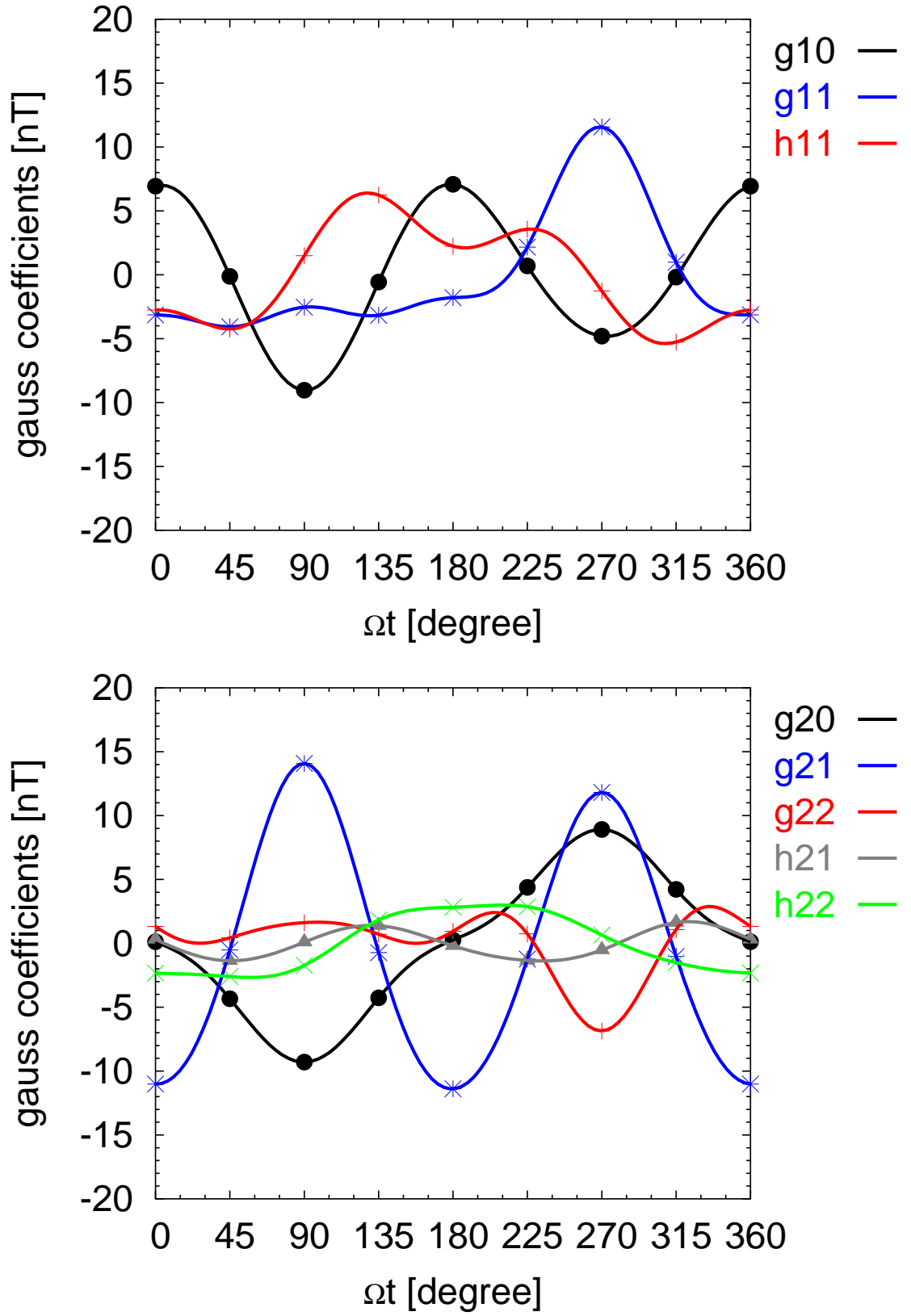
Figure 6.16:   *Harmonic coefficients of the plasma induced magnetic fields during Jupiter's synodical period. The upper panel shows the dipole, the lower panel the quadrupole coefficients.*

the moment of an axial Europa-centric dipole aligned with the z-axis, and the g_2^0 term, an axial, Europa-centric, quadrupole. Sectoral harmonics are those for which degree and order are equal. They represent fields which have their moments in the equatorial plane. In the EPhiO coordinate system the g_1^1 term describes a Europa-centric dipole aligned with the y-axis while the dipole associated with the h_1^1 term is aligned with the $-x$-axis.

The maximum dipole coefficient is found at $\Omega t = 270°$ with a value of $g_1^1 \approx 12$ nT. This coefficient remains nearly constant with a small value of $\approx$ -3 nT between $0°$ and $180°$. The g_1^0 coefficient varies with a period of π but the amplitude is not exactly symmetric. The h_1^1 term also shows a asymmetric behavior. The quadrupole coefficient with the largest values is the g_2^1 term. It is π-periodic with a maximum value of ≈ 14 nT. The g_2^0 can also reach values up to 10 nT and is nearly 2π-periodic.

None of the harmonic coefficients show a pure symmetric behavior. This feature can be explained by the time varying magnetospheric background conditions in our model. Although we use a plasma density model (Figure 5.5) which is symmetric around the centrifugal equator and a background magnetic field (Figure 5.4) which varies symmetric in time, the B_x component of our background magnetic field breaks the symmetry.

The contribution of the single multipoles to the plasma induced magnetic field can be displayed by the spatial power spectrum of the internal magnetic field R_n [*Blakely*, 1995], where R_n is defined as the scalar product $\mathbf{B}_n \cdot \mathbf{B}_n$ averaged over the spherical surface $S(r)$:

$$R_n(r) = \frac{1}{4\pi r^2} \int_0^{2\pi} \int_0^{\pi} \mathbf{B}_n \cdot \mathbf{B}_n \, r^2 \sin\theta \, d\theta \, d\phi \tag{6.7}$$

with

$$\mathbf{B}_n = -\nabla \left(R_c \left(\frac{R_c}{r} \right)^{n+1} \sum_{m=0}^{n} (g_n^m \cos m\phi + h_n^m \sin m\phi) P_n^m(\theta) \right) \tag{6.8}$$

and

$$\mathbf{B} = \sum_{n=1}^{\infty} \mathbf{B}_n \tag{6.9}$$

where $r = R_c$ represents the surface of the ocean. Using the orthogonality property of spherical harmonics, equation 6.7 can be reduced to [*Backus et al.*, 1996]:

$$R_n(r) = \left(\frac{R_c}{r} \right)^{2n+4} (n+1) \sum_{m=0}^{n} \left[(g_n^m)^2 + (h_n^m)^2 \right] \tag{6.10}$$

The set of values of R_n for $n = 1, 2, 3, \ldots$ at a fixed radius r is sometimes called the *Mauersberger-Lowes* spectrum. Thereby the averaged squared field over any sphere is the sum over the spectrum:

$$< |\mathbf{B}|^2 >_{S(r)} = \sum_{n=1}^{\infty} < |\mathbf{B}_n|^2 >_{S(r)} = \sum_{n=1}^{\infty} R_n(r) \tag{6.11}$$
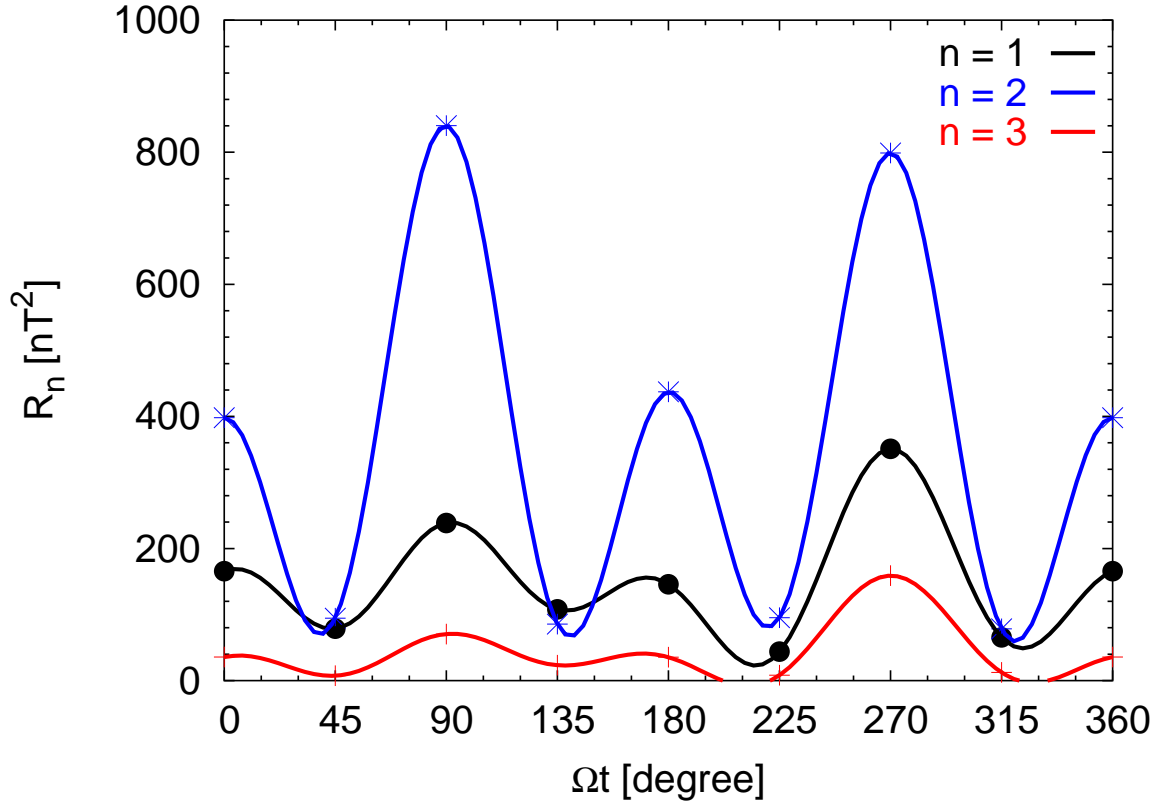
Figure 6.17:   *Spectral coefficients of the Mauersberger-Lowes spectrum for the dipole (n = 1), the quadrupole (n = 2), and the octupole part (n = 3) of the plasma induced magnetic field.*

Figure 6.17 shows the spectral coefficients for dipole, quadrupole and octupole terms at the surface of the ocean. It is obvious that the main spectral power is in the quadrupole field. The plasma induced fields are strongest when Europa is located in the center of the plasma sheet. Smallest values are found when Europa is between the two extreme conditions (inside and outside the plasma sheet), i.e, at $\Omega t = 45°$, $135°$, $225°$, and $315°$. The power in the octupol terms is small compared to dipole and quadrupole contributions. Higher order multipoles ($n > 3$) are even less important. The spectral coefficients for the background field induced dipole term varies between $\sim$14,000 nT^2 and $\sim$88,000 nT^2 (not shown).

Once we have calculated the plasma induced magnetic fields, we include them as initial internal magnetic fields into our model in addition to the background field induced dipole. Coefficients of higher order are only important very close to the surface since according to equation 6.10 $R_n(r) \sim r^{-(2n+4)}$. Therefore, we only consider dipole and quadrupole coefficients when including the plasma induced fields in our model. In the next iteration step, we then repeat the procedure described above and calculate the plasma induced magnetic fields again. All coefficients derived after the second iteration differ from those derived after the first iteration by less than 10%. Therefore, we stop the calculations after the second iteration.

Comparing the dipole and quadrupole coefficients of the plasma induced magnetic fields to

the dipole coefficients of the background magnetic field, which are in the order of 100 nT, it is obvious that the plasma interaction has only a weak impact on the induction process. However, the coefficients derived may have an influence on the lower part of the ionosphere of Europa. Therefore, they may be important when modeling this part of Europa in detail.

The results presented in this section were derived by assuming an almost saturated induction process. Note, that a smaller ocean or an ocean which is less conductive leads to even smaller harmonic coefficients. In addition, stronger time variable ionospheric currents, as they may occur on Callisto, would lead to a stronger induction effect.

6.3   Influence of the induction on the plasma interaction

In the previous section we have shown that the influence of the plasma interaction on the induction process is weak compared to the induction by the background magnetic field. In this section we investigate the reverse process, i.e., the influence of the induction on the plasma interaction. We show that the induction influences the structure of Europa's plasma wake and also the Alfvénic current system at Europa.

As an example, we consider induction taking place in an ocean with 100 km thickness and 50 km below Europa's surface. The conductivity of the ocean is assumed to be 5 S/m. For this set of parameters the induced magnetic field is almost saturated (see Figure 4.5). In order to compare our results with the non-induction case, we concentrate on the E4 flyby conditions again, i.e., when Europa was in the northern magnetospheric hemisphere as well as on the E26 flyby conditions, i.e., when Europa was in the southern magnetospheric hemisphere.

Figure 6.18 shows the overall induced magnetic field for the E4 flyby conditions. Note, that in the coordinate system we use the induced dipole moment is not necessarily in the equatorial plane. The induced dipole moment has a substantial z-component for the E4 flyby conditions. As Europa is located north of the magnetic equator, the induced dipole moment points mainly towards the Jupiter facing direction at the position of Europa.

The induced magnetic field for the E26 flyby conditions is shown in Figure 6.19. Since this flyby occurred in the opposite magnetic hemisphere of Jupiter (see Figure 3.2), the orientation of the induced dipole moment is reversed compared to the E4 flyby conditions. Hence, the induced dipole moment points mainly in the anti-Jovian direction.

6.3.1   Wake structure

In section 6.1.2 we have discussed the plasma density distribution in Europa's wake, neglecting induction in the interior of Europa (see Figure 6.7). Including induction yields a different picture. Figure 6.20 shows that the wake becomes asymmetric. While for the case without induction maximum number densities were found in the central wake region at x = 2.75 R_E, induction effects yield a maximum density at $z \approx \pm 1$ R_E. We will demonstrate in section 6.5 that this might explain the absence of a high ionospheric density peak in the E4 flyby plasma data in the wake.
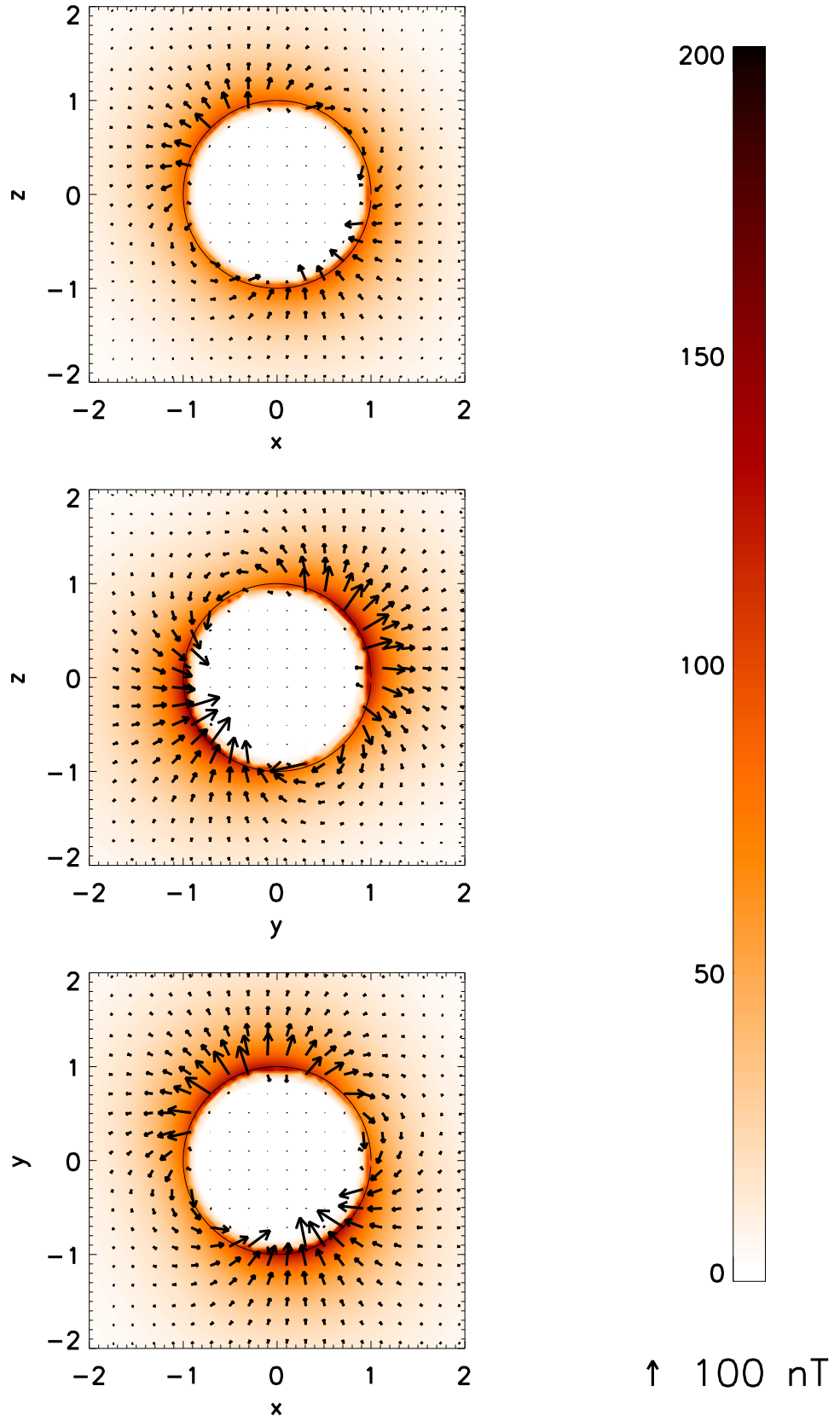
Figure 6.18:   *Induced magnetic field for E4 flyby conditions. Shown are the projections onto the xz- (top), yz- (middle), and equatorial plane (bottom).*
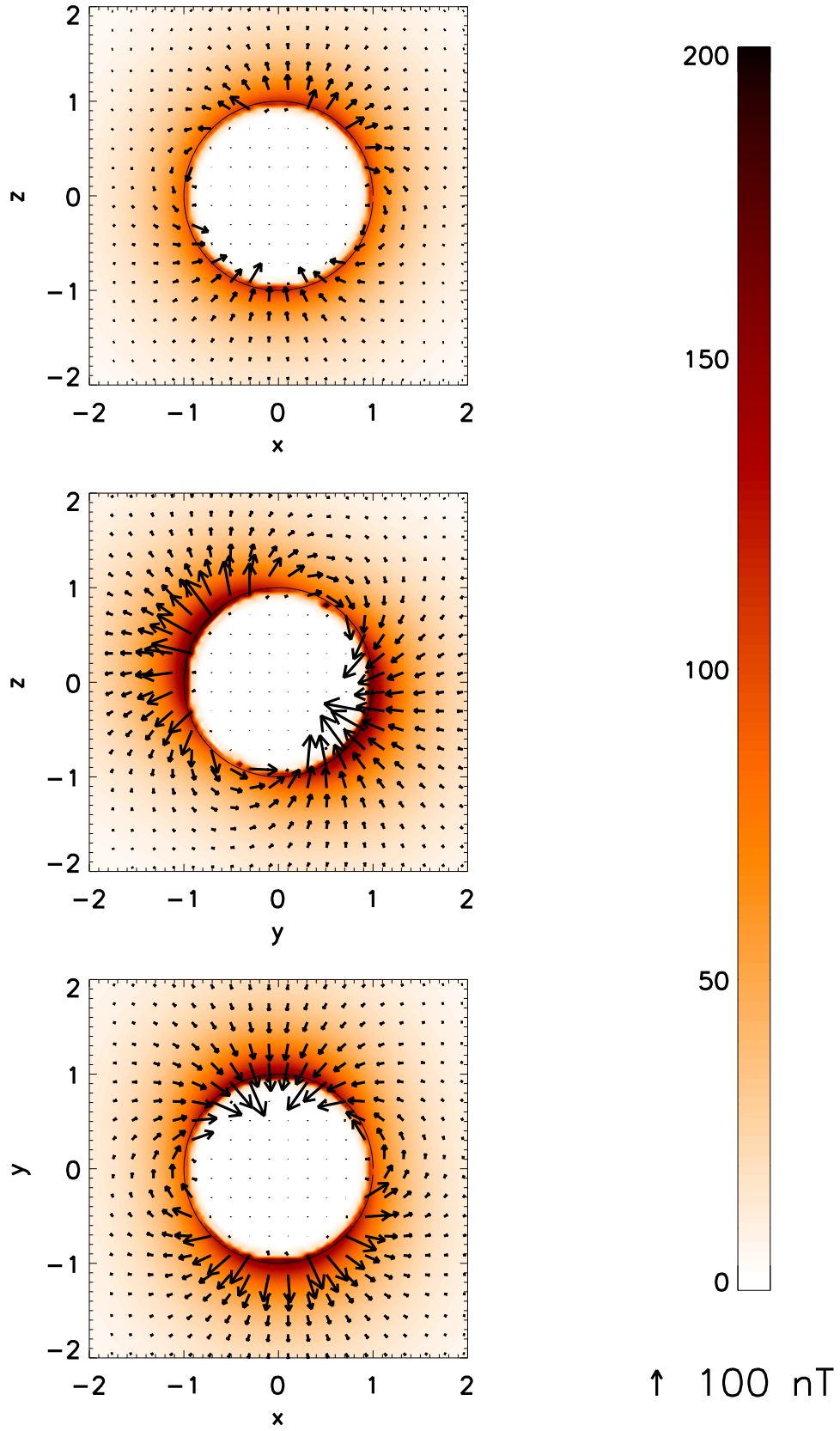
Figure 6.19: *Induced magnetic field for E26 flyby conditions. Shown are the projections onto the xz- (top), yz- (middle), and equatorial plane (bottom).*
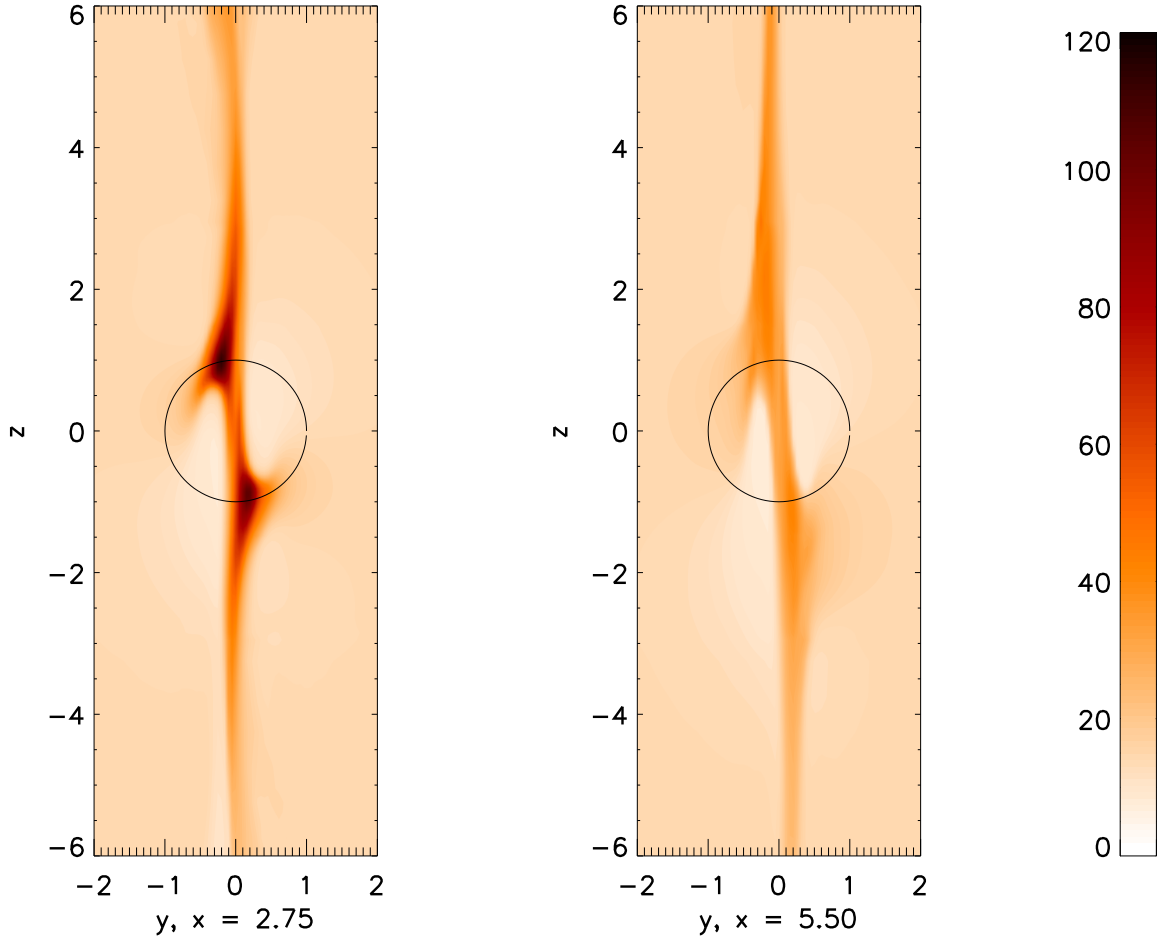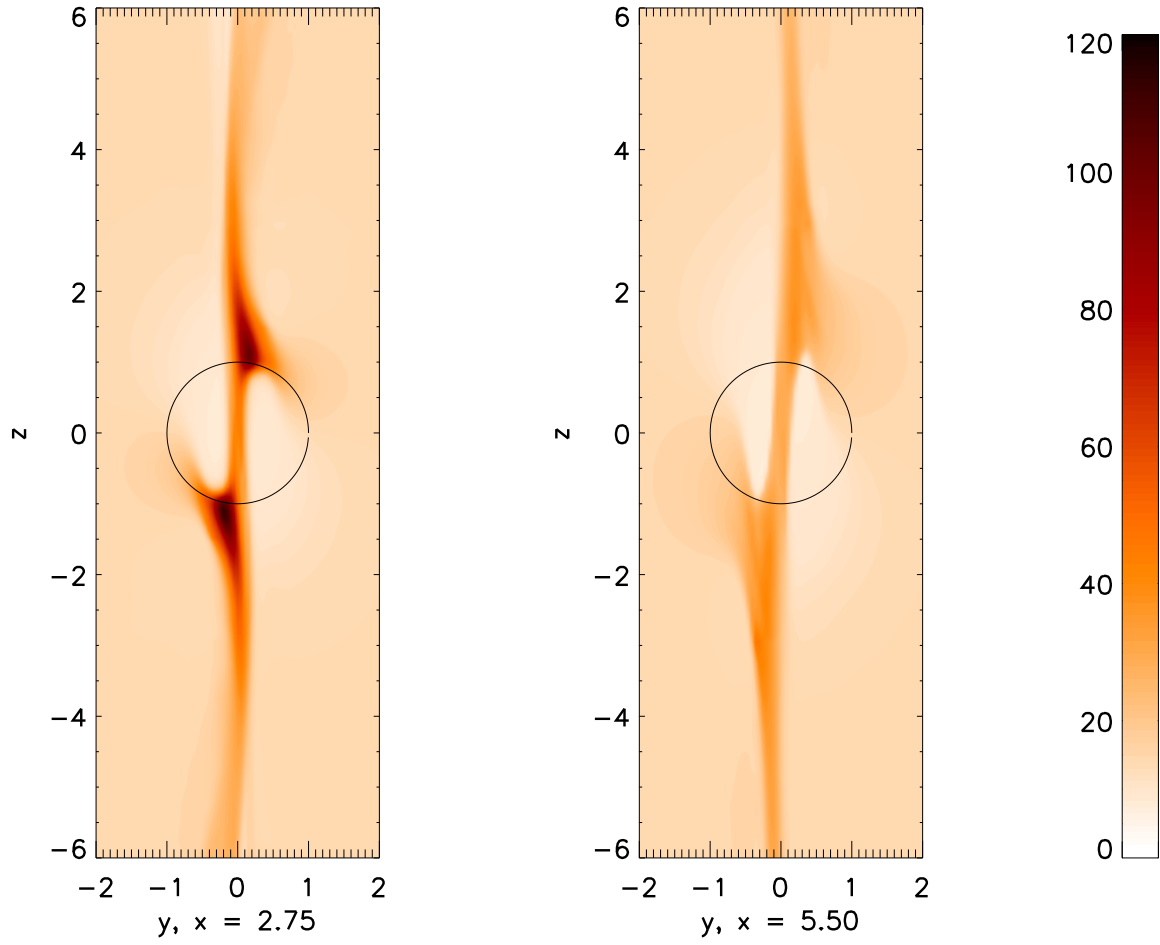
Figure 6.20:   *Electron number density in cm^{-3} in the tail for the E4 flyby conditions with induction. Shown is the yz-plane at x = 2.75 R$_E$ and x = 5.5 R$_E$.*

Differences between the non-induction and the induction case are also visible further downstream. As in Figure 6.7 (induction neglected) the density enhancement at x = 5.5 R$_E$ is concentrated along the z-axis in Figure 6.20 (induction included), but it is deformed. While it is bend towards $-\hat{\mathbf{y}}$ for $z > 0$ the opposite is true for $z < 0$.

The asymmetric wake is a result of the asymmetric plasma pickup in the ionosphere of Europa. Figure 6.21 shows the plasma flux in the yz-plane when induction is included. Compared to the case without induction (see Figure 6.8) a displacement of the plasma flux is visible. It is shown that plasma is transported along the z-axis on the northern anti-Jovian flank while it is transported in the opposite direction on the southern Jupiter-facing flank. This feature is caused by the induced magnetic field shown in Figure 6.18. Note that in the coordinate system used, the induced dipole is not in the equatorial plane.

The E4 flyby occurred when Europa was well above the current sheet. In order to show the influence of induction we study also the opposite case, i.e., when Europa is located well below the current sheet. This was the case for the E26 flyby (see Figure 3.2). Figure 6.22 displays the density structure in the wake for the conditions during this flyby. Again, the asymmetric wake structure is visible. However, now the plasma flux density as well as the plasma flux
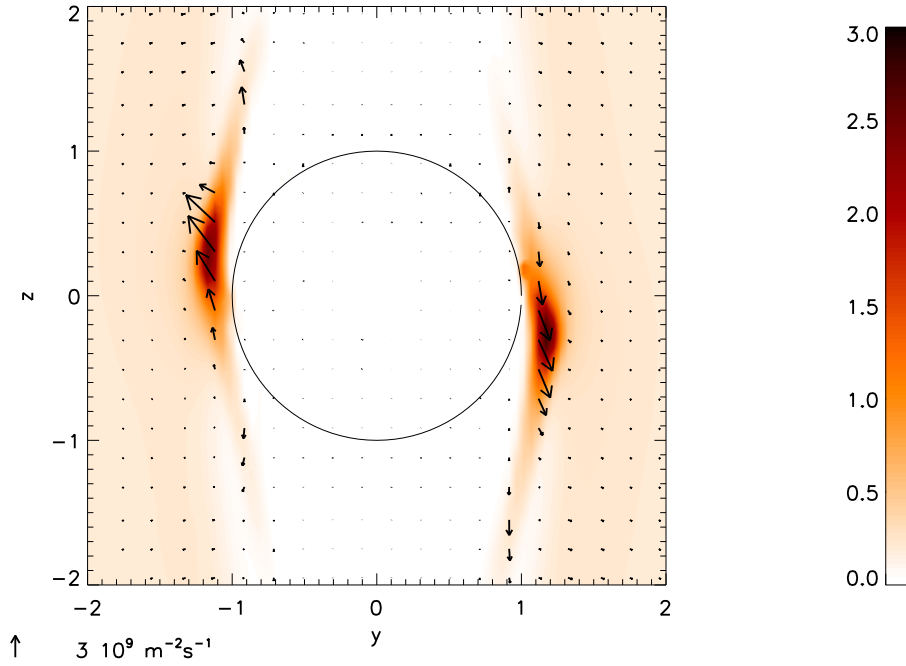
Figure 6.21: Plasma flux n**u** in 10^{10} $m^{-2}s^{-1}$ in the yz-plane.

in the yz-plane (Figure 6.23) is displaced in the opposite way. This is in agreement with the induced magnetic field for the E26 pass (see Figure 6.19) being opposite to the field during the E4 flyby. The density enhancement at x = 2.75 R_E in Figure 6.22 is now concentrated towards $-\hat{\mathbf{y}}$ for $z > 0$ and in the opposite way for $z < 0$. The maximum density is found at $z \approx \pm 1$ R_E again.

6.3.2 Currents in the Alfvén wing

The electric current system in the vicinity of Europa is discussed in section 6.1.3. Away from Europa, currents that correspond to the Alfvén wings can be divided into currents that flow along the Alfvén characteristics (Alfvén currents) and currents that flow in a plane perpendicular to the characteristics (perpendicular currents) [*Neubauer*, 1980]. Both current system are divergence-free separately.

Figure 6.24 displays the Alfvén currents of the northern Alfvén wing through a plane perpendicular to the Alfvén characteristics at $z' = 3.05$ R_E and for the E4 flyby conditions. No induction is included. Note that we use a different coordinate system here: $\hat{\mathbf{z}}'$ is parallel to the Alfvén characteristic $\mathbf{v}_A^-$, $\hat{\mathbf{y}}' = \hat{\mathbf{y}}$, and the x'-axis completes the triad ($\hat{\mathbf{x}}' = \hat{\mathbf{y}}' \times \hat{\mathbf{z}}'$). The Alfvén currents are concentrated on the flanks of the Alfvén wing. The current flows towards Europa on the Jupiter facing flank ($y' > 0$), while the current flows away from Europa on the anti-Jovian side ($y' < 0$).

In Figure 6.25 the Alfvén wing current system at $z' = 9.05$ R_E is plotted. It is shown that

Figure 6.22:   *Electron number density in cm^{-3} in the tail for the E26 flyby conditions with induction. Shown is the yz-plane at x = 2.75 R$_E$ and x = 5.5 R$_E$.*
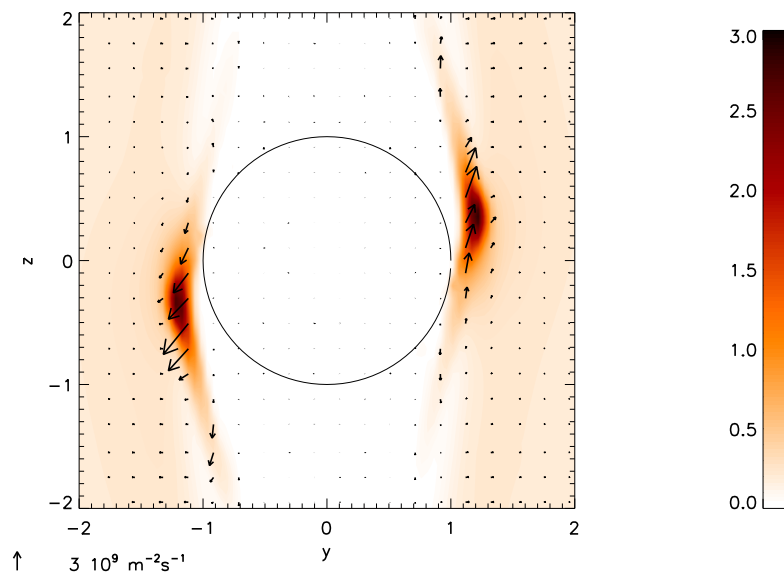
Figure 6.23:   *Plasma flux n$\mathbf{u}$ in 10^{10} m^{-2}s^{-1} in the yz-plane.*
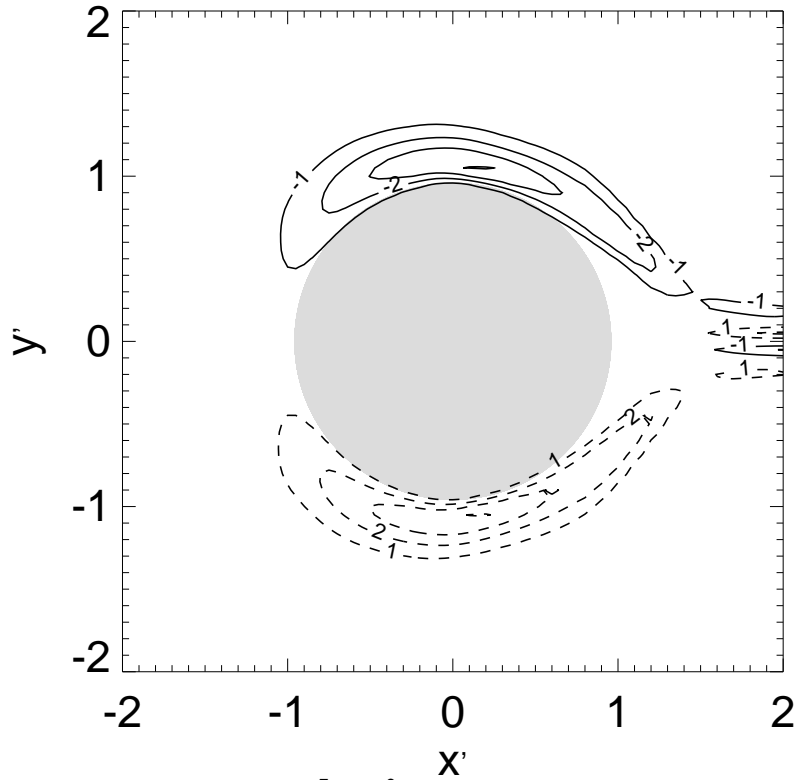
Figure 6.24: *Alfvénic current $j_{z'}$ in 10^{-7} A/m^2 in the northern Alfvén wing at $z' = 3.05$ R_E for the E4 flyby conditions and without induction.*
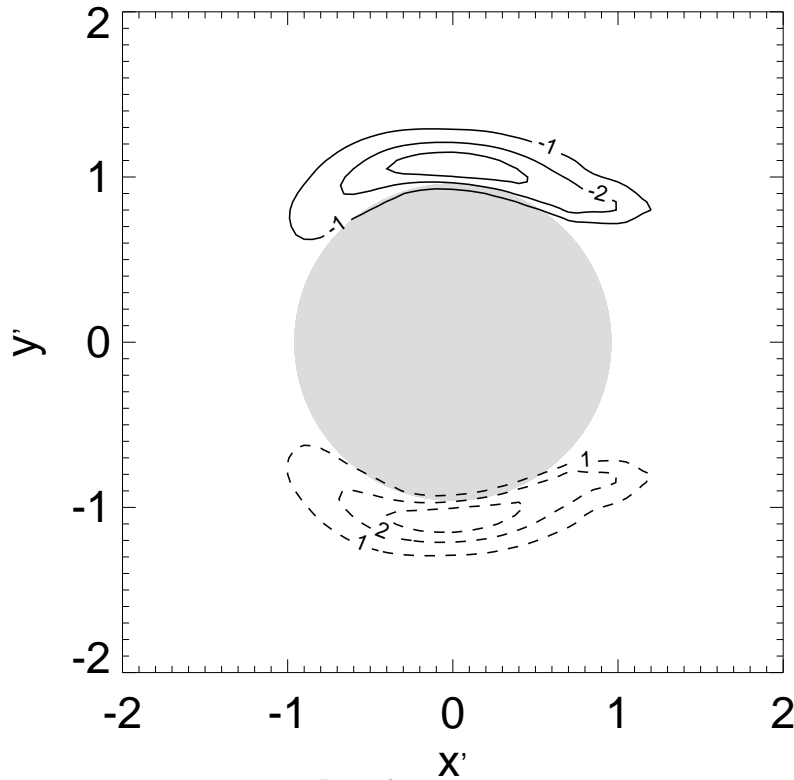
Figure 6.25: *Alfvénic current $j_{z'}$ in 10^{-7} A/m^2 in the northern Alfvén wing at $z' = 9.05$ R_E for the E4 flyby conditions and without induction.*
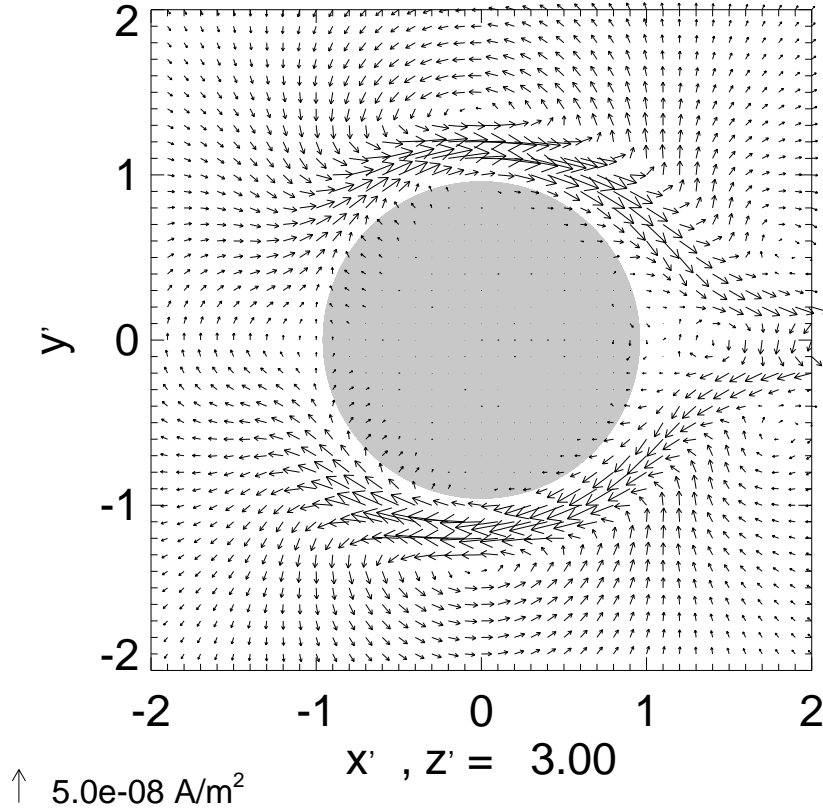
Figure 6.26: *Perpendicular currents around the northern Alfvén wing at $z' = 3.05$ R_E for the E4 flyby conditions and without induction. The length of the arrows is scaled in logarithmical way.*

further away from Europa the general shape of the current system and the absolute values of the Alfvén current is nearly unchanged. A difference is only seen downstream of Europa. There, the diamagnetic currents vanish. This is in agreement with the results obtained in section 6.1.2. We determine a total Alfvén current through the northern Alfvén wing of $\sim 7 \times 10^5$ A for the E4 flyby conditions in our model. This value is in agreement with the results of *Saur et al.* [1998].

Figure 6.26 shows the perpendicular currents projected onto the same plane as in Figure 6.24. Most of the current encircles the Alfvén wing. In addition, current loops on the Jovian and on the anti-Jovian side are visible. Diamagnetic currents can be seen downstream of the Alfvén wing. Note that, if we don't account for induction effects, the Alfvén wing current system for the E26 flyby conditions differs only marginally from the current system for the E4 flyby conditions.

Including induction into our simulations yields a different picture. Figure 6.27 displays the Alfvénic current in the same plane as in Figure 6.24 with induction included. The current density on the anti-Jovian side is enhanced for the E4 flyby conditions (upper panel), while it is reduced on the Jupiter facing side. Note that, the total current remains constant, i.e., the absolute value of the total current on the anti-Jovian side equals the total current on the
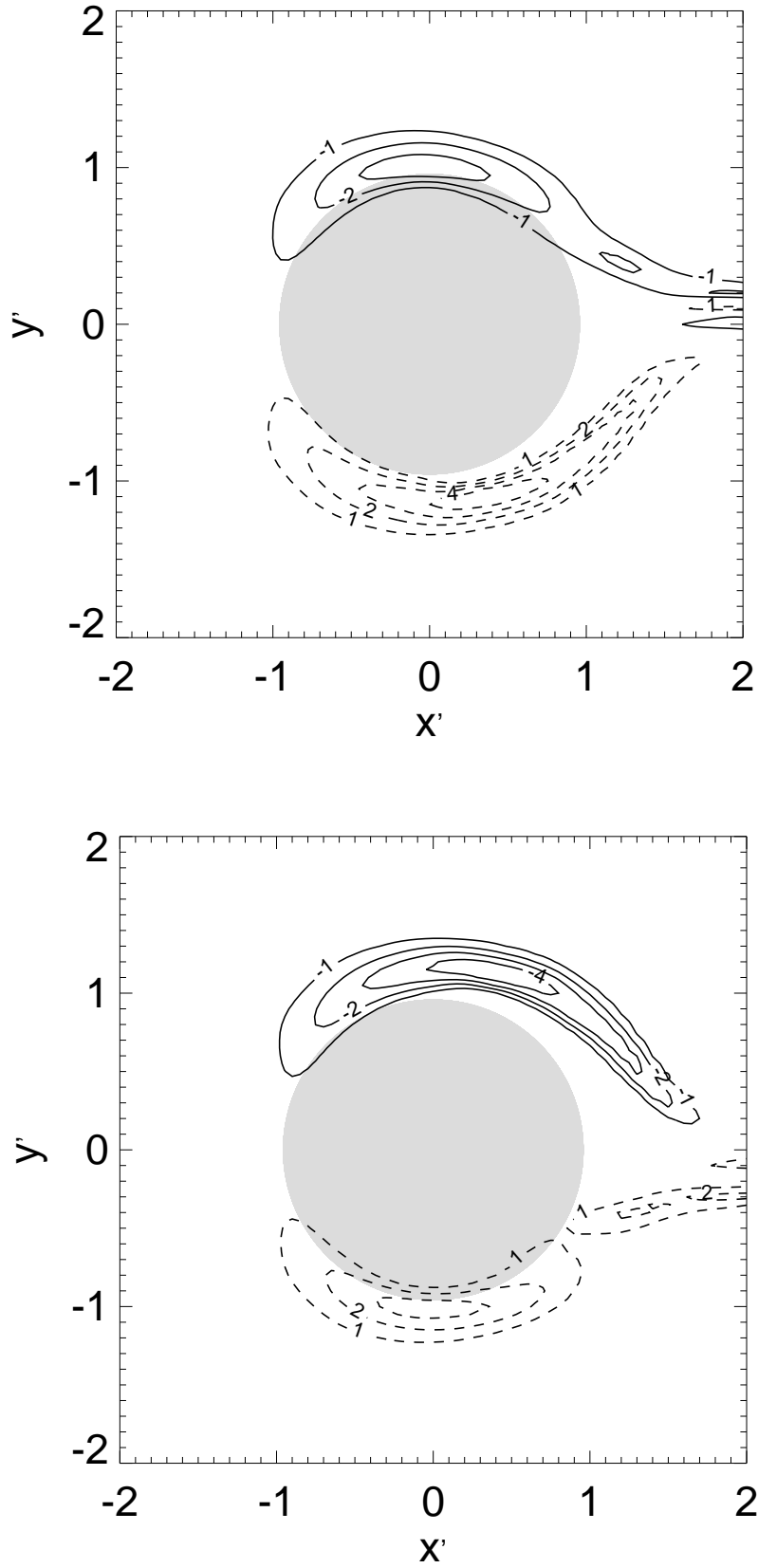
Figure 6.27:   *Alfvénic current $j_{z'}$ in 10^{-7} A/m^2 in the northern Alfvén wing at $z' = 3.05$ R_E with induction for the E4 (top) and E26 (bottom) flyby conditions.*
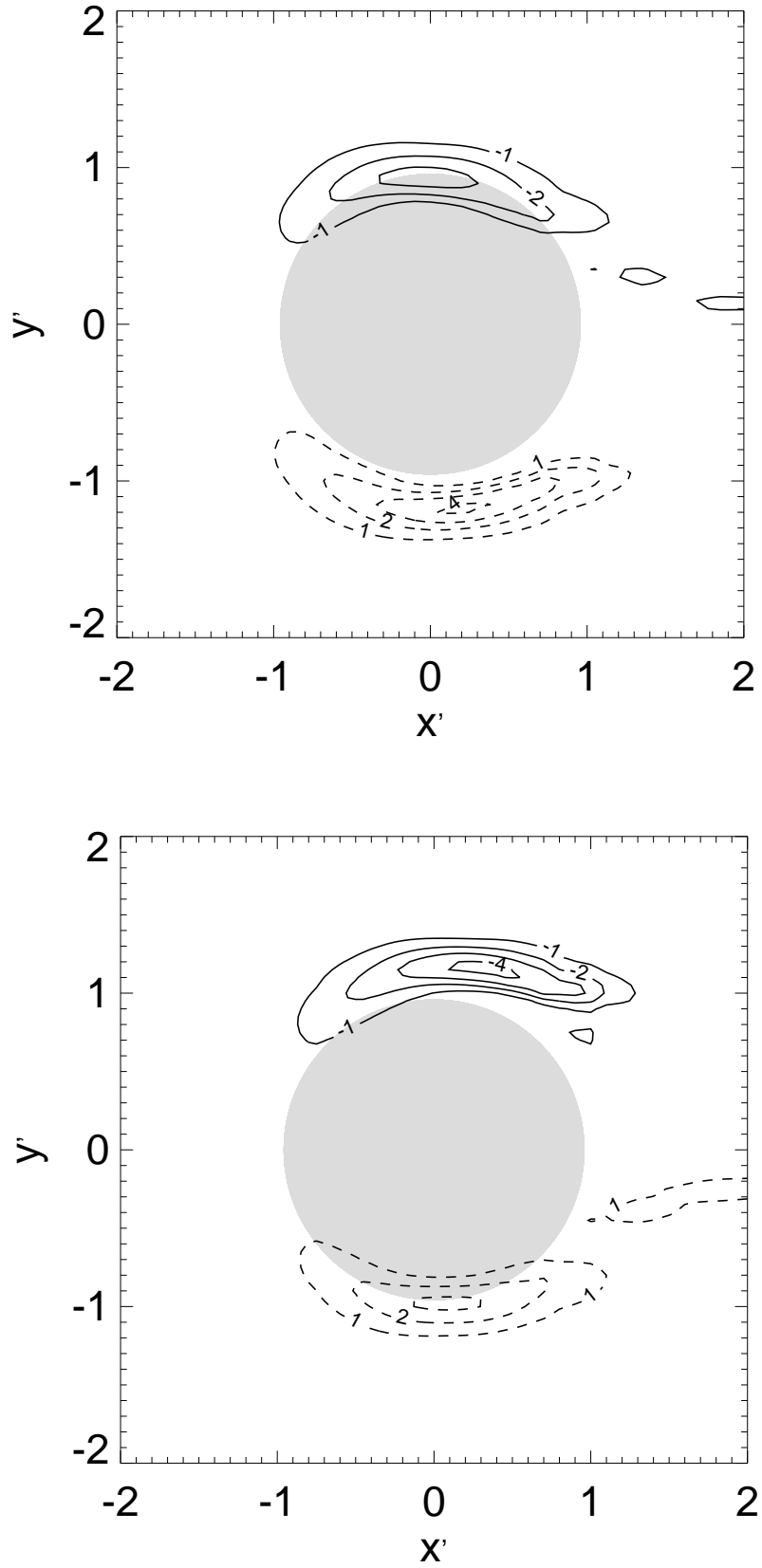
Figure 6.28:   *Alfvénic current $j_{z'}$ in 10^{-7} A/m^2 in the northern Alfvén wing at $z' = 9.05$ R_E with induction for the E4 (top) and E26 (bottom) flyby conditions.*

Jupiter facing side. The current system, and therefore also the Alfvén wing, is displaced and deformed as it was theoretically proposed by *Neubauer* [1999]. This is also true further away from Europa. In Figure 6.28 the displacement away from Jupiter (towards $-\hat{\mathbf{y}}'$) for the E4 conditions and towards Jupiter (towards $\hat{\mathbf{y}}'$) for the E26 conditions is obvious. Note that the opposite is true for the southern Alfvén wing. In addition, the cross section of the Alfvén wing has shrunk.

In summary, including induction influences the plasma interaction. Although the induced magnetic dipole fields fall of with r^{-3}, their influence and effects are still visible at larger distance. For the conditions treated above, they lead to a shrinking and a displacement of the Alfvén wing. Finally, we point out that in order to see these effects in our simulation results, a correct implementation of the induction into our equations was necessary (see section 5.4.1). Usually, the induced magnetic fields outside Europa are potential fields. Therefore, they are rotation-free and cannot influence the current system outside Europa. Thus, simply adding an induced magnetic field on top of a MHD-simulation would not yield the results derived above.

6.4 Verification of the model description of Europa's interior

Before we compare our results with the Galileo flyby data, we verify our description of the satellite interior. As explained in section 5.4.2, we describe the interior of Europa by an 'exotic' plasma. We control the magnetic diffusivity by adjusting the neutral gas density in the interior. In addition, a small magnetic Reynolds number in the interior is required for the proper description of the diffusion of magnetic field into Europa.

Figure 6.29 shows the magnetic diffusivity in our model along the x-axis for the E04 flyby conditions. We are able to maintain a constant magnetic diffusivity in the interior of Europa. Note that the diffusivity jumps over several orders of magnitude at the surface of Europa. The magnetic diffusivity is inversely proportional to the conductivity. Therefore, the jump at the boundary is even larger when modeling lower ocean conductivities. The drop of η close to the surface on the upstream side, indicates the location of the ionosphere.

In Figure 6.30 the magnitude of the plasma bulk velocity along the x-axis is displayed. The bulk velocity is reduced upstream of Europa, but there is no stagnation of the flow. We do not explicitly set the velocity to zero inside Europa. Therefore, inside Europa we have a small bulk velocity with a minimum value close to the center of the moon which is six orders of magnitude smaller than the background velocity.

Figure 6.31 shows the magnetic Reynolds number along the x-axis. This value is given by the ratio of the convection term to the diffusion term:

$$R_m = \frac{|\nabla \times (\mathbf{u} \times \mathbf{B})|}{\eta \, |\nabla^2 \mathbf{B}|} \tag{6.12}$$
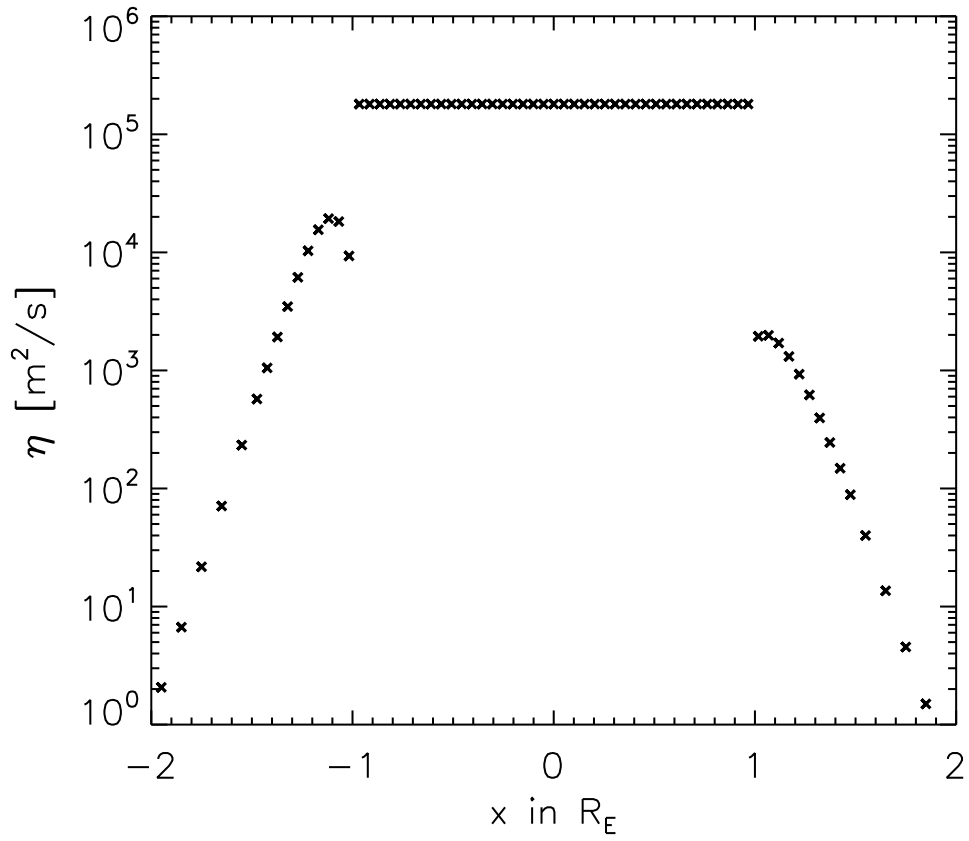
Figure 6.29: *Magnetic diffusivity along the x-axis of the model. The desired conductivity of the ocean is 5 S/m in this case.*
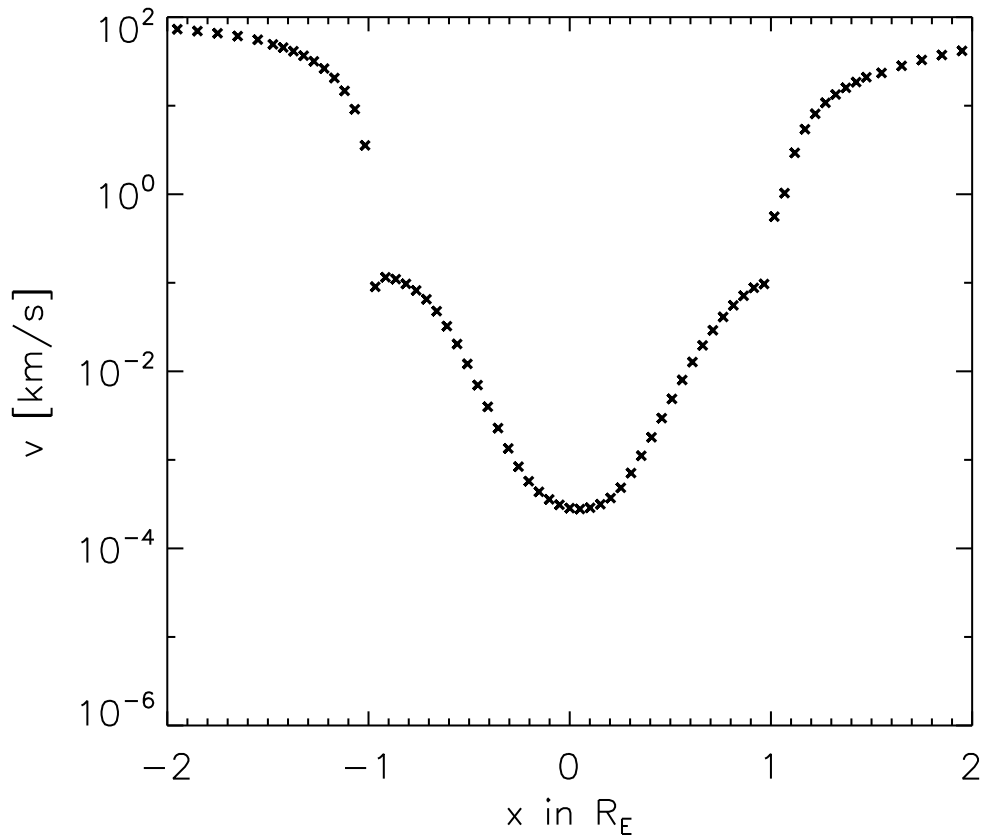

Figure 6.30: *Velocity magnitude along the x-axis of the model.*
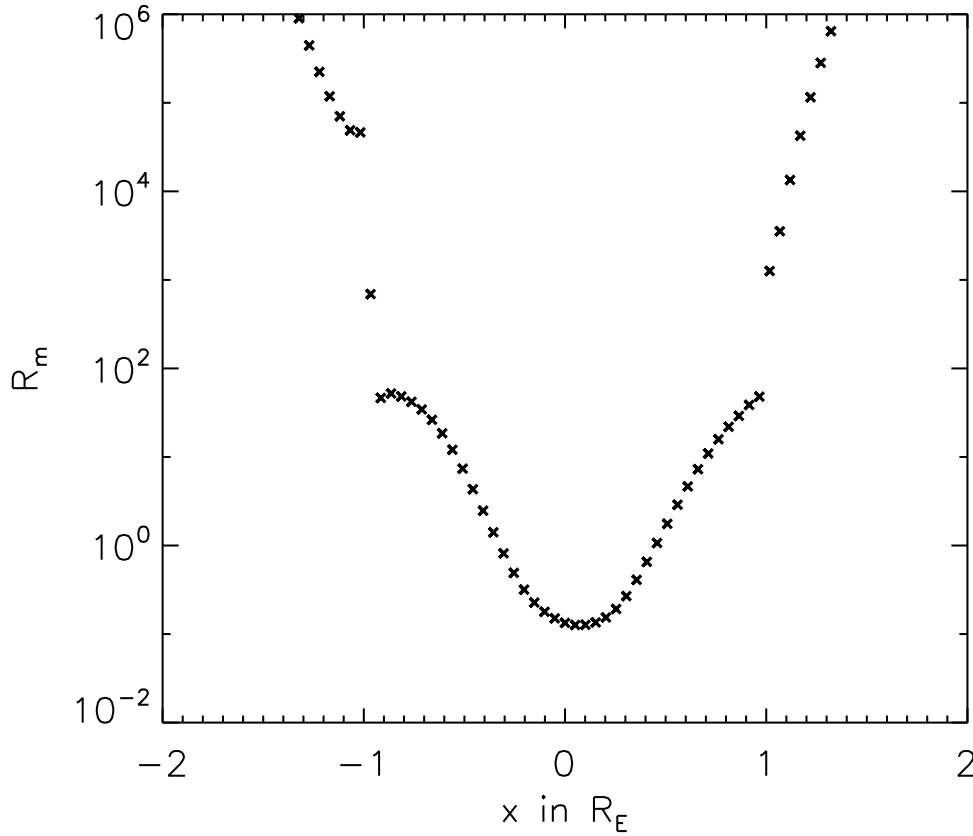
Figure 6.31:   *Magnetic Reynolds number along the x-axis of the model.*

Outside Europa, the convection term dominates. In reality, only diffusion of magnetic field can occur inside the moon. In our model, we are able to reduce the magnetic Reynolds number to small values in the interior of Europa. For $r \leq 0.5$ R_E, the magnetic Reynolds number becomes less then 1, i.e., the magnetic field is transported mainly by diffusion. We are not able to reduce the magnetic Reynolds number immediately when plasma enters the interior of Europa. This could be a problem if we would solve the induction equation for the total magnetic field with our model, since the convection inside Europa could wash away the internal magnetic field. However, as described in chapter 5 we solve the induction equation for the plasma magnetic field. In addition, we use an iterative process to determine the plasma induced fields. Therefore, the small contribution of the convection term in the interior of Europa is of no importance.

A higher spatial resolution close to the surface of Europa would allow for a better description of the interior. The jump in the magnetic diffusivity could than be distributed over more numerical grid points. However, since the code we use does not include adaptive mesh refinement, a higher resolution in the near surface area increases also the computing time rapidly.

6.5   Comparison with Galileo data

In this section we compare our model results with Galileo flyby data (mainly magnetic field data). We are able to determine the so far closest constraints on the conductivity and the thickness of Europa's ocean. We concentrate on flybys that occurred when inductive response is strongest, i.e., when Europa was well outside the current sheet. This was the case for the E4, the E14, and the E26 flyby (see chapter 3). An overview of the Europa encounters is given in table 3.1. In addition, we show that our model results for the E4 pass are in good agreement with the PLS data [*Paterson et al.*, 1999], thereby we see no need for rotation of the upstreaming plasma flow during this flyby.

We discuss each of the flybys separately. For the E4 (6.5.1), the E14 (6.5.2), and the E26 pass (6.5.3), we assume two different ocean thicknesses: 100 km and 25 km. These ocean thicknesses represent the two extreme cases of a thick and a thin conducting subsurface layer (see chapter 2.1.1). The thickness of the crust is assumed to be 50 km. Note that we are not able to resolve the thickness of the ice crust. We compare our model results to the Galileo magnetic field data by using different values for the ocean conductivity. In addition, we show the plasma density and the velocity along the flyby trajectory for each pass separately. For the E4 pass, this values are compared to the Galileo plasma data.

In section 6.5.4, we apply our model to the E12 flyby conditions. During this pass, Europa was located close to the center of the plasma sheet. We discuss the global plasma interaction for this flyby conditions, and display the differences to the plasma interaction when Europa is located outside the current sheet (see section 6.1.1). The E12 flyby is used to determine the calibration factors for the temperature of the magnetospheric electrons (see section 5.2.4).

6.5.1   Europa flyby E4

The first close Europa encounter of Galileo was the E4 flyby on December 19, 1996. This pass occurred in Jupiter's northern magnetic hemisphere (see Figure 3.2), i.e., the magnetic background field at Europa pointed away from Jupiter. Thus, the primary induced dipole moment pointed toward Jupiter. Figure 3.1 shows that the flyby was a equatorial pass, oblique through Europa's wake. Closest approach was at 06:52:58 universal time (UT) at an altitude of 695 km.

Figure 6.32 displays the magnetic field along the trajectory in the EPhiO coordinate system. The red curve shows the magnetic field measured by the Galileo spacecraft [*Kivelson et al.*, 1997]. Our model results for a pure plasma interaction without induction in the interior of the moon are indicated by the dashed black curve. In addition, the predicted field by including induction into our model is shown. We choose different possible values for the conductivity of Europa's ocean and analyze which conductivity fits the measured data best. The smallest ocean conductivity assumed (100 mS/m) is close to the lower limit of 60 mS/m given by *Zimmer et al.* [2000]. The largest conductivity assumed (5 S/m) is the conductivity of Sea water found on earth (see Table 4.1). For larger values of the σ_{oc}, the induction process is saturated, i.e., larger conductivities yield the same results (see section 4.3.3).
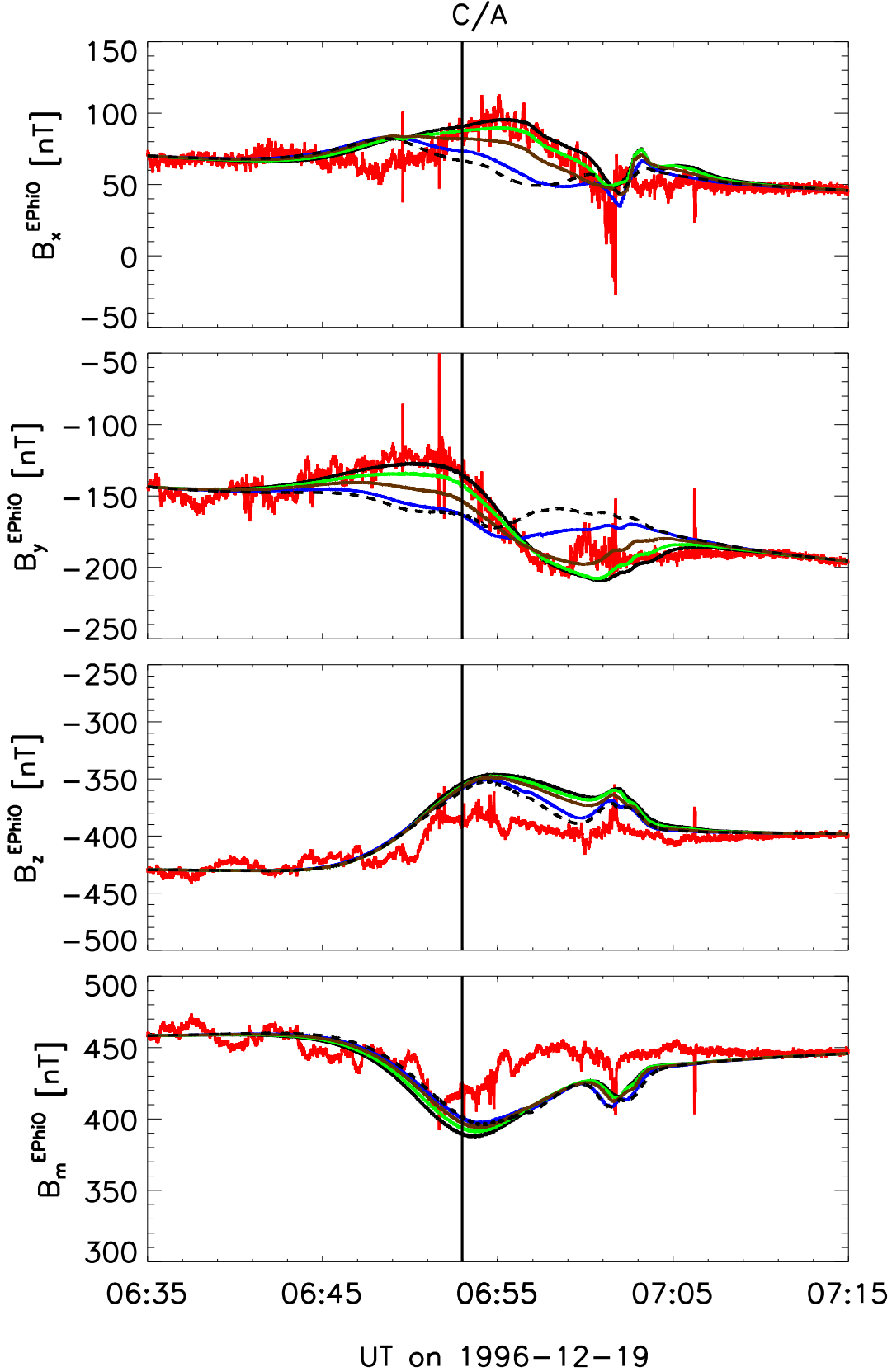
Figure 6.32: *Observed and modeled magnetic field for the E4 flyby in the EPhiO coordinate system. From top to bottom: B_x, B_y, B_z, B_m. The red curve shows the measured field [Kivelson et al., 1997]. The dashed black curve shows the predicted field when no induction is included in our model. The predicted field by including induction is shown for the ocean conductivities σ_{oc}: 100 mS/m (blue), 250 mS/m (brown), 500 mS/m (green), and 5 S/m (black). The assumed thickness of the crust is 50 km and the assumed thickness of the ocean is 100 km.*

The dashed black curve in Figure 6.32 indicates, that a small contribution from the plasma interaction can be found in the B_x and B_y component of the measured data. Modeling the data without induction effects cannot explain these components. As the E4 flyby was an equatorial pass, the main contribution in the B_x and B_y component results from the induced magnetic field in the interior. With the used model of Europa's interior, we are able to reproduce the B_x and B_y component for an ocean conductivity of 500 mS/m or larger. Note that in this case, the induced field is almost saturated for $\sigma_{oc} > 500$ mS/m (see Figure 4.5). Thus, we are not able to set an upper limit for σ_{oc}.

Kabin et al. [1999] suggest a 20° deviation of the plasma flow from the nominal corotation direction for the E4 flyby. In contrast, Figure 6.32 suggests that this rotation of the flow is not necessary. Our model reproduces the local maximum and minimum in the wake region in the B_x component (between UT 07:00 and 07:05) independent from the ocean conductivity used. This suggests, that this feature is caused by the plasma interaction.

Both the B_z component and the magnetic field magnitude can almost completely be explained by the plasma interaction. Panel 3 and 4 of Figure 6.32 show that our model reproduces the overall structure as well as the two local maxima. The negative perturbation of B_z and $|\mathbf{B}|$ occurs in the downstream region where the plasma is accelerated. Thus, the magnetic field strengths is decreased (see section 6.1.1).

Variation of the ocean thickness

The induced magnetic field depends both on the conductivity and the thickness of the ocean as mentioned in section 4.3.3. Thus, the determination of σ_{oc} is not unambiguous. To resolve this ambiguity, we vary the ocean thickness. As an example Figure 6.33 shows our simulation results for an assumed ocean thickness of 25 km. As mentioned above, this represents the extreme case of a thin ocean model. Again, the thickness of the crust is 50 km.

In order to explain the measured magnetic field data, larger ocean conductivities are necessary when using a thinner ocean. Figure 6.33 indicates that in this case ocean conductivities of 1 S/m or less are insufficient to reproduce the B_x and B_y component of the magnetic field when an ocean thickness of 25 km is assumed. A conductivity of, e.g., 5 S/m is needed. We remind the reader that the induced magnetic field is saturated for conductivities larger than 5 S/m. Hence we can only set a lower limit on the ocean conductivity. In reverse, we can conclude that if the ocean conductivity is less than 1 S/m, the ocean has to be thicker than 25 km.

Plasma flow

Figure 6.34 shows our model results for the plasma bulk velocity along the E4 trajectory. The main plasma flow is along the x-axis. A small positive v_y component before $\sim$06:47 UT
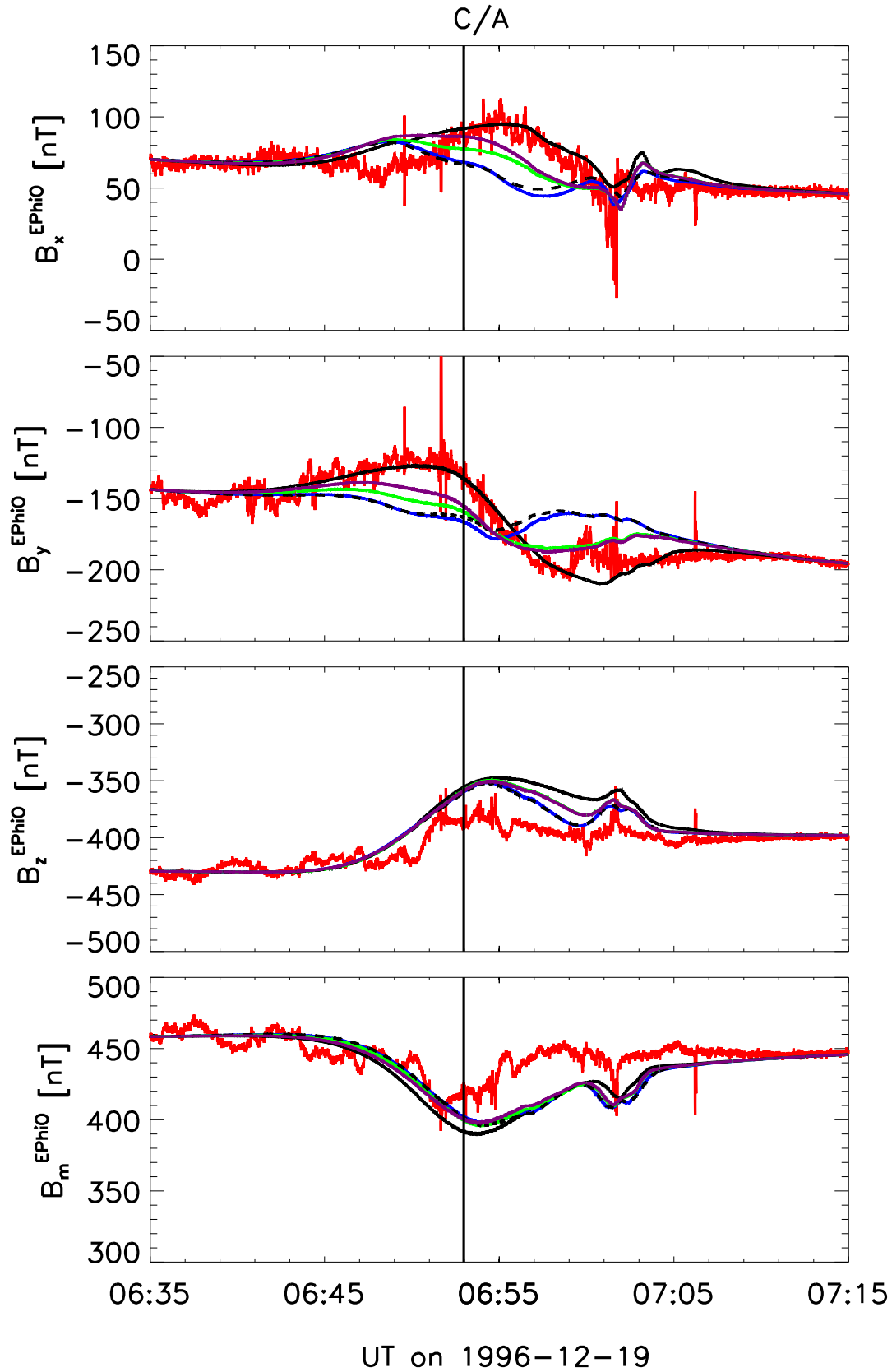
Figure 6.33:   *Same as Figure 6.32 for an ocean thickness of 25 km. The predicted field by including induction is shown for the ocean conductivities* σ_{oc}*: 100 mS/m (blue), 500 mS/m (green), 1 S/m (purple), and 5 S/m (black).*
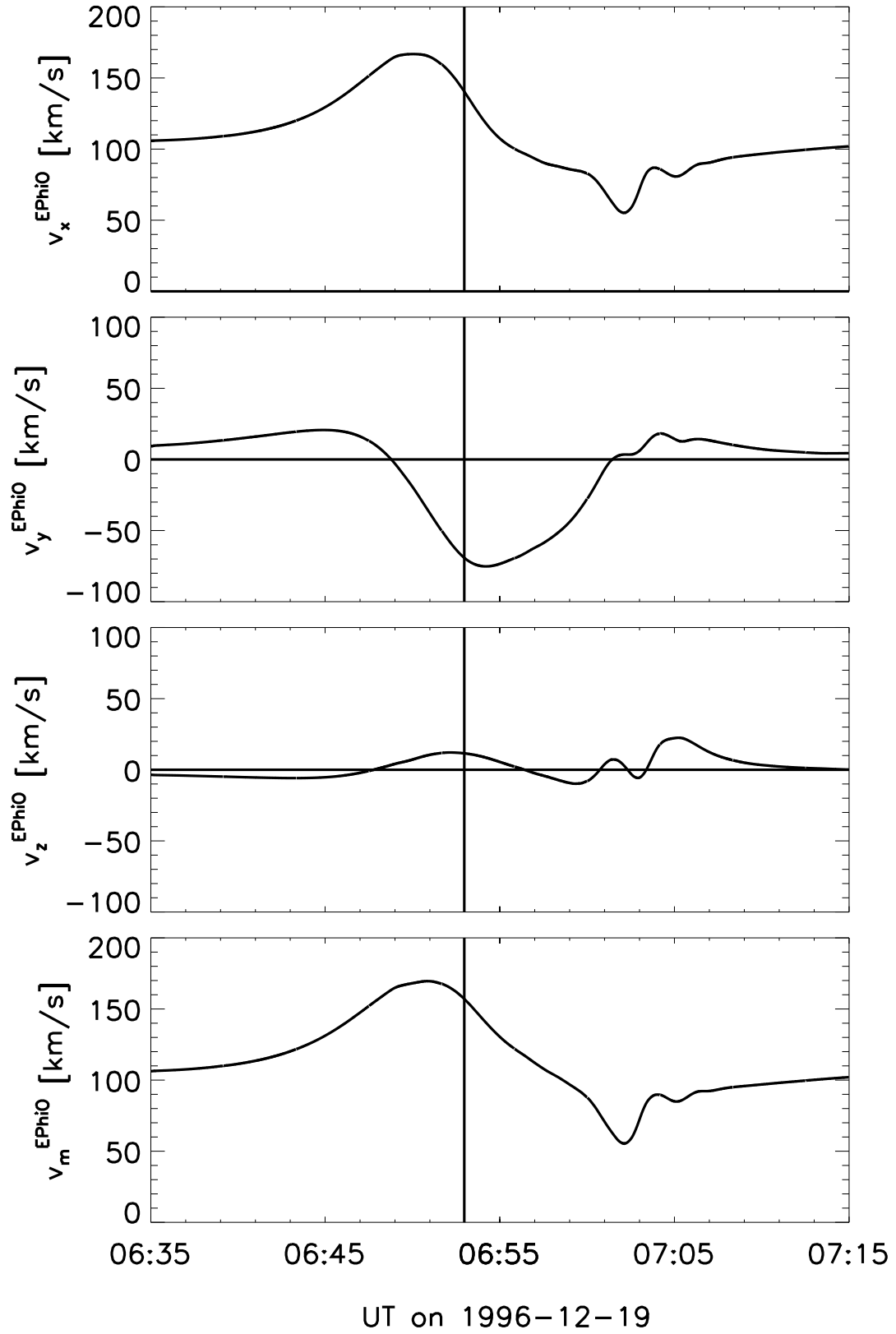
Figure 6.34:   *Components of the bulk velocities during the E4 flyby. From top to bottom: v_x, v_y, v_z, v_m. Coordinates are in EPhiO. The time of closest approach is indicated by the vertical line.*
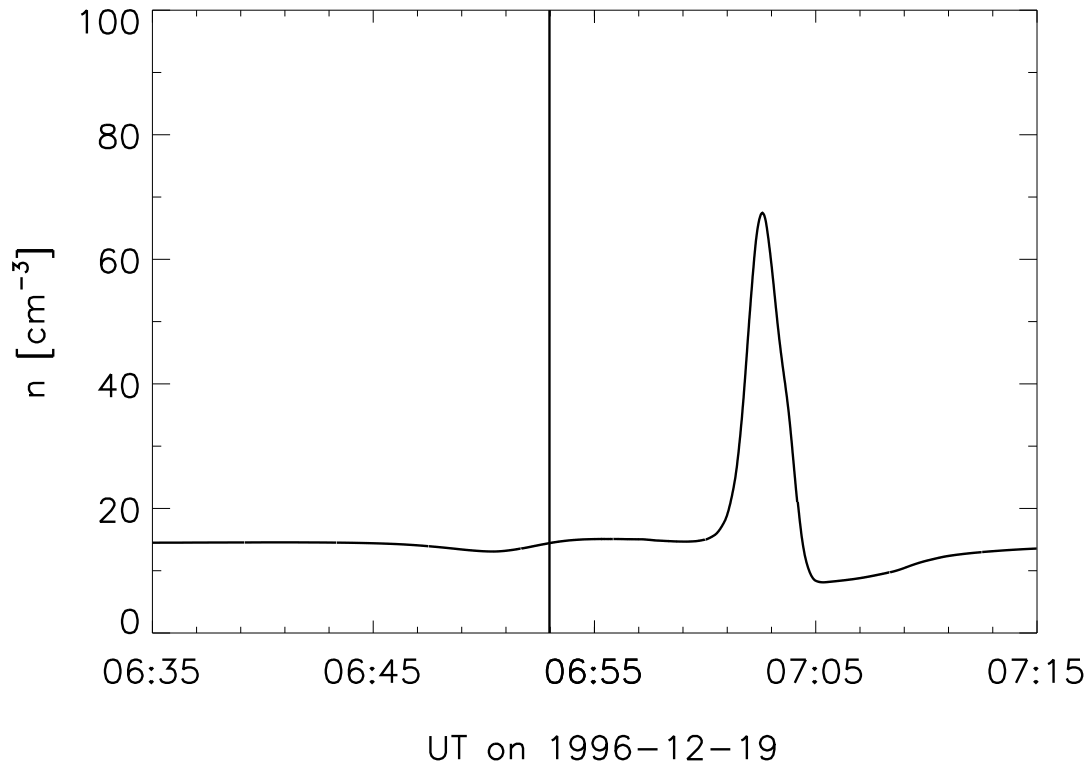
Figure 6.35: *Ion number density during the E4 flyby. The time of closest approach is indicated with a vertical line.*

and a negative y-component thereafter account for the diversion of the plasma flow around Europa. This is associated with an acceleration of the flow visible in the enhanced velocity magnitude. Thereafter the convergence of the flow associated with smaller values of the velocity magnitude and a smaller v_y component is visible.

Figure 6.36 shows the observations from the Galileo PLS experiment. The components of the bulk velocities along the E4 flyby trajectory are shown in the lower four panels. We find that our model results shown in Figure 6.34 and discussed above represent the characteristics of the velocity components along the trajectory quite well. However, the calculated flow speeds obtained with our model are lower in the wake and higher around closest approach than the measured flow speeds.

Plasma density

Figure 6.35 shows the ion number density along the E4 flyby trajectory. The steep density peak in the wake with a value of $\sim$70 cm^{-3} is in agreement with the results of the plasma observations shown in Figure 6.36 [*Paterson et al.*, 1999]. The E4 flyby was oblique through Europa's wake. Therefore, the small spatial extension of the density peak in the wake is in agreement with the wake structure shown in Figure 6.20. With our model we are able, to
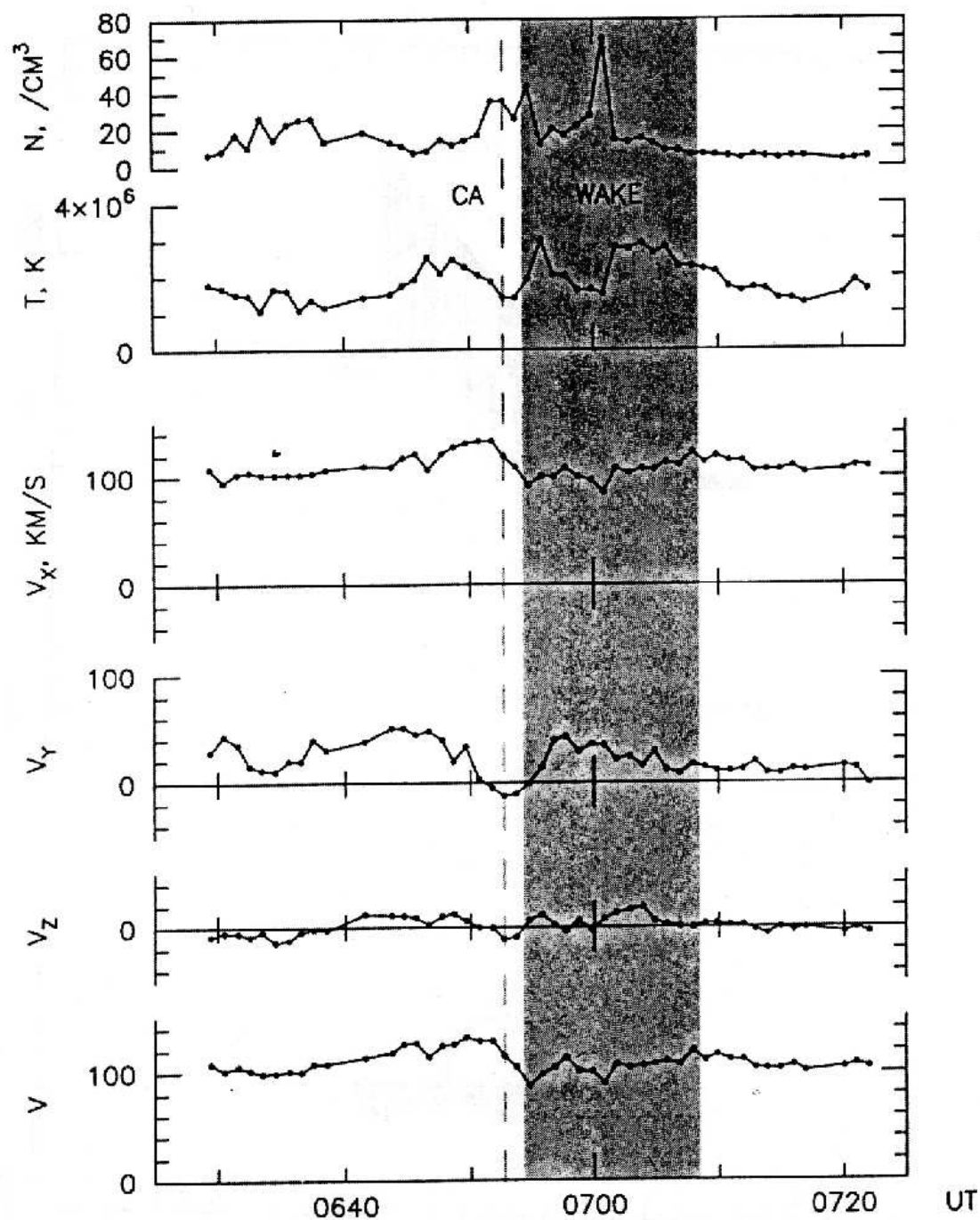
Figure 6.36:   *Observations from the Galileo PLS experiment showing the components of the bulk velocities and the ion number densities during the E4 flyby. Coordinates are in EPhiO. The time of closest approach is indicated with a vertical line. The shaded region is the predicted geometric wake of Europa. (Taken from Paterson et al. [1999])*
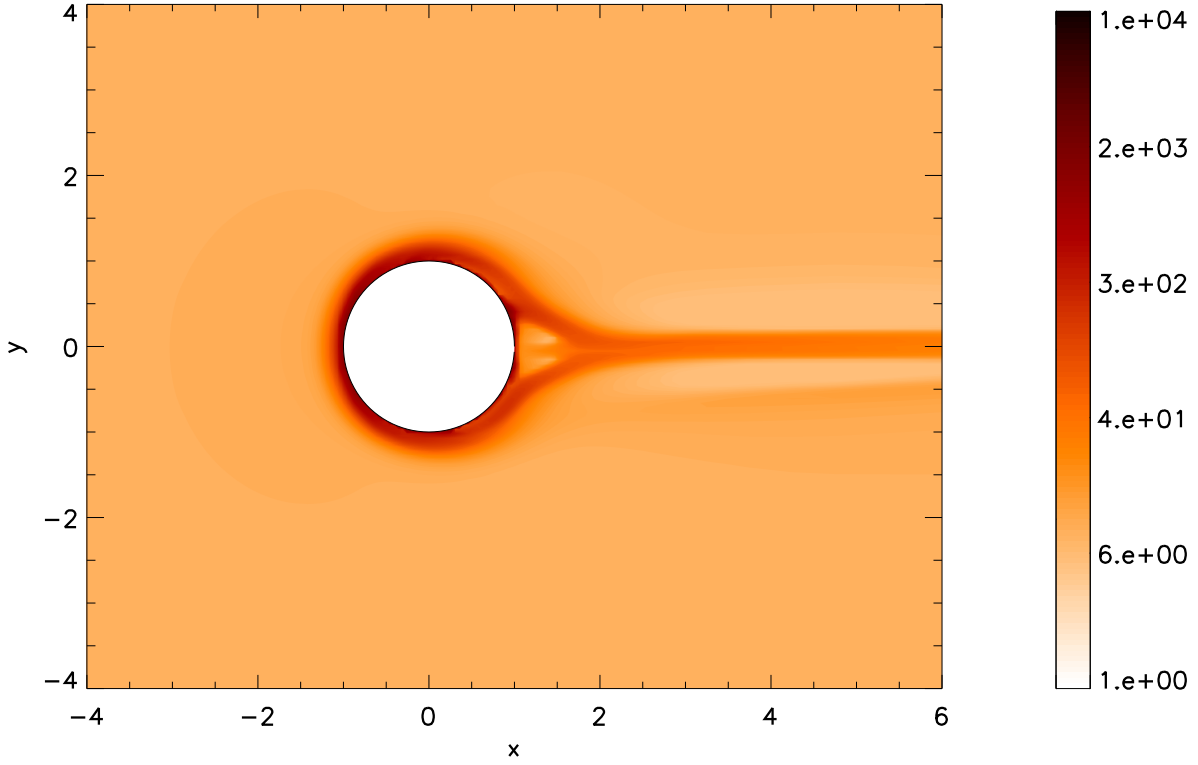
Figure 6.37:   *Electron number density in cm^{-3} in the xy-plane when including induction.*

explain for the first time, the lack of higher ionospheric density signatures in the wake during the E4 flyby. Our model results are contrary to the numerical results of [*Kabin et al.*, 1999; *Liu et al.*, 2000], who show a broad plasma wake, and therefore cannot explain the Galileo PLS measurements [*Paterson et al.*, 1999].

There is a second density maximum at ∼07:02 UT with values up to ∼40 cm^{-3} in the PLS data (see Figure 6.36). Our simulations does not resolve this maximum. However, the density maximum appears around closest approach and at the edge of the predicted geometric wake of Europa. As closest approach was at ∼ (0.9, 1.09, 0.33) R$_E$ (in the coordinate system we use), our simulations suggest that at this point the plasma is still diverted around the moon and the plasma flow has not closed yet (see Figure 6.37). Therefore, we suggest that the first density peak in the data is still in the ionosphere. The absence of this density peak in our simulations may be either due to the fact that the ionosphere is more extended (or has a different structure) than assumed in our model, or due to the simplifications in our model (e.g, neglecting the Hall-term, simplified energy equation).

The second density peak is at ∼ (2.33, 0.04, −0.28) R$_E$. At this point the plasma flow has closed and the wake structure has formed (see Figure 6.37). Thus, this peak represents the crossing of Europa's plasma density wake. The density peak is associated with a dip in the magnetic field data (see Figure 6.32)

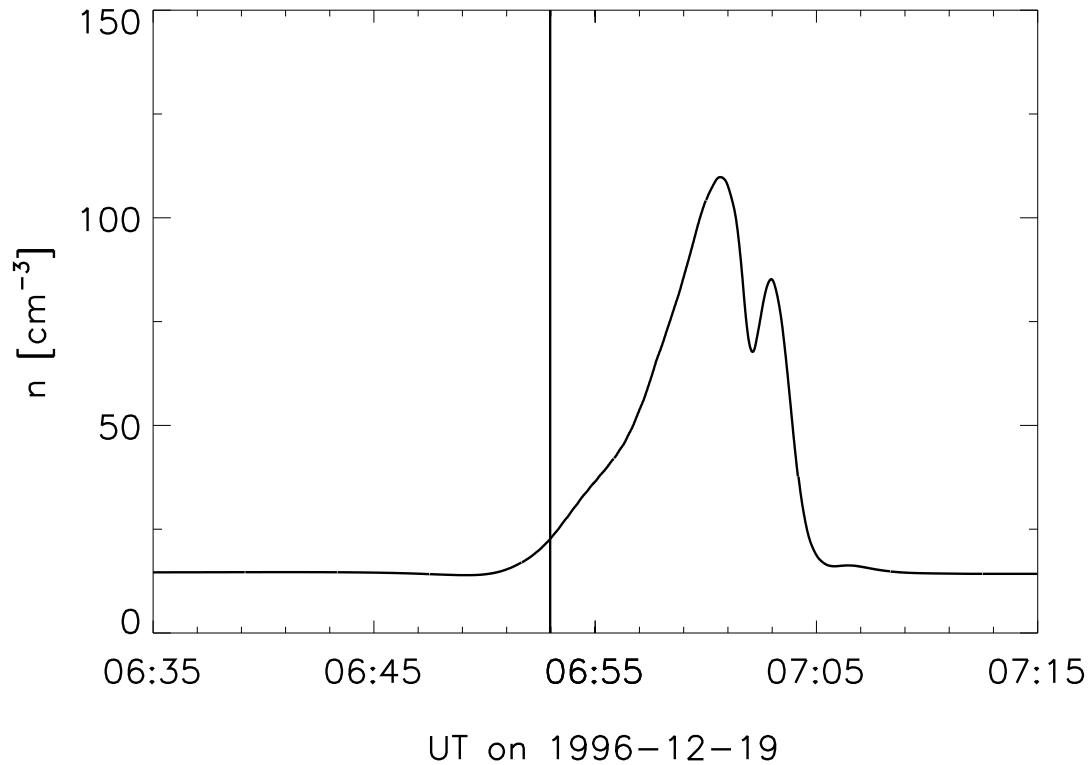Note that we see a double peak structure in the wake, when not including induction (see

Figure 6.38:   *Ion number density during the E4 flyby when not including induction. The time of closest approach is indicated with a vertical line.*

Figure 6.38). This is in agreement with the results shown in Figure 6.7. However, this double peak structure is different from the structure shown in Figure 6.36. First, there is an offset in time between the simulations and the measured data. A fact which may have led other simulators (e.g., *Kabin et al.* [1999]) to speculate on a rotation of the plasma flow. However, from the comparison of the magnetic field data with our simulations, we see no need for a rotation of the flow. Second, the plasma density of the first peak in Figure 6.36 is much lower than that of the second peak. A behavior which is different from our simulations (see Figure 6.38). Hence, we conclude that there is only one density peak in the tail, which we see also in our simulations when including induction (see Figure 6.35). The density peak around closest approach in Figure 6.36 is not a signature of crossing Europa's wake, but of touching Europa's ionosphere.

6.5.2   Europa flyby E14

The Europa flyby, E14, occurred in the low plasma density region above the current sheet (see Figure 3.2). Thus, the induced magnetic field is very similar to that during the E4 flyby. Again, the primary induced dipole moment pointed close to the Jupiter-facing meridian. The trajectory of the E14 pass was at higher altitude and latitude than the E4 pass. Closest approach occurred at an altitude of 1647 km at 13:21:05 UT on March 29, 1998. Figure 3.1 shows that the flyby was an upstream pass which ended downstream.

As in the previous section, we discuss two different assumed ocean thicknesses for the E14 flyby, 100 km and 25 km. We start with an assumed ocean thickness of 100 km. The measured magnetic field (red) along the E14 trajectory in the EPhiO coordinate system is shown in Figure 6.39. In addition, the predicted field by neglecting induction (dashed black) and including induction in a 100 km thick ocean for different assumed ocean conductivities σ_{oc} is displayed. The color code used in Figure 6.39 is the same as in Figure 6.32.

The B_x component of the measured magnetic field cannot be explained by plasma interaction alone. We are able to fit this component very well when using ocean conductivities of 250 mS/m and higher. As mentioned above, an upper limit for σ_{oc} can not be assessed.

The B_y component as well as the B_z component and the magnetic field magnitude can almost be explained by the plasma interaction. The enhancement of B_z and $|\mathbf{B}|$ occurs upstream of Europa where the plasma is slowed down and the magnetic field is compressed. Since the flyby was above the equator, the bending of the magnetic field is visible as a positive perturbation of B_x.

Figure 6.40 shows the simulation results when using a thickness of the ocean of 25 km and a crust thickness of 50 km. In this case ocean conductivities of at least 1 S/m are necessary to reproduce the B_x component of the magnetic field. In reverse, we can conclude that for the E14 flyby the ocean has to be thicker than 25 km for $\sigma_{oc} \leq 1$ S/m. This is the same result as for the E4 flyby.

Plasma flow and density

The velocity of the bulk plasma along the E14 trajectory is shown in Figure 6.41. The negative v_y component accounts for the diversion of the plasma flow around Europa. The enhancement of v_x and of the velocity magnitude is due to the acceleration of the flow. Unfortunately there are no plasma data available for the E14 flyby to compare our results with.

The ion number density along the E14 flyby trajectory is shown in Figure 6.42. As the pass was upstream at a distance larger than 1600 km, no larger density variations are visible. This is in agreement with the results obtained for the electron density by the PWS experiment [*Kurth et al.*, 2001].

6.5.3   Europa flyby E26

The E26 flyby was the crucial flyby to distinguish between a permanent and an induced magnetic dipole moment as source of Europa's internal magnetic field [*Kivelson et al.*, 2000]. This pass occurred south of Jupiter's magnetic equator in a region with low plasma density (see Figure 3.2). Therefore, the induced magnetic field was almost 180° out of phase with its value on the E4 and E14 pass (see Figure 6.18 and 6.19). Closest approach occurred at an altitude of 346 km at 17:59:43 UT on January 03, 2000. The flyby trajectory was upstream of Europa, nearly radial toward Jupiter, and south of Europa's equator.
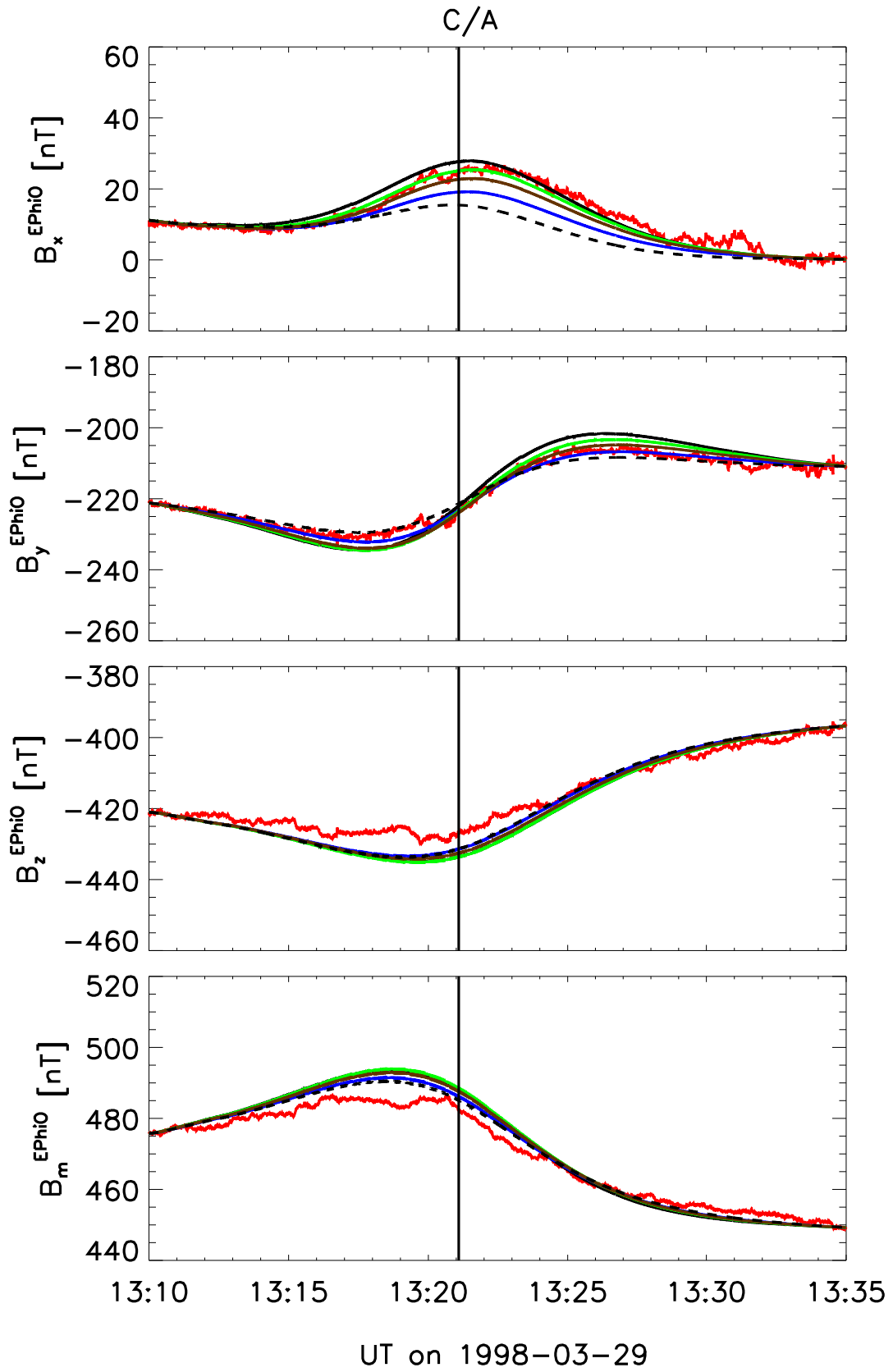
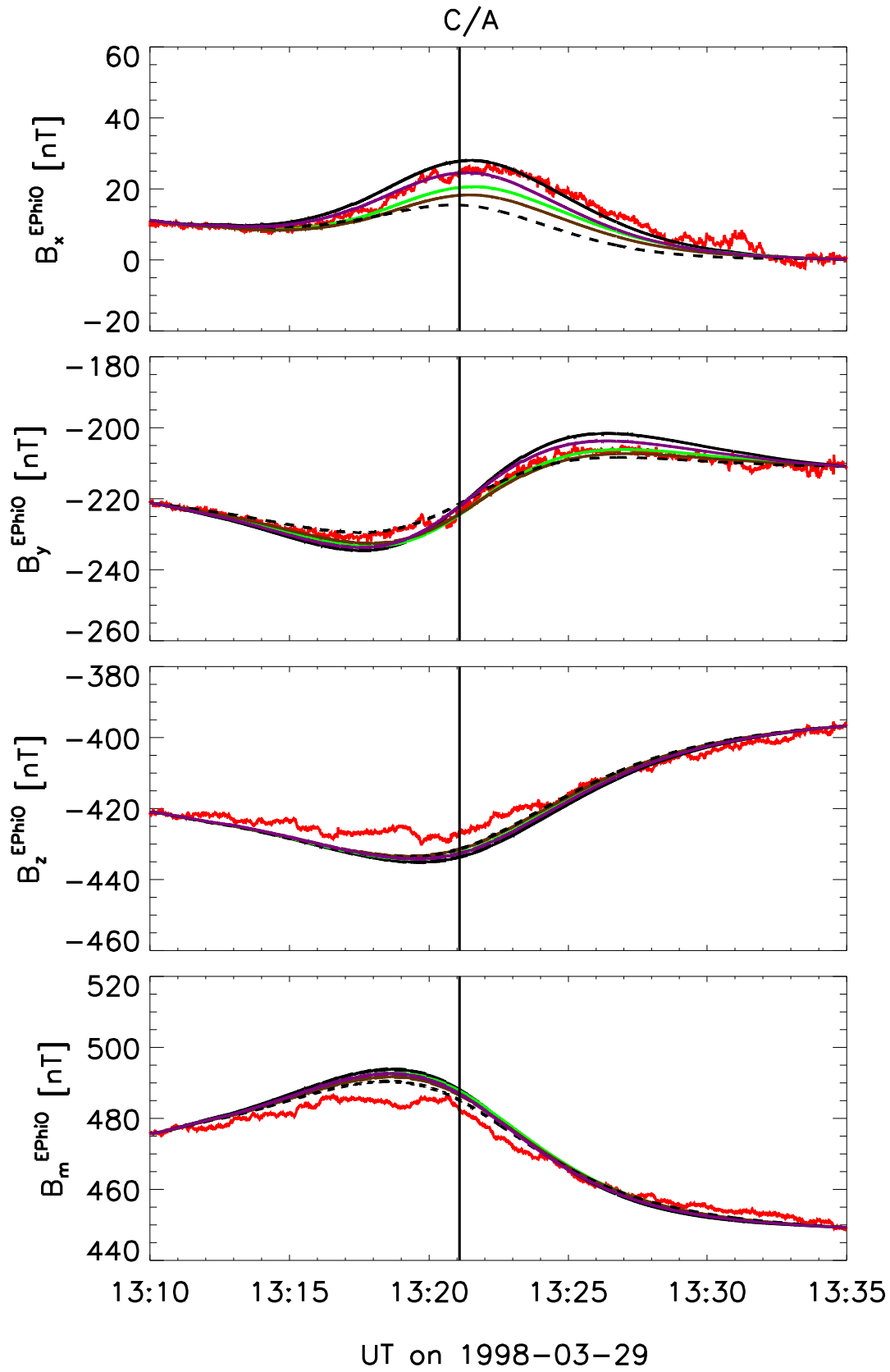**Figure 6.39:**   *Same as Figure 6.32 for the E14 flyby.*

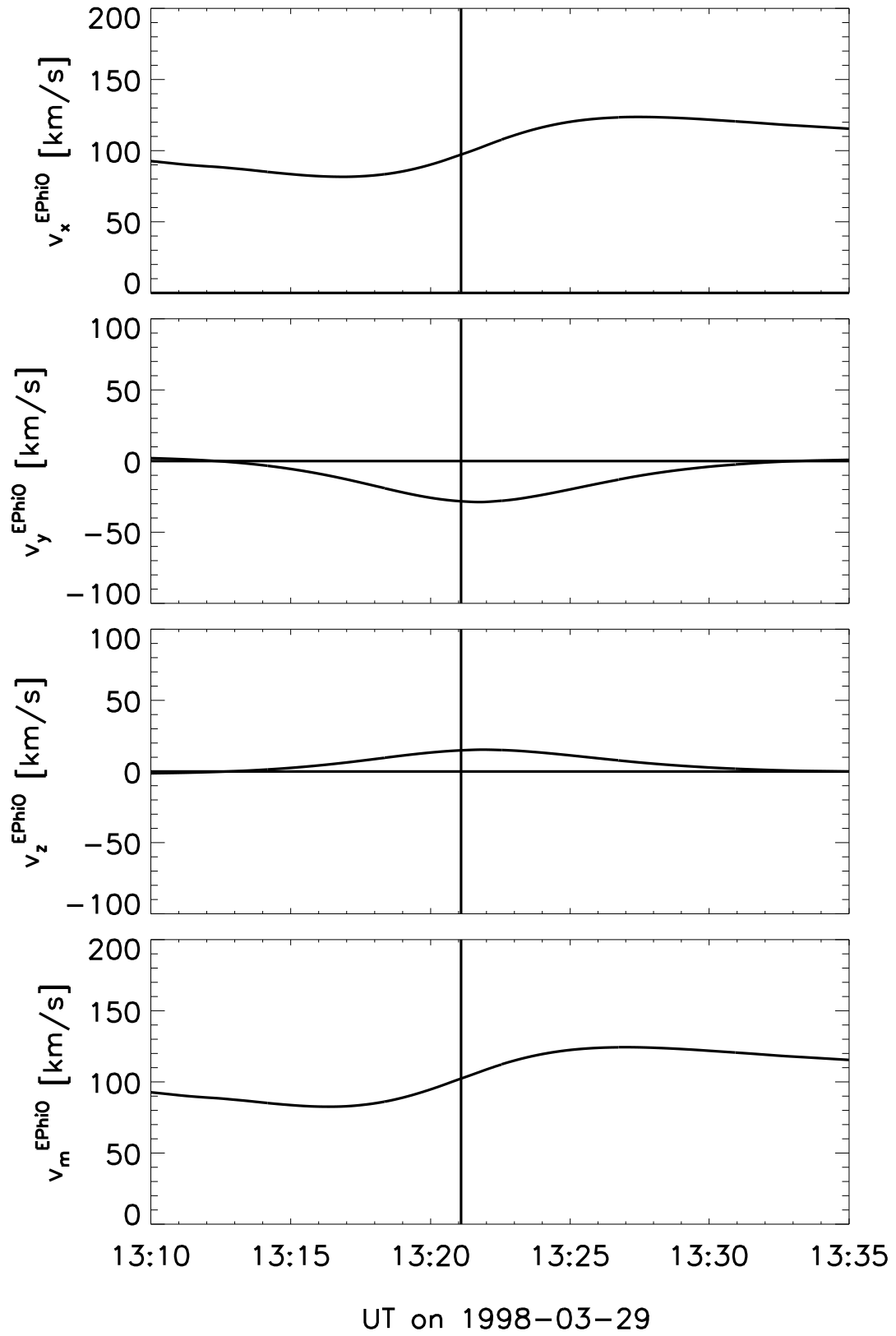**Figure 6.40:** *Same as Figure 6.33 for the E14 flyby.*

Figure 6.41:   *Same as Figure 6.34 for the E14 flyby.*
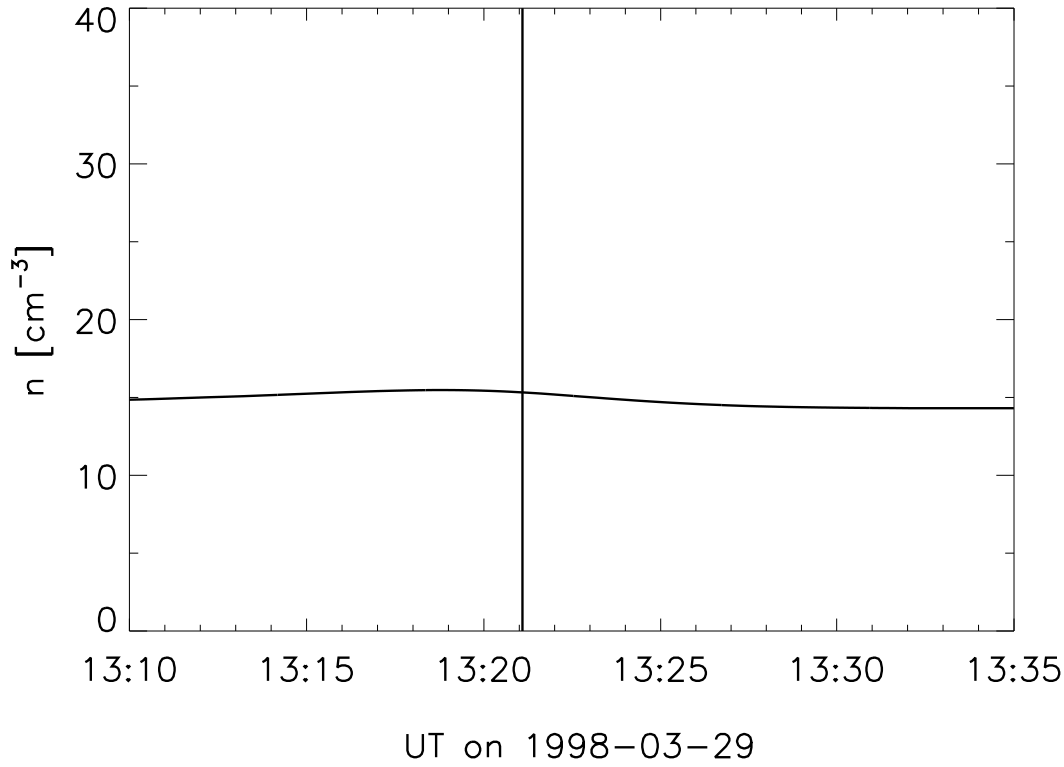
Figure 6.42:   *Same as Figure 6.35 for the E14 flyby.*

Figure 6.43 shows the magnetic field along the trajectory in the EPhiO coordinate system for an ocean conductivity $\sigma_{oc} = 100$ km and a crust thickness of 50 km. We are able to fit the overall structure of the magnetic field fairly well. Since this flyby was very close to Europa and off the equator, contributions from the plasma interaction can be found in every component of the magnetic field.

The bendback of the Alfvén wing leads to an enhancement of the B_x component around closest approach. While we can fit B_x in general, we are not able to fit the double peak structure of this component in detail. However, this structure occurs around closest approach at altitudes which are within or very close to Europa's ionosphere. As we use a simple model of Europa's atmosphere the detailed structure of the magnetic field at this altitudes is beyond the scope of our model. In section 6.2 we show that the influence of the plasma interaction on the induction process is weak. Hence, the details of the plasma interaction do not influence our statement on the conductivity distribution in the interior of Europa.

The B_y component contains contributions from the plasma interaction as well as from the induction. Including induction with ocean conductivities of 250 mS/m and larger improves the fit of this component fairly well. The B_z component also contains contributions from the plasma interaction. Including induction in an ocean with $\sigma_{oc} \geq 250$ mS/m and larger leads to a better fit to the data. By using conductivities of 250 mS/m and larger we can fit the magnetic field magnitude very well. The enhancement of the field magnitude is due to the compressing of the magnetic field upstream of Europa.
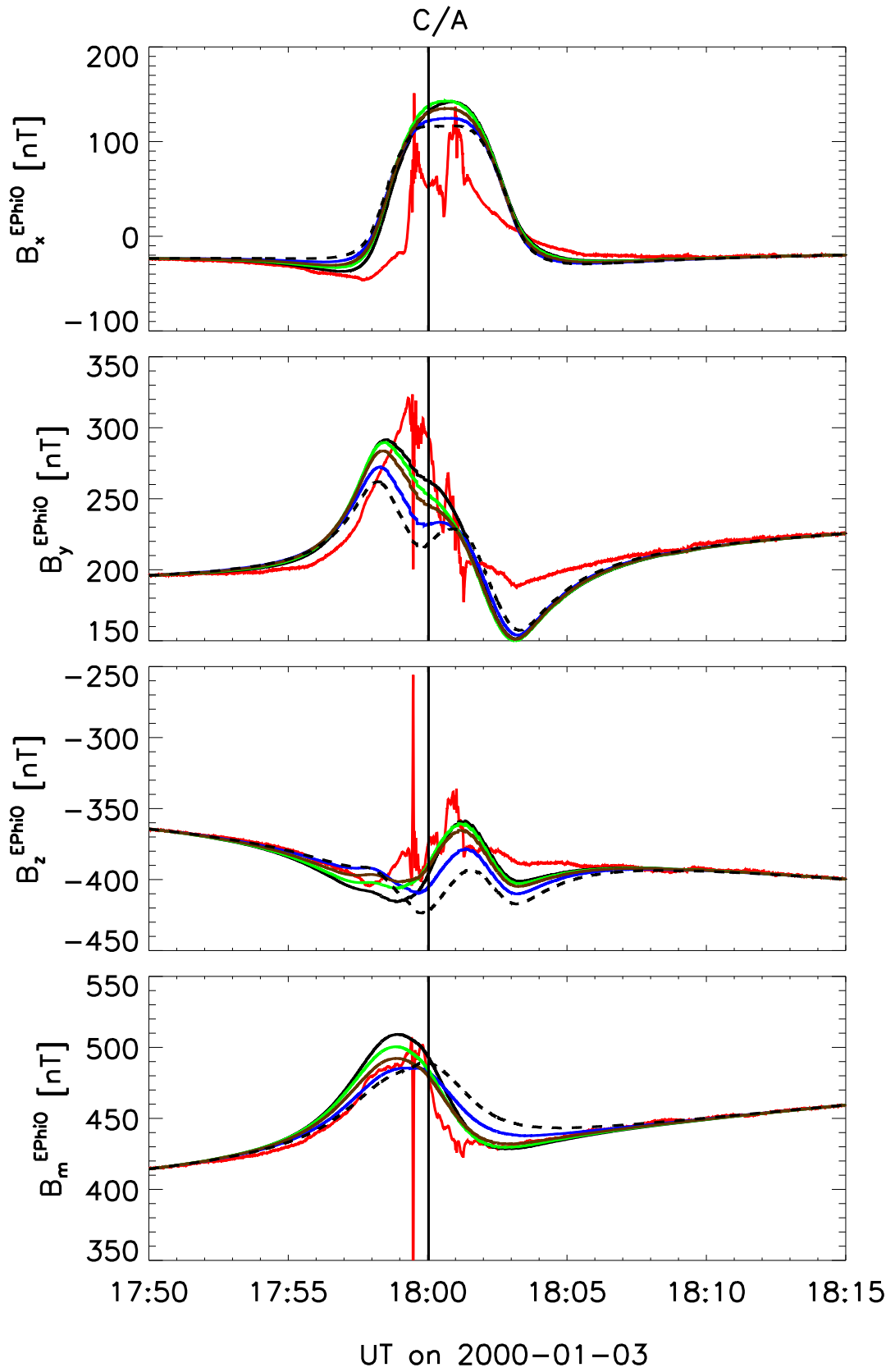
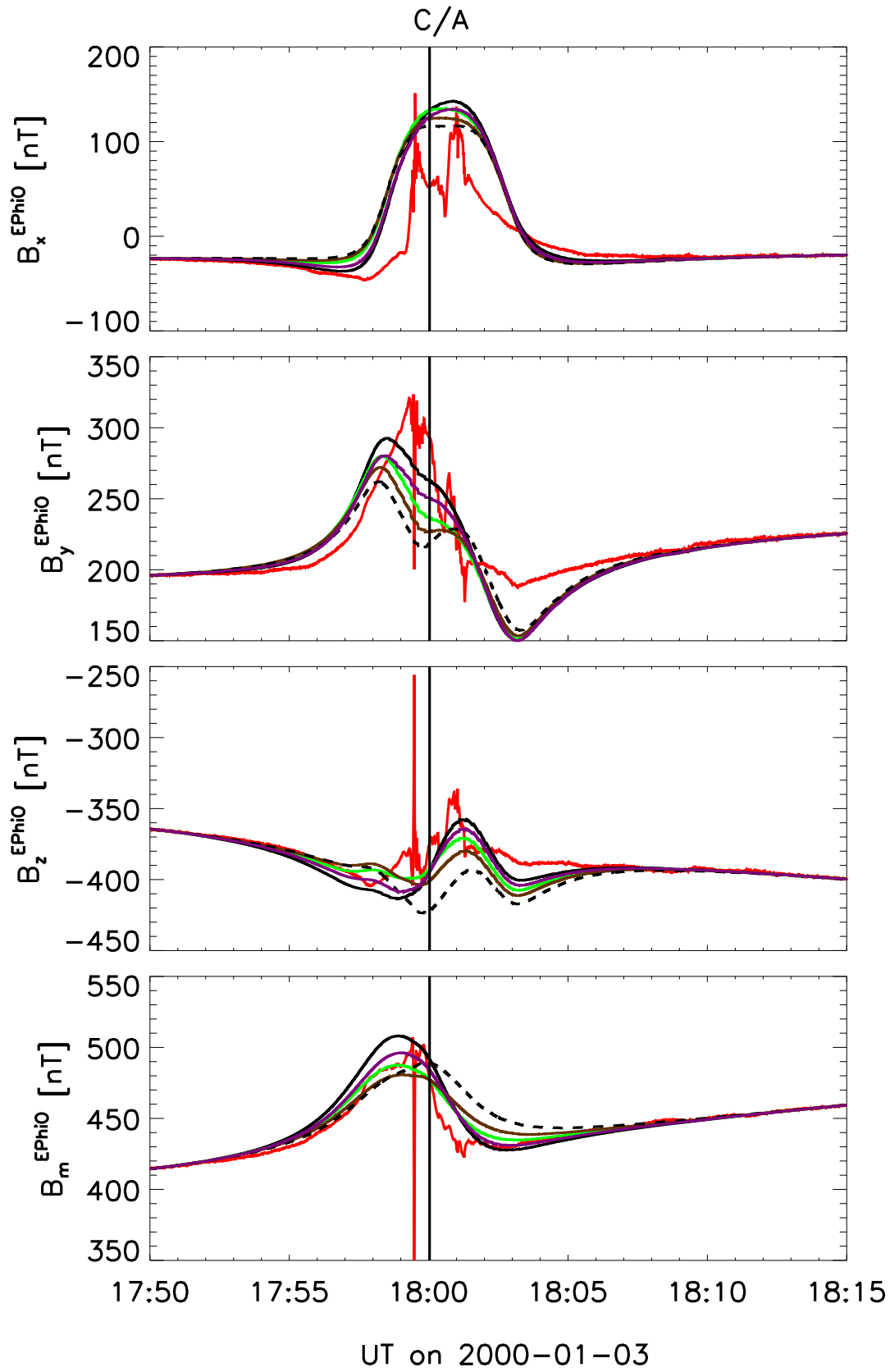***Figure 6.43:***   *Same as Figure 6.32 for the E26 flyby.*

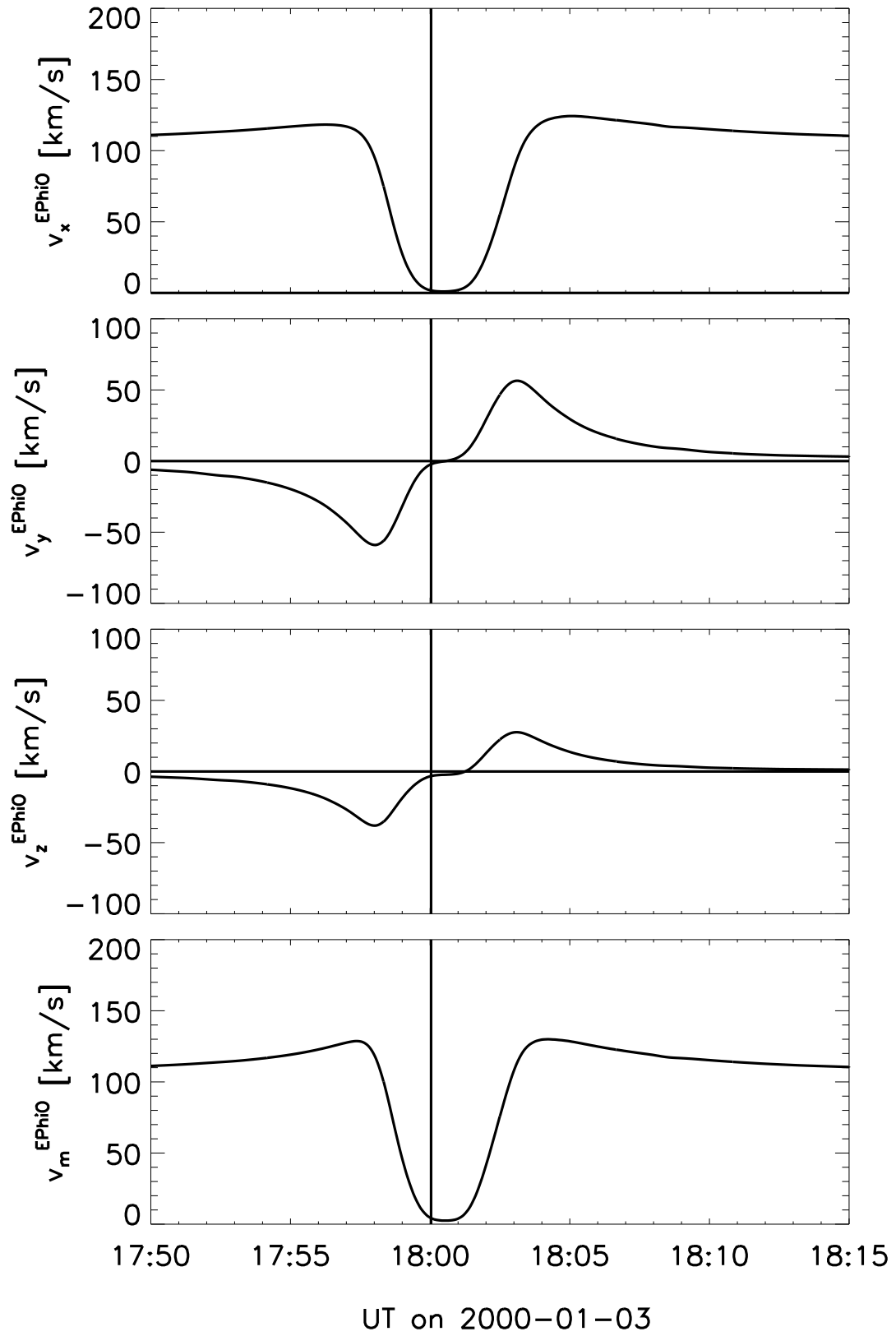**Figure 6.44:**   *Same as Figure 6.33 for the E26 flyby.*

Figure 6.45:   *Same as Figure 6.34 for the E26 flyby.*
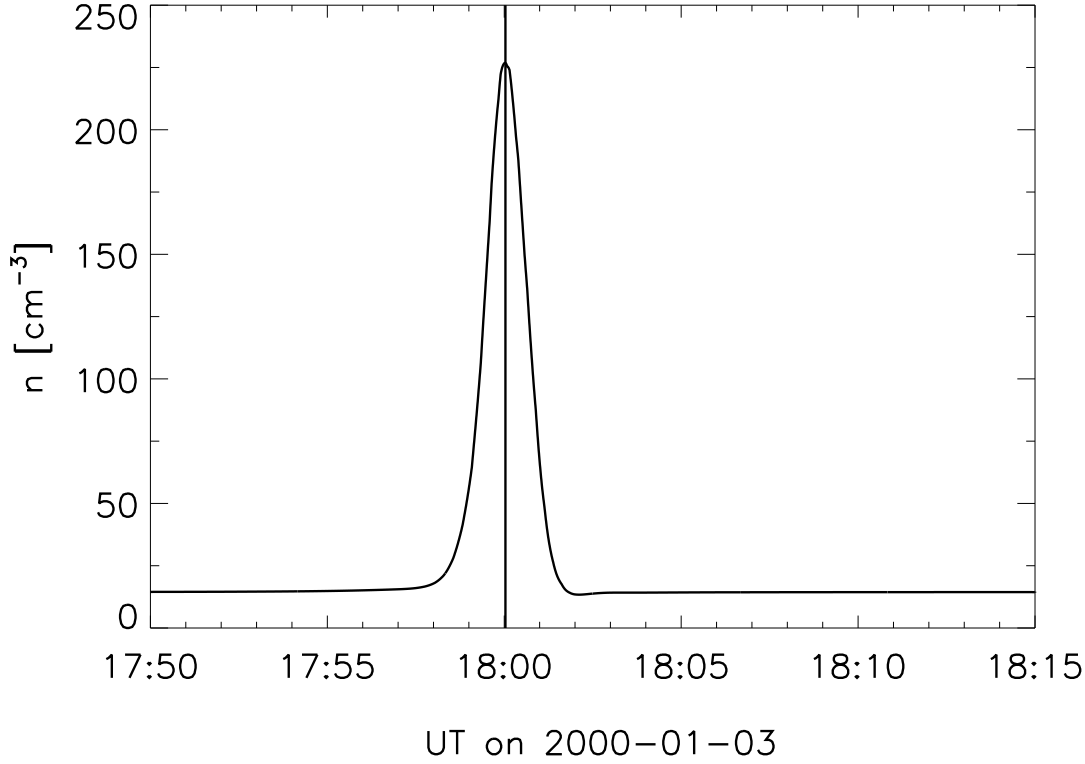
Figure 6.46:   *Same as Figure 6.35 for the E26 flyby.*

In Figure 6.44 we show our simulation results when using an ocean thickness of 25 km and a crust thickness of 50 km. Again, the B_x component is determined mainly by the plasma interaction. Using ocean conductivities larger than 1 S/m improves the fit of the B_y component. For B_z good fits are obtained when using $\sigma_{oc} \geq 500$ mS/m.

Plasma flow and density

The velocity of the bulk plasma along the E26 trajectory is shown in Figure 6.45. Quite evident is the drop of the velocity around closest approach. This supports the idea of crossing the southern Alfvén wing during the flyby. The slowing down of the plasma is associated with the enhancement of the magnetic field strength (see Figure 6.43). The drop in B_x, which leads to the double peak structure in this component, goes along with the drop in the velocity magnitude. The negative v_y and v_z components before closest approach account for the diversion of the flow on the anti-Jovian side upstream of Europa. In contrast, the positive v_y and v_z components after closest approach account for the diversion of the flow on the Jupiter-facing side of Europa.

Figure 6.46 shows the ion number density along the E26 flyby trajectory. At closest approach a large density enhancement with values up to ~ 230 cm^{-3} occurs. This is in agreement with the densities expected for this altitude from the Galileo radio occultation results upstream of
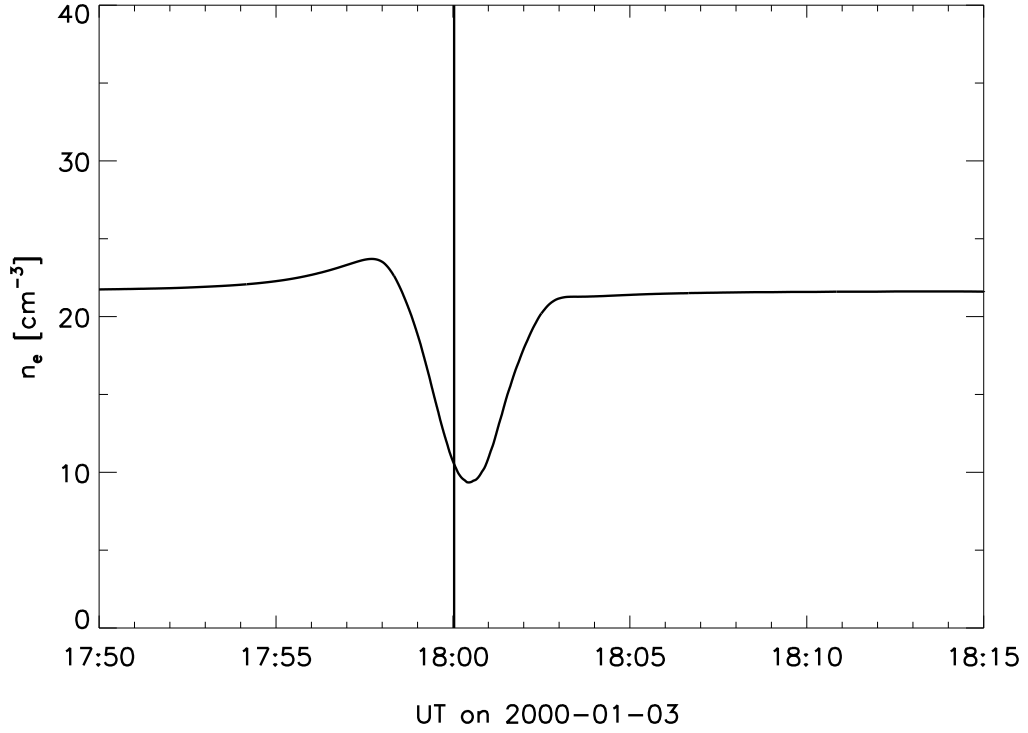
Figure 6.47:   *Magnetospheric electron number density during the E26 flyby. The time of closest approach is indicated with a vertical line.*

Europa [*Kliore et al.*, 1997]. Unfortunately, there are no PLS data available yet to compare with. Interestingly, the electron density profile calculated from the PWS data [*Kurth et al.*, 2001] does not show an enhancement near closest approach. In Figure 6.47 we display the number density of the magnetospheric electrons along the E26 trajectory. Instead, there is a density drop around closest approach. This is consistent with crossing the southern Alfvén wing at this time. However, we still see small magnetospheric densities at this times. Therefore, the ion number density peak in our simulations could be also due to the fact that we do not account for the cooling of magnetospheric electrons. Above the poles, the flow speed is very low. Therefore, plasma which enters this region will last there for a while. Thus, neglecting the cooling of magnetospheric electrons in this region could result in an overestimation of the ionospheric plasma density. Another possibility is the absorption of particles on the surface of Europa above the poles. Particles inside a flux tub connected to Europa gyrate along magnetic field lines and can hit the surface of Europa. Thus, they will be lost. This surface effect, which could lead to an emptying of the flux tube, is not included in our MHD-model. However, because of the low bulk velocity in this region, the freshly created plasma will stay there. Hence, it will not stream toward the tail so that the statements made in section 6.3.1 are still valid.

6.5.4   Europa flyby E12

The E12 flyby on December 16, 1997 was an upstream pass with a trajectory similar to E14 but at lower altitude and latitude (see Figure 3.1). Closest approach was at 12:03:20 UT at an altitude of 204 km. The pass occurred close to the center of the Jovian current sheet (see Figure 3.2), where the highest magnetospheric plasma densities are expected (see Figure 5.5). In addition, the induced magnetic fields are weakest in this region (see Figure 5.4).

Results from the PWS experiment show that the upper hybrid resonance frequency, and therefore also the electron number density, is continuously decreasing along the E12 trajectory (from ~ 600 cm^{-3} to ~ 100 cm^{-3}). No unambiguous explanation for this behavior has been found, so far. Because of the dynamical background conditions for the magnetospheric electron density during this pass, we use the value obtained from our density model (see Figure 5.5) for the proper magnetospheric latitude of the E12 pass. Hence, we choose a background magnetospheric electron density of 240 cm^{-3} as an initial value.

Global plasma interaction

Before we compare our results with the Galileo measurements, we discuss the global plasma interaction for the E12 flyby conditions, i.e., when Europa is located inside the current sheet. Although the basics of this interaction are the same as that discussed in section 6.1, the larger background plasma density yields a stronger nonlinear character of the interaction.

Figure 6.48 and Figure 6.49 show the bulk velocity of the plasma flow for the E12 pass in the xz-plane and in the xy-plane, respectively. Compared to the case when Europa is located outside the current sheet (see section 6.1.1), the extend of the primary interaction region (especially downstream) is much larger now. The Alfvén wings are not visible as clear as in Figure 6.1. The larger magnetospheric plasma density yields a strong nonlinear interaction. Note that the asymmetry in Figure 6.48 is because of the small $-v_z$ component.

The strong nonlinear character of the interaction is also visible in the magnetic field which is displayed in Figure 6.50 and in Figure 6.51 in the xz-plane and in the xy-plane, respectively. The magnetic field close to Europa is over-proportionally bended (more than the Alfvén characteristics). Further away from Europa it follows the Alfvén characteristics. Upstream of Europa where the plasma is slowed down (see Figure 6.48), the magnetic field magnitude is enhanced, reaching larger values than in Figure 6.3. The compressional perturbations of the magnetic field upstream of Europa are transported by the fast mode wave. Since this wave propagates omnidirectional, the wave energy decreases with distance ($\sim r^{-2}$). Thus, upstream of Europa the interaction region is not much larger in extent than for the E4 flyby conditions.

Downstream of Europa we get a different picture. The bending of the magnetic field is strong and the field magnitude downstream of Europa is reduced. The plasma is extensively diverted around the moon and the plasma flow closes at larger distances. Largest flow velocities are found on the flanks of the streaming ionospheric plasma which is swept into the downstream
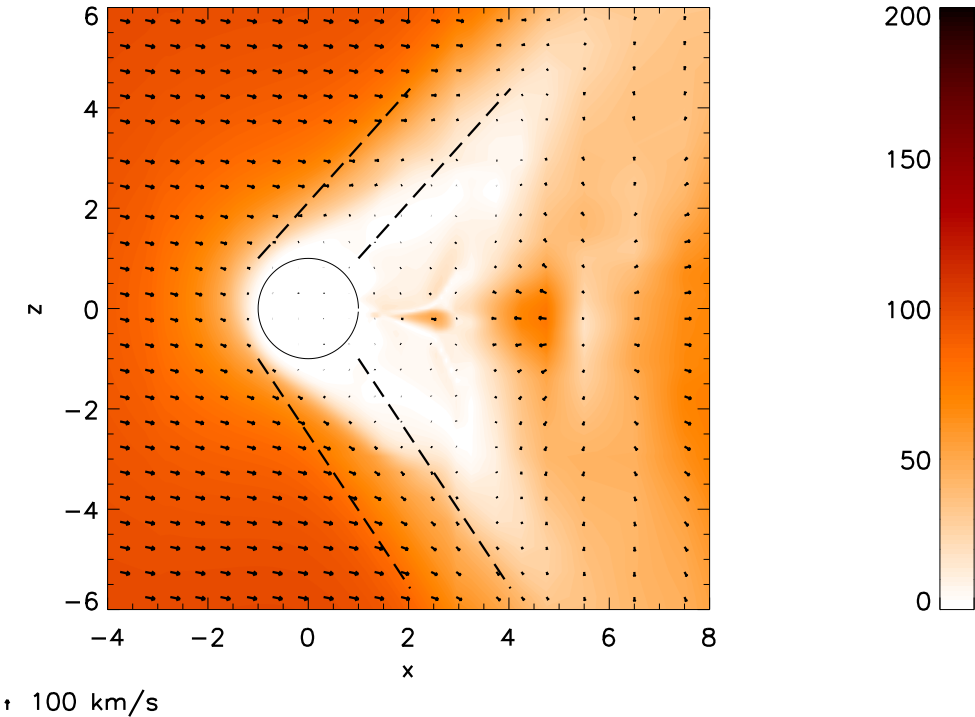
100 km/s

Figure 6.48:   *Plasma bulk velocity in the xz-plane.*
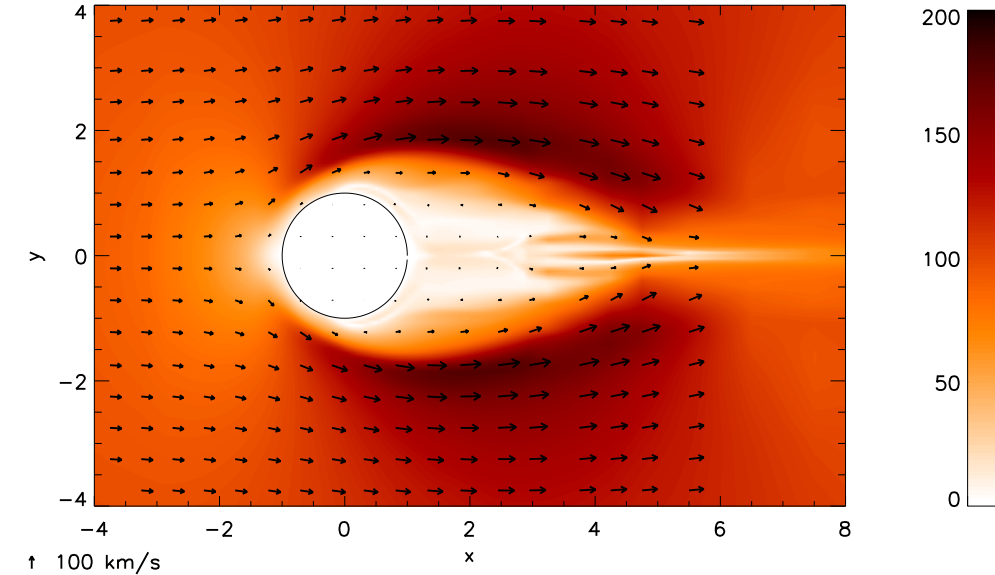

100 km/s

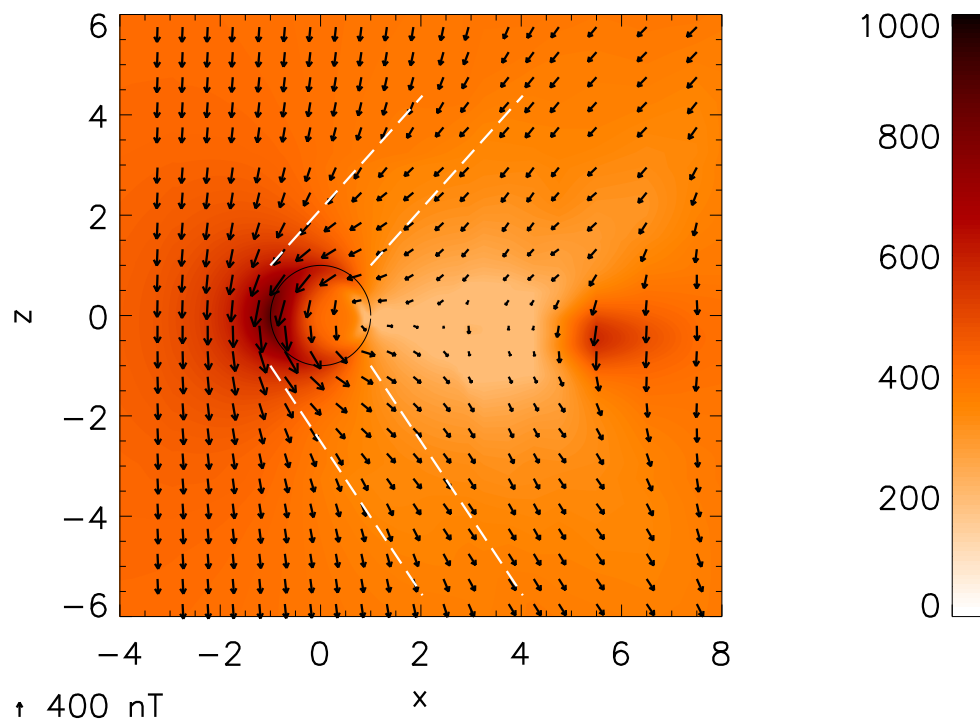***Figure 6.49:***   *Plasma bulk velocity in the equatorial plane.*

Figure 6.50:   *Magnetic field vectors and magnitude in nT in the xz-plane.*
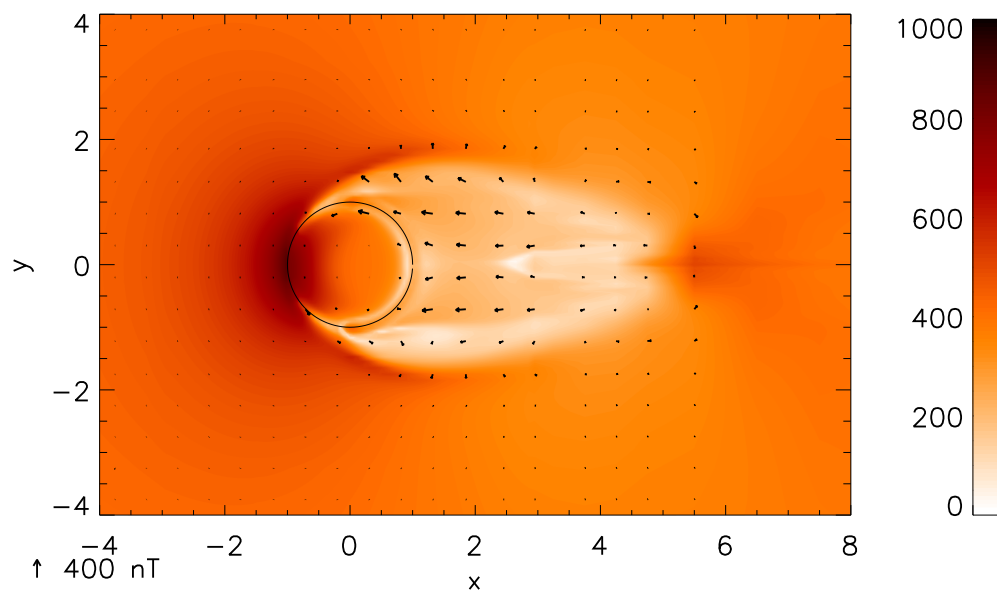

Figure 6.51:   *Magnetic field vectors and magnitude in nT in the equatorial plane.*
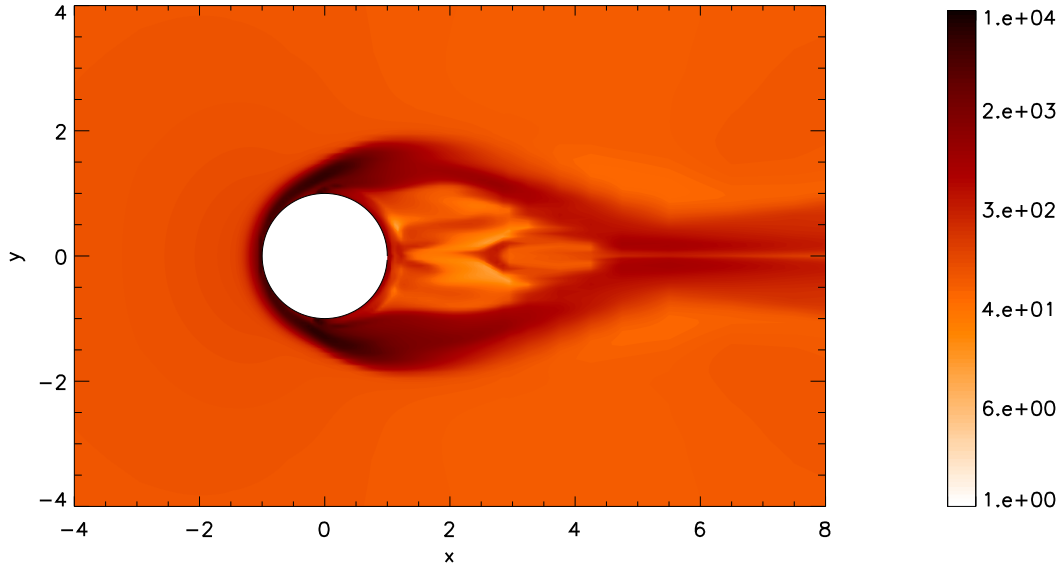
Figure 6.52:   *Electron number density in cm^{-3} in the xy-plane.*

direction (see Figure 6.52). Because of the higher magnetospheric electron density, more atmospheric O_2-molecules are ionized by electron impact. Therefore, the ionospheric plasma density for the E12 flyby conditions is higher than that during the E4 flyby. Maximum ionospheric densities are found again close to the surface with values of $\sim 10,000$ cm^{-3} on the flanks of Europa. The higher ionospheric plasma density leads to a larger pick-up region. The flow inside the area bounded by the streaming ionospheric plasma is slowed down by mass loading. In areas with high ionospheric density the thermal pressure is maximum while the magnetic pressure is minimum.

Where the plasma flow closes, the pick-up plasma is concentrated along the x-axis. There again, the radial extension of Europa's density wake is smaller than the diameter of Europa. Figure 6.53 shows that the enhanced plasma density in the wake expands along the z-axis. Thus, we see the same behavior as for the E4 case but at larger distances. Note that the north-south asymmetry in Figure 6.53 is due to the small v_z component of the upstream magnetospheric plasma.

Although induction effects are weakest when Europa is located in the middle of the plasma sheet, they still influence Europa's plasma environment. Figure 6.54 shows the electron number density in the wake at x = 2.75 R_E and x = 5.5 R_E when we include induction in an ocean with $\sigma_{oc} = 5$ S/m and a thickness of 100 km. As for the cases when Europa is located well outside the plasma sheet (see section 6.3.1), a north-south asymmetry appears in the wake when including induction. Due to the more extensively diverted flow, a structure similar to that in Figure 6.20 is seen at larger distances (x = 5.5 R_E). Because of the smaller inducing magnetic field during the E12 pass, the asymmetries are not as strong as during the E4 pass. The asymmetric wake is again a result of the asymmetric plasma pickup in the ionosphere of Europa, and is caused by the induced magnetic fields.
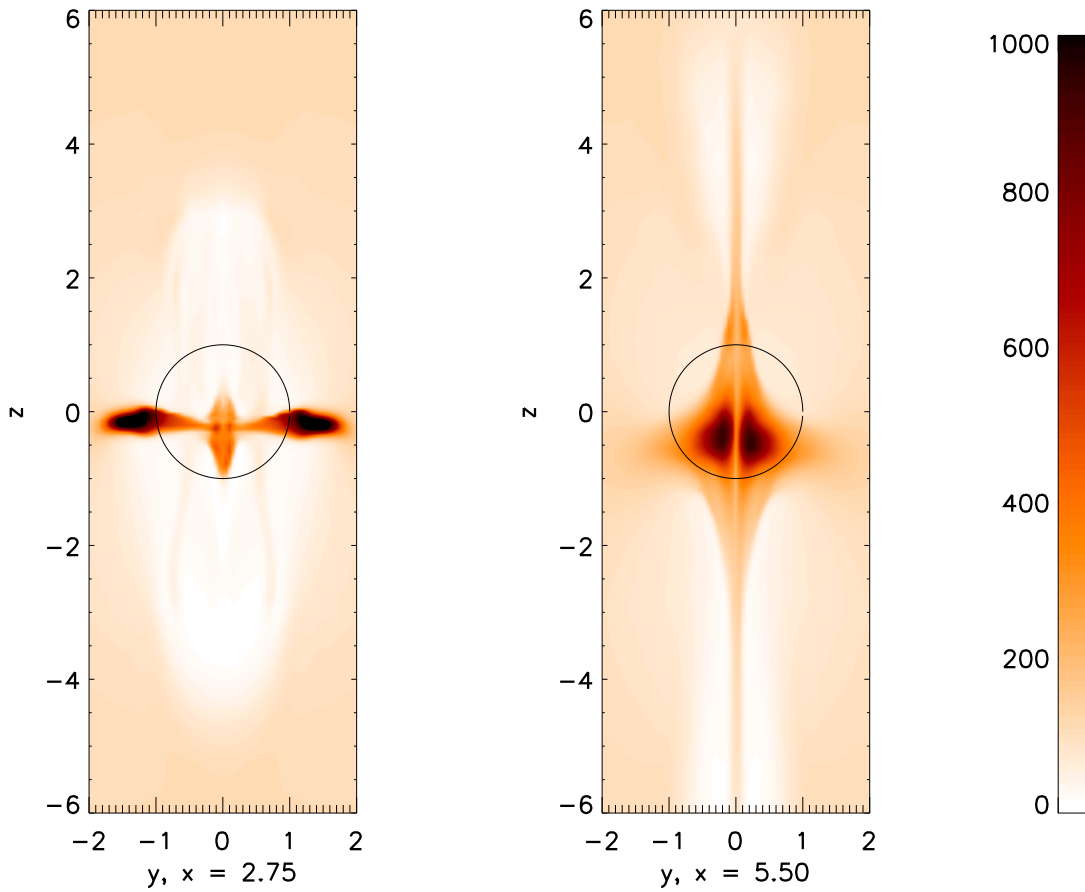
Figure 6.53: *Electron number density in cm^{-3} in the tail. Shown is the yz-plane at x = 2.75 R$_E$ and x = 5.5 R$_E$.*

Comparison with Galileo data

Figure 6.55 displays the magnetic field along the E12 trajectory in the EPhiO coordinate system. The red curve shows the magnetic field measured by the Galileo spacecraft [*Kivelson et al.*, 1999]. Our model results for a pure plasma interaction without induction in the interior of the moon are indicated by the dashed black curve. In addition, the predicted field by including induction into our model is shown for an assumed ocean conductivity σ$_{oc}$ of 5 S/m (solid black). The assumed thickness of the ocean is 100 km.

The two model results shown in Figure 6.55 differ only marginal. Obviously the magnetic field signature is dominated by the plasma interaction. Despite the low altitude at closest approach, the large perturbations due to the interaction of the high density magnetospheric plasma with Europa's atmosphere almost hide the signature of an induced magnetic field. Thus, the E12 pass is not suitable for making statements on the interior of Europa. However, since the structure of the magnetic field along the E12 flyby trajectory is determined mainly by the plasma interaction of the magnetospheric plasma with the atmosphere of Europa, we use this pass to determine the calibration factors for the temperature of the magnetospheric
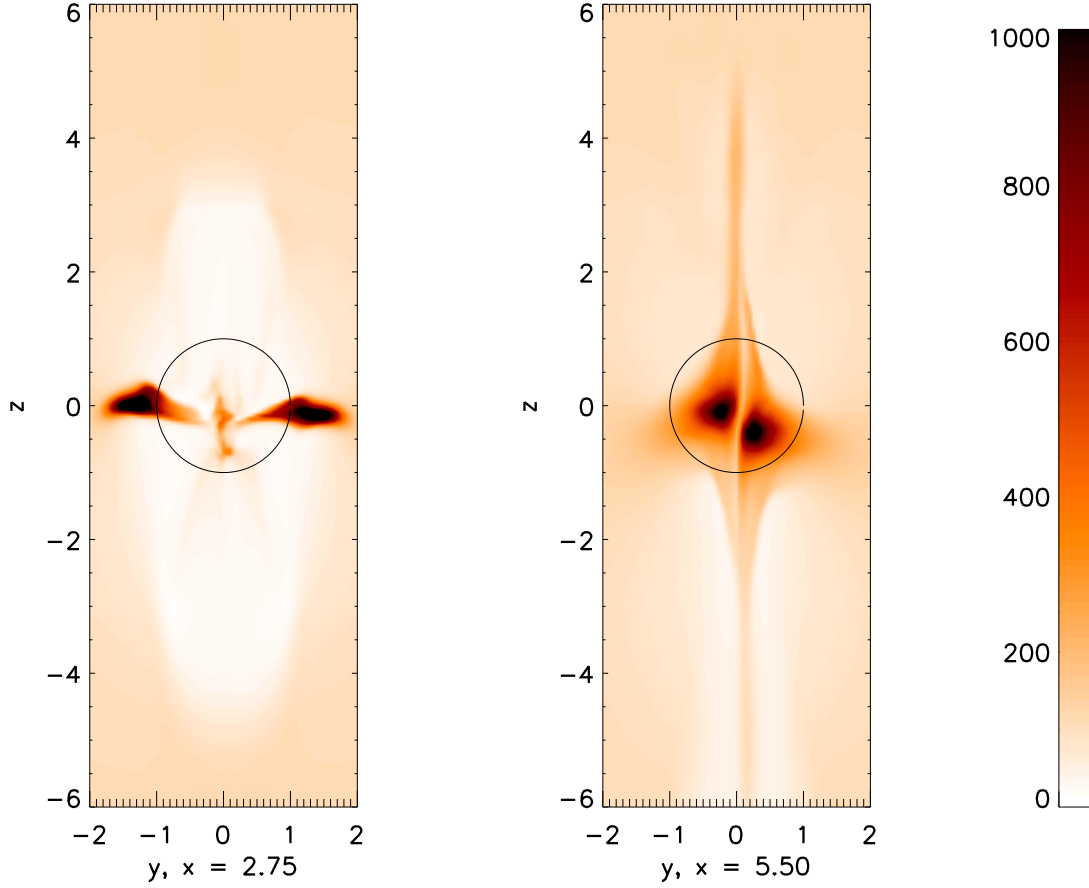
Figure 6.54: *Electron number density in cm^{-3} in the tail when induction is included. Shown is the yz-plane at x = 2.75 R$_E$ and at x = 5.5 R$_E$.*

electrons described in section 5.2.4. For our model we find a scale height $H = 400$ km and a factor $t_0 = 0.1$ most useful to fit the E12 magnetic field magnitude. We use these calibration factors for all the flybys discussed above. Note that changing these factors does not influence the location of the field magnitude maximum.

With the calibration factors determined, we are able to fit the magnetic field magnitude and the B_z component of the E12 pass very well. The increase in magnitude before closest approach is a consequence of the slow down of the plasma flow upstream of Europa (see Figure 6.56). The magnetic field is then compressed and the field magnitude increases. After closest approach the flow velocity increases and the field is slightly depressed, i.e., the magnetic field magnitude decreases. The negative value of v_y indicates the diversion of the flow around the moon.

Large perturbations of B_x and B_y occur shortly before closest approach at times when Galileo is upstream of Europa at $\sim (-1.02; -0.55; -0.03)$ R$_E$ (in our coordinate system). When we neglect the small value of v_y of the background velocity, this position represents the magnetic equator where we do not expect such large perturbations in B_x. We find perturbations of B_x and B_y at later times, i.e., when Galileo is on the flank of the moon at $\sim (-0.51; -1.09; -0.17)$ R$_E$. Since Galileo is south of the equatorial plane at this time,
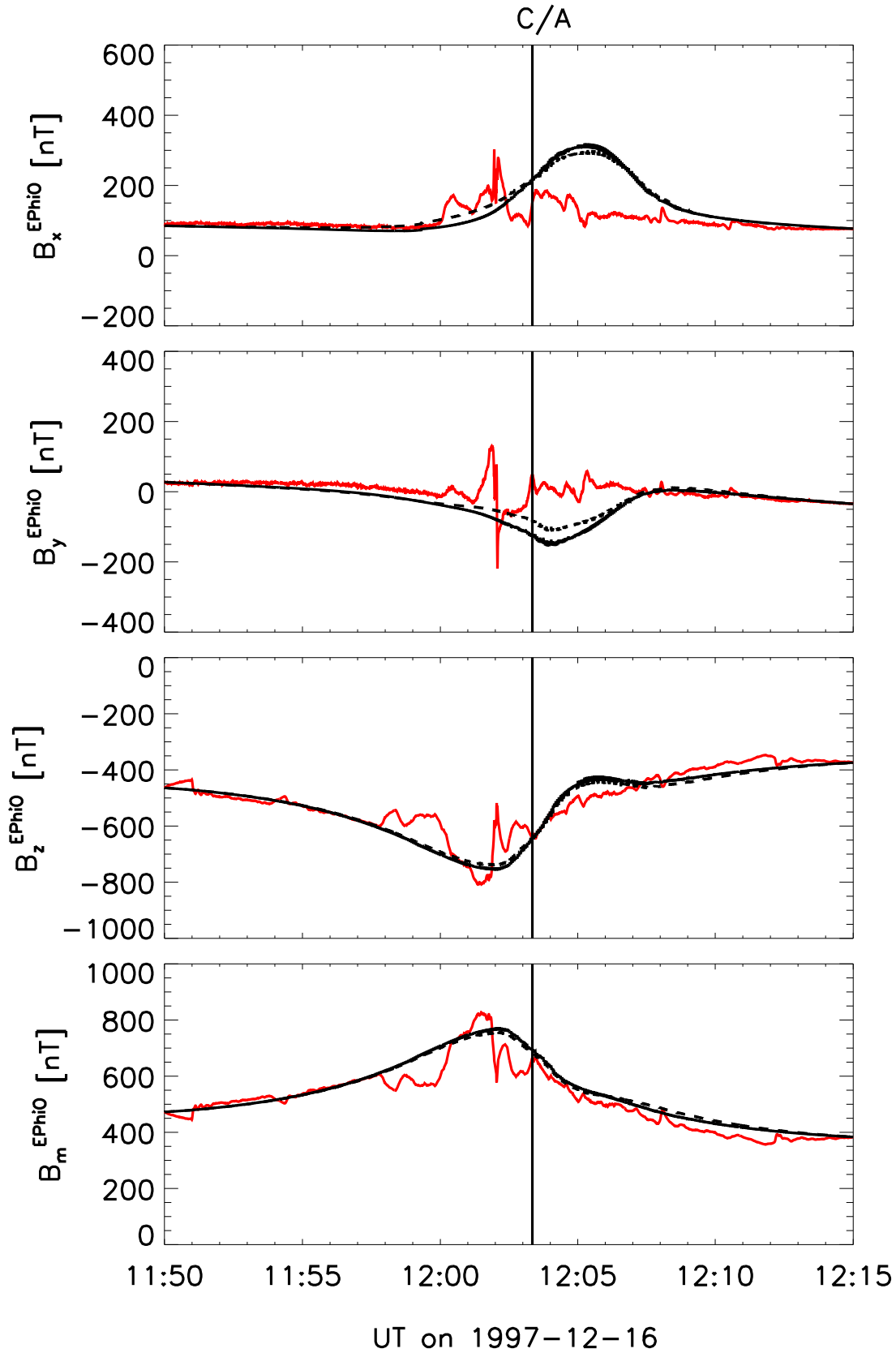
Figure 6.55:   *Observed and modeled field for the Europa E12 flyby in the EPhiO coordinate system.
The red curve shows the measured field. The dashed black curve shows the predicted field when no
induction is included in our model. The predicted field by including induction is shown for an ocean
conductivity σ_{oc} of 5 S/m (solid black). Here the thickness of the crust is 50 km and the thickness of
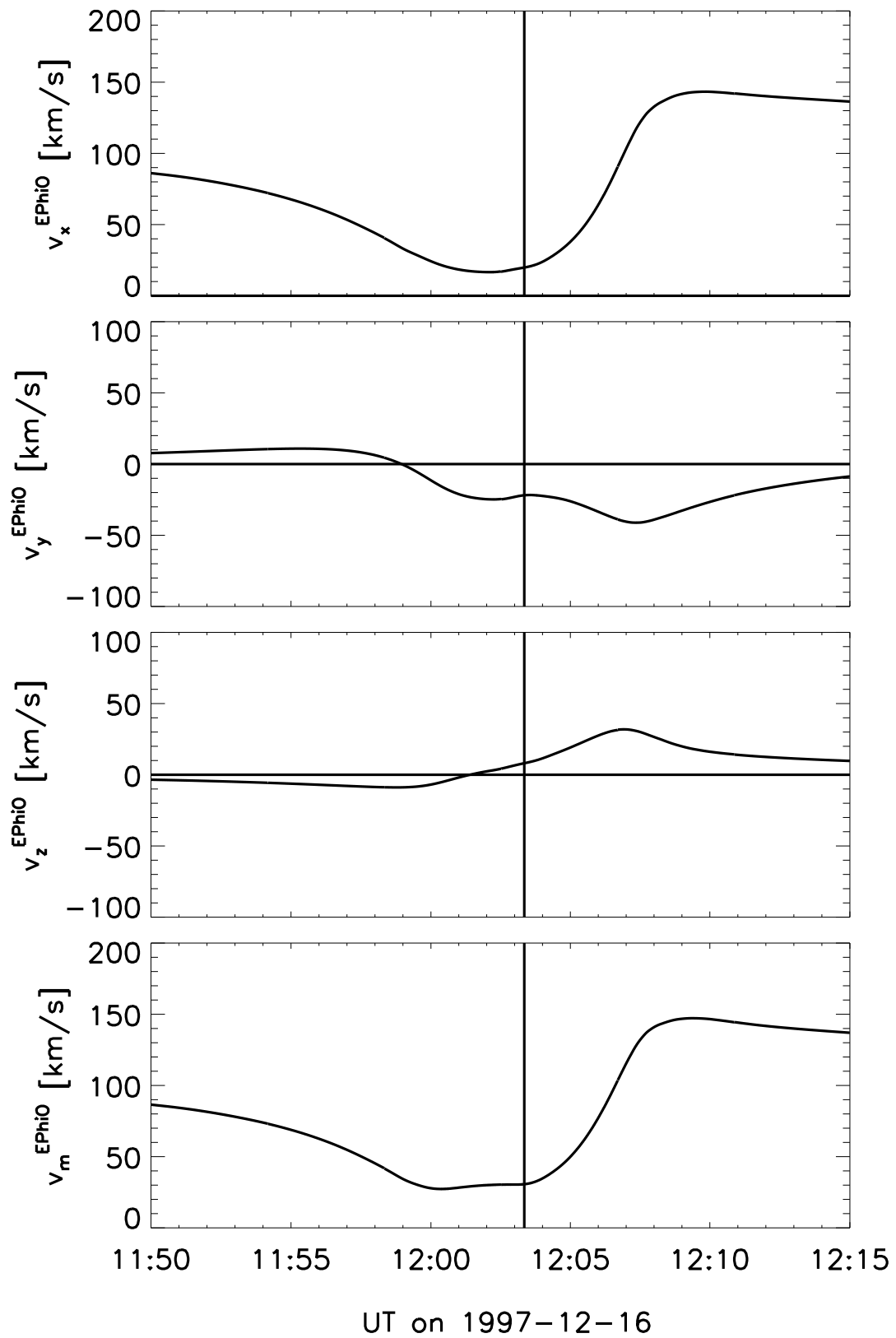the ocean is 100 km.*

Figure 6.56:   *Components of the bulk velocities during the E12 flyby. Coordinates are in EPhiO.*
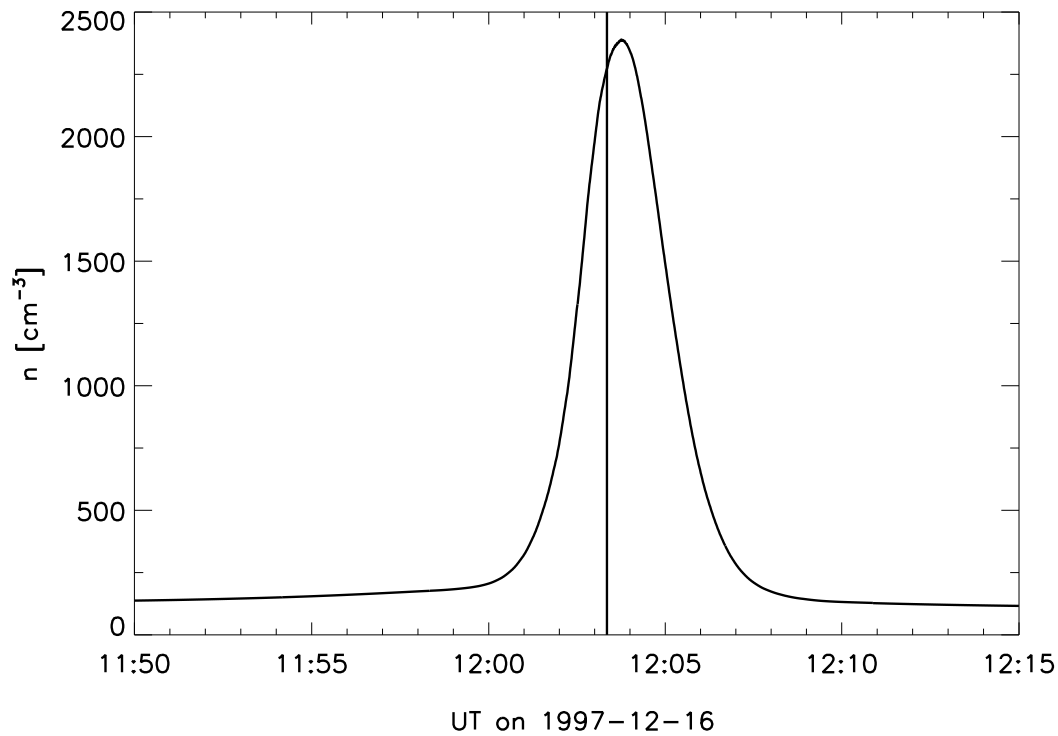*The time of closest approach is indicated by the vertical line.*

Figure 6.57:   *Ion number density during the E12 flyby. The time of closest approach is indicated by the vertical line.*

the enhancement in B_x and B_y in our model is due to the over-proportional bending of the magnetic field at this point (see Figure 6.50). There could be several reasons for the discrepancy in B_x and B_y between our model and the measured data: the dynamic magnetosphere during the E12 encounter, the detailed structure of the lower atmosphere (which might be different from our model atmosphere), or effects which are not included into our model, e.g., the Hall effect. However, we use the E12 flyby for the calibration of our model, which is done by calibrating the magnetic field magnitude of this pass. In addition, we show in section 6.2 that the plasma interaction has only a weak impact on the induction process. Hence, the results obtained for the internal conductivity distribution are not effected by the fine structure of Europa's atmosphere.

Figure 6.57 shows the ion number density along the Galileo trajectory for the E12 pass as calculated by our model. Near closest approach a density peak occurs with values up to 2400 cm^{-3}. This suggests that we cross the ionosphere of Europa. The high plasma density is then a consequence of the ionospheric plasma, generated by electron impact ionization. This is in agreement with the electron densities measured by *Kliore et al.* [1997] upstream of Europa. Results obtained from the PWS data do not show an enhanced electron density near closest approach [*Kurth et al.*, 2001]. The lack of the ionospheric signature in the PWS data is not yet understood. Since Europa is located in the middle of the magnetospheric plasma sheet

during the E12 encounter, the ionosphere should be even denser than, e.g., for the E4 flyby where Galileo radio occultation measurements were made.

6.5.5   Conclusions

In this section we have compared our model results with the Galileo flyby data. We here focused on passes that occurred when Europa was located outside the current sheet, i.e., when the inductive response is strongest. By modeling the time dependent plasma interaction of Europa with the Jovian magnetosphere we get the so far closest constraints on the conductivity and the thickness of the satellites subsurface ocean. In addition, we explain the Galileo plasma measurements [*Paterson et al.*, 1999] along the E4 trajectory. In contrast to *Kabin et al.* [1999], we see no need for a deviation of the upstreaming plasma flow from the nominal corotation direction during the E4 flyby.

The determination of the conductivity of Europa's ocean is not unambiguous. The induced magnetic field depends both on the conductivity and the thickness of Europa's internal ocean (see chapter 4). We investigate two possible extreme cases discussed in the literature. First, a subsurface ocean with a thickness of 100 km, and second a thin subsurface ocean with a thickness of 25 km. We are not able to spatially resolve the thickness of the outer ice crust. Therefore, we use a constant thickness of 50 km for this upper shell, which includes the elastic and the ductile ice layer (see section 2.1.1). However, an ice crust of 50 km represents the extreme case of a thick crust. Note that a thinner ice crust, e.g., 5 km, would lead to almost the same results, because the magnetic field at the spacecraft altitude would differ only by a few nT from that presented here.

Our results for the E14 and the E26 flyby show, that the conductivity of Europa's ocean has to be ≥ 250 mS/m when using an ocean thickness of 100 km. Using the thin ocean model (25 km), we find that the conductivity of Europa's ocean has to be larger than 1 S/m for the E14 flyby. The results of modeling the E26 pass, suggest an ocean conductivity larger than 500 mS/m. Note that because of the different flyby geometries of the passes used, the lower limit of the suggested ocean conductivity may differ from pass to pass.

Remarkably, the E4 flyby is most useful to determine the conductivity of Europa's ocean. This flyby sets even closer constraints on the conductivity distribution inside Europa than the two other flybys. Comparing our results for the E4 pass to the Galileo flyby data we find that σ_{oc} has to be in the order of 500 mS/m or larger for an assumed ocean thickness of 100 km. Assuming a thickness of 25 km for Europa's ocean, σ_{oc} has to be in the order of several S/m or larger.

In summary, we suggest the conductivity of Europa's ocean to be 500 mS/m or larger independent of the oceans thickness. Figure 4.5 shows that this is also true for a thickness of Europa's ocean larger than 100 km. We point out that we are not able to set an upper limit on the ocean conductivity since the induction is almost saturated for σ_{oc} larger than 5 S/m. In addition, we suggest that for ocean conductivities ≤ 1 S/m Europa's ocean has to be thicker than 25 km.

Finally, we remind the reader that at these high ocean conductivities no influence of the

mantle or core is visible in the data when using the synodical period of Jupiter.

6.6   Summary and Discussion

Including induction into our equations enables us to investigate Europa's interaction with the ambient magnetospheric environment in a different way than previous models. Results like the displacement and the deformation of the Alfvén current system due to induction effects are in agreement with theoretical considerations, and cannot be achieved by simply adding an internal magnetic dipole on top of a MHD-simulation.

We have shown that Europa's wake is deformed owing to induction effects. The expansion of the plasma density along the z-axis in connection with the asymmetries caused by induction explains the lacking of high ionospheric plasma densities convected downstream during the E4 pass in the Galileo measurements. With our model we are able to explain the high ionospheric densities measured by *Kliore et al.* [1997] as well as the ion number densities measured by *Paterson et al.* [1999] in the wake along the E4 trajectory. For this pass we see also no need for a rotation of the upstreaming plasma flow.

By modeling Galileo flybys, when Europa was located outside the plasma sheet, we are able to get some closer constraints on the conductivity of Europa's internal ocean. We find a conductivity of Europa's ocean of 500 mS/m or larger most suitable to explain the magnetic flyby data (regardless of thickness). If the thickness of Europa's ocean is only 25 km or less, ocean conductivities of more than 1 S/m are necessary to fit the Galileo data.

Because of the high complexity of Europa's electrodynamic interaction with the Jovian magnetosphere, we have to make some simplifications in our model. We use for instance a simplified energy equation when modeling the plasma interaction. Therefore, we have to adjust the electron impact production rate. Calibration parameters are determined by adjusting the magnetic field magnitude during the E12 pass. We neglect the direct contribution of mass loading in the energy equation. However, the influence of the internal energy on the other MHD-equations is given only by the gradient of the thermal pressure in the momentum equation. We have shown, that the thermal pressure is not the dominant pressure, and that a thermal pressure calculated by assuming an isothermal plasma yields the same structure of Europa's plasma wake, although the expansion of the plasma flow along the z-axis would be slightly increased. In a more advanced model one could include a more detailed energy equation. Then, however, the temperature of the magnetospheric electrons has to be calculated separately.

Several other mechanisms are not included into our model, e.g., the Hall effect, or finite gyroradius effects. These effects may introduce additional asymmetries in Europa's electrodynamic interaction. They might be responsible for some details of the magnetic field structure, e.g., the double peak structure of the B_x component during the E26 flyby, or the difference in B_x and B_y between our model results and the data during the E12 pass. Recent HST/STIS images indicate that Europa's atomic oxygen emission is non-uniform [*McGrath et al.*, 2004]. This might suggest that the atmosphere of Europa is inhomogeneous or vari-

able in time. An inhomogeneous atmosphere could also be responsible for some differences between our model and the measured data.

We have shown that the induced magnetic fields due to the time varying plasma interaction are small compared to those induced by the background magnetic field. Effects from an inhomogeneous atmosphere, the Hall effect, or other mechanisms discussed above would probably change some of the harmonic coefficients of the plasma induced field, but only on a small scale. Hence, they have no influence on our results on the conductivity distribution in Europa's interior. However, they may affect the lower part of Europa's ionosphere.

We are not able to resolve the solid ice crust with our model. This is also true for the lowest part of Europa's atmosphere. A higher resolution close to the surface would allow for a better study of these regions. Since the magnetic diffusivity jumps over several orders of magnitude on the surface of Europa's ocean, a higher spatial resolution would also allow for a better description of the boundary conditions on the surface.

SUMMARY

In this thesis we develop, for the first time, a model to describe the periodic time-dependent interaction of the satellite Europa with the Jovian magnetosphere. As a new feature, with regard to stationary models, we include periodic induced magnetic fields from the interior of the moon. These magnetic fields are caused by electromagnetic induction in an electric conducting ocean below the surface of Europa. By comparing our results with the Galileo measurements we can address a series of interesting questions.

A subsurface ocean on Europa would likely be very salty, and therefore, highly conductive. Thus, a time-variable magnetic field will induce currents in such an ocean which generate an induced magnetic field opposite to the inducing field. The primary time-varying magnetic field experienced by Europa is due to the rotation of Jupiter's tilted magnetic dipole. In addition, magnetospheric plasma is streaming past Europa, interacting with the moons thin atmosphere and ionosphere, and with the time-varying magnetic field from the interior of the moon. The ionosphere, formed mainly by electron impact ionization, enables a large electric current system. Since the magnetospheric plasma density and the magnetic background field at Europa vary periodically, the electric current system outside Europa also varies in time. This leads to a second order induction effect in the conducting subsurface ocean.

Our model solves the MHD-flow problem and the internal induction problem simultaneously. For the solution we make use of the periodicity and the quasi-stationarity of the problem. We extend the ideal MHD model ZEUS 3D [*Stone and Norman*, 1992*a;b*] in order to include the influence of the internal induced magnetic field and the neutral atmosphere on the plasma. Our model is a time-dependent 3D, single-fluid model that calculates self-consistently plasma density, velocity, and internal energy of the fluid, and the magnetic field. We use a simplified equation for the internal energy. In order to compensate the resulting overestimation of the electron impact production rate, we solve an additional continuity equation for the magneto-spheric electrons and implement a spatial dependent calibration factor for their temperature.

In a preparatory study, we investigate whether a fixed permanent dipole moment is present in the interior of the moon in addition to the induced dipole moment. In doing so, we fit data from several low altitude passes to models of increasing complexity. Superimposing an induced magnetic dipole moment that is driven by the time variation of the measured external magnetic field of Jupiter improves the fits and reduces the rms-error that characterizes the difference between the model and the data. The inductive response is found to be $\sim 97\%$ of the theoretical maximum inductive response for a highly conductive sphere. The largest surface equatorial field caused by a fixed internal dipole moment is less than 25 nT. This should be compared with the magnitude of the induced field which can be of order 100 nT. We thereby confirm the presence of an inductive response and conclude that the dipole coefficients of the constant intrinsic field contribute at best in a very minor way to the magnetic field.

The inclusion of the time-dependent induced magnetic fields in our model is the main advantage over previous models of Europa's interaction. This allows us, for example, to study the influence of the induction on the plasma interaction. We find that the Alfvén current system is displaced and deformed due to induction effects. This is in agreement with theoretical considerations [*Neubauer*, 1999]. When including induction, the northern Alfvén wing is displaced away from Jupiter when the moon is in the northern Jovian magnetic hemisphere, and towards Jupiter when the moon is in the southern Jovian magnetic hemisphere. The opposite is true for the southern Alfvén wing. Due to the induction, the cross section of the Alfvén wing has shrunk and the current density has become asymmetric.

Our model also allows us to calculate the plasma induced magnetic fields. We determine these fields in an iterative process. The induced magnetic fields of the plasma currents are complicated and contain higher order multipoles. The dominating terms are the quadrupole terms. The plasma induced fields are strongest when Europa is located in the center of the plasma sheet and weakest when in-between the two extreme conditions, i.e. the center of the plasma sheet and outside the plasma sheet. We find that the harmonic coefficients of the plasma induced magnetic fields are an order of magnitude smaller than the harmonic coefficients of the background magnetic field induced dipole. Therefore, we conclude that the plasma interaction only has a weak impact on the induction process. However, we would like to point out that the plasma induced magnetic field may still influence the lower part of Europa's ionosphere. In cases with stronger time variable ionospheric currents, as they may occur on Callisto, the plasma induced magnetic fields can lead to a stronger induction effect if the ocean is located close to the surface.

We compare our results to the Galileo spacecraft measurements. With our model we are able to explain the high ionospheric densities measured by *Kliore et al.* [1997]. Our model also explains what happens to the ionospheric plasma convected downstream. The plasma is swept into the wake region and is concentrated along the x-axis. Due to pressure gradients in the wake, the plasma is also accelerated away from z = 0. Thus, it is redistributed in the xz-plane. We show that the internal induced magnetic fields deform Europa's wake. As a result of the asymmetric pickup, caused by the induced magnetic fields, the highest plasma densities in the wake are found away from the equator. The expansion of the plasma density along the z-axis in connection with the asymmetries caused by induction could explain why Galileo measurements [*Paterson et al.*, 1999; *Gurnett et al.*, 1998] did not detect high densities of the

ionospheric plasma in the wake along the E4 trajectory. For the E4 pass we also see no need for a rotation of the upstreaming plasma flow.

By modeling the Galileo flybys, that occurred when Europa was located outside the plasma sheet, we are able to get some closer constraints on the conductivity of Europa's internal ocean. We find for the conductivity of Europa's ocean values of 500 mS/m or larger most suitable to explain the magnetic flyby data independent of the ocean thickness. If the thickness of Europa's ocean is only 25 km or less, the ocean conductivity has to be larger than 1 S/m. At these high values for the ocean conductivity, the induction is almost saturated. Hence, we are not able to set an upper limit on the conductivity of Europa's ocean.

The strong evidence for the presence of a deep water ocean beneath the icy surface puts Europa among the most interesting targets for planetary exploration in our solar system. A Europa orbital mission could provide more extensive time and space coverage of the magnetic field in the vicinity of Europa. This would allow for a more detailed investigation of the 3-dimensional conductivity distribution inside the moon and a determination of the thickness of Europa's ice crust. In addition, periods other than the synodic rotation period of Jupiter, e.g., Europa's orbital period or periods due to asymmetries of Jupiter's magnetosphere, would be available to an orbiting space craft, and would allow for a deeper sounding of the moons interior.

Bibliography

Anderson, J. D., E. L. Lau, W. L. Sjogren, G. Schubert and W. B. Moore, Europa's differentiated internal structure: Inferences from two Galileo encounters, *Science*, *276*, 1236–1239, 1997*a*.

Anderson, J. D., S. G. Turyshev, S. W. Asmar, M. K. Bird, A. S. Konopliv, T. P. Krisher, E. L. Lau, G. Schubert and W. L. Sjogren, Radio-science investigation on a Mercury orbiter mission, *Planet. Space Sci.*, *45*, (1), 21–29, 1997*b*.

Anderson, J. D., G. Schubert, R. A. Jacobson, E. L. Lau, W. B. Moore and W. L. Sjogren, Europa's differentiated internal structure: Inferences from four Galileo encounters, *Science*, *281*, 2019–2022, 1998.

Backes, H., *Titan's Interaction with the Saturnian Magnetospheric Plasma*, Dissertation, Institut für Geophysik und Meteorologie der Universität zu Köln, 2004.

Backus, G., R. Parker and C. Constable, *Foundations of Geomagnetism*, Cambridge Univ. Press, New York, 1996.

Bagenal, F., Empirical model of the Io plasma torus: Voyager measurements, *J. Geophys. Res.*, *99*, (A6), 11043–11062, 1994.

Banks, P. M. and G. Kockarts, *Aeronomy*, vol A, Academic Press, San Diego, Calif., 1973.

Baumjohann, W. and R. A. Treumann, *Basic Space Plasma Physics*, Imperial College Press, 1996.

Belton, M. J. S. et al., Galileo's first images of Jupiter and the Galilean satellites, *Science*, *274*, (5286), 377–385, 1996.

Billings, S. and S. Kattenhorn, The great thickness debate: Ice shell thickness models for Europa and comparisons with estimates based on flexure at ridges, *Icarus*, *177*, 397, 2005.

Blakely, R. J., *Potential Theory in Gravity & Magnetic Applications*, Cambridge Univ. Press, New York, 1995.

Brown, M. E., Potassium in Europa's Atmosphere, *Icarus*, *151*, 190–195, 2001.

Brownlee, J., H. Campins, M. Rieke, G. Rieke and C. Hergenrother, Near-infrared coma colors of comet Hale-Bopp, *Bull. American Astron. Soc.*, September 1996.

Carlson, R. W. et al., Near-infrared spectroscopy and spectral mapping of Jupiter and the Galilean satellites: Results from Galileo's initial orbit, *Science*, *274*, 385–388, 1996.

Carlson, R. W. et al., Hydrogen Peroxide on the Surface of Europa, *Science*, *283*, 2062, 1999.

Carr, M. H. et al., Evidence for a subsurface ocean on Europa, *Nature*, *391*, 363–365, 1998.

Cassen, P., R. T. Reynolds and S. J. Peale, Is there liquid water on Europa, *Geophys. Res. Lett.*, *6*, (9), 731–734, 1979.

Clarke, J. T. et al., Ultraviolet emissions from the magnetic footprints of Io, Ganymede and Europa on Jupiter, *Nature*, *415*, (6875), 997, 2002.

Connerney, J. E. P., M. H. Acuña and N. F. Ness, Modeling the Jovian current sheet and inner magnetosphere, *J. Geophys. Res.*, *86*, 8370–8384, 1981.

Crary, F. J., F. Bagenal, L. A. Frank and W. R. Paterson, Galileo plasma spectrometer measurements of composition and temperature in the Io plasma torus, *J. Geophys. Res.*, *103*, (A12), 29359–29370, 1998.

Cravens, T. E., C. N. Keller and B. Ray, Photochemical sources of non-thermal neutrals for the exosphere of Titan, *Planet. Space Sci.*, *45*, (8), 889–896, 1997.

Deschamps, F. and C. Sotin, Thermal convection in the outer shell of large icy satellites, *J. Geophys. Res.*, *106*, (E3), 5107, 2001.

Dessler, A. J., *Physics of the Jovian Magnetosphere*, Cambridge Univ. Press, New York, 1983.

Drell, S. D., H. M. Foley and M. A. Ruderman, Drag and propulsion of large satellites in the ionosphere: An Alfvén propulsion engine in space, *J. Geophys. Res.*, *70*, 3131–3145, 1965.

Durham, W. B. and L. A. Stern, Rheological Properties of Water Ice-Applications to Satellites of the Outer Planets, *Annu. Rev. Earth. Planet. Sci.*, *29*, 295, 2001.

Geissler, P. E., R. Greenberg, G. Hoppa, P. Helfenstein, A. McEwen, R. Pappalardo, R. Tufts, M. Ockert-Bell, R. Sullivan, R. Greeley, M. J. S. Belton, T. Denk, B. E. Clark, J. Burns and J. Veverka, Evidence for non-synchronous rotation of Europa, *Nature*, , (391), 368, 1998.

Goertz, C. K., Io's interaction with the plasma torus, *J. Geophys. Res.*, *85*, (A6), 2949–2956, 1980.

Goldreich, P. and D. Lynden-Bell, Io, a Jovian unipolar inductor, *Astrophys. J.*, *156*, 59–78, 1969.

Greeley, R., C. F. Chyba, J. W. Head, T. B. McCord, W. B. McKinnon, R. T. Pappalardo and P. H. Figueredo, Geology of Europa, in *Jupiter. The planet, satellites and magnetosphere*, edited by F. Bagenal, Cambridge Univ. Press, 2004.

Greenberg, R., P. Geissler, B. Tufts and G. Hoppa, Habitability of Europa's crust: The role of tidal-tectonic processes, *J. Geophys. Res.*, *105*, 17551, 2000.

Gurnett, D. A., W. S. Kurth, A. Roux, S. J. Bolton, E. A. Thomsen and J. B. Groene, Galileo plasma wave observations near Europa, *Geophys. Res. Lett.*, *25*, (3), 237–240, 1998.

Hall, D. T., D. F. Strobel, P. D. Feldman, M. A. McGrath and H. A. Weaver, Detection of an oxygen atmosphere on Jupiter's moon Europa, *Nature*, *373*, (6516), 677–679, 1995.

Hall, D. T., P. D. Feldman, M. A. McGrath and D. F. Strobel, The far-ultraviolet oxygen airglow of Europa and Ganymede, *Astrophys. J.*, *499*, (5), 475, 1998.

Hansen, C. J., D. E. Shemansky and A. R. Hendrix, Cassini UVIS observations of Europa's oxygen atmosphere and torus, *Icarus*, *176*, (2), 305, 2005.

Huba, J. D., Hall Magnetohydrodynamics - A Tutorial, in *Lecture Notes in Physics*, edited by J. Buechner, C. Dum, and M. Scholer, Lecture Notes in Physics, 166–192, Springer, 615 Auflage, 2003.

Hussmann, H., T. Spohn and K. Wieczerkowski, Thermal Equilibrium States of Europa's Ice Shell: Implications for Internal Ocean Thickness and Surface Heat Flow, *Icarus*, *156*, 143, 2002.

Ip, W.-H., Europa's oxygen exosphere and its magnetospheric interaction, *Icarus*, *120*, 317–325, 1996.

Itikawa, Y., A. Ichimura, K. Onda, K. Sakimoto, K. Takayanagi, Y. Hatano, H. Nishimura and S. Tsurubuchi, Cross sections for collisions of electrons and photons with oxygen molecules, *J. Phys. Chem. Ref. Data*, *18*, 23–42, 1989.

Jackson, D. D., Interpretation of inaccurate, insufficient and inconsistent data, *Geophys. J. R. astr. Soc.*, *28*, 97–109, 1972.

Johnson, R. E., F. Leblanc, B. V. Yakshinskiy and T. E. Madey, Energy Distributions for Desorption of Sodium and Potassium from Ice: The Na/K Ratio at Europa, *156*, (1), 136, 2002.

Johnson, R. E., R. W. Carlson, J. F. Cooper, C. Paranicas, M. H. Moore and M. C. Wong, Radiation effects on the surfaces of the Galilean satellites, in *Jupiter. The planet, satellites and magnetosphere*, edited by F. Bagenal, Cambridge Univ. Press, 2004.

Kabin, K., M. R. Combi, T. I. Gombosi, A. F. Nagy, D. L. DeZeeuw and K. G. Powell, On Europa's magnetospheric interaction: A MHD simulation of the E4 flyby, *J. Geophys. Res.*, *104*, (A9), 19983, 1999.

Kargel, J. S., S. K. Croft, J. I. Lunine and J. S. Lewis, Rheological properties of ammonia-water liquids and crystal-liquid slurries - Planetological applications, *Icarus*, *89*, 93, 1991.

Kargel, J. S. et al., Europa's Crust and Ocean: Origin, Composition, and the Prospects for Life, *Icarus*, *148*, (1), 226, 2000.

Kaufman, A. A. and P. Eaton, *The Theorie of Inductive Prospecting*, Methods in Geochemistry and Geophysics, Bd. 33, Elsevier, 2001.

Khurana, K. K., Euler potential models of Jupiter's magnetospheric field, *J. Geophys. Res.*, *102*, 11295, 1997.

Khurana, K. K., M. G. Kivelson and C. T. Russell, Interaction of Io with its torus: Does Io have an internal magnetic field?, *Geophys. Res. Lett.*, *24*, (19), 2391–2394, 1997.

Khurana, K. K., M. G. Kivelson, D. J. Stevenson, G. Schubert, C. T. Russell, R. J. Walker and C. Polanskey, Induced magnetic fields as evidence for subsurface oceans in Europa and Callisto, *Nature*, *395*, 777–780, 1998.

Khurana, K. K., M. G. Kivelson, V. M. Vasyliunas, N. Krupp, J. Woch, A. Lagg, B. H. Mauk and W. S. Kurth, The configuration of Jupiter's magnetosphere, in *Jupiter. The planet, satellites and magnetosphere.*, edited by F. Bagenal, Cambridge Univ. Press, 2004.

Kim, Y. K., K. K. Irikura, M. E. Rudd, M. A. Ali, P. M. Stone, J. S. Coursey, R. A. Dragoset, A. R. Kishore, K. J. Olsen, A. M. Sansonetti, G. Wiersma, D. S. Zucker and M. A. Zucker, Electron-Impact Ionization Cross Section for Ionization and Excitation Database (version 3.0), [Online] Available: http://physics.nist.gov/ionxsec [2006, January 4]., 1997.

Kivelson, M. G., K. K. Khurana, S. Joy, C. T. Russell, D. J. Southwood, R. J. Walker and C. Polanskey, Europa's magnetic signature: Report from Galileo's first pass on 19 December 1996, *Science*, *276*, 1239–1241, 1997.

Kivelson, M. G., K. K. Khurana, D. J. Stevenson, L. Bennett, S. Joy, C. T. Russell, R. J. Walker, C. Zimmer and C. Polanskey, Europa and Callisto: Induced or intrinsic fields in a periodically varying plasma environment, *J. Geophys. Res.*, *104*, (A3), 4609–4625, 1999.

Kivelson, M. G., K. K. Khurana, C. T. Russell, M. Volwerk, R. J. Walker and C. Zimmer, Galileo magnetometer measurements strengthen the case for a subsurface ocean at Europa, *Science*, *289*, 1340–1343, 2000.

Kivelson, M. G., K. K. Khurana and M. Volwerk, The Permanent and Inductive Magnetic Moments of Ganymede, *Icarus*, , (157), 507–522, 2002.

Kivelson, M. G., F. Bagenal, W. S. Kurth, F. M. Neubauer, C. Paranicas and J. Saur, Magnetospheric interactions with satellites, in *Jupiter. The planet, satellites and magnetosphere.*, edited by F. Bagenal, chapter 21, 513–536, Cambridge Univ. Press, 2004.

Kliore, A. J., D. P. Hinson, F. M. Flasar, A. F. Nagy and T. E. Cravens, The ionosphere of Europa from Galileo radio occultations, *Science*, *277*, (5324), 355–358, 1997.

Kuiper, G. P., Infrared observations of planets and satellites, *Astron. J.*, *62*, 295, 1957.

Kuramoto, K., Y. Saiganji and T. Yamamoto, Oscillating Magnetic Dipole Moment of Europa Induced by Jovian Magnetic Field: A Possible Probe for Detecting Europa's Ocean, *Lunar and Planetary Science*, *29*, 1254, 1998.

Kurth, W. S., D. A. Gurnett, A. M. Persoon, A. Roux, S. J. Bolton and C. J. Alexander, The plasma wave environment of Europa, *Planet. Space Sci.*, , (49), 345–363, 2001.

Lahiri, B. N. and A. T. Price, Electromagnetic induction in non-uniform conductors, *Phil. Trans. Roy.*, 509–540, 1939.

Lanczos, C., *Linear Differential Operations*, D. Van Nostrand Company, 1961.

Lane, A. L., R. M. Nelson and D. L. Matson, Evidence for sulphur implantation in Europa's UV absorption band, *Nature*, *292*, 38, 1981.

Leblanc, F., R. E. Johnson and M. E. M. E. Brown, Europa's Sodium Atmosphere: An Ocean Source, *Icarus*, *159*, (1), 132, 2002.

Liu, Y., A. F. Nagy, K. Kabin, M. R. Combi, D. L. Dezeeuw, T. I. Gombosi and K. G. Powell, Two-species, 3D, MHD Simulation of Europa's Interaction with Jupiter's Magnetosphere, *Geophys. Res. Lett.*, *27*, (12), 1791, 2000.

Lowrie, W., *Fundamentals of Geophysics*, Cambridge Univ. Press, 1997.

Mauk, B. H., D. G. Mitchell, S. M. Krimigis, E. C. Roelof and C. P. Paranicas, Energetic neutral atoms from a trans-Europa gas torus at Jupiter, *Nature*, *421*, (6926), 920, 2003.

McCord, T. B. et al., Salts on Europa's surface detected by Galileo's near infrared mapping spectrometer, *Science*, *280*, 1242–1245, 1998.

McCord, T. B. et al., Hydrated salt minerals on Europa's surface from the Galileo near-infrared mapping spectrometer (NIMS) investigation, *J. Geophys. Res.*, *104*, (E5), 11827, 1999.

McCord, T. B. et al., Thermal and radiation stability of the hydrated salt minerals epsomite, mirabilite, and natron under Europa environmental conditions, *J. Geophys. Res.*, *106*, (E2), 3311, 2001.

McGrath, M. A., E. Lellouch, D. F. Strobel, P. D. Feldman and R. E. Johnson, Satellite atmospheres, in *Jupiter. The planet, satellites and magnetosphere.*, edited by F. Bagenal, Cambridge Univ. Press, 2004.

Moroz, V. I., Infrared Spectrophotometry of the Moon and the Galilean Satellites of Jupiter, *Sov. Astron.*, *9*, (6), 999, 1966.

Nabighian, M. N., *Electromagnetic Methods in Applied Geophysics*, vol 1, Soc. Explor. Geophys., 1988.

Neubauer, F. M., Nonlinear standing Alfvén wave current system at Io: Theory, *J. Geophys. Res.*, *85*, (A3), 1171–1178, 1980.

Neubauer, F. M., Oceans inside Jupiter's moons, *Nature*, *395*, 749–750, 1998*a*.

Neubauer, F. M., The sub-Alfvénic interaction of the Galilean satellites with the Jovian magnetosphere, *J. Geophys. Res.*, *103*, (E9), 19843–19866, 1998*b*.

Neubauer, F. M., Alfvén wings and electromagnetic induction in the interiors: Europa and Callisto, *J. Geophys. Res.*, *104*, (A12), 28671+, 1999.

Pappalardo, R. T. et al., Geological evidence for solid-state convection in Europa's ice shell, *Nature*, *391*, 365–368, 1998.

Pappalardo, R. T. et al., Does Europa have a subsurface ocean. Evaluation of the geological evidence, *J. Geophys. Res.*, *104*, (E10), 24015, 1999.

Paranicas, C., R. W. McEntire, A. F. Cheng, A. Lagg and D. J. Williams, Energetic charged particles near Europa, *J. Geophys. Res.*, *105*, (A7), 16005, 2000.

Paranicas, C., R. W. Carlson and R. E. Johnson, Electron bombardment of Europa, *Geophys. Res. Lett.*, *28*, (4), 673, 2001.

Paranicas, C., J. M. Ratliff, B. H. Mauk, C. Cohen and R. E. Johnson, The ion environment near Europa and its role in surface energetics, *Geophys. Res. Lett.*, *29*, (5), 18, 2002.

Parkinson, W., *Introduction to Geomagnetism*, Scottish Academic Press, 1983.

Paterson, W. R., L. A. Frank and K. L. Ackerson, Galileo plasma observations at Europa: Ion energy spectra and moments, *J. Geophys. Res.*, *104*, 22779 – 22791, 1999.

Pedersen, L. B., Interpredation of potential field data: A generalized inverse approach, *Geophys. Prospect.*, , (25), 199, 1975.

Piddington, J. H. and J. F. Drake, Electrodynamic effects of Jupiter's satellite Io, *Nature*, *217*, 935–937, 1968.

Pospieszalska, M. K. and R. E. Johnson, Magnetospheric ion bombardment profiles of satellites: Europa and Dione, *Icarus*, *78*, 1–13, 1989.

Press, W. H., S. A. Teukolsky, W. T. Vetterling and B. P. Flannery, *Numerical Recipes in Fortran*, Cambridge Univ. Press, 2. Auflage, 1986.

Reynolds, J., *An Introduction to Applied and Enviromental Geophysics*, John Wiley, Baffins Lane, Chichester, West Sussex PO19 1UD, England, 1997.

Saur, J., D. F. Strobel and F. M. Neubauer, Interaction of the Jovian magnetosphere with Europa: Constraints on the neutral atmosphere, *J. Geophys. Res.*, *103*, (E9), 19947–19962, 1998.

Saur, J., F. M. Neubauer, J. E. P. Connerney, P. Zarka and M. G. Kivelson, Plasma interaction of Io with its plasma torus, in *Jupiter. The planet, satellites and magnetosphere*, edited by F. Bagenal, chapter 22, Cambridge Univ. Press, 2004.

Schenk, P., Thickness constraints on the icy shells of the galilean satellites from a comparison of crater shapes, *Nature*, *417*, 419, 2002.

Schilling, N., Wechselwirkung von Induktions- und Plasmaeffekten bei Europa, Diplomarbeit, Institut für Geophysik und Meteorologie der Universität zu Köln, Köln, 2000.

Schubert, G., T. Spohn and R. T. Reynolds, Thermal histories, compositions and internal structures of the moons of the solar system, in *Satellites*, edited by J. A. Burns and M. S. Mathews, Univ. of Ariz. Press, 1986.

Schunk, R. W. and A. F. Nagy, *Ionospheres - Physics, Plasma Physics, and Chemistry*, Cambridge Atmospheric and Space Science Series, Cambridge Univ. Press, Cambridge, UK, 2000.

Shematovich, V. I. and R. E. Johnson, Near-surface oxygen atmosphere at Europa, *Adv. Space Res.*, *27*, (11), 1881, 2001.

Shematovich, V. I., R. E. Johnson, J. F. Cooper and M. C. Wong, Surface-bounded atmosphere of Europa, *Icarus*, *173*, 480–498, 2005.

Sittler, E. C. and D. F. Strobel, Io plasma torus electrons: Voyager 1, *J. Geophys. Res.*, *92*, (A6), 5741–5762, 1987.

Smith, R. A. et al., The Galilean satellites and Jupiter - Voyager 2 imaging science results, *Science*, *206*, 927, 1979*a*.

Smith, R. A. et al., The Jupiter system through the eyes of Voyager 1, *Science*, *204*, (4396), 951–972, 1979*b*.

Sohl, F., T. Spohn, , D. Breuer and K. Nagel, Implications from Galileo Observations on the Interior Structure and Chemistry of the Galilean Satellites, *Icarus*, *157*, (1), 104, 2002.

Southwood, D. J., M. G. Kivelson, R. J. Walker and J. A. Slavin, Io and its plasma environment, *J. Geophys. Res.*, *85*, (A11), 5959–5968, 1980.

Spohn, T. and G. Schubert, Oceans in the icy Galilean satellites of Jupiter, *Icarus*, *161*, (2), 456, 2003.

Squyres, S. W., R. T. Reynolds, P. M. Cassen and S. J. Peale, Liquid water and active resurfacing on Europa, *Nature*, *301*, (589720), 225–226, 1983.

Srivastava, S., Theory of the Magnetotelluric Method for a Spherical Conductor, *Geophys. J. Royal Astron. Soc.*, *11*, 373–378, 1966.

Stacey, F., *Physics of the Earth*, Brookfield Press, Brisbane, 1992.

Stone, J. M. and M. L. Norman, Zeus-2D: A radiation magnetohydrodynamics code for astrophysical flows in two space dimensions. I. The hydrodynamic algorithms and tests, *Astrophys. J. Suppl. Ser.*, *80*, 753–790, 1992*a*.

Stone, J. M. and M. L. Norman, Zeus-2D: A radiation magnetohydrodynamics code for astrophysical flows in two space dimensions. II. The magnetohydrodynamic algorithms and test, *Astrophys. J. Suppl. Ser.*, *80*, 791–818, 1992*b*.

Telford, W. M., L. P. Geldart and R. E. Sheriff, *Applied Geophysics*, Cambridge Univ. Press, 2. Auflage, 1990.

Thomas, N., F. Bagenal, T. W. Hill and J. K. Wilson, The Io neutral clouds and plasma torus, in *Jupiter. The planet, satellites and magnetosphere*, edited by F. Bagenal, chapter 23, 561–591, Cambridge Univ. Press, 2004.

Torr, D. G., The photochemistry of atmospheres, in *Upper Atmosphere*, edited by J. S. Levine, 165–278, Academic Press, San Diego, Calif., 1985.

Wait, J., A Conducting Sphere in a Time Varying Magnetic Field, *Geophysics*, *16*, 666, 1951.

Ward, S. H. and G. W. Hohmann, Electromagnetic theory for geophysical applications, in *Electromagnetic methods in applied geophysics - theory*, edited by M. N. Nabighian, vol 3, Soc. Explor. Geophys., Tusla, 1987.

Weiss, J. W., Appendix 2: Planetary parameters, in *Jupiter. The planet, satellites and magnetosphere*, edited by F. Bagenal, Cambridge Univ. Press, 2004.

Wiggins, R. A., The General Linear Inverse Problem: Implication of Surface Waves and Free Oscillations for Earth Structure, *Reviews of Geophys.*, , (10), 251–285, 1972.

Zimmer, C., K. K. Khurana and M. G. Kivelson, Subsurface oceans on Europa and Callisto: Constraints from Galileo magnetometer observations, *Icarus*, 2000.

Acknowledgments

Ich versichere, dass ich die von mir vorgelegte Dissertation selbständig angefertigt, die benutzten Quellen und Hilfsmittel vollständig angegeben und die Stellen der Arbeit - einschließlich Tabellen, Karten und Abbildungen -, die anderen Werken im Wortlaut oder dem Sinn nach entnommen sind, in jedem Einzelfall als Entlehnung kenntlich gemacht habe; dass diese Dissertation noch keiner anderen Fakultät oder Universität zur Prüfung vorgelegen hat; dass sie - abgesehen von unten angegebenen Teilpublikationen - noch nicht veröffentlicht worden ist sowie, dass ich eine solche Veröffentlichung vor Abschluss des Promotionsverfahrens nicht vornehmen werde. Die Bestimmungen dieser Promotionsordnung sind mir bekannt. Die von mir vorgelegte Dissertation ist von Prof. F. M. Neubauer betreut worden.

Köln, April 2006

Teilpublikationen

Schilling, N., K.K. Khurana, M.G. Kivelson, Limits on an intrinsic dipole moment in Europa, J. Geophys. Res., 109, E5, 2004

Lebenslauf

PERSÖNLICHE DATEN

Nico Schilling
Hahnenstraße 20
50354 Hürth
geboren am 27. Juni 1974 in Chemnitz
verheiratet, Nationalität deutsch

BILDUNGSWEG

seit August 2001   **Universität zu Köln**
Promotionsstudium

09.1994 - 01.2001   **Universität zu Köln**
Studium der Geophysik
Abschluss: Diplom-Geophysiker

09.1991 - 07.1993   **Ruperti-Gymnasium**, Mühldorf am Inn
Abschluss: Abitur

09.1990 - 07.1991   **Erweiterte Oberschule**, Zschopau

09.1980 - 06.1990   **Polytechnische Oberschule des Friedens**, Ehrenfriedersdorf

BERUFLICHE TÄTIGKEITEN

seit August 2001   **Universität zu Köln**
Wissenschaftlicher Mitarbeiter

02.2001 - 08.2001   **University of California**, Los Angeles (USA)
Visitor am Institute of Geophysics and Planetary Physics

04.1998 - 01.2001   **Universität zu Köln**
Studentische Hilfskraft

SONSTIGE TÄTIGKEITEN

10.1993 - 09.1994   Grundwehrdienst in Traunstein und Füssen